Design of Monopile Foundations to Support the DTU 10 MW Offshore Wind Turbine

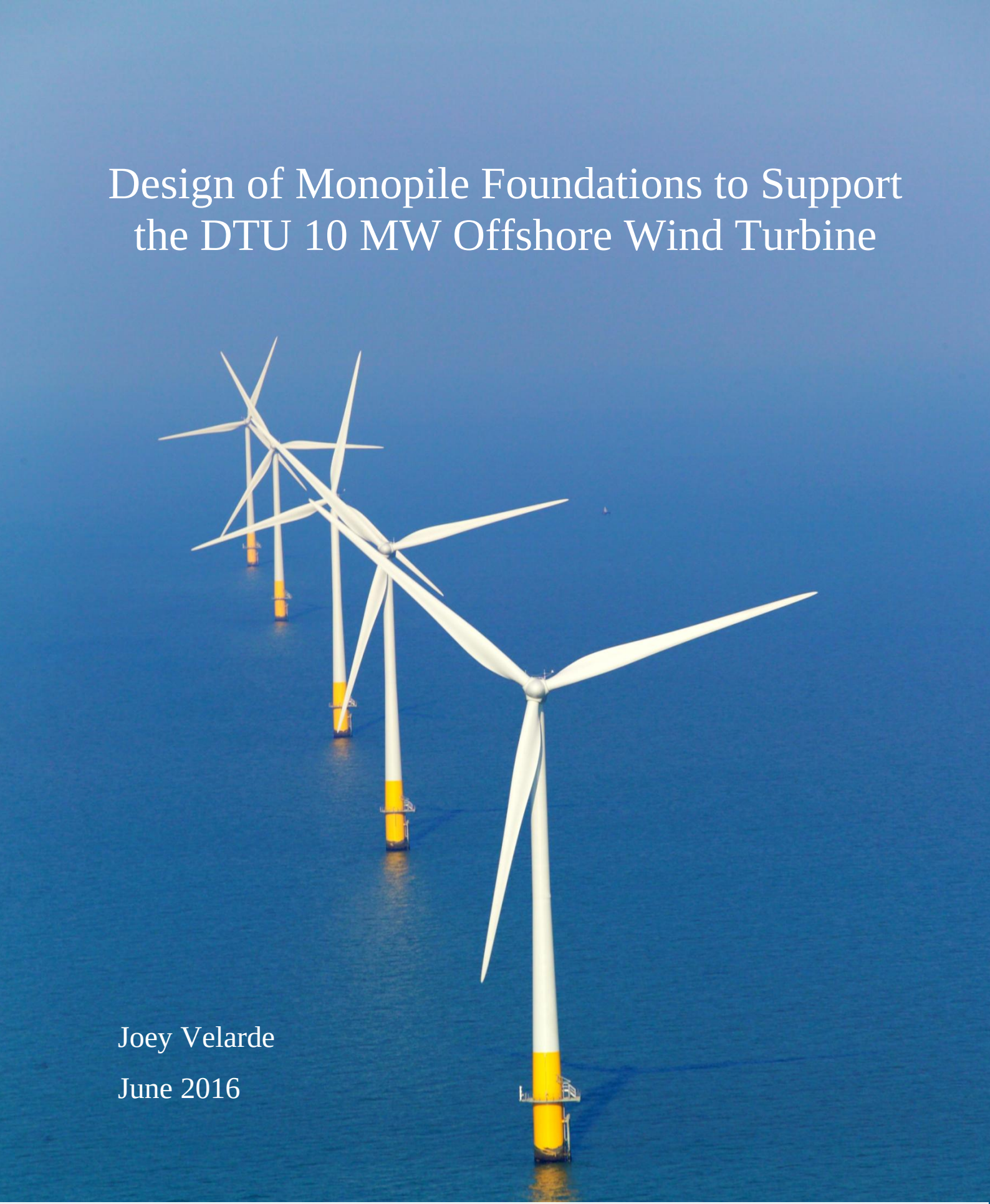

Joey Velarde

June 2016

Design of Monopile Foundations to Support the DTU 10 MW Offshore Wind Turbine

MASTER THESIS

For obtaining the degree of Master of Science in Offshore Engineering at Delft University of Technology & Master of Science in Technology-Wind Energy at Norwegian University of Science and Technology

Joey Velarde

June 2016

European Wind Energy Master – Offshore Engineering Track

Delft University of Science and Technology
Faculty of Mechanical, Maritime and Materials Engineering
Department of Maritime and Transport Technology
Section of Offshore and Dredging Engineering

Norwegian University of Science and Technology
Faculty of Engineering Science and Technology
Department of Marine Technology

Cover photo: http://www. wonderfulengineering.com

NTNU Trondheim
Norwegian University of Science and Technology
Department of Marine Technology – Group of Marine Structures

MSC THESIS IN MARINE TECHNOLOGY

SPRING 2016

FOR

STUD.TECHN. Joey Velarde

Design of monopile foundations to support the DTU 10MW wind turbine
Design av monopælfundamenter som støtter DTU 10MW referansevindturbinen

Background:

The offshore wind industry is an important part of the growing renewable energy sector. Economies of scale are pushing for larger turbines (6-10 MW), which require larger support structures. For shallow and intermediate water depths, large monopile foundations are still considered to be most promising with respect to the levelized cost of energy (LCOE). In order to design the structure, one must incorporate pile-soil interaction effects with the hydrodynamic and aerodynamic load effects.

There are many challenges in extending the use of monopile technology to larger turbines and deeper water. The typical lowest resonance period of such structures is 3-5 seconds, which coincides with the second, third and fourth excitation frequencies of ocean waves. As such, nonlinear high-frequency wave loads in relatively shallow water (15-50m) can lead to springing- and ringing-type responses. Free-surface diffraction may also become important for relatively short waves. The resonance period is partly determined by the soil-structure interaction, which is a complex problem for such large piles.

The aim of this project is to establish monopile designs (diameter, pile length, thickness) to support the DTU 10MW reference wind turbine for a reference location, taking into account the required pile depth for different water depths. In order to verify the design, a limited set of fatigue and ultimate limit state conditions should be checked.

The basic design of the monopiles will be established during the pre-thesis project. In the main thesis work, the preliminary designs will be evaluated for fatigue and ultimate limit strength. The effects of different types of hydrodynamic loading on the results for various water depths will be considered.

Assignment:
The following tasks should be addressed in the thesis work:

1. Literature study on the design of monopile foundations and hydrodynamic loads. The basic theory and methods for wind turbine aerodynamics as well as coupled dynamic analysis should be also studied.

2. Establish a representative set of wind-wave conditions for fatigue analysis and select conditions along the 50-year contour for ultimate limit state analysis.

3. Perform simulations with first order waves and Morison-type wave loading in order to estimate structural responses, including an analysis of the fatigue life and of survivability.

4. Investigate the effects of diffraction on the fatigue life by including MacCamy-Fuchs loading (computed externally to RIFLEX and applied as nodal loads). Investigate the effects of second order wave loads on the ultimate loads.

5. Examine design challenges related to different water depths.

6. Conclude the work and give recommendations for future work.

7. Write the MSc thesis report.

In the thesis the candidate shall present his personal contribution to the resolution of problem within the scope of the thesis work.

Theories and conclusions should be based on mathematical derivations and/or logic reasoning identifying the various steps in the deduction.

The candidate should utilize the existing possibilities for obtaining relevant literature.

The thesis should be organized in a rational manner to give a clear exposition of results, assessments, and conclusions. The text should be brief and to the point, with a clear language. Telegraphic language should be avoided.

The thesis shall contain the following elements: A text defining the scope, preface, list of contents, summary, main body of thesis, conclusions with recommendations for further work, list of symbols and acronyms, reference and (optional) appendices. All figures, tables and equations shall be numerated.

The supervisor may require that the candidate, in an early stage of the work, present a written plan for the completion of the work. The plan should include a budget for the use of computer and laboratory resources that will be charged to the department. Overruns shall be reported to the supervisor.

The original contribution of the candidate and material taken from other sources shall be clearly defined. Work from other sources shall be properly referenced using an acknowledged referencing system.

The thesis shall be submitted in two copies as well as an electronic copy on a CD:
Signed by the candidate
The text defining the scope included
In bound volume(s)
Drawings and/or computer prints which cannot be bound should be organized in a separate folder.

Supervisors:
Asst. Prof. Erin Bachynski (NTNU)
Prof. Gudmund Reidar Eiksund (NTNU)
Prof. Andrei Metrikine (TU Delft)
Asst. Prof. Eliz-Mari Lourens (TU Delft)

Deadline for master thesis: 17.6.2016

Abstract

Further advancements in the offshore wind industry, which come with the use of larger wind turbines at deeper water, require larger support structures. For shallow and intermediate water depths, monopile foundations still remain the most widely-used and cost-effective support structure due to the relative simplicity of fabrication and installation. The aim of this study is to investigate the challenges and feasibility of extending monopile technology for larger wind turbines and deeper water.

Preliminary monopile designs to support the DTU 10 MW reference wind turbine were established for water depths 20 m, 30 m, 40 m and 50 m. For large diameter piles, applying lateral soil stiffness derived from API method underpredicts lateral deflections at both seabed and pile toe. To properly account for the pile-structure interaction and the rigid pile behaviour, lateral soil stiffness was derived using finite element software Plaxis 3D.

To verify the preliminary design, ULS and FLS analyses were done using 1^{st} order and 2^{nd} order wave models applied with Morison's equation. For the ULS analysis, the 2^{nd} order wave model predicts a response which is 1.9 times higher than the 1^{st} order prediction for a water depth of 20 m. The sum-frequency effects and higher wave particle acceleration for the 2^{nd} order wave model explain this result. For the FLS analysis, it was found that designing monopiles for higher water depths increases contribution of hydrodynamic loads to fatigue damage. A more sophisticated wave model is desired to increase accuracy in fatigue damage prediction at deeper water.

Lastly, a method for predicting total fatigue damage using a fewer number of representative sea states is introduced. A Fatigue Damage Parameter (FDP) is established to correlate fatigue damage to environmental condition by means of parameters thrust, H_s and T_p. Using at least 30% of the total number of conditions results in at least 90% accuracy in damage prediction. The applicability of the method to other structures and environments is left for future work.

Preface

This master thesis has been conducted at Norwegian University of Technology and Science (NTNU) − Department of Marine Technology during spring semester 2016. The thesis is a requirement for completing the European Wind Energy Master program coordinated by Delft University of Technology (TU Delft).

Forever I shall remain indebted to Prof. Erin Bachynski for her immense knowledge, patience and strong supervision throughout this study. Her enthusiasm and passion for offshore wind energy research has kept me inspired and motivated to accomplish this work. Likewise, I would like to express gratitude to Prof. Andrei Metrikine and Prof. Eliz-Mari Lourens from TU Delft − Offshore Engineering Section for their critical review and suggestions to further this study. I also thank Prof. Gudmund Reidar Eiksund and PhD graduate Stian Baardsgaard Hanssen of NTNU − Department of Civil and Transport Engineering for the great support, particularly on the geotechnical issues encountered.

Pursuing this international masters program would not be possible without the scholarship and financial support from the European Commission (EC) and Global Sustainable Electricity Partnership (GSEP). There are no words to express how grateful I am to these organizations for giving me such an opportunity. Participating in this masters program has not only taught me technical skills and knowledge, but has also made me a better person for having a greater perspective in life.

Lastly, I would like to thank all the friends I met along the way, especially my fellow master students, for making the last 2 years of my life unforgettable.

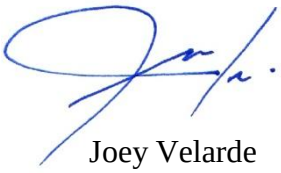

Joey Velarde

Trondheim, Norway

Contents

List of Tables

List of Figures

Nomenclature

Abbreviations

ALS	Accidental Limit State
API	American Petroleum Institute
AMSC	American Superconductor
BEM	Blade Element Momentum
DLC	Design Load Case
DNV	Det Norske Veritas
ETM	Extreme Turbulence Model
FE	Finite Element
FDP	Fatigue Damage Parameter
FFT	Fast Fourier Transform
FLS	Fatigue Limit State
HS	Hardening Soil (model)
IEC	International Electrotechnical Commission
IFFT	Inverse Fast Fourier Transform
JONSWAP	Joint North Sea Wave Observation Project (spectrum)
LE	Linear Elastic (soil model)
LAT	Lowest Astronomical Tide
LCOE	Levelized Cost of Energy
MARINA	Marine Renewable Integrated Application Platform
MC	Mohr-Coulomb (soil model)
MSE	Mean Square Error
NCM	Normal Current Model
NSS	Normal Sea State
NTM	Normal Turbulence Model
OWT	Offshore Wind Turbine
PM	Pierson-Moskowitz (spectrum)
PDF	Probability Density Function
PSD	Power Spectral Density
RNA	Rotor-Nacelle Assembly
SLS	Serviceability Limit State
SSS	Severe Sea State
ULS	Ultimate Limit State

Latin Symbols

A_p	Gross end area of pile [m^2]
A_s	Side surface area [m^2]
c	Soil cohesion [kN/m^2]
C_1, C_2, C_3	Coefficients as a function of φ' [-]
C_D	Drag coefficient [-]
C_m	Hydrodynamic mass coefficient [-]
C_M	Inertia coefficient [-]
D	Pile diameter [m]
E	Young's modulus [Pa]
f_s	Unit skin friction capacity [kPa]
k	Initial modulus of subgrade reaction [kN/m^3]
H_{max}	Maximum wave height [m]
H_s	Significant wave height [m]
$H_{s,50}$	50-Year significant wave height [m]
k	Wave number [rad/m]
K	Coefficient of lateral pressure [-]
K_C	Keulegan – Carpenter number [-]
N_q	Bearing capacity factor [-]
N_f	Number of cycles to failure [-]
p_o	Overburden pressure at the point in question [kPa]
p_o'	Effective overburden pressure at the point in question [kPa]
p_u	Ultimate bearing capacity at depth H [kPa]
P	Soil lateral reaction [N]
q	Unit end bearing capacity [kPa]
Q_d	Pile axial resistance [kN]
Q_f	Pile skin friction resistance [kN]
Q_p	Pile tip resistance [kN]
R_e	Reynolds number [-]
T	Wave period [s]
T_p	Peak Spectral Period [s]
T_z	Zero mean crossing period [s]
U	Wave-induced particle velocity [m/s]
$\dot{U}$	Wave-inducd particle acceleration [m/s^2]
U_c	Current velocity [m/s]
U_w	Wind speed [m/s]

Greek Symbols

α, β, γ	Fatigue damage parameter constants
ζ	50-year water level [m]
ζ_{el}	Wave elevation [m]
δ	Friction angle [°]
ε_{50}	Triaxial loading stiffness [kN/m^2]
ε_{ur}	Triaxial unloading and reloading stiffness [kN/m^2]
ε_{oed}	Oedometer loading stiffness [kN/m^2]
γ	Effective soil unit weight [kN/m^3]
γ_{sat}	Saturated unit weight [kN/m^3]
γ_{eff}	Effective unit weight [kN/m^3]
φ	Angle of internal friction for sand [°]
ϕ	Velocity potential [-]
ν	Poisson's ratio [-]
ω	Wave circular frequency [rad/s]
ψ	Soil dilatancy angle [°]
λ	Wave Length [m]

Chapter 1.
Introduction

The offshore wind energy market, particularly in Europe, has achieved a rapid growth in the past several years. At the end of 2014, 408 new offshore wind turbines were installed and connected to the grid, accounting for 1,484.4 MW annual installed capacity. Cumulatively, there are 2,488 offshore wind turbines giving 8045.3 MW installed capacity in 11 European countries at the end of 2014. Among these European countries, UK has the largest amount of installed capacity accounting for about 56% of the total installations [1]. The offshore wind energy's market growth is related to the European Union's renewable energy policies, which aim for at least 27% of the final energy consumption from renewable energy sources at the end of 2030 [2].

To further increase the power generation efficiency of offshore wind farms, upscaling of offshore wind turbines has been done. If designed correctly, OWT with larger capacities tend to reduce the levelized cost of energy (LCOE) due to increased power output for the same amount of space. LCOE allows direct comparison of the cost of energy generated using different technologies and is calculated as the total cost to build and operate a power-generating asset over the amount of power produced throughout its service life. This upscaling procedure leads to larger wind turbines with rated power capacities on the order of 8 MW to 10 MW. Currently, the largest wind turbine in the market is the SeaTitan 10MW wind turbine. It was developed by AMSC and it features a direct drive generator and a 190 m rotor diameter.

Larger offshore wind turbines require larger support structures. While monopile foundations still remain the most widely-used support structure due to relative simplicity of fabrication and installation, several challenges arise when extending the technology for larger wind turbines and for higher water depths. This includes potential significance of nonlinear high-frequency wave loads that can cause springing and ringing structural responses. In addition, the effect of diffraction in hydrodynamic loading can also be important especially for

relatively short waves. Lastly, the soil-structure interaction for larger monopiles greatly differs from slender and flexible piles on which current industry design methodology is based. Larger wind turbines also result in increase in loads and occurrence of nonlinear hydrodynamic effects, which has a direct impact on fatigue life of the structure.

Foundation costs account for around 25% to 34% of the total cost of an OWT [3]. This means that driving down the cost of OWT support structure could significantly reduce the cost of energy and establish offshore wind energy as a more competitive renewable energy source. Adapting a more accurate load and structural response prediction would increase the confidence in the design process, thereby avoiding over-conservative designs while maintaining an adequate factor of safety.

In this study, preliminary monopile designs for four water depths are established to support the DTU 10 MW offshore wind turbine. Pile-soil interaction is accounted by deriving nonlinear PY curves using FE method. To verify adequacy of the design, ultimate limit state and fatigue limit state analyses were conducted using representative design load cases and different hydrodynamic load models. Lastly, a method for predicting fatigue damage using fewer number of representative sea states is introduced. The proposed procedure could potentially reduce the amount of computational time in fatigue limit state analyses.

Chapter 2.

Theoretical Background & Related Work

This chapter presents literature review on the design of monopile foundations for offshore wind turbines. Theories on hydrodynamic wave models and fatigue limit states are also presented.

2.1 Design of Monopile Foundations

2.1.1 Monopile Support Structure

In general, the choice for an offshore wind support structure depends on water depth, soil conditions and environmental conditions at the project location. Shown in Figure 2.1 are different existing support structure concepts (from left to right: monopile, tripod, jacket, tri-pile, gravity base structure, spar floater, semisubmersible floater). Based on structural configuration, the type of offshore wind support structures can be divided into the following categories:

a) monopile structures
b) tripod structures
c) lattice structures
d) gravity structures
e) floating structures

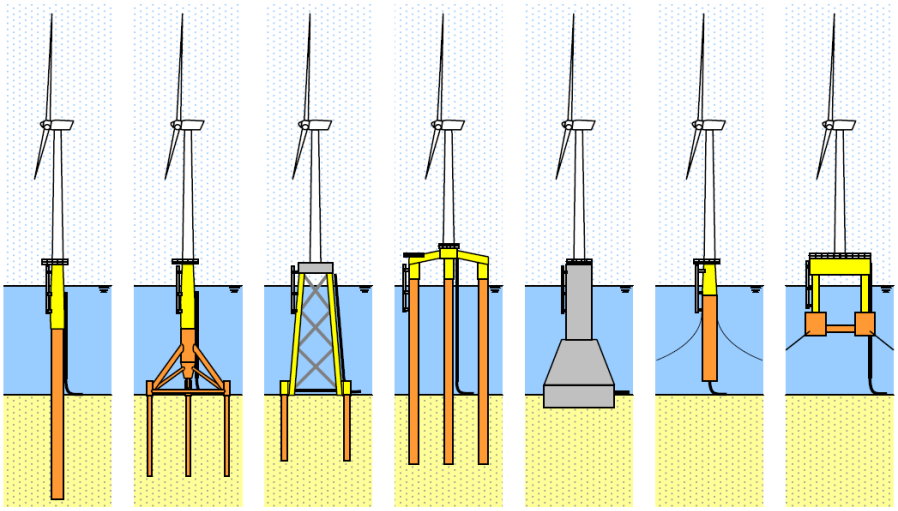

Figure 2.1 Existing support structure concepts [4]

Monopile

Monopile structures are very well applicable to water depth range of 0 to 25 [5]. Due to their simplicity of fabrication and installation, it remains to be the most common type of offshore wind turbine support structure installed up to date. Figure 2.2 shows that during 2014, 91% of fully installed European OWT were founded on monopiles. Cumulatively, it remains to be the most common type at 78.8% share, followed by gravity-based foundations, jacket and tripod at 10.4%, 4.7% and 4.1%, respectively [1].

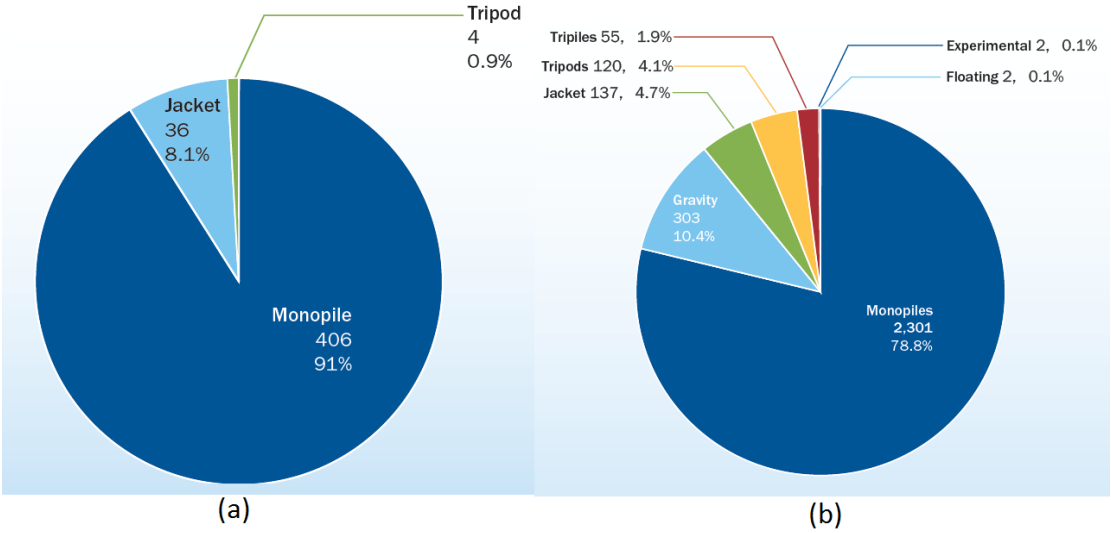

Figure 2.2 Share of substructure types at the end of 2014 (a) year 2014 (b) cumulative [1]

A monopile support structure is exposed to both horizontal and vertical loads. The horizontal loads are transferred to the soil by mobilizing lateral resistance of the soil through bending, while the vertical loads are carried by the pile wall friction and tip resistance. The pile diameter shall be large enough to provide required stiffness.

The limitation of the monopile concept is its applicability for higher water depths. As the water depth increases, the required diameter to provide enough stiffness also increases. Fabrication and installation of very large-diameter piles can be difficult due to limitations on available steel plates sizes and pile driving capacity, respectively [4]. In addition, conventional pile driving techniques generate noise that concerns surrounding marine life.

Components of monopile-supported OWT

Offshore wind turbine components are illustrated in Figure 2.3. A monopile consists of a large-diameter steel tube called foundation pile, which is driven into the seabed using a steam or hydraulic-powered hammer. The foundation pile, transition piece and tower are the main components of the support structure, which holds the rotor-nacelle assembly (RNA). The nacelle houses electronic and mechanical parts of the turbine, such as gearbox and generator.

The foundation pile is the part that transmits the loads acting on the wind turbine into the seabed, where the load is taken by subgrade reaction. It is connected to the tower by the transition piece by means of grouting. The transition piece allows installation of appurtenances such as boat landing, ladder and platform, and can be used to correct misalignments during pile driving to have a vertical tower. The foundation pile and transition piece assembly defines the ”substructure”, which is connected to the RNA by the tower.

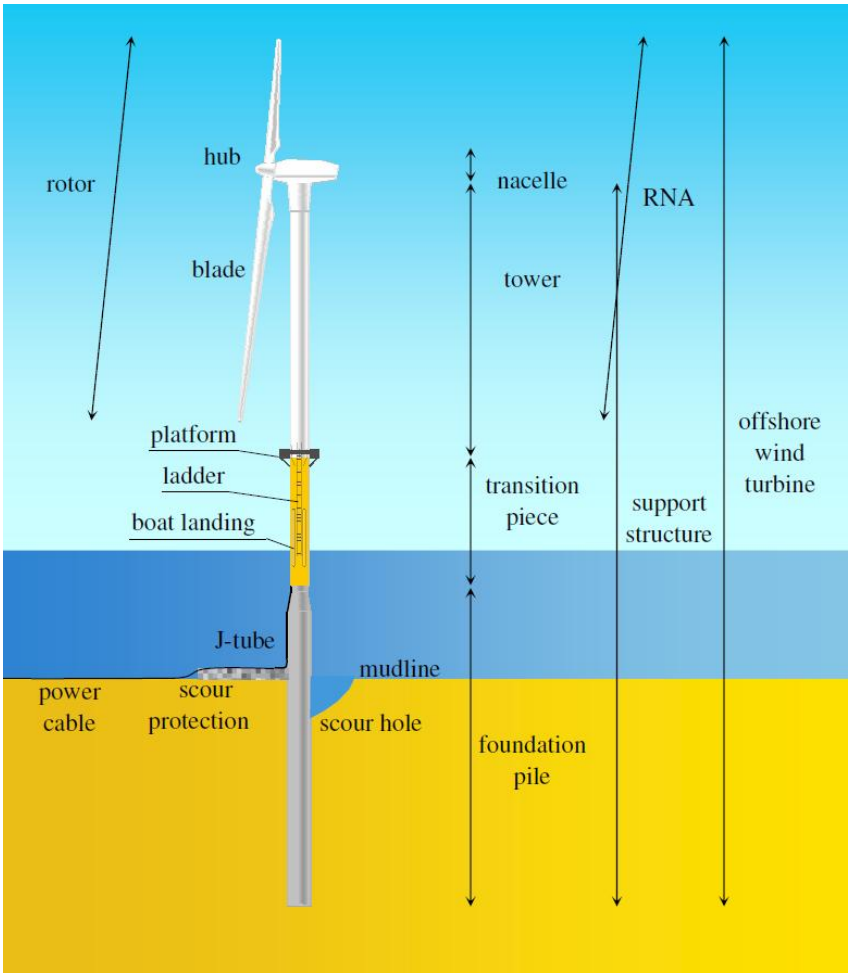

Figure 2.3 Offshore wind turbine components [6]

2.1.2 Design Methodology

The general function of an offshore wind turbine is to generate electricity at high efficiency. To achieve this function, the support structure shall be designed such that the wind turbine can withstand all loads during its service life. For a monopile foundation, the self weight generates the axial loads while wind and wave generate torsional loads, lateral loads and bending moments in the structure. The relatively high bending moments usually govern the design of the foundation. The main objective of the design of support structure is to determine the dimensions of its components, taking into account operability, load resistance and economics [4]. A design life of at least 20 years is recommended by IEC [7].

For the design of bottom-fixed offshore wind support structures, the following recommendations and standards are highly relevant:

a) IEC 61400-1,2005 (Wind Turbines - Part 1: Design Requirements)
b) IEC 61400-3,2009 (Wind Turbines – Part 3: Design Requirements for offshore wind turbines) [7]
c) DNV-OS-J101, 2014 (Design of Offshore Wind Turbine Structures) [5]
d) GL Guideline for the Certification of Offshore Wind Turbine, 2012 [8]

Design Sequence

The International Electrotechnical Commission (IEC) outlines the design process for an offshore wind turbine system as shown in Figure 2.4. The procedure starts with defining site-specific external conditions, which mainly include wind, wave and current data, bathymetry and soil conditions. Using the information on the site conditions and wind turbine, a design basis is formulated common to both support structure design and RNA design. The design is an iterative process and is completed once it is able to satisfy all applicable design load cases and limit states set by design standards. An integrated wind turbine design is typically adapted, which considers the dynamic interaction between the RNA, tower, and the support structure.

In current industry practice, the wind turbine manufacturer takes responsibility for the verification of the RNA, while the support structure design verification is done by the designer [4].

The details on the design procedure for a monopile support structure are shown in Figure 2.5. The process starts by determining the design elevations and allowed natural frequency using both environmental data and wind turbine properties. An iterative procedure is adapted in determining the required pile diameter, thickness and embedment depth. Current monopile design practice suggests that the initial pile length shall be set equal to ten times the monopile diameter (10D). The pile length is then reduced until desired foundation stiffness is achieved, while still satisfying pile stability requirements [9]. The pile dimensions are optimized and the

design is completed once the structure satisfies requirements on natural frequency, stability, structural strength and fatigue.

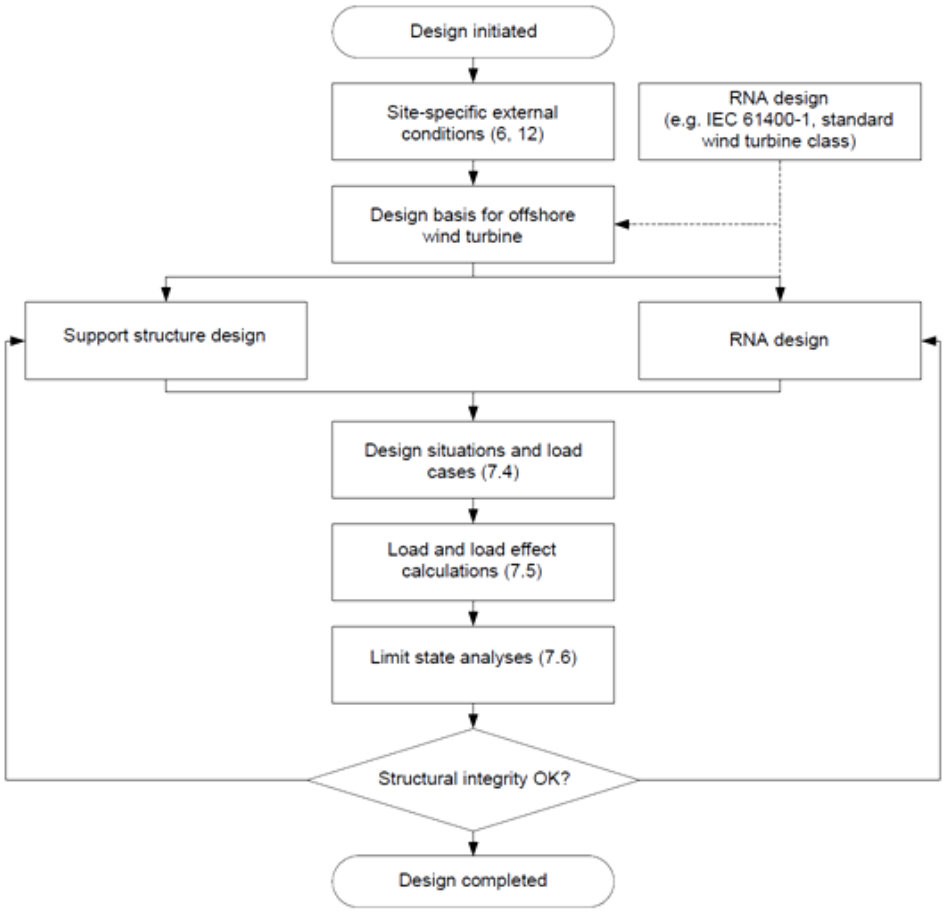

Figure 2.4 Design Process for an offshore wind turbine [7]

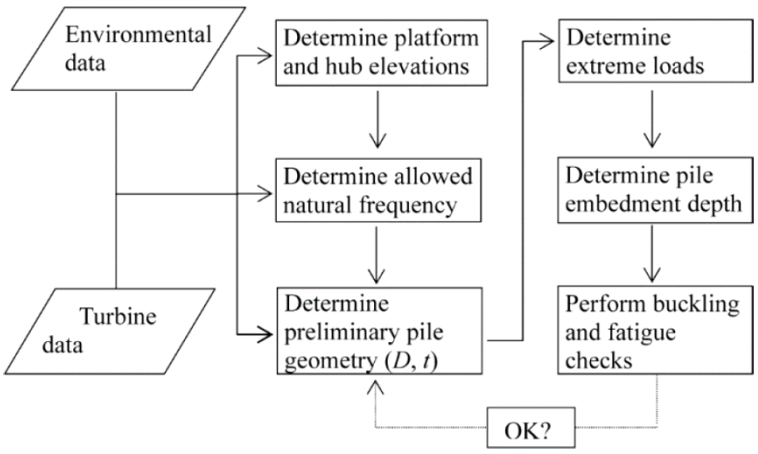

Figure 2.5 Design process for a monopile support structure [10]

Limit States

Following the simulation of the design load cases and calculation of corresponding load and load effects, limit state analyses shall be performed. The following limit states shall be satisfied:

a) Ultimate Limit State (ULS)
b) Serviceability Limit State (SLS)
c) Accidental Limit State (ALS)
d) Fatigue Limit State (FLS)

The ULS analysis verifies that the structural strength and stability of the members, as well as the strength of the connecting joints, are within the acceptable values. The SLS analysis verifies that the maximum deformations of the structure are within the acceptable values during operation. In particular, the RNA and the pile deflections are investigated. The ALS analysis considers the effect of impacts due to ship collision in the support structure and dropped heavy objects. Lastly, the FLS analysis verifies that the structure is able to withstand accumulated damage throughout structure's design life [4].

2.1.3 Design Criteria

The support structure shall satisfy strength requirements and allowable deformations during operation. In addition to having a sound structural integrity, the support structure shall permit the offshore wind turbine to perform its intended functions. Requirements for a wind turbine that shall be considered in the design of the support structure are summarized as follows [4]:

a) The hub height should be set such that it results in high efficiency and adequate safety
b) Cables and other electrical appurtenances for exporting the generated power shall be considered in the design
c) Access for operation and maintenance shall be considered in the design
d) Enough clearance between the blades and the structure shall be observed
e) Motion and acceleration of the RNA shall be limited to avoid damage to components

This section discusses criteria on design elevations, natural frequency, strength and allowable deformation to make sure that the above-mentioned requirements are satisfied by the design.

Design Elevations

The preliminary design of a support structure is based mainly on established design elevations, mainly the interface level and the hub height. The interface level defines the elevation of the interface between the tower and the substructure, and also defines the location of the main platform. The interface level must be high to minimize hydrodynamic loads on the platform. This elevation is determined from the highest crest elevation, which is defined by the 50-year highest still water level and 50-year storm surge [4]. In addition, an air gap is included to avoid loads due to wave run-up. The determination of the interface level is illustrated in Figure 2.6.

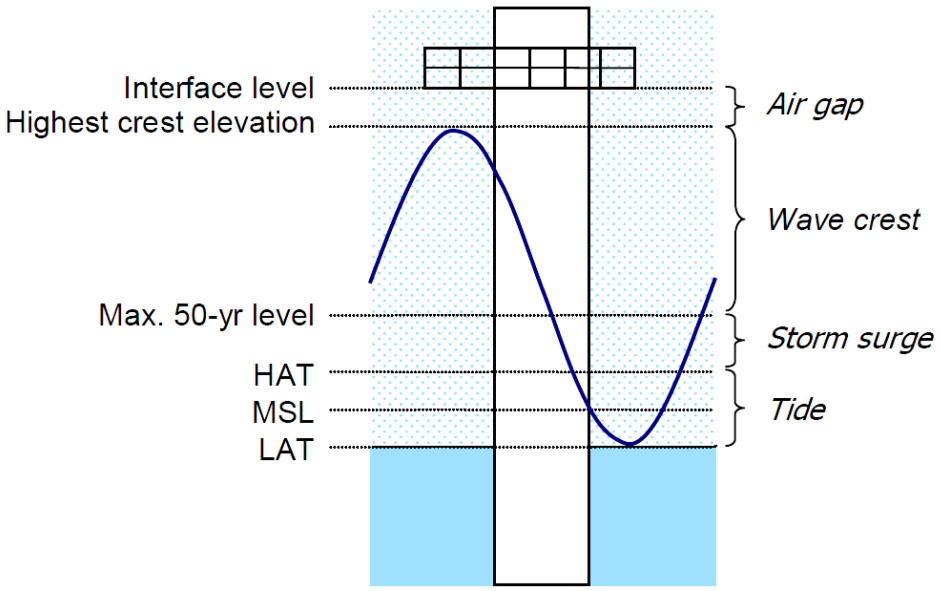

Figure 2.6 Determination of interface level [4]

For offshore wind turbines, the hub height is selected as low as possible to minimize overturning moment due to aerodynamic loads [4]. The hub height can be calculated from the defined interface level by setting a blade clearance. The interface level, hub height, 50-year water level (ζ) and maximum wave height (H_{max}) are defined by the following equations, respectively [5]:

$$z_{interface} = LAT + \Delta z_{tide} + \Delta z_{surge} + \zeta + \Delta z_{airgap} \tag{2.1}$$

$$z_{hub} = z_{interface} + \Delta z_{clearance} + \frac{1}{2} D_{rotor} \tag{2.2}$$

$$\zeta = 0.65\, H_{max} \tag{2.3}$$

$$H_{max} = 1.86\, H_{s,50} \tag{2.4}$$

where:

LAT = lowest astronomical tide

Δz_{tide} = tidal range

Δz_{surge} = 50 year storm surge

Δz_{airgap} = air gap, typically 1.5 m

$\Delta z_{clearance}$ = blade clearance, typically 5 - 8 m

ζ = 50-year water level

$H_{s,50}$ = 50-year significan wave height

H_{max} = maximum wave height

Natural Frequencies

The overall natural frequency of an offshore wind turbine is a major design driver for the support structure as it defines the structure's dynamic behaviour. The support structure shall be designed such that the overall natural frequency does not coincide with the frequency of excitation. This avoids the occurrence of resonant behaviour of the structure, which could significantly amplify the stresses and contribute to fatigue damage or failure.

Offshore wind turbines are subject to excitations due to wind and waves. For wave excitation, mild sea states are associated with higher wave frequencies. This further reduces the ideal frequency range. For wind excitation, the frequency is governed by the rotational frequency (1P) of the rotor. The rotational frequency is a defined by the range starting at the minimum rotational speed at cut-in wind speed and ending at the maximum rotational speed. In addition, the blade passing frequency (3P) shall also be avoided in the design. This accounts for the excitation generated when each blade passes by the tower.

Strength Criteria

Two failure modes are considered in the strength design criteria, which are (1) yielding and (2) buckling. Yielding occurs when the stress in the material exceeds the yield strength or the elastic limit, which results in permanent deformations. Buckling, on the other hand, refers to sudden collapse of the structure either globally or locally. Global buckling is usually caused by a compressive force less than the ultimate compressive strength of the material. The slenderness of the element highly influences the probability of global buckling occurrence. Local buckling refers to structural instability that occurs locally along the structural element. Relevant parameters for buckling analysis include [4]:

a) slenderness parameter
b) buckling length
c) normal force in the structure or element
d) bending moment in the structure or element

For foundation piles, yielding is considered to be the more critical failure mode. The soil supporting the pile, both externally and internally, makes buckling less likely to occur [4].

Foundation Stability Criteria

According to DNV [5], the design criteria for monopile foundations is divided into (1) axial loading and (2) combined lateral and moment loading. For laterally loaded piles founded in sand, the deformation criteria are more critical than the ultimate lateral capacity. For axially loaded piles, the ultimate capacity is considered to be more critical [4].

Lateral Stability

In combination with the API standard, the criteria set by the Germanischer Lloyd (GL) in the "Guideline for the Certification of Offshore Wind Turbines" are usually employed. For lateral loading of the pile, the criteria include the so-called "vertical tangent" or "zero-toe-kick" criterion, which states that the neutral line of the pile under maximum horizontal loading must be vertical for at least one location [8]. The other 2 criteria relates to the maximum lateral deflections at the mudline and pile toe, respectively. Since there are no specific values stated in GL (2012), values for maximum deflections adopted by TU Delft based on practical experience are adopted for this study as well [9]. In addition, DNV [5] suggests a maximum rotation at the pile head, which is defined to be at the same level as the seabed. It states that the maximum rotation at the pile head should be less than $0.50°$, coming from a $0.25°$ installation tolerance and $0.25°$ accumulated rotation at seabed. The 4 criteria are summarized as follows:

a) A vertical tangent criterion or "zero-toe-kick" criterion at the monopile's deflection curve
b) A maximum lateral deflection at mudline of 120 mm
c) A maximum lateral deflection at pile toe of 20 mm
d) A maximum rotation at mudline of 0.50°

For large-diameter piles, satisfying the vertical tangent criterion requires a flexible pile behaviour. Figure 2.7 illustrates how flexible and rigid piles behave under static loading. Since the rigid pile tends to rotate rigidly when subjected to large lateral loading, it results in a "toe-kick" at the deep end of the pile. Adopting the vertical tangent criterion for rigid piles leads to increasing the pile length until flexible behaviour is reached [9], and satisfying such criterion leads an inefficient design in economic point of view.

Axial Stability

DNV [5] requires that the design axial load on the pile head does not exceed the design axial resistance, which is calculated from the pile skin friction and pile tip resistance. The design axial resistance can be calculated using the following equations from API [11]:

$$Q_d = Q_f + Q_p \tag{2.5}$$

$$Q_f = f_s A_s \tag{2.6}$$

$$Q_p = q A_p \tag{2.7}$$

where:

Q_d [kN]= axial pile resistance

Q_f [kN]= skin friction resistance

Q_p [kN]= pile tip resistance

f_s [kPa]= unit skin friction capacity

A_s[m^2]= side surface area

q [kPa]= unit end bearing capacity

A_p[m^2]= gross end area of pile

For piles in cohesionless soil, the shaft friction (f) and end bearing capacity (q) can be calculated as follows:

$$f = Kp_o \tan\delta \tag{2.8}$$

$$q = p_o{}' N_q \tag{2.9}$$

where:

K [-]= coefficient of lateral pressure

p_o [kPa]= overburden pressure at the point in question

δ [-]= friction angle

$p_o{}'$ [kPa]= effective overburden pressure at the point in question

N_q [-]= bearing capacity factor

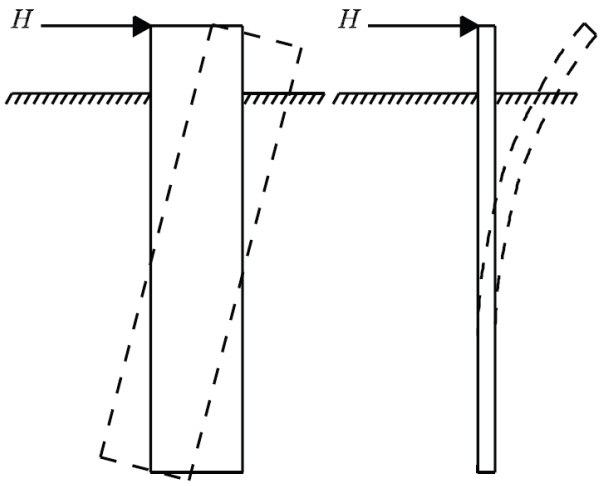

Figure 2.7 Flexible versus rigid pile behaviour [12]

2.1.4 Design Loads

For ULS, DNV [5] recommends that the characteristic values of environmental loads or load effects shall be taken as the 98% quantile in the distribution of the annual maximum loads or load effect. This results in a design loads having a return period of **50 years** as shown in Table 2.1.

Table 2.1 Statistical terms used for characteristic loads and load effects [5]

Term	Return Period [years]	Quantile in distribution of annual maximum	Probability of exceedance in distribution of annual maximum
100-year value	100	99% quantile	0.01
50-year value	50	98% quantile	0.02
10-year value	10	90% quantile	0.10
5-year value	5	80% quantile	0.20
1-year value	-	Most probable highest value in one year	

2.1.5 Soil-structure interaction

Current Practice

In modeling soil-monopile interaction, the current practice follows recommendations from American Petroleum Institute (API) which is the so-called “p-y method”. The method is a Winkler-type approach, which employs uncoupled nonlinear springs represented by the p-y curves to support the monopile along the embedded length as illustrated in Figure 2.8. This p-y relation is empirically derived from piles with diameters of approximately 2 meters or less, which implies a flexible pile behaviour [9].

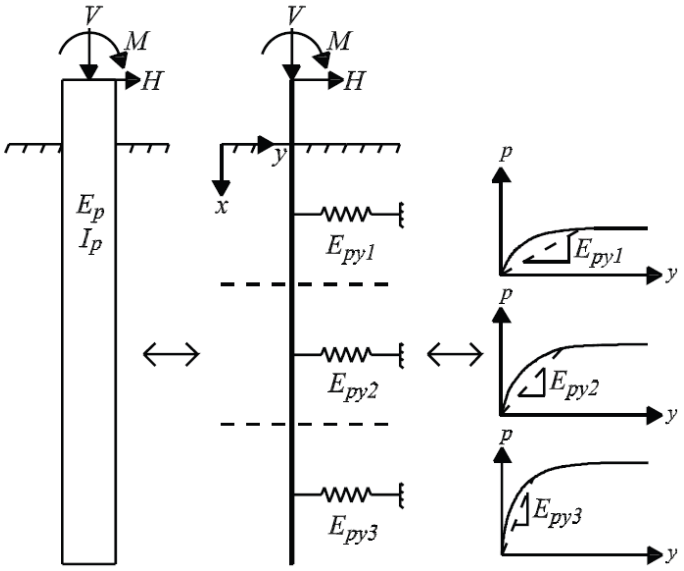

Figure 2.8 Winkler model approach [12]

Typically, monopiles supporting offshore wind turbines have diameters ranging from 3 to 5 meters and embedment lengths ranging from 20 to 30 meters. It depends on both load magnitude and soil conditions, but usually the pile length to pile diameter ratio (L/D ratio) is approximately equal to 5 [13]. The API method is based on testing of two identical steel piles with L/D ratio of 34.4, while currently installed monopiles have L/D ratio of less than 10 [12]. This leads to the pile behaviour to be "rigid" rather than being flexible. Thus, the p-y method may not be accurate for predicting soil-structure interaction for large-diameter monopiles due to different pile behaviour and soil reaction mechanisms between a flexible and a rigid pile [14].

To have a more accurate p-y relation for rigid piles, a 3D finite element model can be alternatively employed.

API Method

The lateral soil resistance-deflection relationship (p-y curve) is non-linear and varies along the depth (H) of the monopile. API approximates the p-y relation of sand as a function of the ultimate lateral bearing capacity (p_u), which depends whether the soil is in shallow depth or deep depth. The ultimate lateral bearing capacity is taken as the smaller value between the 2 conditions. The following expressions are recommended by API in constructing p-y curves for sand:

$$P = A\, p_u \tanh\left[\frac{k\, H}{A\, p_u} y\right] \tag{2.10}$$

$$p_{us} = (C_1\, H + C_2\, D)\, \gamma H \quad \text{for shallow depths} \tag{2.11}$$

$$p_{ud} = C_3\, D\, \gamma\, H \quad \text{for deep depths} \tag{2.12}$$

$$p_u = min\{p_{us}, p_{ud}\} \tag{2.13}$$

where:

A = factor to account for cyclic or static loading condition, given by:

$A = 0.9$ for cyclic loading

$A = \left(3 - 0.8\frac{H}{D}\right) \geq 0.9$ for static loading

P = soil reaction

y = lateral deflection (m)

p_u = ultimate bearing capacity at depth H (kN/m)

k = initial modulus of subgrade reaction (kN/m^3)

H = depth of soil below mudline (m)

γ = effective soil unit weight (kN/m^3)

φ’ = angle of internal friction for sand (deg)

C_1, C_2, C_3 = coefficients as a function of φ'

D = pile diameter (m)

The initial modulus of subgrade reaction (k) and the coefficients (C_1, C_2, and C_3) are both functions of the angle of internal friction (φ') and are determined from Figure 2.9 – (a) and (b), respectively.

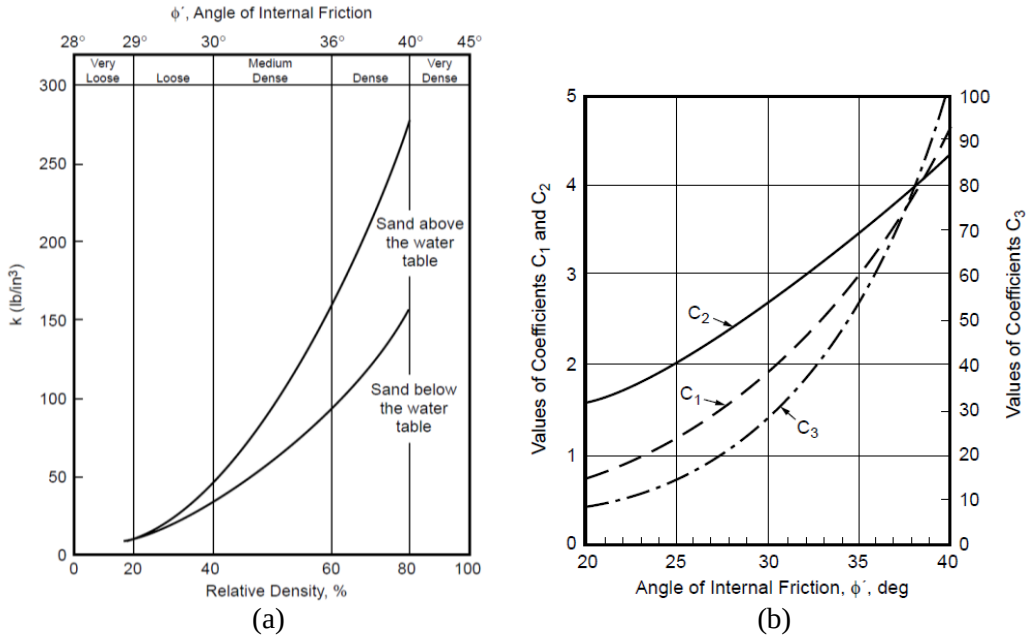

Figure 2.9 Initial modulus of subgrade reaction (a) and (b) coefficients [11]

Finite Element Method

Modeling soil-pile interaction in commercial finite elements (FE) programs, such as PLAXIS and ABAQUS, removes uncertainty associated with the pile behaviour being rigid [13]. It allows modeling the interface between pile and soil, accounting material properties of both media.

Material Models in Plaxis 3D

Plaxis 3D, as the name suggests, is a three-dimensional finite element program primarily used in the analysis of deformation, stability and groundwater flow in the field of geotechnical engineering. The program features include the use of "Boreholes" to define soil strata, "High-order elements" to model deformations and stresses in soil, "Interfaces" to simulate thin zones for soil-structure interaction and "Stress paths" for visualizing load-displacement curves and stress-strain diagrams [15].

Several advanced constitutive models are available to simulate the non-linear and time-varying soil and/or rock behaviour. The soil stress-strain behaviour, for instance, is highly non-linear and can be modelled at different levels of accuracy depending on how much information is available. Among several models available, the Linear Elastic model, Mohr-Coulomb model and Hardening Soil model are selected and discussed as follows [16]:

a) Linear Elastic model (LE)

The Linear Elastic model is based on Hooke's law of isotropic linear elasticity. The model is not applicable in modeling soil behaviour, but is mainly used to model behaviour of stiff structures in the soil such as concrete walls. This model implies infinite soil strength since the stress states are not limited in this model. The model requires 2 elastic parameters, i.e. Young's Modulus (E) and Poisson's ratio (ν).

b) Mohr-Coulomb model (MC)

The Mohr-Coulomb model is a linear elastic perfectly plastic model. It is a first order approximation, wherein a constant average stiffness or a constantly increasing stiffness for each soil layer is estimated. The model requires 5 input parameters, i.e. E and ν for soil elasticity, friction angle (φ) and cohesion (c) for soil plasticity, and dilatancy angle (ψ). The limiting stress states are based on parameters φ, c and ψ.

c) Hardening Soil model (HS)

The Hardening soil model is considered as an advanced soil model. Similar to the Mohr-Coulomb model, the limiting stress states are based on parameters φ, c and ψ. The difference lies in estimating the soil stiffness, where the HS model uses the following stiffness parameters: the triaxial loading stiffness (ε_{50}) , the triaxial unloading and reloading stiffness (ε_{ur}), and the oedometer loading stiffness (ε_{oed}). These stiffness parameters are illustrated from typical triaxial test and oedometer test results shown in Figure 2.10. Another difference is that the HS model uses a hyperbolic stress-strain curve, which offers a better estimate than a bi-linear curve in the Mohr-Coulomb model.

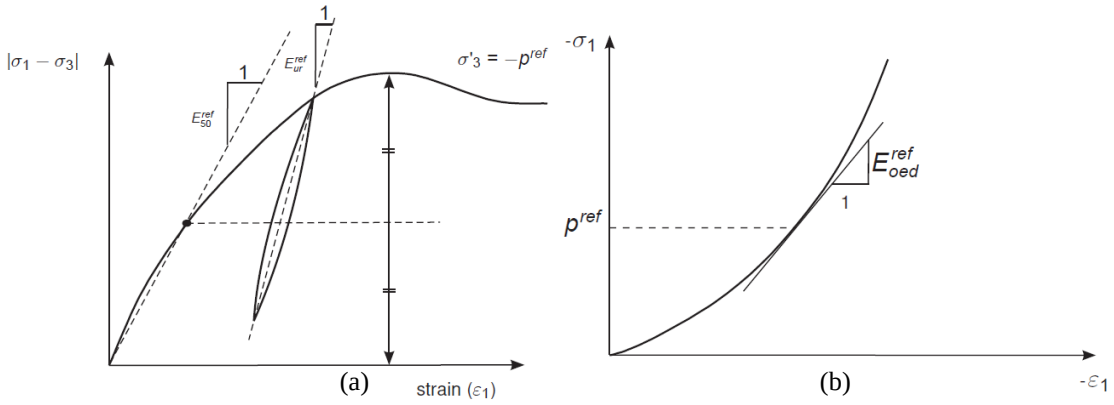

Figure 2.10 Soil stiffness parameters
(a) E_{50}^{ref} and E_{ur}^{ref} for drained triaxial test; (b) E_{oed}^{ref} in oedometer test [16]

Extraction of soil springs

NTNU PhD candidate Stian Baard Overgaard Hanssen developed a methodology in extracting soil reaction springs from Plaxis 3D. This approach is valid for circular pile placed in an arbitrary soil volume. The pile displacements (y-values) are given as default output of node values in Plaxis 3D output program, whereas the corresponding p-values are found by integration of horizontal stresses at the soil-pile interface [17].

The mentioned methodology for extracting the p-values in hollow cylindrical monopiles involves creating "interface" for both the outer (positive interface) and inner (negative interface) regions of the pile to account soil-structure interaction on both sides. The stress distribution along the circumference of a rigid structure subjected to lateral loading is illustrated in Figure 2.11. For large-diameter structures, shear tractions along the circumference of the structure, in addition to lateral reactions of the soil, must be considered in response analysis [18].

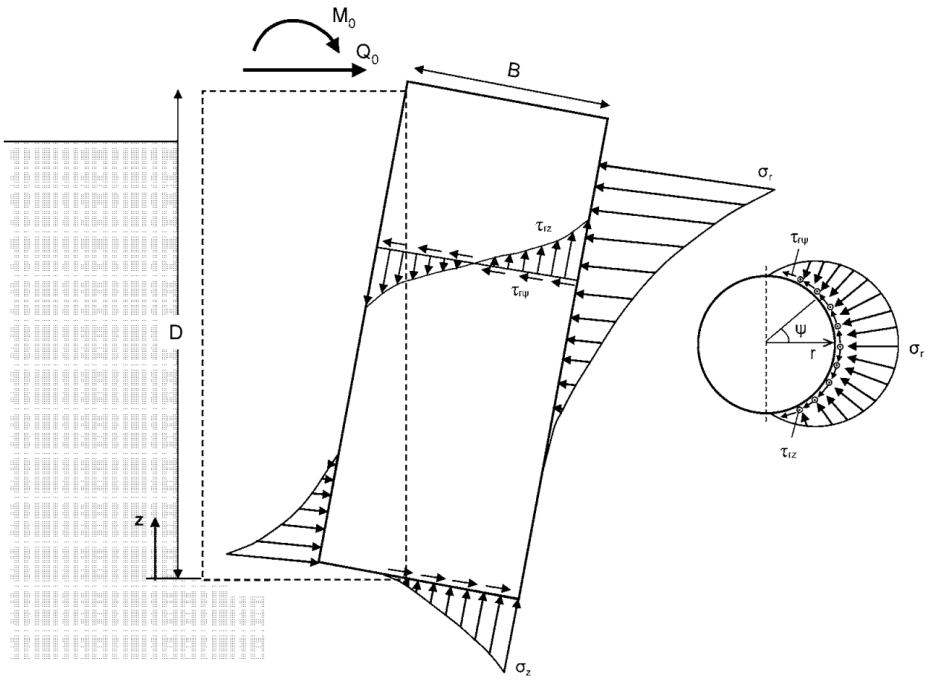

Figure 2.11 Stresses at pile-soil interface [modified figure from 18]

The stress along the direction of the applied load (x-direction) is calculated for each node of the elements along the circumference of the pile by projection of both normal and shear stresses as illustrated in Figure 2.12. From trigonometry, the stress in x-direction of each node is given by:

$$\sigma_x = \sigma_N \cos\alpha + \tau_{r\alpha} \sin\alpha$$

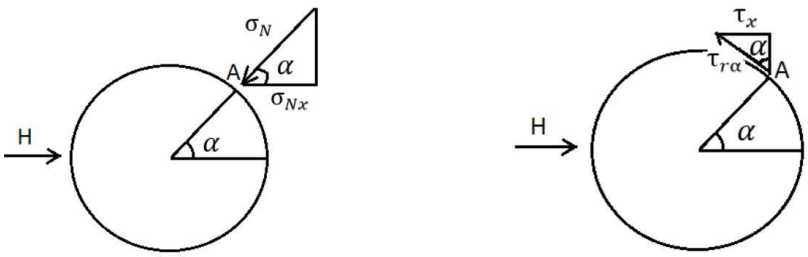

Figure 2.12 Projection of normal and shear stresses in loading direction [19]

Knowing the x-component of the stresses at each node of the elements, the x-component of the stresses for each Gaussian integration point ($\boldsymbol{\sigma_{x,i}}$) is calculated from the shape functions ($\boldsymbol{N_j}$), where j is the node number. The representative stress in each element in x-direction ($\boldsymbol{\sigma_x}$) can be then calculated from the stresses in the Gaussian integration points [19]. Information about the shape functions, integration points and element applied in Plaxis 3D is presented in Appendix A.

Finally, the total force per unit length (p) is calculated by summing up the contributions from all elements in a row and dividing it by the height of the element row (dz) using the following expression:

$$p = \frac{\sum_1^k \sigma_{x,i} A_i}{dz} \tag{2.14}$$

The height of the element row (dz) is illustrated in Figure 2.13. It should be noted that each row of elements corresponds to a single point in the p-y curve. Thus, the number of points in the p-y curve depends on the size of the element or structured mesh.

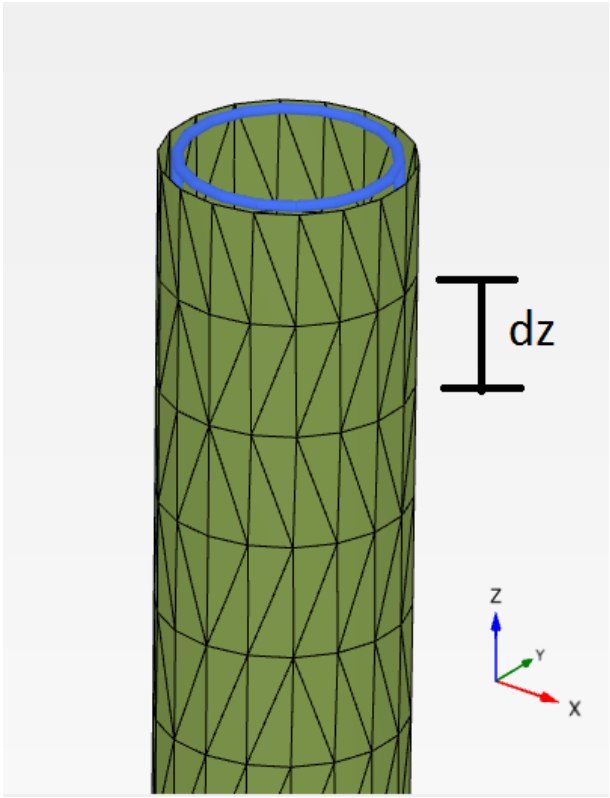

Figure 2.13 Structured mesh for the pile-soil interface

It should be noted that only the lateral stiffness of the soil represented by the p-y curves is extracted from the FE model, and thus shall be used as one of the main inputs in modeling and simulation of the monopile behaviour in Riflex.

In principle, it is possible to extract the rotational springs (M-θ curves) along the length of the pile using the same methodology formulated by PhD candidate Stian Baard Overgaard Hanssen. Figure 2.14 compares the error in the calculated pile displacement between beam model represented by using p-y curve only and by using both p-y and M-θ curves.

It shows that for $\frac{L}{D} \geq 5$, the error of not accounting for the rotational springs is less than 5%. On the other hand, the error increases significantly for $\frac{L}{D} \leq 5$. This observation applies for both linear and nonlinear lateral springs [17]. Since most monopile design practice results in having $\frac{L}{D} \geq 5$ for offshore wind applications, the use of only p-y curves does not give significant error in modelling the pile behaviour.

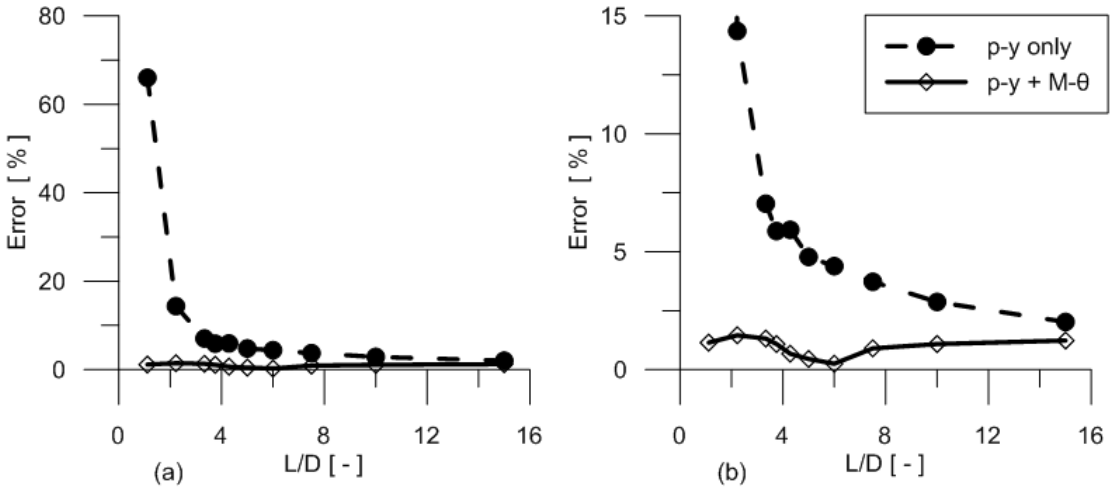

Figure 2.14 Error in calculated pile head displacement
The right hand figure (b) is a zoom of left hand figure (a) [17].

2.2 Hydrodynamic Load and Wave Model

Nonlinear high-frequency wave loads can cause springing- and ringing-type structural responses on offshore structures. The nonlinear effect on both ultimate limit state and fatigue life of the structure can be studied by comparing results from both linear and nonlinear wave models. In addition, free-surface diffraction can become significant in the fatigue life of non-slender structures. This chapter focuses on both hydrodynamic load model and wave model adopted in this study.

2.2.1 Hydrodynamic Load Model

Morison Equation

The forces acting on a cylinder in an oscillatory flow can be efficiently calculated using the Morison equation. The equation describes the total force per unit length as the sum of the drag force and inertia force. The drag force, which is proportional to the square of velocity, is written in the form $\frac{1}{2}\rho C_D D U|U|$ such that the force is in the same direction as the velocity. The inertia force is further composed of the hydrodynamic mass force $\left(\rho C_m A\dot{U}\right)$ and Froude-Krylov force $\left(\rho A\dot{U}\right)$. The hydrodynamic mass describes the force necessary to accelerate the body and the surrounding fluid, while the Froude-Krylov force is due to the pressure gradient developed around the structure from the fluid motion. Note that the inertia force dominates drag force for large, non-slender structures. The following equations lead to the formulation of the Morison equation [20]:

$$F_{Morison} = \frac{1}{2}\rho C_D D U|U| + \rho C_m A\dot{U} + \rho A\dot{U} \tag{2.15}$$

$$F_{Morison} = \frac{1}{2}\rho C_D D U|U| + \rho(C_m + 1)A\dot{U} \tag{2.16}$$

$$F_{Morison} = \frac{1}{2}\rho C_D D U|U| + \rho C_M A\dot{U} \tag{2.17}$$

$$F_{Morison} = F_{Drag} + F_{Inertia} \tag{2.18}$$

where:

U – wave-induced particle velocity [m/s]

$\dot{U}$ – wave-inducd particle acceleration [m/s^2]

A - cylinder cross-sectional area [m^2]

C_m – hydrodynamic mass coefficient equal to 1.0 for circular cylinders [-]

C_D - drag coefficient [-]

C_M - inertia coefficient [-]

$F_{Morison}$ - hydrodynamic force per unit length [N/m]

ρ – fluid density [kg/m^3]

If the structure is also subject to current forces, the drag term of the Morison equation can be modified to include current velocity (U_c) as follows [6]:

$$F_{Drag} = \frac{1}{2}\rho C_D D(U + U_c)|(U + U_c)| \tag{2.19}$$

Hydrodynamic Coefficients

The use of Morison's equation requires values for drag (C_D) and inertia (C_M) coefficients, which vary as a function of Reynolds number (R_e), Keulegan-Carpenter number (K_C) and relative roughness (k/D). For oscillatory viscous flow, the frequency parameter (β) defined as the ratio between R_e and K_c can also be used. The following equations define these parameters [21]:

$$R_e = \frac{u_{max}\ D}{\nu} \tag{2.20}$$

$$K_C = \frac{u_{max}\ T}{D} \tag{2.21}$$

$$\beta = \frac{R_e}{K_C} = \frac{D^2}{\nu T} \tag{2.22}$$

where:

u_{max} - maximum orbital particle velocity

T - wave period [s]

ν – fluid kinematic viscosity [m2/s]

D – diameter [m]

An experimental study done by Sarpkaya [22] investigates how C_D and C_M varies with R_e and C_D for oscillatory flows for smooth and sand-roughed cylinders. Figure 2.15 and Figure 2.16 shows variation of C_D and C_M with K_C, respectively, for different values of R_e and β. It shows that variation in both C_D and C_M for smooth cylinders becomes significant at Re higher than 20,000.

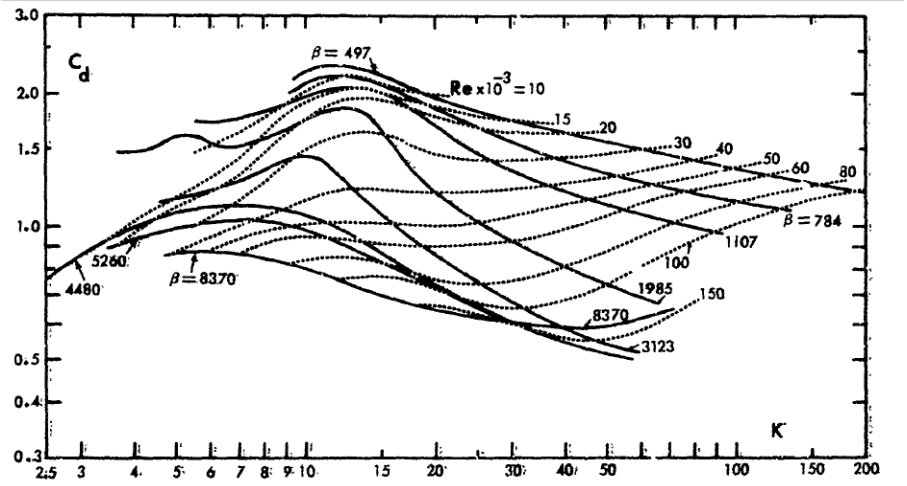

Figure 2.15 C_D versus K_c for constant values of Re and beta [22]

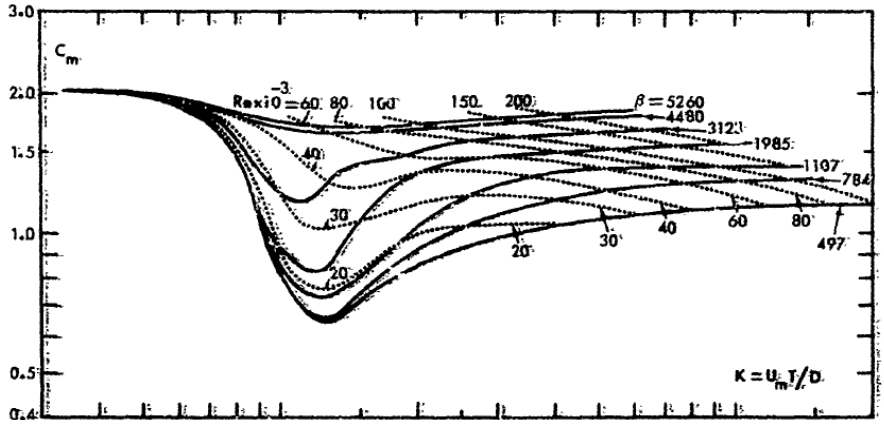

Figure 2.16 C_M versus K_c for constant values of Re and beta [22]

Figure 2.17 and Figure 2.18, on the other hand, show how relative roughness affects C_D and C_M, respectively. At the given K_C, the drag coefficient drops to a minimum value (drag crisis) and rises asymptotically to a maximum value depending on relative roughness. Similarly, the inertia coefficient increases to a maximum value (inertia crisis), and then drops asymptotically depending on the relative roughness. Note that the minimum value of C_D occurs at the same Reynolds number as to where the maximum C_M occurs. [22]. Higher relative roughness generally increases the asymptotic value of C_D and decreases the asymptotic value for C_M.

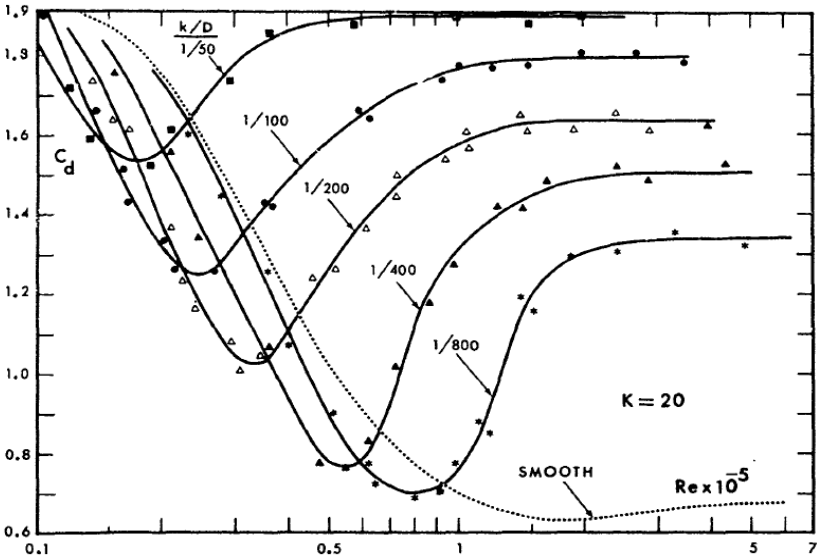

Figure 2.17 C_D versus Re for various values of k/D; K = 20 [22]

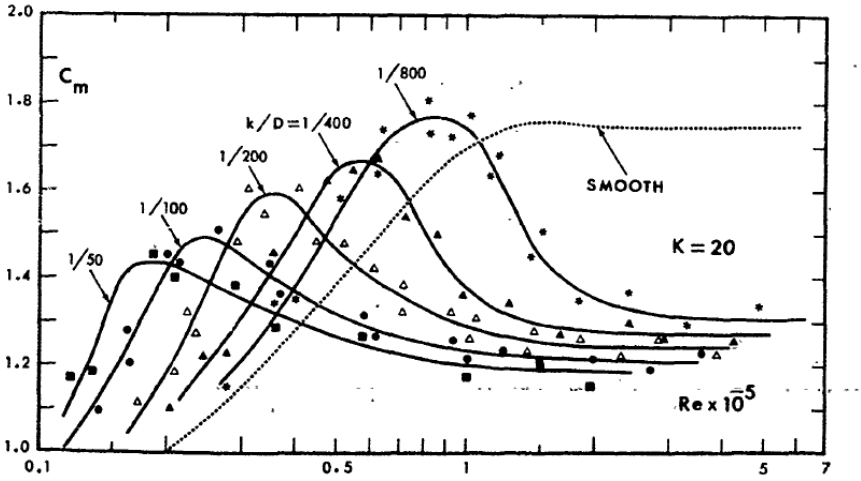

Figure 2.18 C_M versus Re for various values of k/D; K = 20 [22]

2.2.2 Hydrodynamic Wave Model

Current industry practice for fatigue damage calculation of offshore wind turbines involves the use of linear wave theory combined with the Morison equation. This subchapter focuses on higher order Stoke's theory, particularly on second order irregular wave.

Linear Wave Kinematics

The Airy first-order theory states that the water particle motion of a harmonic wave in deep water follows a circular motion, with the diameter of the orbit decreasing along the depth. For intermediate water depths where the water depth becomes small relative to the wave length ($\lambda < 0.5d$), water particles assume an elliptical motion as illustrated in Figure 2.19.

For regular sinusoidal waves propagating on finite water depths, the following equations based on linear wave theory describe the velocity potential, dispersion relation, wave profile, wave velocity and wave acceleration, respectively [23]:

$$\phi = \frac{g\zeta_a}{\omega} \frac{\cosh k\,(z+h)}{\cosh kh} \cos(\omega t - kx) \tag{2.23}$$

$$\omega^2 = gk\ \tanh(\mathrm{kh}) \tag{2.24}$$

$$\zeta = \zeta_a\ \sin(\omega t - kx) \tag{2.25}$$

$$u = \omega\,\zeta_a \frac{\cosh k(z+h)}{\sinh kh} \sin(\omega t - kx) \tag{2.26}$$

$$\dot{u} = \omega^2\,\zeta_a \frac{\cosh k(z+h)}{\sinh kh} \cos(\omega t - kx) \tag{2.27}$$

where:

ϕ - velocity potential

ζ_a - wave amplitude

ω - wave circular frequency; equal to $2\pi/T$

k – wave number; equal to $2\pi/\lambda$

T, λ – wave period and wave length

u - x-component of velocity

$\dot{u}$ - x-component of acceleration

h – average water depth

z – vertical coordinate

x – direction of wave propagation

t – time variable

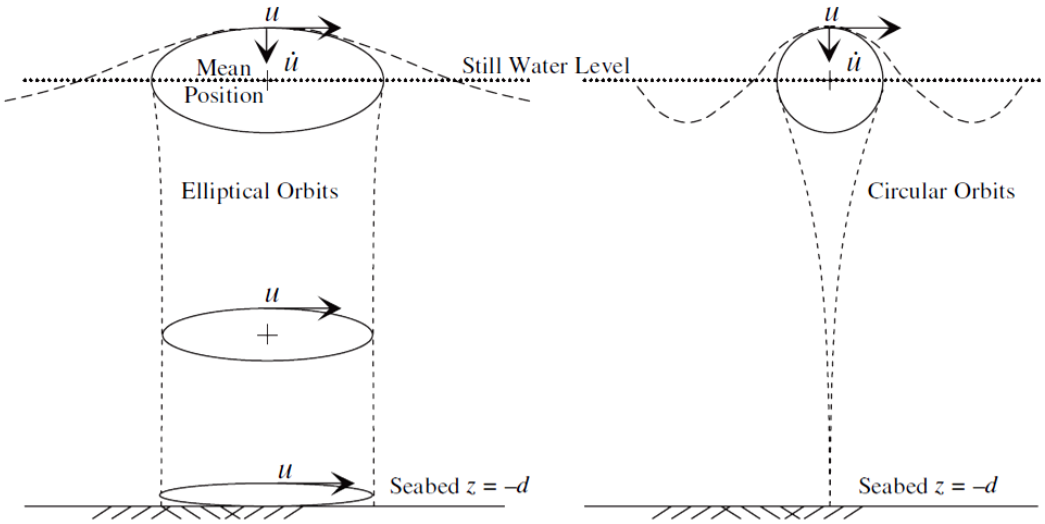

Figure 2.19 Wave particle motion based on Airy first-order wave theory (a) Intermediate water depth: 0.05d < λ < 0.5d; (b) Deep water: λ>0.5d [24]

Since the linear wave theory is only valid up to mean sea water level, the wave kinematics has to be extrapolated up to the instantaneous water level. Among several methods that have been proposed to extrapolate wave kinematics, Wheeler stretching is frequently used in practical applications due to its simplicity and applicability in moderate sea states despite under prediction of wave velocity for steep irregular waves [25]. It is done by redistribution of wave kinematics profile at the still water level to instantaneous water level as shown in Figure 2.20 using the following relation:

$$z = \frac{z_s - \zeta}{1 + \frac{\zeta}{h}} \tag{2.28}$$

where:

z_s - stretched vertical coordinate [m]

ζ - wave elevation [m]

h - water depth [m]

Other methods of extrapolation include the second-order model and method of Grue et al. A study conducted by Haver, Stansberg [25] compared the three wave prediction methods (Wheeler, second-order and Grue's method) with actual wave measurements. Considering extreme waves, the study demonstrates that Wheeler's method significantly underpredicts wave particle velocities below mean water level. Using measured or second order wave elevation as input to the Wheeler method improves predictions near the surface, but still underestimates wave particle velocity below mean water level. On the other hand, the method of Grue fairly predicts wave particle velocities above mean water level, but overpredicts velocities under mean water level. The study concludes that the second-order model predicts kinematics with highest accuracy at all water levels, particularly when considering extreme irregular sea states.

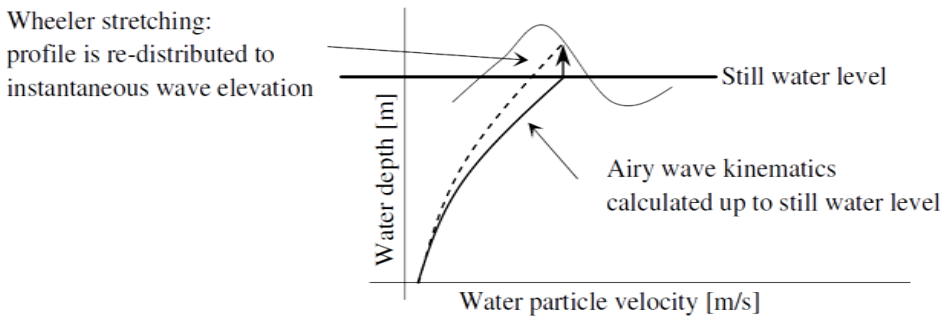

Figure 2.20 Airy wave kinematics up to the still water level and Wheeler stretching [6]

Second Order Stokes

In linear wave theory, free surface condition is satisfied at mean free-surface level. Analysis using second order theory, on the other hand, gives the following advantages in terms of satisfying boundary conditions [23]:

a) satisfy impermeability of the body at 1st order instantaneous position
b) allows pressure to be equal to atmospheric pressure on the instantaneous free-surface
c) account nonlinearities in the velocity of the fluid particles on the free surface

Pertubation analysis, with the wave amplitude (ε) as a small parameter, is the most common method in solving wave-structure problems [23]. As incident waves become steeper, higher order effects become more significant. Thus, considering higher order terms in the pertubation analysis gives a better estimate of wave kinematics, wave loads and structural response. From pertubation theory, the velocity potential can be written in the following form [26]:

$$\phi = \widetilde{\phi_1}\varepsilon + \widetilde{\phi_2}\varepsilon^2 + \widetilde{\phi_3}\varepsilon^3 + \cdots \tag{2.29}$$

The applicability of Stokes theory depends on the two parameters wave height and water depth as illustrated in Figure 2.21.

Unlike the first order solution where the wave load and structural response have zero mean value and oscillate with the frequency of the incident wave, the second order solution could result in a mean value (drift force) and oscillatory behaviour at both difference-frequency ($\omega_i - \omega_j$) and sum-frequency($\omega_i + \omega_j$). Note that the difference-frequency behaviour is only generated if two interacting regular wave components do not have the same frequency ($\omega_i \neq \omega_j$) [26].

The existence of the nonlinear wave effects can be illustrated by integrating the pressure along the surface of the body considering all terms up to second order. From Bernoulli equation, the pressure can be expressed as:

$$p = -\rho g z - \rho\frac{\partial \phi_1}{\partial t} - \rho\frac{\partial \phi_2}{\partial t} - \rho\frac{1}{2}\nabla\phi_1 \cdot \nabla\phi_2 \tag{2.30}$$

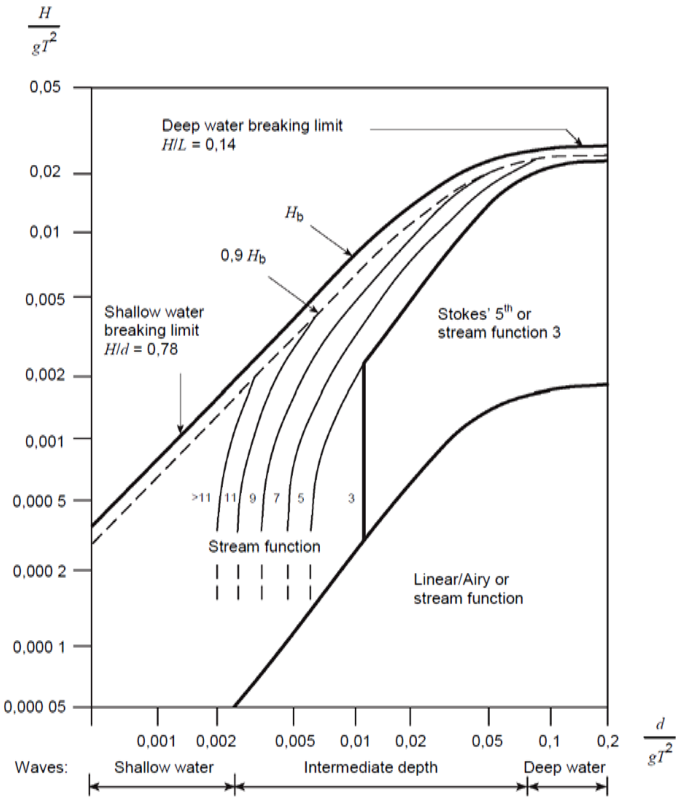

Figure 2.21 Regular wave theory selection diagram [7]

Considering two regular deep water incident waves with frequencies ω_1 and ω_2, propagating along x-direction, the square-velocity term at x = 0 can be expressed as:

$$\left.\frac{\partial \phi_1}{\partial x}\right|_{x=0} = A_1 \cos(\omega_1 t + \varepsilon_1) + A_2 \cos(\omega_2 t + \varepsilon_2) \tag{2.31}$$

$$\left(\left.\frac{\partial \phi_1}{\partial x}\right|_{x=0}\right)^2 = {A_1}^2 \cos^2(\omega_1 t + \varepsilon_1) + {A_2}^2 \cos^2(\omega_2 t + \varepsilon_2) + 2A_1A_2 \cos(\omega_1 t + \varepsilon_1)\ \cos(\omega_2 t + \varepsilon_2) \tag{2.32}$$

Applying trigonometric functions and algebra,

$$\left(\frac{\partial \phi_1}{\partial x}\Big|_{x=0}\right)^2 = \frac{\left({A_1}^2 + {A_2}^2\right)}{2} + \frac{{A_1}^2 \cos[2(\omega_1 t + \varepsilon_1)]}{2} + \frac{{A_2}^2 \cos[2(\omega_2 t + \varepsilon_2)]}{2} + \mathrm{A_1A_2}\cos[(\omega_1 + \omega_2)\mathrm{t} + \varepsilon_1 - \varepsilon_2] + \mathrm{A_1A_2}\cos[(\omega_1 - \omega_2)\mathrm{t} + \varepsilon_1 - \varepsilon_2] \quad (2.33)$$

The first term, which is a constant term, corresponds to the mean wave (drift) effect. The second, third and fourth terms corresponds to the sum-frequency terms with oscillation frequencies $2\omega_1$, $2\omega_2$ and $(\omega_1 + \omega_2)$, respectively. The last term corresponds to the difference-frequency term at frequency $(\omega_1 - \omega_2)$, which is responsible for the slow drift effects [26].

Slow drift motions are more relevant for large floating structures, particularly in the design of mooring lines and thrusters. The sum-frequency forces, on the other hand, can excite resonant behaviour of marine structures which are referred to as "springing" and "ringing" responses [23].

Second Order Irregular Waves

In practice, long-crested linear irregular waves are used to simulate irregular sea. Irregular waves are generated by superposition of sinusoidal waves with different amplitude and phase angle. Using second order irregular waves for offshore wind turbine simulations could generate nonlinear responses of the structure.

Stochasticity

The irregularities of sea are usually expressed thru a site-specific power spectrum. This involves the assumption that the waves can be described by a stationary random process. Site-specific wave measurements are used to estimate statistical parameters that define standard wave spectrum.

The Pierson-Moskowitz (PM) spectrum is derived from measurements in the Atlantic Ocean and requires a significant wave height (H_s) and a period, which is either the zero mean crossing period (T_z) or the peak spectral period (T_p). The Joint North Sea Wave Observation Project (JONSWAP) spectrum is widely used for North Sea applications and requires the parameters H_s, T_p and peak enhancement factor (γ). An average peak enhancement factor equal to 3.3 is used for North Sea. Another popular spectrum is the TMA spectrum, which has the same implementation as the JONSWAP spectrum but includes a correction factor to be applicable for finite shallow water depths. At relatively shallow water shallow water ($H_s/d > 0.3$), the seabed friction affects the wave motion making the crest steeper and the trough flatter. It should be noted that a correction shall be applied to first-order spectrum in order to incorporate second-order peaks due to sum-frequency effects. [24].

Second-Order Wave Formulation

Following the derivation done by Veldkamp and van der Tempel [24], the second-order irregular waves can be generated by applying correction factors to first-order irregular waves. The first-order elevation can be expressed as sum of regular sinusoidal waves as follows:

$$\eta^{(1)}(t) = \sum_n a_n \cos(\omega_n t) + b_n \sin(\omega_n t) \tag{2.34}$$

where:

$$a_n = \sqrt{S(f_n)\Delta f N(0,1)} \tag{2.35}$$

$$b_n = \sqrt{S(f_n)\Delta f N(0,1)} \tag{2.36}$$

where $S(f_n = \omega_n/(2\pi))$ is the power spectral density and N(0,1) is a random normal variable with zero mean and variance equal to one. The first-order wave particle velocity and acceleration can be expressed as:

$$u^{(1)}(t,z) = \sum_n \omega_n \frac{\cosh[k_n(z+d)]}{\sinh[k_n d]}[a_n \cos(\omega_n t) + b_n \sin(\omega_n t)] \tag{2.37}$$

$$\dot{u}^{(1)}(t,z) = \sum_n {\omega_n}^2 \frac{\cosh[k_n(z+d)]}{\sinh[k_n d]}[-a_n \sin(\omega_n t) + b_n \cos(\omega_n t)] \tag{2.38}$$

The second-order elevation can be expressed as:

$$n^{(2)}(t) = \sum_{m=1}^{N}\sum_{n=m}^{N} \delta H_{mn}[(a_m a_n - b_m b_n)\cos(\omega_{mn} t) + (a_m a_n + b_m b_n)\sin(\omega_{mn} t)] \tag{2.39}$$

where:

$$H_{mn} = \frac{\frac{g k_m k_n}{\omega_m \omega_n} - \frac{1}{2g}(\omega_m^2 + \omega_m\omega_n + \omega_n^2) + \frac{g}{2}\frac{\omega_m k_n^2 + \omega_n k_m^2}{\omega_m \omega_n \omega_{mn}}}{1 - \frac{g k_{mn}}{\omega_{mn}^2}\tanh(k_{mn} d)} - \frac{g k_m k_n}{2\omega_m \omega_n} + \frac{1}{2g}(\omega_m^2 + \omega_m\omega_n + \omega_n^2) \tag{2.40}$$

$$\delta = \begin{cases} 1/2 & if\ m = n \\ 1 & if\ m \neq n \end{cases} \tag{2.41}$$

The wave numbers are found by dispersion relation and by the following conversions:

$$\omega_m^2 = g k_m \tanh(k_m d) \tag{2.42}$$

$$k_{mn} = k_m + k_n \tag{2.43}$$

$$\omega_{mn} = \omega_m + \omega_n \tag{2.44}$$

The expression for the second-order wave velocity can be expressed as:

$$u^{(2)}(t,z) = \sum_{m=1}^{N}\sum_{n=1}^{m} \eta_{mn}^{(2)}(t) U_{mn}\omega_{mn} \frac{\cosh[k_{mn}(z+d)]}{\sinh(k_{mn}d)} \tag{2.45}$$

where:

$$U_{mn} = 1 + \frac{k_{mn}\tanh(k_{mn}d)}{4H_{mn}}\left(\frac{g^2 k_m k_n + \omega_m^2\omega_n^2}{\omega_m\omega_n\omega_{mn}^2} - 1\right) \tag{2.46}$$

Finally, the wave particle velocity and acceleration can be expressed as:

$$u^{(2)}(t,z) = \sum_{m=1}^{N}\sum_{n=1}^{m} H_{mn}U_{mn}\omega_{mn}\frac{\cosh[k_{mn}(z+d)]}{\sinh(k_{mn}d)} x\,[(a_m a_n - b_m b_n)\cos(\omega_{mn}t) + (a_m a_n + b_m b_n)\sin(\omega_{mn}t)] \tag{2.47}$$

$$\dot{u}^{(2)}(t,z) = \sum_{m=1}^{N}\sum_{n=1}^{m} H_{mn}U_{mn}\omega_{mn}^2\frac{\cosh[k_{mn}(z+d)]}{\sinh(k_{mn}d)} x\,[(-a_m a_n + b_m b_n)\sin(\omega_{mn}t) + (a_m a_n + b_m b_n)\cos(\omega_{mn}t)] \tag{2.48}$$

Wave Generation

Using a formulated standard wave spectrum, a standard algorithm can be used to generate elevation time series. A widely-used algorithm is the inverse fast Fourier transform (IFFT) method, which under the assumption that phase angle is randomly distributed, can generate harmonic waves of different frequencies which can be superimposed to form the irregular time series [6]. Figure 2.22 illustrates the conversion from time to frequency domain and from frequency to time domain using FFT and IFFT, respectively.

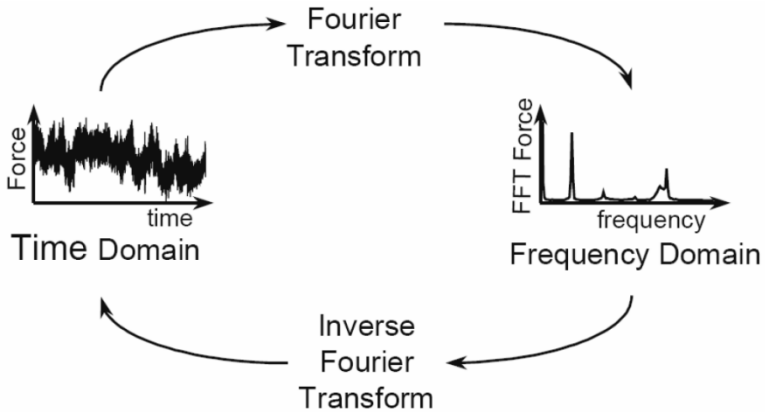

Figure 2.22 Conversion between time and frequency domains using FFT and IFFT [6]

From the first-order sea surface elevations, second-order wave kinematics can be calculated by applying corrections presented in the previous subsection. And by introducing the calculated wave kinematics with the hydrodynamic load model, i.e. Morison equation, the hydrodynamic load time series can be generated.

Figure 2.23 illustrates the general industry practice for time domain fatigue calculations. The wave spectrum, wave kinematics and load model adopted directly influence load time series calculation. Note that the methodology in generating wave time series can also be used for ultimate limit state analysis, particularly in simulation of different design load cases.

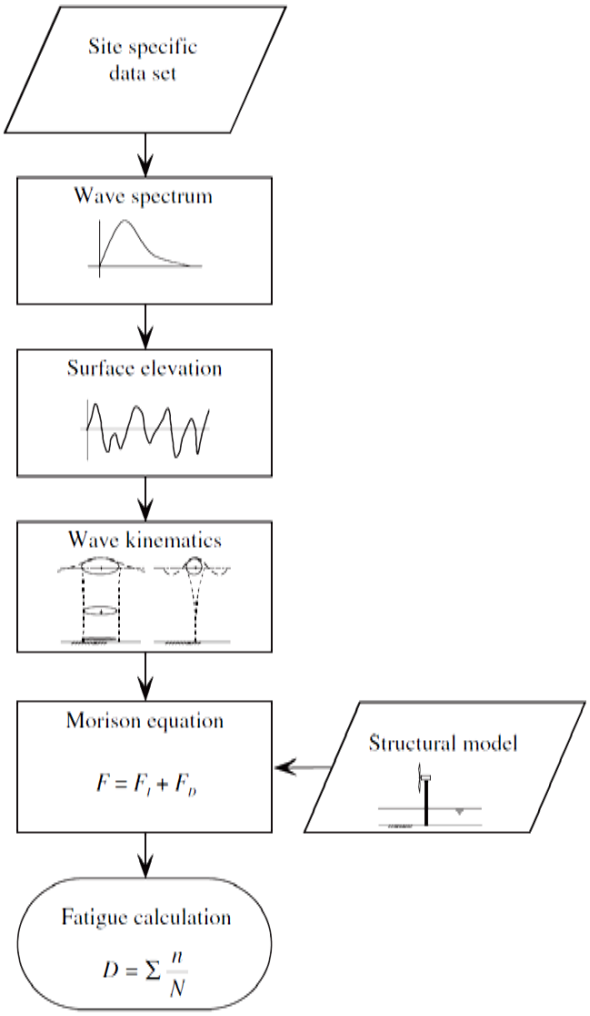

Figure 2.23 Flowchart for wave modelling for time domain fatigue calculation [24]

MacCamy-Fuchs Method

The main assumption of Morison equation is that the structure is slender relative to the wave length, such that near-field diffraction does not occur. Diffraction occurs when the presence of the structure affects the surrounding wave field, which modifies the magnitude of the inertia force. Such effect is significant for large monopile foundations for offshore wind applications. Diffraction is considered in Morison equation by modifying the inertia coefficient (C_M) using MacCamy-Fuchs equation. The C_M is modified as a function of cylinder diameter to wave length ratio as shown in Figure 2.24 [6].

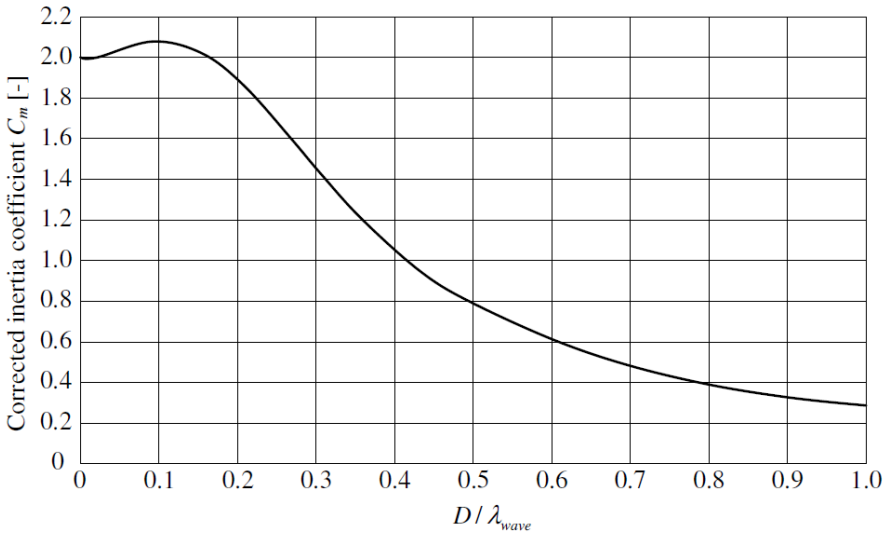

Figure 2.24 MacCamy-Fuchs diffraction correction of the inertia coefficient Cm [6]

In this study, hydrodynamic loads modified with MacCamy-Fuchs equation are calculated to account for surface diffraction analytically. Linear incoming waves with forces integrated up to mean water level are used as main inputs. The force per unit length (dF) at x = 0 is formulated as follows [27]:

$$dF(z) = \sum_{n=1}^{N} \frac{4\rho g \zeta_a}{k} \frac{\cosh k(z+h)}{\cosh kh} G \cos(\omega t - \varepsilon - \alpha) \tag{2.49}$$

where

$$\tan \alpha = \frac{J_1'(k\alpha)}{J_2'(k\alpha)} \tag{2.50}$$

and

$$G = \frac{1}{\sqrt{(J_1'(k\alpha))^2 + (Y_1'(k\alpha))^2}} \tag{2.51}$$

in which *J* and *Y* are Bessel functions.

2.3 Fatigue Theory

Offshore wind turbines are subject to cyclic loading due to wind, wave and current during throughout their service life. The support structure must be designed such that its fatigue failure does not occur during its intended service life, which can be taken as 20 years if it is not specified [5].

Integrated time-domain simulations are usually employed for fatigue life prediction of offshore structures due to their ability to account for nonlinearities associated with wind turbine control and responses due to aerodynamic and hydrodynamic loading. Finite element programs are commonly used to calculate time history of stresses based on wind turbine data and environmental conditions. Stress reversals in time history, which are also called stress cycles, are associated with fatigue damage. The stress range and average stress are two important parameters for fatigue damage calculation [28].

2.3.1 S-N Curve

The S-N curve defines the fatigue resistance of a structure or of a structural component by specifying the number of cycles to failure (N_f) versus the stress range (S). S-N curve parameters are defined based on laboratory tests, where fatigue failure is said to have occurred when cracks has propagated through the thickness of the structure or one of its component [5]. One of the bases for fatigue life prediction is the Wöhler's equation, which relates cycles of constant stress range $(\Delta\sigma)$ with a certain amount of damage. It assumes that damage accumulates linearly with the number of stress cycles (N). The Wöhler's equation can be used to calculate N_f as follows [28]:

$$N_f(\Delta\sigma)^m = \bar{a} \tag{2.52}$$

which can practically be written as

$$\log(N_f) = \log(\bar{a}) - m \log(\Delta\sigma) \tag{2.53}$$

The material parameter m refers to the negative inverse slope of the S-N curve while the parameter $\log(\bar{a})$ refers to the intercept of log N axis. To account for the effect of plate thickness on fatigue strength of welded joints, a reference thickness (t_{ref}) and thickness exponent (k) were introduced to the equation as follows [29]:

$$\log(N_f) = \log(\bar{a}) - m \log\left(\Delta\sigma\left(\frac{t}{t_{ref}}\right)^k\right) \tag{2.54}$$

The S-N curve necessary for fatigue analysis is defined in the fatigue analysis section.

2.3.2 Rainflow Cycle Counting and Palmgren-Miner's Rule

Several cycle counting methods have been proposed to determine the stress range distribution for a given stress time history. The stress range distribution defines the number of stress cycle occurrences for all specified stress ranges. Three of the most common methods include level crossing, peak cycle and rainflow cycle counting. Among the three methods, rainflow cycle counting has the advantage of accounting all peaks once, including small amplitude peaks, which makes the method appropriate for fatigue damage calculation [28].

From the number of stress range distribution, the fatigue life of a structure can be predicted by calculating the cumulative fatigue damage. DNV [5] recommends the use of Palmgren-Miner's summation rule, which calculates the linearly cumulative damage as:

$$D = \sum_{i=1}^{I} \frac{n_i(\Delta\sigma_i)}{N_{f,i}(\Delta\sigma_i)} \tag{2.55}$$

where:

D = cumulative fatigue damage

I = total number of stress range blocks

n_i = number of cycles in the i^{th} stress block

$N_{f,i}$ = number of cycles to failure at stress range of the ith block (from S-N curve)

The design criterion is defined as $D \leq 1.0$, which means that fatigue failure occurs once the calculated cumulative damage exceeds 1.0. Note that this method assumes that damages caused by different stress cycles are independent from each other, such that a given stress cycle would have caused the same damage regardless of when in the service life of structure it occurs. Such assumption is practical for metallic materials used for monopiles [30].

Chapter 3.

Design Basis

3.1 DTU 10MW Reference Wind Turbine

To support the upscaling of offshore wind turbines, the Light Rotor project was founded by the Danish Energy Agency. A 10 MW reference wind turbine was established in cooperation with Denmark Technical University (DTU) and Vestas Wind Systems. The “DTU 10 MW Reference Wind Turbine”, or in short “DTU 10 MW RWT”, acts as a design benchmark where future large offshore wind turbine designs can be compared. Likewise, simulation tools can be developed based on the DTU 10 MW RWT to make upscale designs more cost effective [31].

Key Parameters

The DTU 10MW Reference Wind Turbine (DTU 10MW RWT) consists of an optimized blade, a drive train and a tower. It was inspired by the NREL 5MW reference wind turbine and was designed for an offshore site (IEC Class 1A), which is associated with higher turbulence characteristics. It has a hub height of 119 m relative to the mean seawater level and a rotor diameter of 178.3 m. The other key parameters are summarized in Table 3.1. The wind turbine power curve and thrust curve are shown in Figure 3.1.

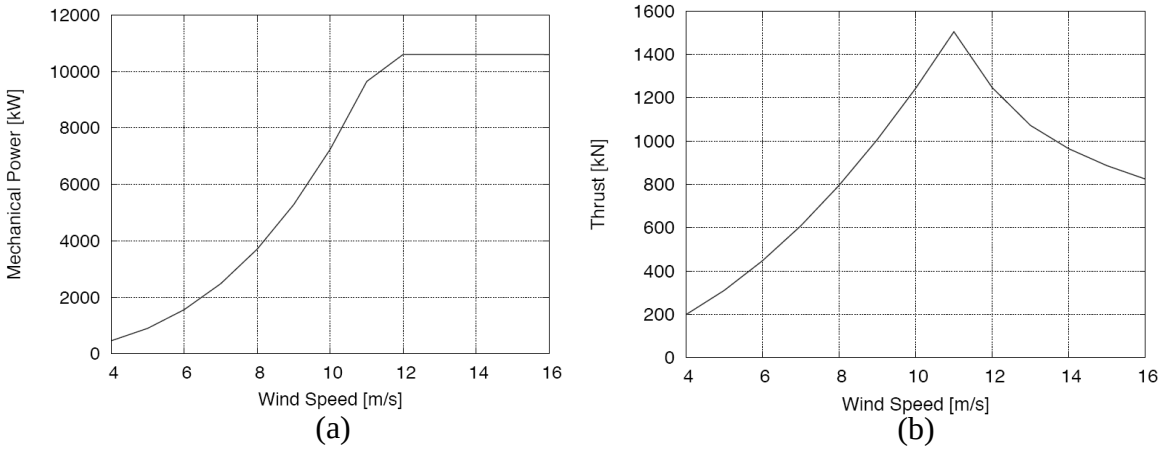

Figure 3.1 Mechanical power and thrust curve of DTU 10 MW RWT [31]

Table 3.1 Key parameters of the DTU 10 MW Reference Wind Turbine [31]

DTU 10 MW RWT Key Parameters	
Wind Regime	IEC Class 1A
Rotor Orientation	Clockwise rotation - Upwind
Control	Variable Speed, Collective Pitch
Cut in wind speed	4 m/s
Cut out wind speed	25 m/s
Rated wind speed	11.4 m/s
Rated power	10 MW
Number of blades	3
Rotor Diameter	178.3 m
Hub Diameter	5.6 m
Hub Height	119.0 m
Drivetrain	Medium Speed, Multiple-Stage Gearbox
Minimum Rotor Speed	6.0 rpm
Maximum Rotor Speed	9.6 rpm
Maximum Generator Speed	480.0 rpm
Gearbox Ratio	50
Maximum Tip Speed	90.0 m/s
Hub Overhang	7.1 m
Shaft Tilt Angle	5.0 deg
Rotor Precone Angle	-2.5 deg
Blade Prebend	3.332 m
Rotor Mass	227962 kg
Nacelle Mass	446036 kg
Tower Mass	628442 kg

1P and 3P Frequency Range

To avoid load amplification due to resonance, it is necessary to design the support structure such that the overall natural frequency of the OWT falls outside the blade passing intervals, 1P and 3P. Figure 3.2 graphically shows 1P and 3P regions of the DTU 10 MW RWT, as well as the wave energy spectrum as a function of frequency.

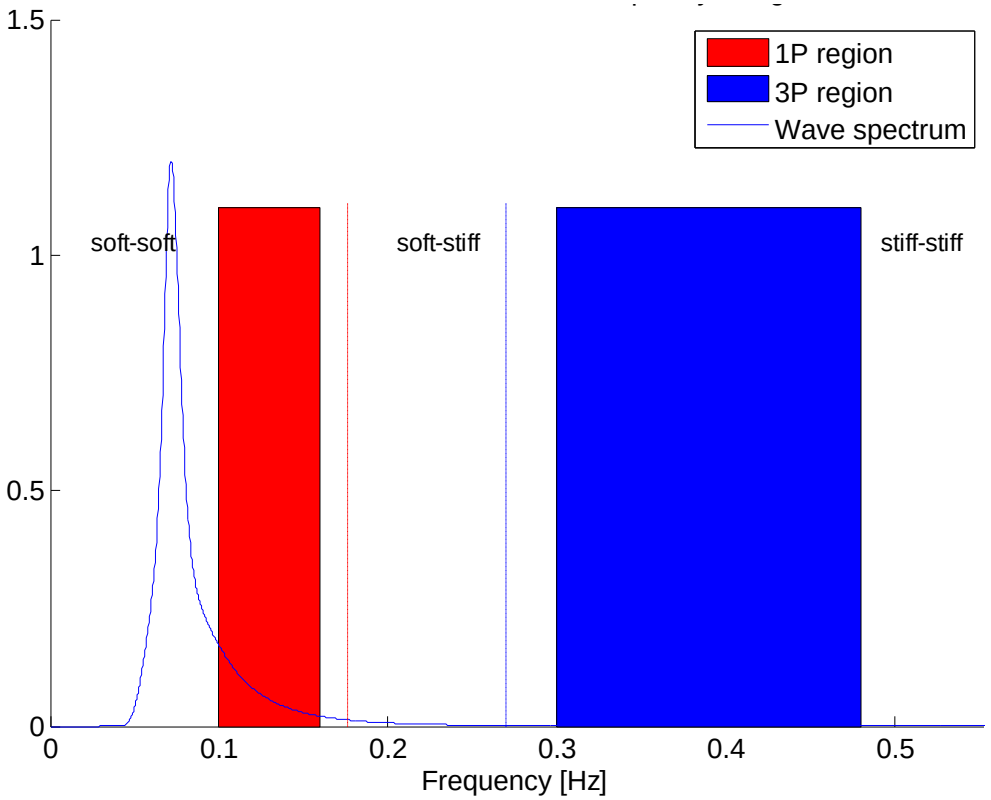

Figure 3.2 Blade passing frequency intervals, 1P and 3P

JONSWAP spectrum is used to define the wave spectrum for the extreme sea state (H_s = 9.9 m, T_p = 14 sec) corresponding to the maximum significant wave height in the 50-year contour surface. It should be noted that for mild sea states associated with shorter period (T_p), the spectrum would shift to the right towards higher frequency. This reduces the range of the soft-stiff region at which the overall natural frequency of the structure shall ideally be designed. Applying a 10% safety margin makes the soft-stiff region to range from 0.18 Hz to 0.27 Hz.

The occurrence of marine growth is expected to reduce the overall natural frequency of the structure. To account for this, the desired natural frequency for the preliminary design is chosen to be on the higher end of the soft-stiff region. Thus, the desired overall natural frequency is chosen to be **0.25 Hz**.

3.2 Tower Structural Design

The DTU 10 MW RWT comes with a tower design whose material properties are defined in Table 3.2. The material properties are based on S355 steel, whose density is increased by 8% to account for secondary steel. The tower has a base diameter of $8.3\,m$ and increases linearly to $5.5\,m$ at the top. The tower has a total height of $115.63\,m$. Table 3.3 summarizes the thickness and outer diameter variation along the height of the tower [31].

Note that the original dimensions of the tower presented are modified to achieve the desired overall stiffness and natural frequency. The details about the modified tower design are discussed in the Preliminary Design section.

Table 3.2 Material parameters for tower [31]

Tower material property	
Density, ρ $[kg/m^3]$	8500
Yield strength, σ_y $[MPa]$	355
Youngs's modulus, E $\left[N/_{m^2}\right]$	2.10E+11
Shear modulus, G $\left[N/_{m^2}\right]$	8.08E+10
Poisson's ratio, ν	0.3

Table 3.3 Initial structural design of tower [31]

Height [m]	D_outer [m]	t [mm]
0	8.3	38
11.5	8.0215	38
11.501	8.0215	36
23	7.7431	36
23.001	7.743	34
34.5	7.4646	34
34.501	7.4646	32
46	7.1861	32
46.001	7.1861	30
57.5	6.9076	30
57.501	6.9076	28
69	6.6292	28
69.001	6.6291	26
80.5	6.3507	26
80.501	6.3507	24
92	6.0722	24
92.001	6.0722	22
103.5	5.7937	22
103.501	5.7937	20
115.63	5.5	20

3.3 Site-specific Metocean Conditions

3.3.1 Location

An offshore wind turbine support structure is designed based on the metocean conditions, which highly depend on the project location. Since the larger number of offshore wind development occurs at North Sea, the project location is chosen to be at the central part of the North sea.

The ”Marine Renewable Integrated Application Platform”, or in short ”MARINA - Platform”, is a European project which aims to further advance the technology developments in marine renewable energy industry particularly in offshore wind and ocean energy converters. Part of

which is the Work Package 3 (MARINA WP3) which focuses on concepts identification. It covers the identification of metocean conditions in selected European sites for concept comparison [32].

Based on identified water depths, investigations of bottom-fixed combined concepts shall be carried out for Sites 1, 5 and 15. Site 15, located at Denmark, North Sea Center (55.13N, 3.43E) is chosen for the purpose of this study. The general characteristics of Site 15 are summarized in Table 3.4.

Table 3.4 General information of Site 15 [33]

Site 15 Characteristics	
Water Depth [m]	29
Distance to shore [km]	300
50-year U_w at 10 m [m/s]	27.2
50-year H_s [m]	8.66
Mean value of T_p [s]	6.93

3.3.2 Long-term Wind and Wave Distribution

The MARINA Platform Project provides marginal and joint distributions of wind and wave data for the study location (Site 15). The National and Kapodistrian University of Athens (NKUA) provided the 10 years (2001-2010) hourly raw data for the 5 selected offshore sites. Both marginal and joint distributions are obtained by fitting analytical solutions to raw data and are characterized by one-hour mean wind speed at 10 m above mean sea level (U_w), significant wave height (H_s) and spectral peak period (T_p) [32].

The joint probability density function (PDF) of U_w, H_s, and T_p is defined by the marginal PDF of U_w (f_{U_w}), a PDF of H_s conditional on U_w ($f_{H_s|U_w}$) and a PDF of T_p conditional on H_s ($f_{T_p|H_s}$). These distributions are defined by parameters summarized in Table 3.5 and by the following equations:

$$f_{U_w}(u) = \frac{\alpha_U}{\beta_U}\left(\frac{u}{\beta_U}\right)^{\alpha_U - 1} exp\left[-\left(\frac{u}{\beta_U}\right)^{\alpha_U}\right] \tag{3.1}$$

$$f_{T_p|H_s}(t|h) = \frac{1}{\sqrt{2\pi}\sigma_{LTC}t}\ exp\left[-\frac{1}{2}\left(\frac{\ln(t) - \mu_{LTC}}{\sigma_{LTC}}\right)^2\right] \tag{3.2}$$

$$\mu_{LTC} = c_1 + c_2 h^{c_3} \tag{3.3}$$

$${\sigma_{LTC}}^2 = d_1 + d_2\ exp(d_3 h) \tag{3.4}$$

$$f_{H_s|U_w}(h|u) = \frac{\alpha_{HC}}{\beta_{HC}}\left(\frac{h}{\beta_{HC}}\right)^{\alpha_{HC} - 1} exp\left[-\left(\frac{h}{\beta_{HC}}\right)^{\alpha_{HC}}\right] \tag{3.5}$$

$$\alpha_{HC} = a_1 + a_2 u^{a_3} \tag{3.6}$$

$$\beta_{HC} = b_1 + b_2\, u^{b_3} \tag{3.7}$$

Finally, the joint PDF of U_w, H_s, and T_p can be expressed as

$$f_{U_w,H_s,T_p}(u,h,t) = f_{U_w} \cdot f_{H_s|U_w} \cdot f_{T_p|H_s} \tag{3.8}$$

Note that a power law wind speed profile is adapted for transforming wind speeds between hub height and at 10 m above mean sea level. The wind speed profile is defined by:

$$U(z) = U_{10}\left(\frac{z}{10}\right)^a \tag{3.9}$$

where:

$\alpha_U, \beta_U, \alpha_{HC}, \beta_{HC}$ - shape and scale parameters [-]

μ_{LTC}, σ_{LTC} – mean and standard deviation of ln(H_s) as lognormal distribution parameters

$a_1, a_2, a_3, b_1, b_2, b_3, c_1, c_2, c_3, d_1, d_2, d_3$ – nonlinear curve fitting parameters [-]

U_{10} - mean wind speed at reference height of 10 m [m/s]

a – exponent equal to 0.1 for the selected site [-]

Table 3.5 Joint probability distribution parameters for Site 15 [32]

Parameter	Value
α_U	2.309
β_U	8.926
a_1	1.702
a_2	0.195
a_3	1.000
b_1	0.454
b_2	0.065
b_3	1.479
c_1	1.588
c_2	0.219
c_3	0.682
d_1	0.010
d_2	0.150
d_3	-0.703

3.3.3 Fifty-year Environmental Contour Surface

The environmental contour surface graphically illustrates the derived joint distribution of wind and wave climate. A return period of 50 years is recommended for ultimate limit state analysis. The critical combinations of the mean wind speed (U_w), H_s and T_p should be selected from the 50-year contour surface for Site No. 15, which is shown in Figure 3.3. Note that U_w corresponds to a reference height of 10 m above MSL.

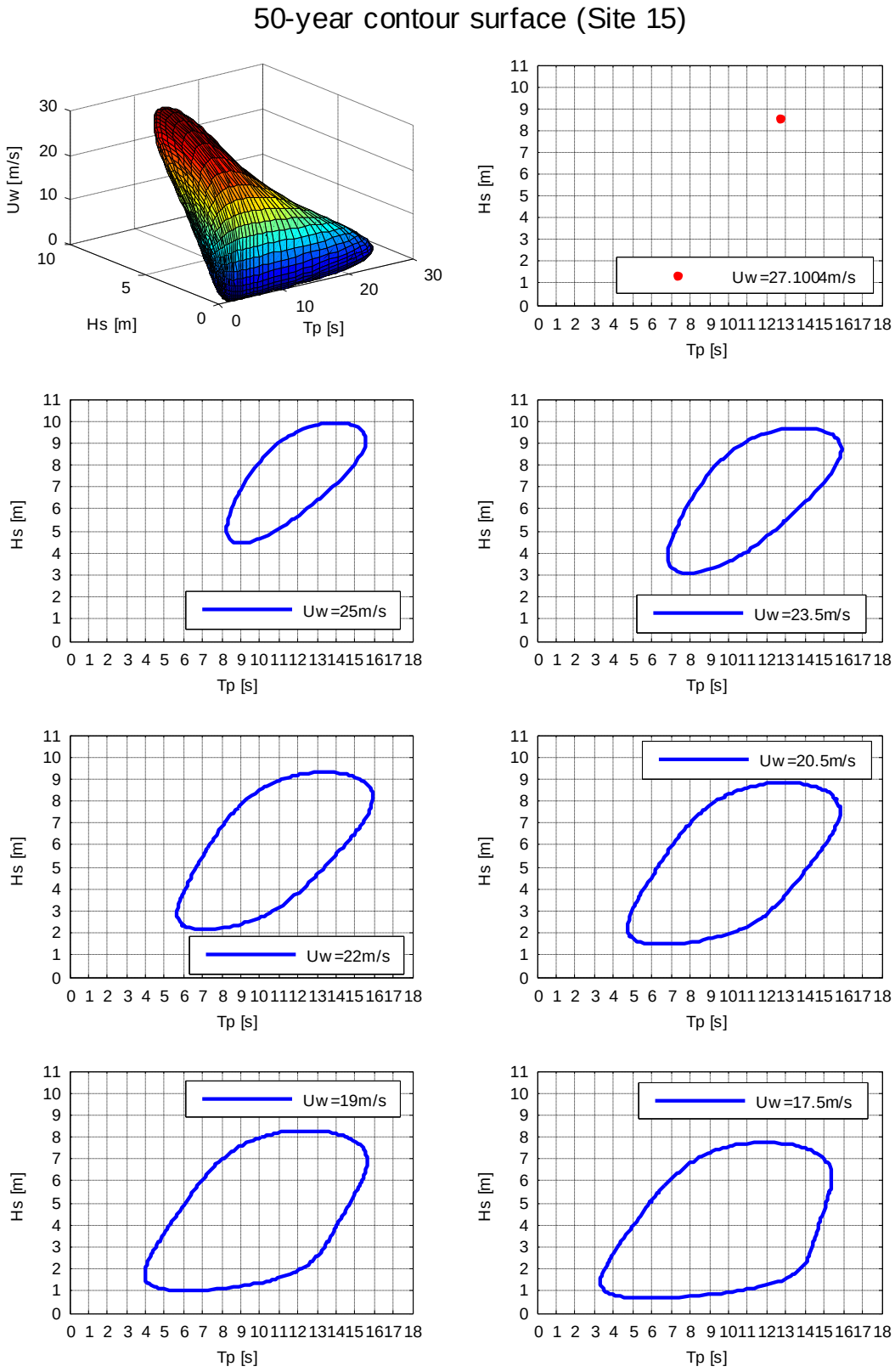

Figure 3.3 Fifty-year contour surface for Site No. 15 [32]

For preliminary ULS analysis of structures not sensitive to waves, considering the 50-year environmental conditions corresponding to the (1) maximum U_w and (2) maximum H_s are good representative design values. Table 3.6 summarizes the critical environmental conditions for the design of the monopile structure.

Table 3.6 Representative conditions of the 50-year contour surface [32]

Parameter	Condition with maximum U_w	Condition with maximum H_s
U_w [m/s]	27.1	25.3
H_s [m]	8.6	9.9
T_p [s]	12.7	14

3.3.4 Water Depth

To determine the viability of using monopile support structures for large wind turbines, different water depths shall be investigated. The following water depths shall be considered in the design: 20 m, 30 m, 40 m and 50 m.

3.3.5 Current

Current loads shall be taken into account in the design of an offshore support structure. For extreme conditions, surface current with a 10-year return period is usually used. This value can be taken as 0.55 m/s for the central north sea [34].

3.3.6 Water Levels

For site 15, the following set of water levels is assumed:

Table 3.7 Water level description for site 15

Water levels for site 15	
50-year tidal range, Δz_{tide} [m]	5
Lowest Astronomical Tide, LAT [m]	-2.5
50-year positive storm surge, Δz_{surge} [m]	3

3.3.7 Marine Growth

For offshore structures, the growth of marine organisms on the submerged part of the structure must be considered in the design. The effect of marine growth becomes significant when evaluating wave and current loads, due to the increase in effective diameter. Moreover, the additional mass associated with marine growth could affect the overall natural frequency of the structure.

It is recommended that the marine growth thickness and density be assessed according to local conditions. If no information is available, the marine growth thickness can be taken as summarized in Table 3.8 while the marine growth density can be taken as $1400\ kg/m^3$ [8].

Table 3.8 Marine growth thickness for various water depth [8]

Depth from MSL [m]	Marine growth thickness [mm]
above (+)1.5	0
(+) 1.5 to (-) 4.0	160
(-) 4.0 to (-) 15.0	100
under (-) 15.0	50

For simplicity, a uniform marine growth thickness of **130 mm** is accounted along the length of the monopile from seabed to seawater level. The density of the marine growth is set to $1400\ kg/m^3$.

3.3.8 Corrosion

Corrosion refers to the natural process of degradation of the material, usually metal, due to chemical reaction with the environment. The loss of material due to corrosion affects the structural integrity of the structure and therefore must either be prevented, controlled or accounted for in the design. For simplicity of this thesis study though, it is assumed that the splash zone is fully protected against corrosion. The effect of corrosion is most relevant at sections within the atmospheric and splash zone, whereas critical sections considered for the monopile design usually occurs below the mudline.

3.3.9 Scour Protection

For this project, it is assumed that the support structure is scour protected, but the design of the scour protection is not dealt with. The effect of scour protection in soil stiffness and natural frequency of the structure is assumed to be negligible.

3.4 Soil-Structure interaction

The site location, Site 15, has no available data regarding soil conditions and soil stratigraphy. For simplicity, it is assumed that the site has a single sand layer. The assumed sand has a friction angle of $\mathbf{36°}$ and a saturated unit weight of $\mathbf{20\ kN/m^3}$.

3.4.1 Soil Parameters

The pile-soil interaction due to lateral load is represented by P-Y curves, which are calculated using both the API method and the Finite Element Method. The parameters used for API method and Finite Element Method are summarized in Table 3.9 and Table 3.10, respectively. For the Finite Element Method, the Hardening Soil (HS) Model is employed in Plaxis 3D. The HS model is chosen due to its capability in capturing the hyperbolic increase in stiffness of sand.

Table 3.9 Soil parameters for API Method

Parameter	Value
Angle of internal friction, φ' [°]	36
Initial modulus of subgrade reaction, k [kN/m^3]	24440
Coefficient, C1 [-]	3.2
Coefficient, C2 [-]	3.6
Coefficient, C3 [-]	60
Unit weight – saturated, γ_{sat} $[kN/m^3]$	20
Unit weight – effective, γ_{eff} $[kN/m^3]$	10.2

Table 3.10 Soil parameters for FE Method using Hardening Soil model

Parameter	Value
Drainage type [-]	Drained
Unit weight – unsaturated, γ $[kN/m^3]$	17
Unit weight – saturated, γ_{sat} $[kN/m^3]$	20
Secant stiffness in standard drained triaxial test, ${E_{50}}^{ref}$ $[kN/m^2]$	4.50E+04
Tangent stiffness for primary oedometer loading, ${E_{oed}}^{ref}$ $[kN/m^2]$	3.75E+04
Unloading and reloading stiffness, ${E_{ur}}^{ref}$ $[kN/m^2]$	1.20E+05
Power for stress-level dependency of stiffness, m [-]	0.5
Effective Cohesion, ${c'}_{ref}$ $[kN/m^2]$	1
Effective angle of internal friction, φ' [°]	36
Angle of dilatancy, ψ[°]	6
Poisson's ratio, ν [-]	0.3

3.4.2 Plaxis Model

The general steps in modeling pile-soil interaction in Plaxis 3D includes defining the soil properties, defining the structure (pile), applying the load and generating the mesh. Figure 3.4 shows the FE model of the pile embedded in the soil. By default, meshes for both soil and pile are generated using triangular elements as shown.

To generate force-displacement relationship along the pile length, a force shall be applied at the top of the pile. Note that the pile head is elevated 0.5 m above the ground to avoid the applied load being directly taken by the soil layer at the ground level.

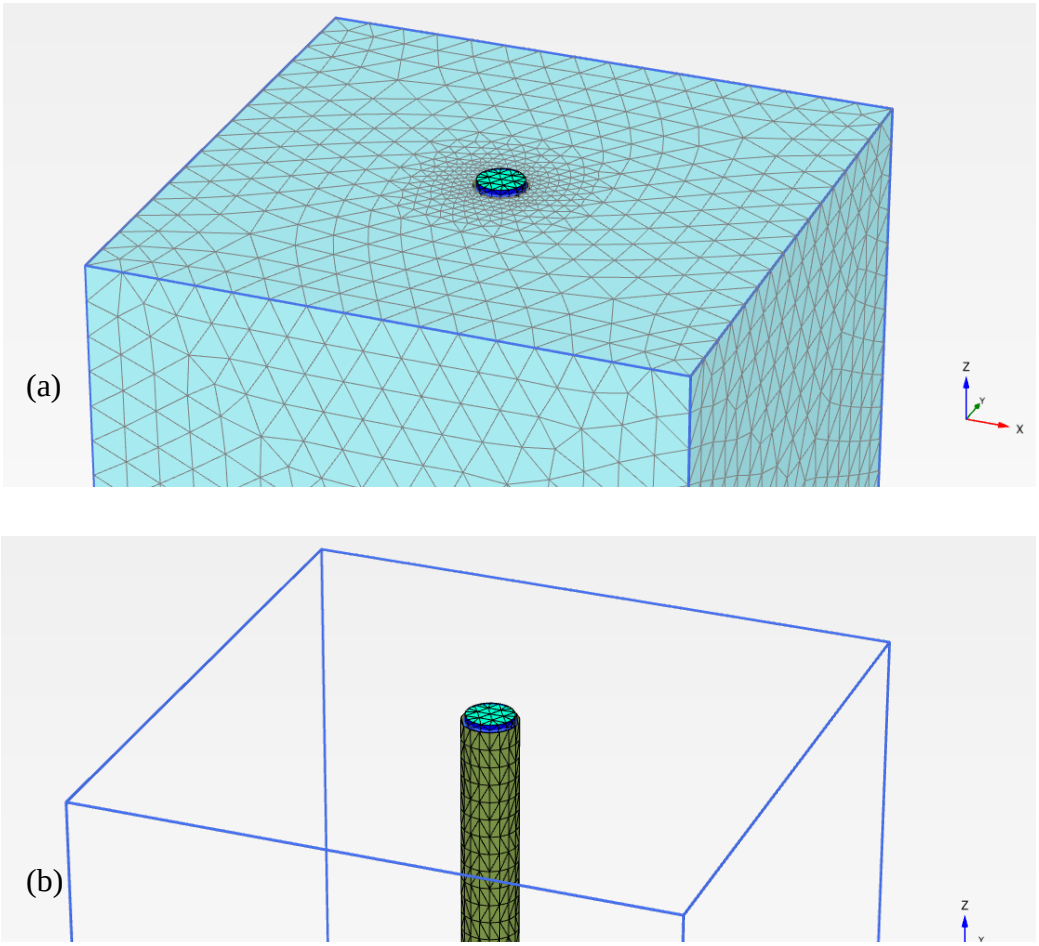

Figure 3.4 FE model of the pile-soil interaction in Plaxis 3D
(a) meshed pile and soil strata (b) meshed pile structure

The detail of the pile structure model is illustrated in Figure 3.5. A rigid plate is attached on top of the pile as shown in Figure 3.5a. This plate receives the applied concentrated load and allows a more even force distribution along the circumference of the pile. Figure 3.5 b shows the generated positive and negative pile interface where the soil-pile interaction can be investigated.

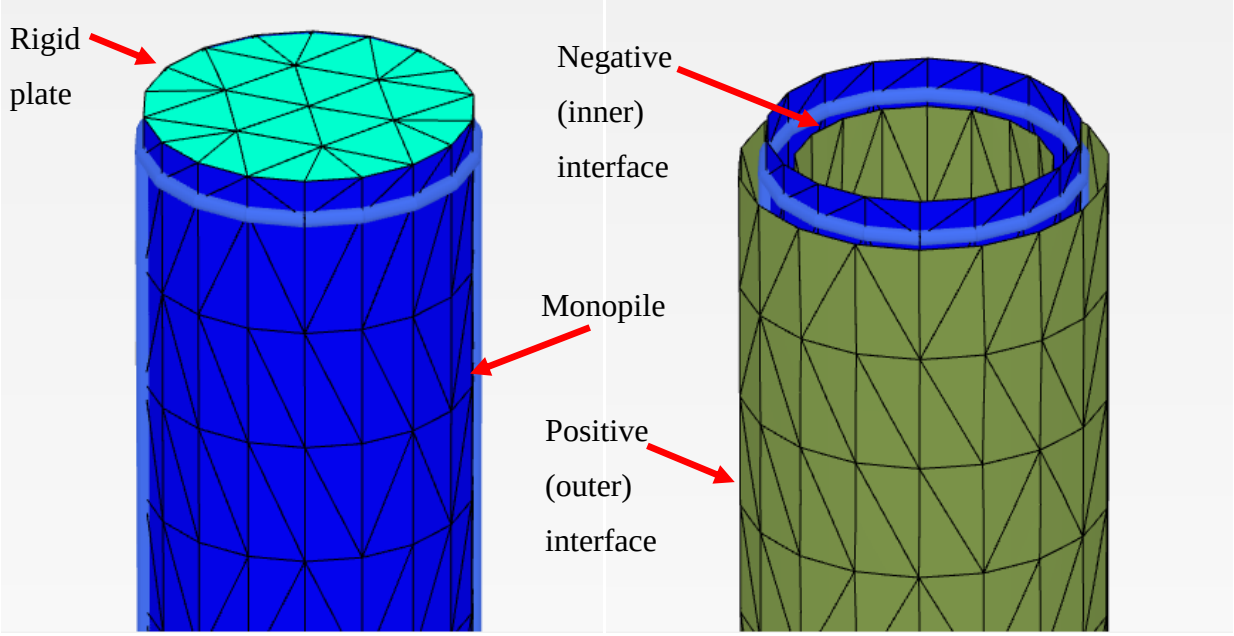

Figure 3.5 Pile structure model
(a) rigid plate and pile (b) positive and negative interface of the pile

After generating the mesh for the defined soil and pile structure, the simulation can be done by defining different phases or stages. Only two stages are necessary for the purpose of generating the p-y curves. The initial phase involves establishing or activating the soil strata and pile structure, including the generated pile interfaces. The second phase is the "loading" phase where the concentrated load is applied at the center of the rigid plate, which allows even distribution of the load along the circumference of the pile. The results are viewed in a separate program, "Plaxis Output", which generates both tabulated and graphical output.

The $30{,}000\ kN$ concentrated load applied is about three times the design lateral load, which must be sufficient to be set as the upper limit of the P-Y curves. The resulting soil displacement in the direction of the applied load is illustrated in Figure 3.6, while the interface stresses and pile displacement are illustrated in Figure 3.7. The positive and negative interfaces stresses and pile deflection are the main outputs required to extract the p-y curves. The interface stresses are used to calculate force distribution along the length of the pile,

whereas the latter gives the corresponding lateral deflections along the direction of the load. Note that each simulation (each applied load) corresponds to a single point in the p-y curves.

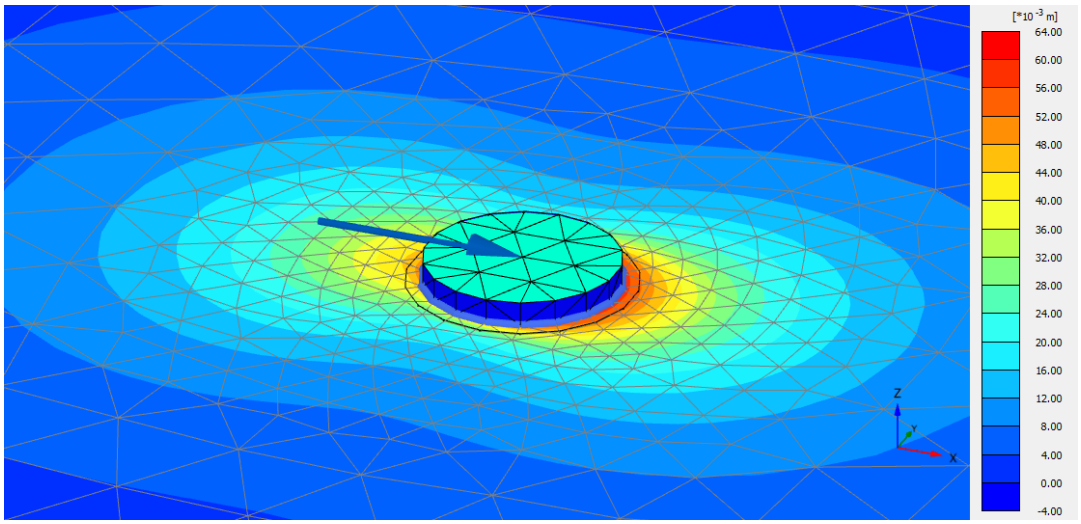

Figure 3.6 Soil displacement along the direction of the load for P = 30,000 kN

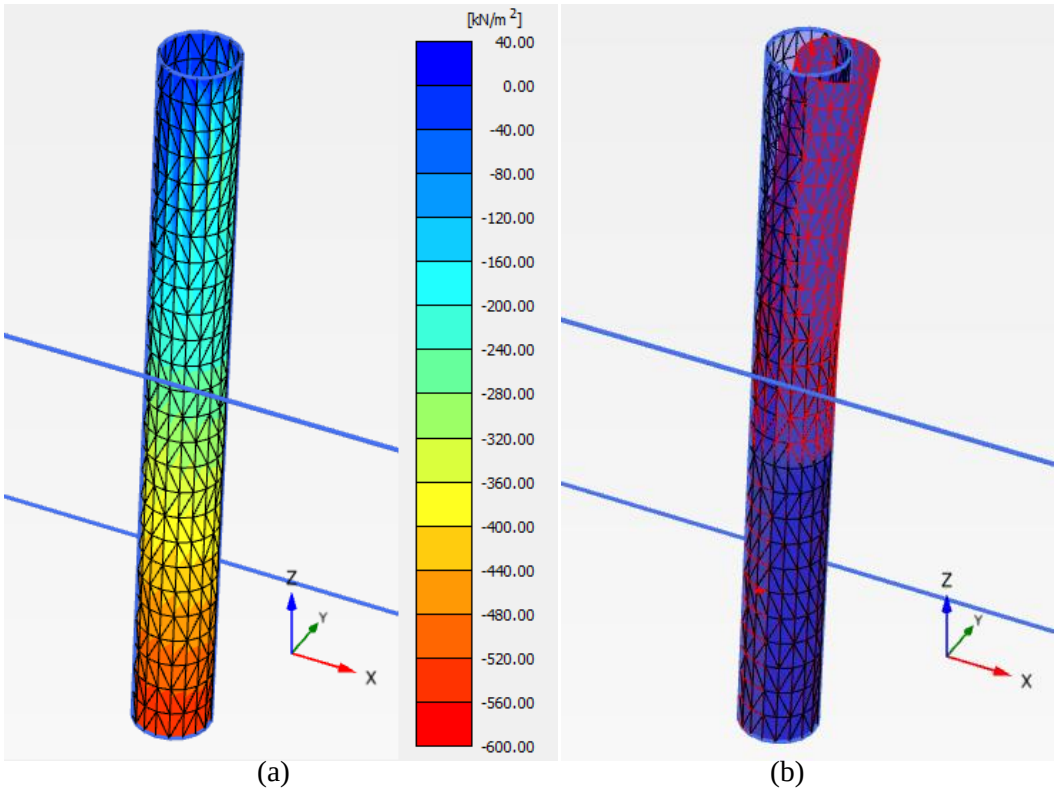

(a) (b)

Figure 3.7 Graphical stress and displacement output
(a) Stress at the positive interface (b) pile deflection

3.4.3 Nonlinear P-Y Curve

The nonlinear p-y curves for a pile having an 8 m (10D) diameter, 100 mm thickness and 80 m embedment length are calculated using both API method and FE method. The extracted P-Y curves for the shallow depth are illustrated in Figure 3.8. It verifies that the soil stiffness consistently increases with depth for at least until twice the diameter (2D). The stiffness on the shallow region of the soil has a more significant influence in the overall static and dynamic response of the structure compared to the deeper part of the soil.

Furthermore, the results from the FE method are compared with API method as shown in Figure 3.9 and Figure 3.10. For shallow depth (z = -1.25 m), there is a good agreement between FE method and API method. As the depth of the soil increases, the API method starts to overestimate the soil stiffness as illustrated in Figure 3.10. This can be explained by the fact that the API method has a linear increase in stiffness with depth, whereas the FE method has a parabolic increase. This means that at deeper depths, the use of API method further overestimates the soil stiffness. The nonlinear PY curves derived for each diameter and pile embedment depth are summarized presented in Appendix B.

It should be noted that the effect of having a scour protection is neglected in both p-y curves, since it requires design details of the scour protection. Having a scour protection would lead to an additional increase in stiffness in the shallow depths. Furthermore, certain phenomena like soil stiffening due to pile driving and cyclic stiffening which might increase soil stiffness [14] are also neglected.

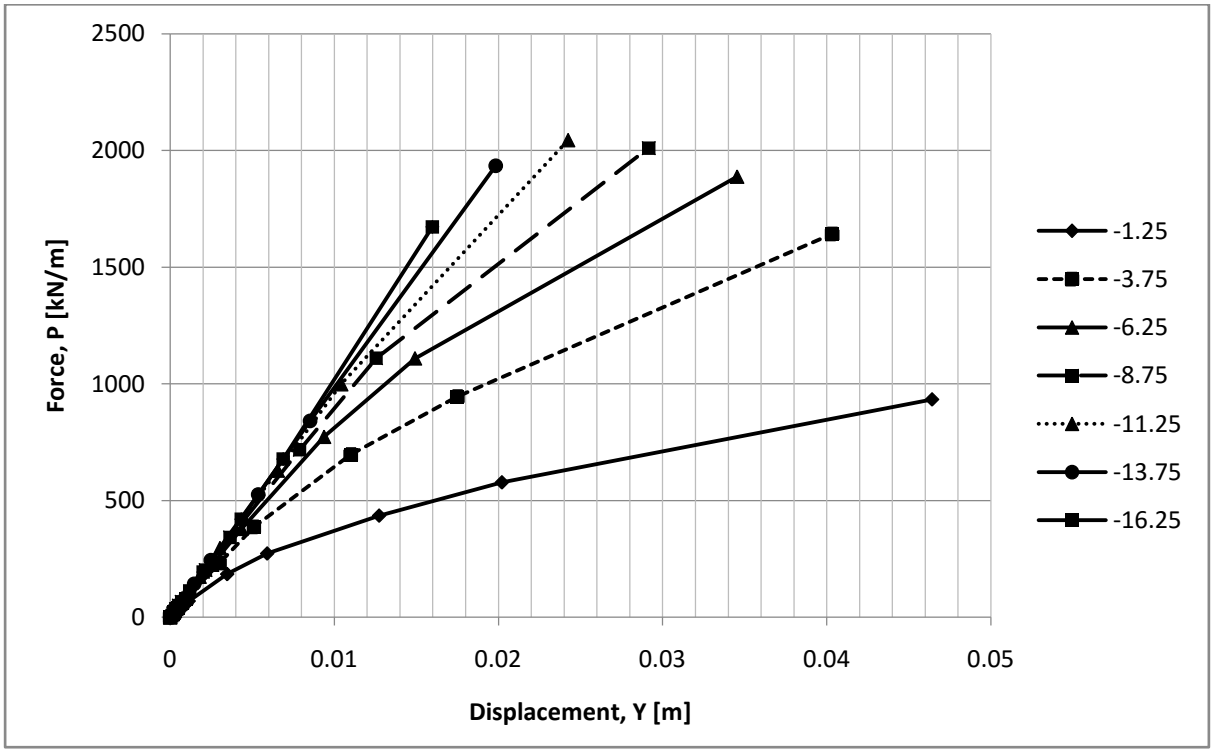

Figure 3.8 Extracted P-Y curves for shallow part of the soil

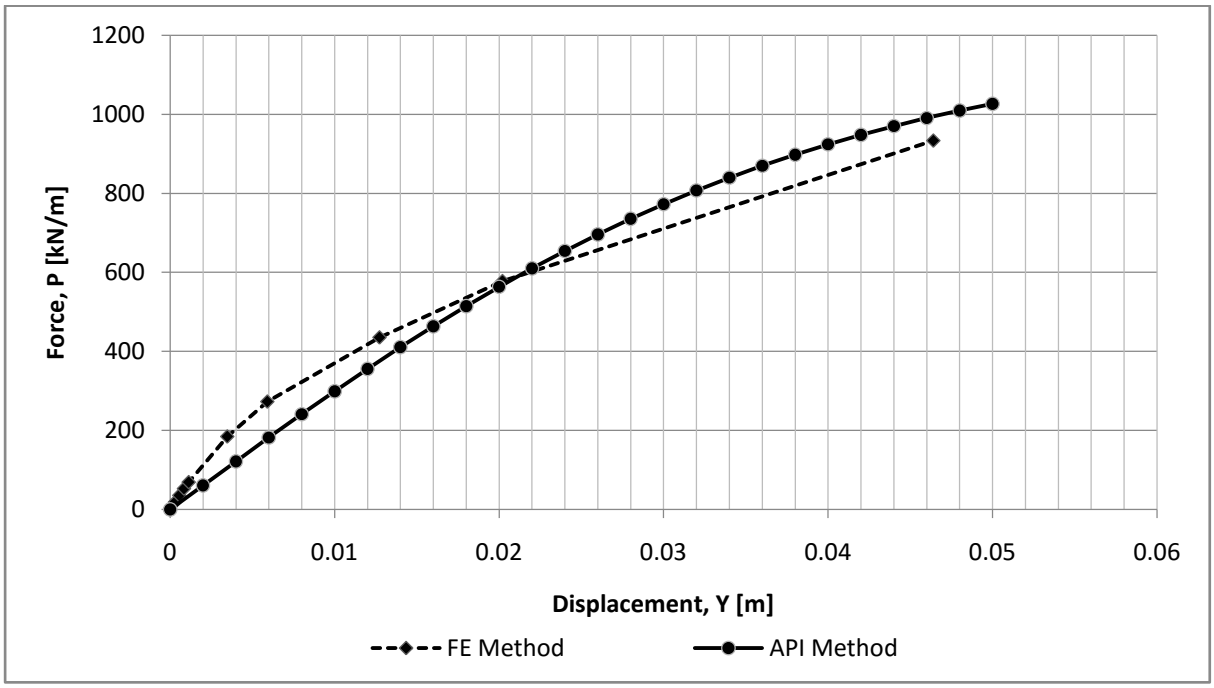

Figure 3.9 P-Y curve for API method and FE method at shallow depth (z = -1.25 m)

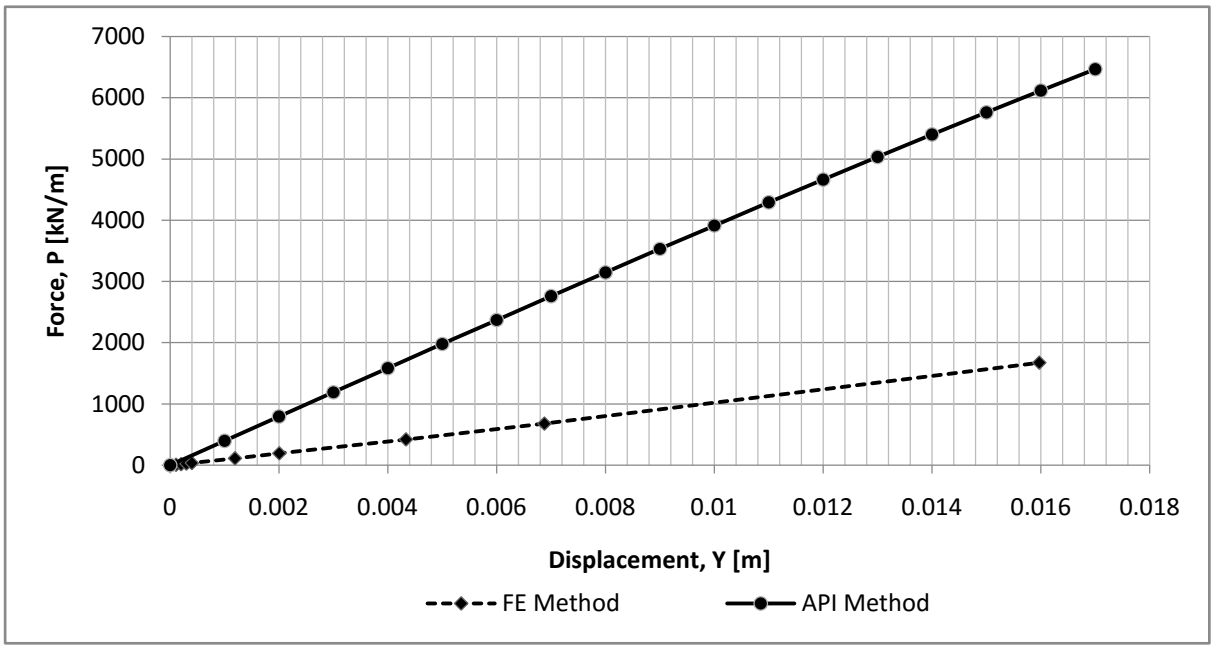

Figure 3.10 P-Y curve for API method and FE method at mid-depth (z = -16.25 m)

3.5 Extreme Load Preliminary Estimates

The monopile foundation shall be able to withstand extreme load combinations from wind, wave and current, while also taking into account lateral deflection limits along the length of the pile. For preliminary design, the extreme loads are calculated based on values presented in Table 3.11.

The wave parameters (Hs and Tp) are chosen from the 50-year contour surface with the maximum Hs, whereas the design wind speed (Uw) is chosen as the rated wind speed as it gives the maximum thrust force in the rotor and is therefore more conservative. Lastly, the current with 10-year return period is selected as prescribed. Morison's equation is used to calculate the hydrodynamic loads.

Other parameters used in the calculation are summarized in Table 3.12. Before wave and current loads calculation can be done, an initial pile diameter of 8 m is assumed. For preliminary analysis, further simplifications are made by not accounting drag loads from other

appurtenances (i.e. ladder, boat landing, j-tubes) and diffraction effects in the drag and inertia coefficients, respectively.

Table 3.11 Environmental conditions for extreme load calculation

Parameter	Design Value
U_{wind} [m/s]	11.4 (rated)
H_s [m]	9.9 (50-year)
T_p [s]	14.0 (50-year)
$U_{current}$ [m/s]	0.55 (10-year)

Table 3.12 Other parameters for extreme load calculation

Parameter	Value
Pile Diameter, Dpile [m]	8.0
Drag coefficient, CD [-]	1.0
Inertia coefficient, CM [-]	2.0
Water depths [m]	20, 30, 40, 50
Hub height [m]	119.0
Safety factor [-]	1.35
g [m/s^2]	9.81
Seawater density [kg/m^3]	1025

The calculated horizontal loads and moment at seabed are shown in Figure 3.11 and Figure 3.12, respectively. Although wave horizontal loads are higher in magnitude, the wind load has a higher contribution to overturning moment since the load is applied at the hub height. Increasing the water depth also increases both horizontal load and moment contributions due to waves, but causes a very small increase in overturning moment due to wind. This results from the wind load magnitude being the same and the only increase in overturning moment comes from the slight increase in moment arm from increasing the water depth. The loads due to the 10-year current are not significant compared to load contributions from wind and wave. Note that a safety factor of 1.35 for environmental loads is applied in the calculation.

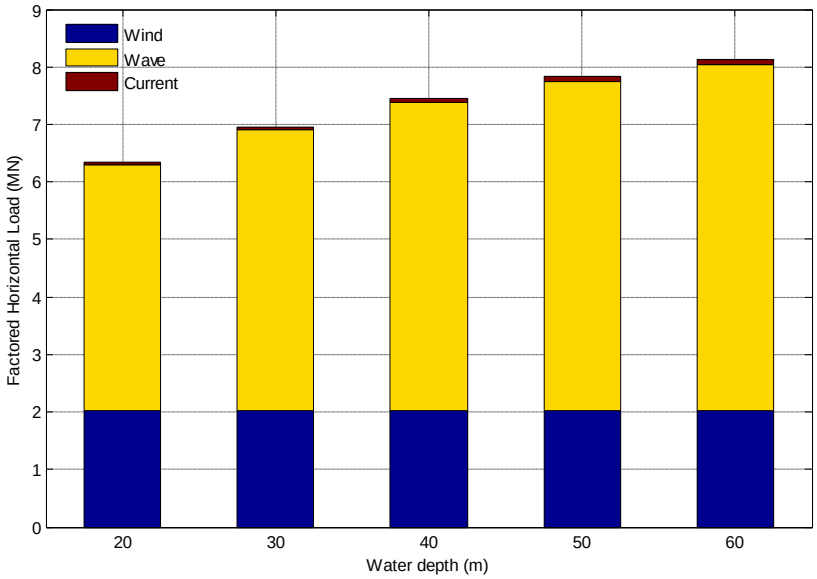

Figure 3.11 Factored horizontal load at seabed for different water depths

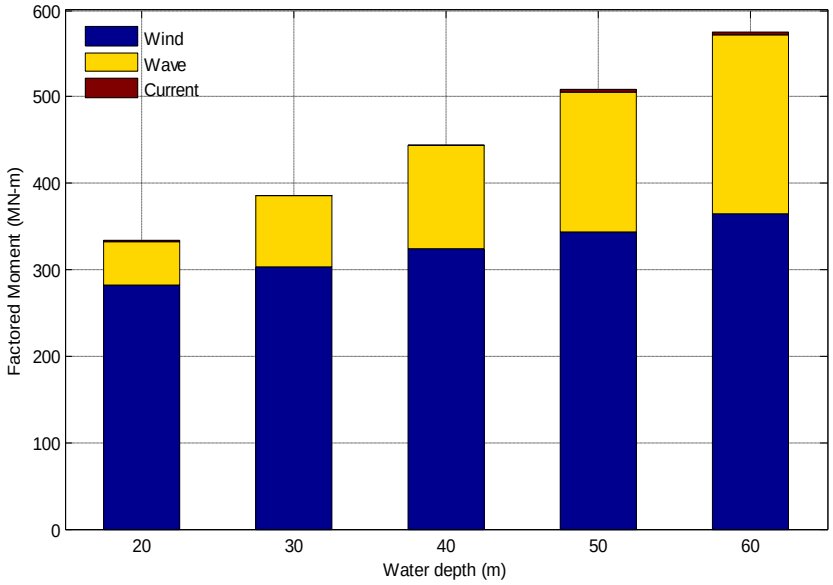

Figure 3.12 Factored moment at seabed for different water depths

To be able to investigate if ultimate limit state and serviceability limit states are satisfied for a given monopile diameter, the design loads for each diameter and water depth are calculated as shown in Figure 3.13 and Figure 3.14. The design loads include the hydrodynamic loads due to waves and current, as well as aerodynamic loads. It should be noted that the hydrodynamic loads are estimated at instantaneous water level using Morison's equation with linear wave kinematics.

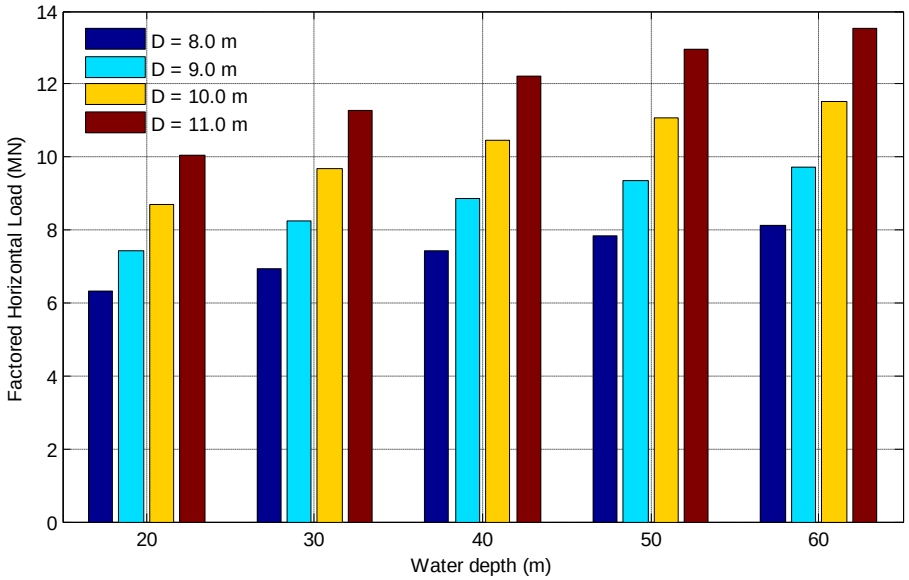

Figure 3.13 Factored horizontal load at seabed for each water depth and pile diameter

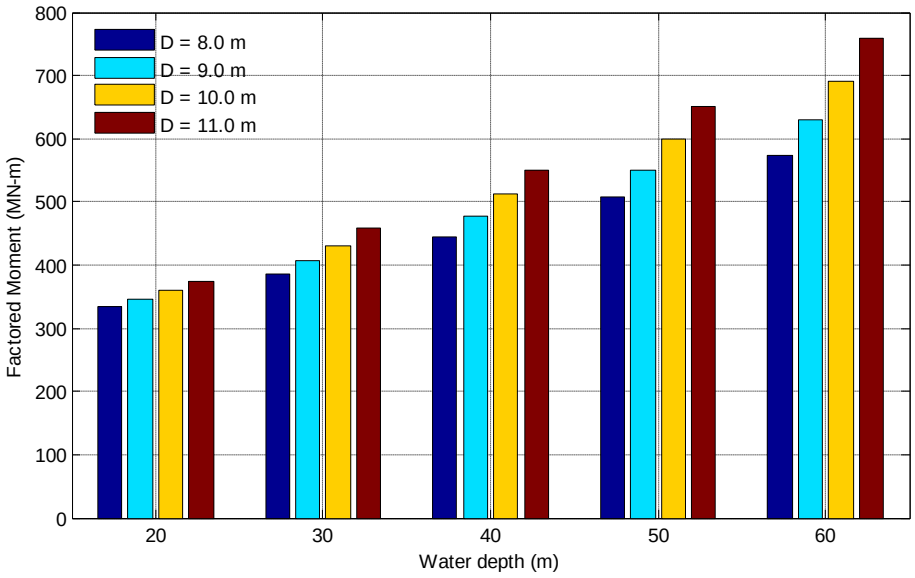

Figure 3.14 Factored moment at seabed for each water depth and pile diameter

Increasing the diameter increases the design lateral load, mainly due to the increase in hydrodynamic loads. Considering the design loads at the 20 m water depth, increasing the pile diameters does not lead to significant increase in the bending moment at seabed. However, due to natural frequency and economic considerations, the least monopile diameter that can satisfy design criteria is the better option.

Chapter 4.
RIFLEX Model

4.1 Design Elevations

The design elevations are determined based on the parameters summarized in Table 4.1, while the calculated interface level and hub height are summarized in Table 4.2. Note that the hub elevation specified in the DTU 10 MW RWT key parameters is adopted, resulting to a clearance of 10.9 m between the blade and the platform.

Table 4.1 Parameters for Interface level and hub height calculation

Parameter	Value
Lowest Astronomical Tide, LAT [m]	-2.5
50-year tidal range, Δz_{tide} [m]	5.0
50-year positive storm surge, Δz_{surge} [m]	3.0
Airgap, Δz_{airgap} [m]	1.5
$H_{s,50}$ [m]	9.9
H_{max} [m]	18.4
50-year water level, ζ [m]	12.0
Clearance, $\Delta z_{clearance}$ [m]	10.9
Rotor diameter [m]	178.3

Table 4.2 Interface level and hub height

Design Elevation	Value
$z_{interface}$ [m]	19.0
z_{hub} [m]	119.0

4.2 RIFLEX Model

RIFLEX is a modeling tool developed for the analysis of flexible marine risers and other slender structures. The program is capable of static, dynamic and Eigenvalue analysis based on finite element modeling. In addition, the program is suitable for modeling wind turbines by being able to apply blade element momentum (BEM) theory for aerodynamic load calculation and nonlinear soil springs for considering soil-pile interaction.

RIFLEX is one of the programs supported by SIMA, which is a joint industry project between MARINTEK and Statoil. SIMA provides a more convenient user interface for entering input data and for verifying the model by a 3-dimensional model visualization.

4.2.1 DTU 10 MW RIFLEX model

The DTU 10 MW RWT is modeled in RIFLEX as shown in Figure 4.1. Unidirectional design loads due to wind, wave and current are applied for the SLS check and yield check.

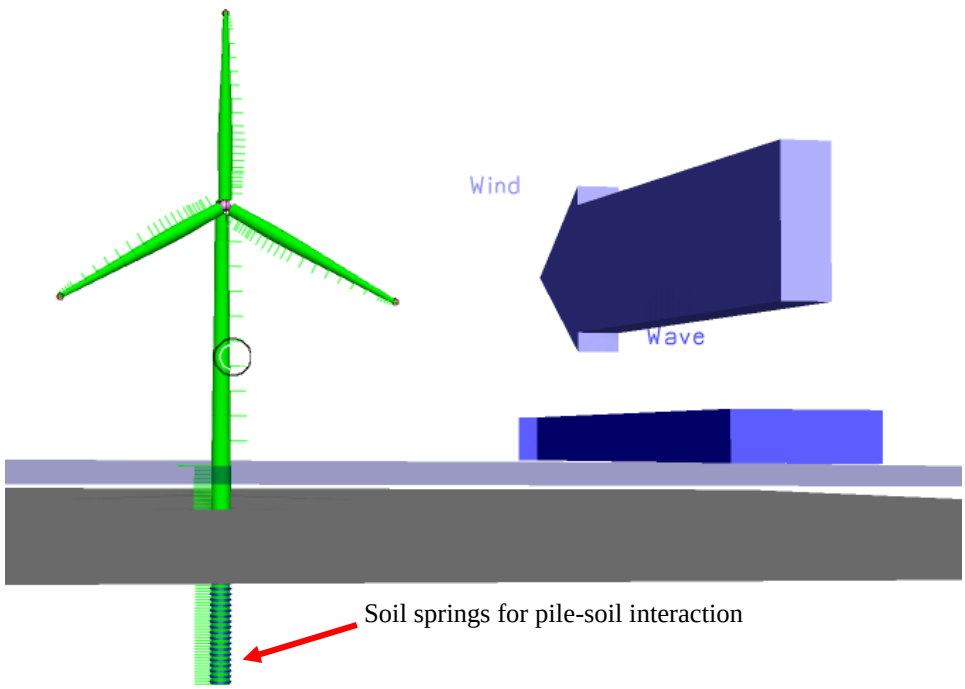

Figure 4.1 DTU 10 MW model in RIFLEX

The wind turbine blades follow the original airfoil geometric design. The tower is modelled as an axisymmetric pipe having 10 sections of constant diameter each, decreasing from a specified diameter at the bottom to the top of the tower. Similarly, the monopile is modelled in RIFLEX as an axisymmetric pipe. Both tower and monopile have a linearly elastic material with Young's modulus, $E = 210\,\text{MPa}$ and shear modulus, $G = 80.8\,\text{MPa}$. The monopile segment below the ground is laterally supported by the nonlinear PY curves derived from Plaxis 3D. Following the element size in Plaxis 3D, the monopile below the ground is supported by a lateral resistance for every 2.5 m length. In RIFLEX, lateral resistance is given by the spring coinciding with the XY-plane as shown in Figure 4.1.

4.2.2 Model assumptions

The following assumptions and simplifications are made in modelling the DTU 10MW RWT in RIFLEX:

a) The transition piece is not modelled in detail. Instead, the component is accounted for by adding a $500\ tonne$ point mass at the calculated interface level ($z_{int} = 19.0\,\text{m}$)
b) The tower is modelled by 10 sections, each having a constant diameter
c) The tower material density is increased by 8% to account for the the mass of secondary structures ($\rho = 8500\,\frac{\text{kg}}{\text{m}^3}$) [31]
d) The tower-pile interface coincides with the MSL
e) The effect of marine growth is neglected for preliminary dimensioning of the monopile. It is expected that the presence of marine growth would slightly decrease the overall natural frequency of the monopile. The target natural frequency of $0.25\,\text{Hz}$ is chosen such that it lies closer to the upper limit of the ideal frequency range
f) The effect of scour protection is negligible

4.3 TurbSim

TurbSim is a stochastic and full-field inflow turbulence tool developed by National Renewable Energy Laboratory (NREL) to simulate three-dimensional wind speed vectors in a spatially fixed, two-dimensional vertical rectangular grid. It incorporates coherent turbulent structures, which properly represent spatial and temporal wind field caused by instabilities in boundary layer flows. Such effects are not well-represented by the IEC Turbulence Models (NTM) [35].

The impact of organized or coherent inflow turbulence on the dynamic response of wind turbines was studied by Kelley [36] based on field experimentations. It was concluded coherent turbulence develops from stable, nocturnal atmospheric boundary layer which leads to higher fatigue damage during nighttime. As wind turbine blades pass through the turbulent region, the associated resonant flow fields impart transient loads which are propagated from the rotor to the entire support structure. The effect of coherent structures in energy intensity and wind velocity components is illustrated in Figure 4.2, where higher peaks can be observed.

For this study, wind fields for ULS and FLS simulations are generated using TurbSim and exported to SIMA Riflex model.

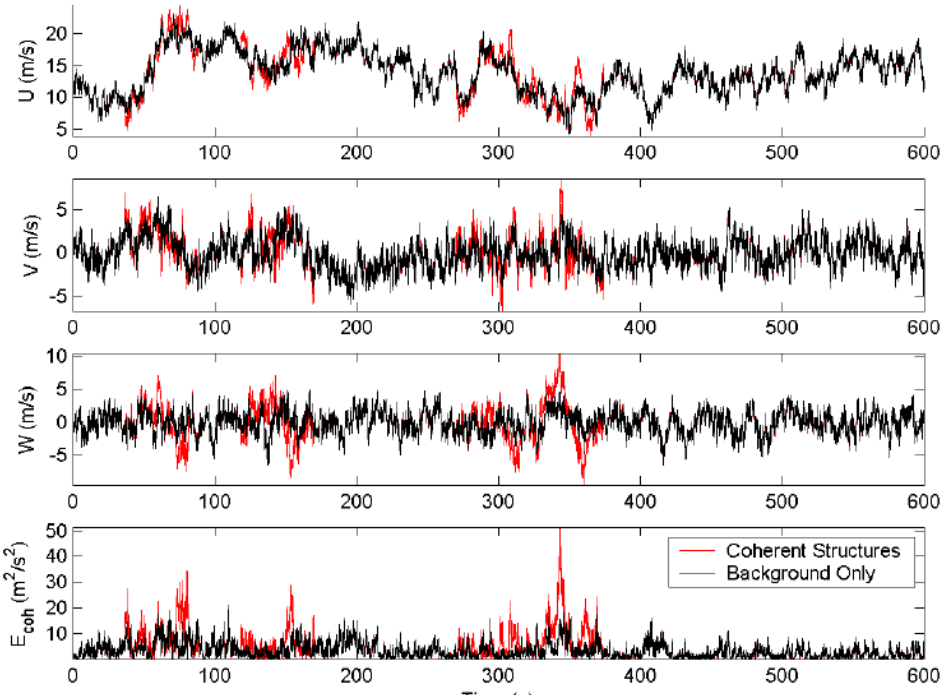

Figure 4.2 Example of coherent turbulent structure

A coherent turbulent structure of intensity CTKE (E_{coh}) being added to the streamwise (U), crosswind (V), and vertical (W) wind components at a given grid point location [36]

Chapter 5.

Preliminary Design

5.1 Initial Monopile Diameter and Tower Dimensions

After establishing the wind turbine model for diameters 8.0 m, 9.0 m and 10.0 m, the next step is to determine the required pile diameter. The monopile thickness is based on the assumed diameter-thickness ratio of 80 [37]. The initial criteria is that the target natural frequency of 0.25 Hz (natural period of 4 s) can be achieved as the pile penetration depth is decreased. The natural frequencies calculated for different pile diameters having a penetration depth of 80 m at 20 m water depth are summarized in Table 5.1. It shows that even at 10.0 m pile diameter, the natural frequency only increased to 0.22 Hz. From a practical point of view, a further increase in monopile diameter to reach the desired stiffness could cause challenges in manufacturing and installation. In this case, the original tower design needs to be modified to reach the desired natural frequency.

Table 5.1 Natural frequency at 20m water depth for different pile diameters

Monopile diameter [m]	Monopile thickness [mm]	Natural Period [s]	Natural frequency [Hz]
8	100	5.008	0.200
9	110	4.721	0.212
10	125	4.531	0.221

5.2 Modified tower diameter

The tower diameter is modified for every monopile diameter. As the chosen monopile diameter is increased, the tower diameter can be reasonably increased by applying the same scaling factor (i.e. pile diameter increases by 12.5% from 8.0 m to 9.0 m). The modified tower diameters, both at the base and at the top, are summarized in Table 5.2. The chosen design values are from the exact values rounded up to the nearest 0.25 m increment. Note that the tower dimensions for the 8.0 m monopile diameter remain unchanged to keep the design proportion.

Table 5.2 Modified tower diameter at base and top

Monopile Diameter	Tower diameter scale	Exact value		Chosen value	
		Tower diameter at base [m]	Tower diameter at top [m]	Tower diameter at base [m]	Tower diameter at top [m]
8.0	1.000	8.30	5.50	8.30	5.50
9.0	1.125	9.34	6.19	9.50	6.25
10.0	1.250	10.38	6.88	10.50	7.00

Monopile diameter and scaled tower thickness

For each water depth, a combination of pile diameter and modified tower thickness shall be chosen according to the target natural frequency. For the thickness to have a definite value, the scale factors are fixed to 1.25, 1.50, 1.75 and 2.00. The effect of scaling the tower thickness to the natural frequency is investigated for each monopile diameter.

Figure 5.1, Figure 5.2, Figure 5.3 and Figure 5.4 show this relationship for water depths 20 m, 30 m, 40 m and 50 m. The chosen values for the tower diameters are applied in these calculations.

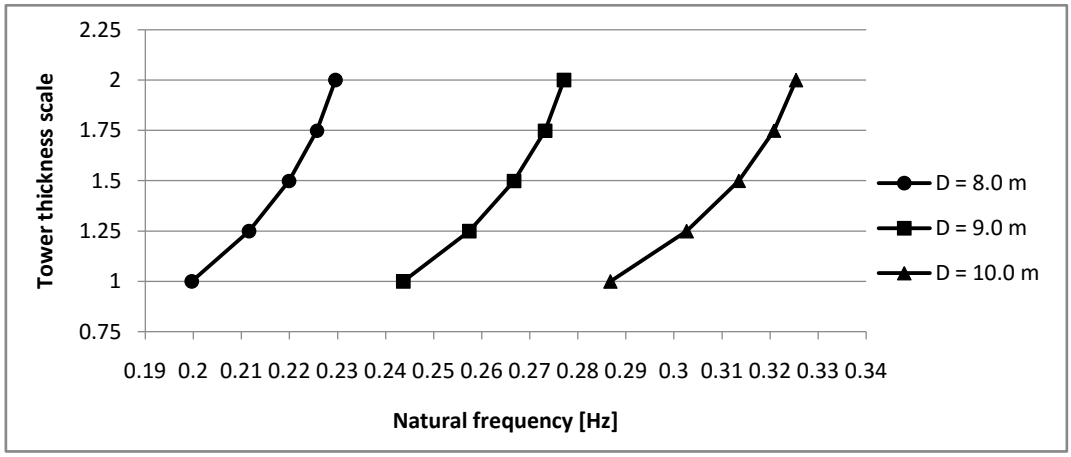

Figure 5.1 Design natural frequencies for 20 m water depth

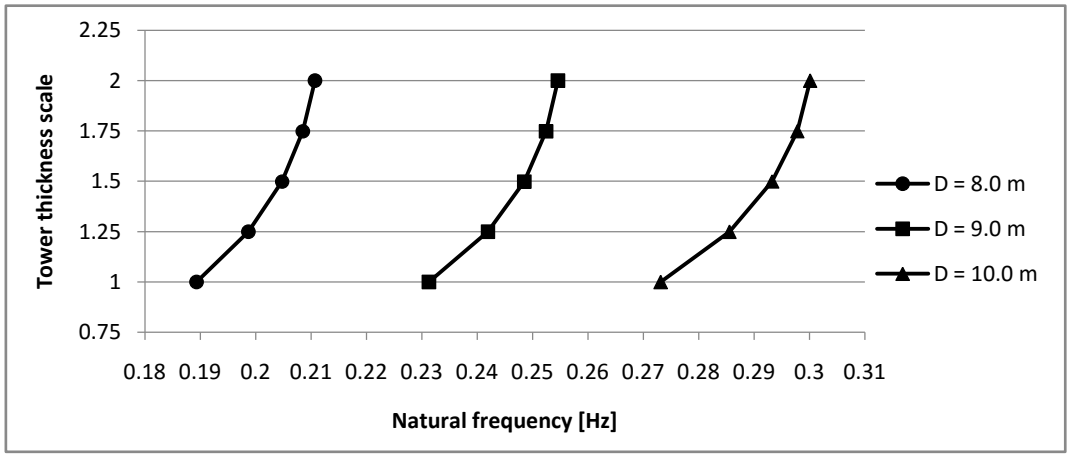

Figure 5.2 Design natural frequencies for 30 m water depth

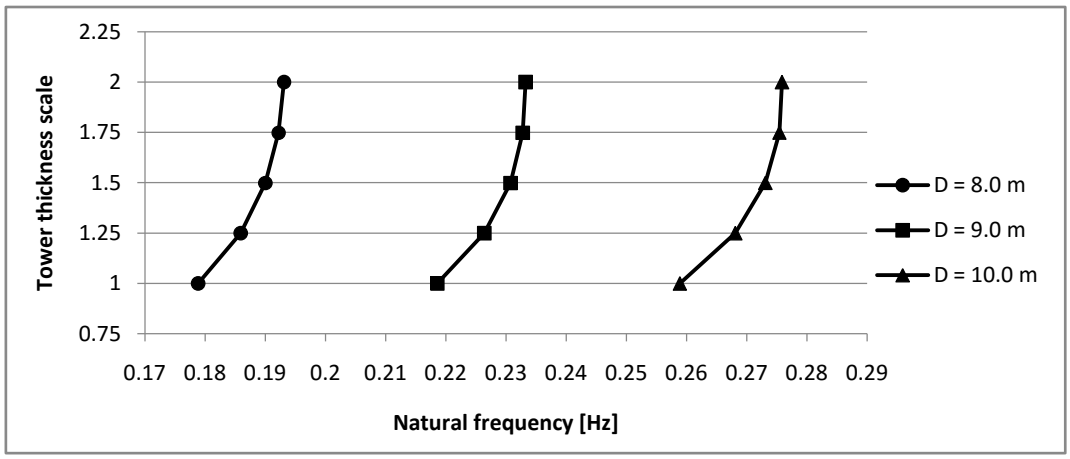

Figure 5.3 Design natural frequencies for 40 m water depth

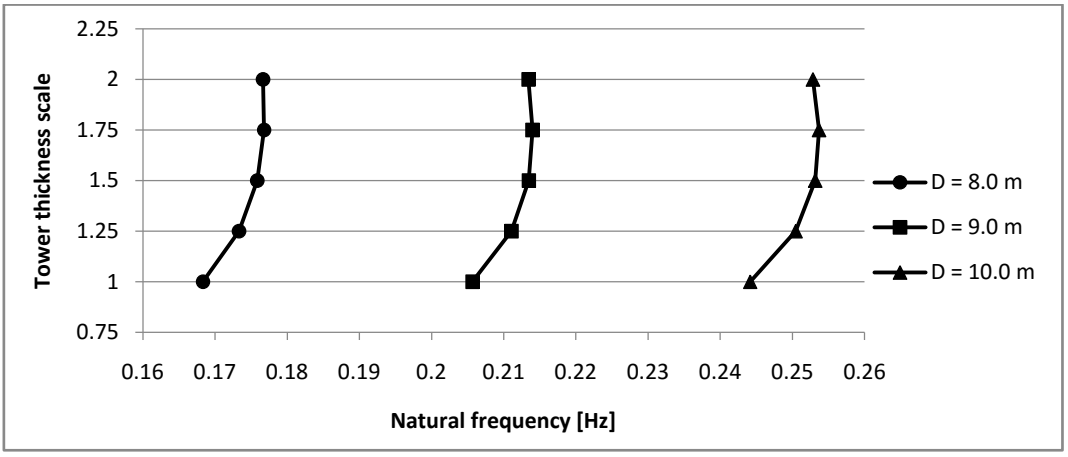

Figure 5.4 Design natural frequencies for 50 m water depth

From these figures, a combination of pile diameter and tower thickness can be chosen such that the natural frequency is higher than 0.25 Hz. The combination of pile diameter and tower thickness having the smallest dimensions and natural frequency higher than 0.25 Hz were selected as optimum dimensions. In the case of the 20 m water depth where the target natural frequency lies at the higher end of the 9 m pile diameter range, the 10 m pile diameter could also be considered satisfactory. However, the increasing the pile diameter could lead to overly conservative designs as compared to increasing the tower thickness. Choosing a higher pile diameter could in fact decrease the required embedment depth of the pile to reach target natural frequency, such that the amount of steel required is about the same. Nevertheless, the smaller diameter is more preferred considering manufacturing, handling and installation procedure involved in larger diameter piles.

Note that the natural frequencies are calculated based on an 80.0 m penetration depth. Thus, the calculated natural frequencies are expected to decrease as the monopile length is reduced during the design procedure. The initial pile diameter and tower thickness scale for water depths 20 m, 30 m, 40 m and 50 m are summarized in Table 5.3.

Table 5.3 Initial pile diameter and tower thickness scale for different water depths

Water depth [m]	Pile Diameter [m]	Tower thickness scale [-]	Natural frequency at 80 m penetration depth [Hz]
20	9.0	1.25	0.257
30	9.0	1.75	0.252
40	10.0	1.00	0.259
50	10.0	1.50	0.253

Modified tower dimensions

The tower dimensions are modified based on the chosen tower diameter and tower thickness scale for different water depths. Table 5.4, Table 5.5, Table 5.6 and Table 5.7 summarize the modified tower dimensions and corresponding structural properties for water depths 20 m, 30 m, 40 m and 50 m, respectively.

Table 5.4 Modified tower dimensions for 20 m water depth

Section	Height [m]	D_{outer} [m]	t [mm]	$A_{cross\ section}$ [m^2]	Mass per length [kg/m]	Radius of gyration [m]	Second moment of inertia [m^4]
1	0 11.5	9.50	47.5	1.4106	11989.75	3.3420	15.7545
2	11.501 23	9.14	45	1.2856	10927.78	3.2152	13.2902
3	23.001 34.5	8.78	42.5	1.1663	9913.69	3.0884	11.1248
4	34.501 46	8.42	40	1.0526	8947.49	2.9616	9.2330
5	46.001 57.5	8.06	37.5	0.9446	8029.16	2.8348	7.5912
6	57.501 69	7.69	35	0.8422	7158.72	2.7081	6.1763
7	69.001 80.5	7.33	32.5	0.7454	6336.15	2.5813	4.9667
8	80.501 92	6.97	30	0.6543	5561.47	2.4545	3.9417
9	92.001 103.5	6.61	27.5	0.5688	4834.67	2.3277	3.0817
10	103.501 115.63	6.25	25	0.4889	4155.75	2.2009	2.3682

Table 5.5 Modified tower dimensions for 30 m water depth

Section	Height [m]	D_{outer} [m]	t [mm]	$A_{cross\ section}$ [m^2]	Mass per length [kg/m]	Radius of gyration [m]	Second moment of inertia [m^4]
1	0 11.5	9.50	66.5	1.9708	16751.91	3.3353	21.9241
2	11.501 23	9.14	63	1.7963	15268.61	3.2089	18.4965
3	23.001 34.5	8.78	59.5	1.6297	13852.16	3.0824	15.4843
4	34.501 46	8.42	56	1.4709	12502.55	2.9560	12.8526
5	46.001 57.5	8.06	52.5	1.3200	11219.80	2.8296	10.5683
6	57.501 69	7.69	49	1.1769	10003.88	2.7031	8.5997
7	69.001 80.5	7.33	45.5	1.0417	8854.82	2.5767	6.9165
8	80.501 92	6.97	42	0.9144	7772.60	2.4502	5.4899
9	92.001 103.5	6.61	38.5	0.7950	6757.23	2.3238	4.2929
10	103.501 115.63	6.25	35	0.6834	5808.70	2.1974	3.2996

Table 5.6 Modified tower dimensions for 40 m water depth

Section	Height [m]	D_{outer} [m]	t [mm]	$A_{cross\ section}$ [m^2]	Mass per length [kg/m]	Radius of gyration [m]	Second moment of inertia [m^4]
1	0 11.5	10.50	38	1.2490	10616.18	3.6989	17.0881
2	11.501 23	10.11	36	1.1395	9685.50	3.5621	14.4583
3	23.001 34.5	9.72	34	1.0348	8796.15	3.4253	12.1416
4	34.501 46	9.33	32	0.9351	7948.13	3.2885	10.1123
5	46.001 57.5	8.94	30	0.8402	7141.43	3.1517	8.3458
6	57.501 69	8.56	28	0.7501	6376.06	3.0150	6.8186
7	69.001 80.5	8.17	26	0.6649	5652.01	2.8782	5.5083
8	80.501 92	7.78	24	0.5846	4969.29	2.7414	4.3936
9	92.001 103.5	7.39	22	0.5092	4327.89	2.6046	3.4541
10	103.501 115.63	7.00	20	0.4386	3727.82	2.4678	2.6709

Table 5.7 Modified tower dimensions for 50 m water depth

Section	Height [m]	D_{outer} [m]	t [mm]	$A_{cross\ section}$ [m^2]	Mass per length [kg/m]	Radius of gyration [m]	Second moment of inertia [m^4]
1	0 11.5	10.50	57	1.8700	15895.34	3.6922	25.4932
2	11.501 23	10.11	54	1.7062	14502.30	3.5558	21.5718
3	23.001 34.5	9.72	51	1.5495	13171.08	3.4193	18.1170
4	34.501 46	9.33	48	1.4002	11901.69	3.2829	15.0906
5	46.001 57.5	8.94	45	1.2581	10694.12	3.1465	12.4558
6	57.501 69	8.56	42	1.1233	9548.39	3.0100	10.1778
7	69.001 80.5	8.17	39	0.9958	8464.48	2.8736	8.2231
8	80.501 92	7.78	36	0.8756	7442.40	2.7372	6.5599
9	92.001 103.5	7.39	33	0.7626	6482.15	2.6007	5.1581
10	103.501 115.63	7.00	30	0.6569	5583.72	2.4643	3.9892

5.3 Monopile Embedment Depth

To determine the minimum pile embedment depth necessary to reach the target natural frequency, the RIFLEX model has to be modified for each penetration depth. For each pile embedment length, a different set of lateral soil springs is derived from Plaxis 3D and is entered in RIFLEX. This ensures that the lateral soil stiffness takes into account the complex shift from flexible pile behaviour to rigid pile behaviour as the embedment length is reduced.

For water depths 20 m and 30 m having a designed pile diameter of 9.0 m, the effect of varying the pile embedment length to the overall natural frequency of the wind turbine is illustrated in Figure 5.5. It is found that reducing the embedment length from 9D to 6D makes no significant influence on the overall natural frequency. The target natural frequency of 0.25 Hz is achieved when the embedment lengths are set to **4D (35 m)** and **5D (45 m)** for water

depths 20 m and 30 m, respectively. Further decrease beyond these embedment lengths significantly reduces the natural frequency.

For water depths 40 m and 50 m having a designed pile diameter of 10.0 m, a similar behaviour is found as illustrated in Figure 5.6. No significant change in natural frequency occurs from normalized pile embedment length 10D to 5D. Based on the target natural frequency, the embedment length for water depths 40 m and 50 m are set to **3.5D (35 m)** and **4.5D (45.0 m)**, respectively.

It should be noted that selecting a higher tower thickness scale could increase stiffness and could result in a lower embedded length required. In the case of water depth 30 m, for instance, choosing the next higher tower scale of 2.0 still results in 4D embedment length being inadequate. Thus, choosing the least tower thickness scale that gives the target natural frequency is more practical in this case.

In addition, the monopile thickness can also be modified as part of the optimization process. But since changing the thickness also changes the pile deflection behaviour, the nonlinear P-Y curves for soil has to be extracted for every change in the pile thickness.

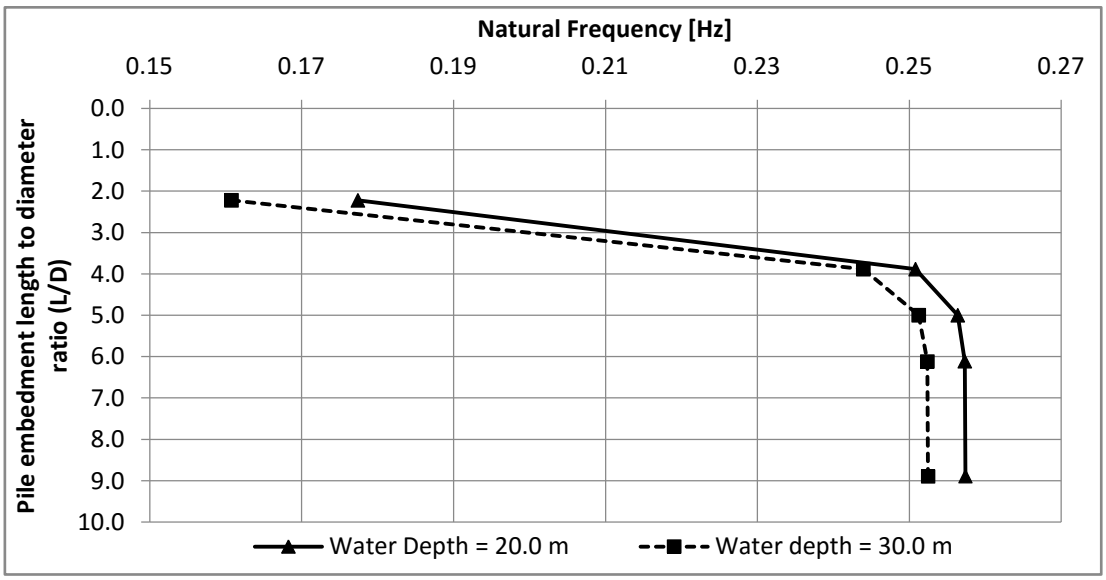

Figure 5.5 Pile embedment length versus natural frequency for the 9.0 m diameter pile

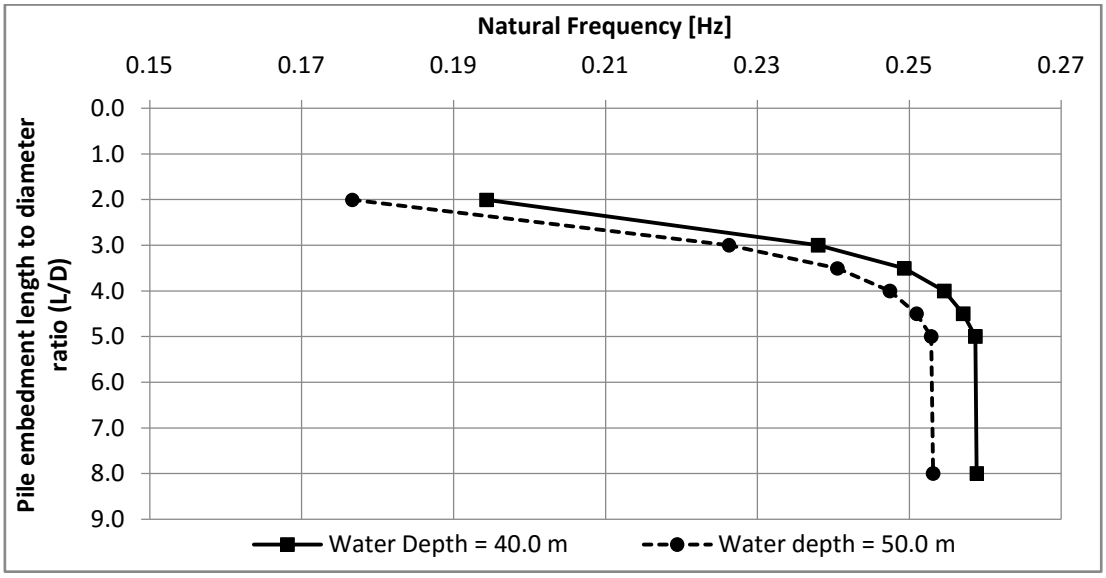

Figure 5.6 Pile embedment length versus natural frequency for the 10.0 m diameter pile

The optimum pile embedment length is the shortest length that satisfies both stability and strength criteria. If lateral stability criteria are not satisfied, the pile length has to be increased. Likewise if the strength criteria are not satisfied, the pile cross sectional dimension has to be increased.

5.4 Foundation Stability Check

After determining the necessary embedment length for each water depth, the preliminary design of the monopile foundation must now be verified if it satisfies stability requirements. These requirements include the rotation at mudline not exceeding **0.50°** and the lateral deflections at mudline and pile toe not exceeding **120 mm** and **20 mm**, respectively.

The calculated extreme loads, which vary per water depth and pile diameter, are applied to each preliminary monopile design. Table 5.8 summarizes the resulting rotation and lateral

deflection at critical points. Comparing the resulting figures to the allowable values, it can be concluded that the preliminary designs pass the three stability check requirements.

Table 5.8 Monopile design stability check for different water depths

Water depth [m]	Pile Diameter [m]	Penetration depth [m]		Design horizontal force [MN]	Design moment [MNm]	Rotation at mudline [deg]	Maximum lateral deflection [mm]		Remark
							Mudline	Pile toe	
20	9	4 D	35	7.44	345.8	0.0020	33.3	-4.9	Pass
30	9	5 D	45	8.24	407.4	0.0020	52.5	-2.7	Pass
40	10	3.5 D	35	10.46	511.5	0.0022	87.2	-6.4	Pass
50	10	4.5 D	45	11.07	598.8	0.0022	101.9	-4.0	Pass

The calculated rotations at the mudline are very low compared to the allowable value of 0.50°. This is because the monopiles are designed to have a large dimension, and therefore high stiffness, in order to achieve the desired natural frequency at the given water depths. The deflection at the mudline, on the other hand, increases with water depth and pile diameter. The increase in water depth and pile diameter increases the hydrodynamic loads to the structure, which causes higher lateral deflection at the mudline. Lastly, the pile toe dimensions tend to be higher for monopiles designed with shorter penetration depth (20 m and 40 m water depth), which entails a more rigid pile behaviour. The negative values are indicate that the deflection at the end of the pile is opposite of the loading direction with respect to the vertical reference axis.

As discussed in the literature review, the vertical tangent criterion or “zero-toe-kick” criterion is disregarded in the design process. To satisfy the vertical tangent criterion, the monopile has to be designed such that it has a flexible behaviour. For large-diameter monopiles to have a flexible behaviour, higher embedment depths would be necessary which are not preferable in economic point of view.

5.5 Yield Check

Following the foundation stability check, the stresses along the pile must be checked against yielding. The stresses, which are also calculated based on the design loads, are illustrated in Figure 5.7 as function of penetration depth. Comparing to the yield strength of 355 MPa (S355 steel), the preliminary designs for the four water depths greatly satisfy the yield check. Similarly, this is due to the large stiffness values of the piles which are chosen to achieve the target natural frequency.

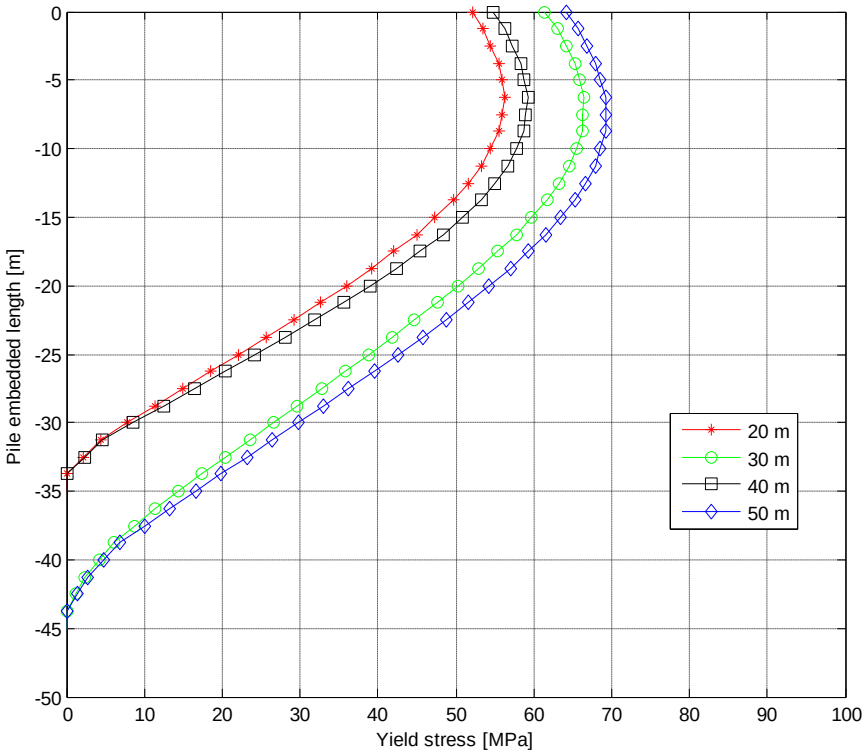

Figure 5.7 Yield stresses from to design loads for different water depths

5.6 Final Preliminary Design

For each water depth, a monopile design is established such that satisfies natural frequency requirements, yield check and foundation stability check. This proves that a monopile design can still satisfy design criteria without implementing the vertical tangent or “zero-toe-kick”

criterion in the determination of pile embedment depth. The final preliminary design is summarized in Table 5.9. Note that each pile diameter corresponds to a tower design, whose details are discussed in the previous section.

Table 5.9 Final preliminary monopile foundation design.

Water depth [m]	Pile Diameter [m]	Pile thickness [mm]	Tower D scale [-]	Tower thickness scale [-]	Penetration depth (m)		Natural period [s]	Natural frequency [Hz]
20	9	110	1.125	1.25	4 D	35	3.987	0.251
30	9	110	1.125	1.75	5 D	45	3.980	0.251
40	10	125	1.25	1	3.5 D	35	4.010	0.249
50	10	125	1.25	1.5	4.5 D	45	3.985	0.251

For the same monopile diameter, it is found that the pile embedment depth highly depends on the water level. For the 20 m and 30 m water depths having pile diameter of 9.0 m, the necessary embedment depths are 35 m and 45 m, respectively. While for the 40 m and 50 m water depths having pile diameter of 10.0 m, the necessary embedment depths are also 35 m and 45 m, respectively.

5.7 Effect of using soil stiffness from API

The preliminary monopile designs were based on soil springs derived from finite element method, particularly with the use of Plaxis 3D. To investigate the difference between the FE method and API method, the static and dynamic properties of the monopile designs are compared by using API-derived soil springs in the established Riflex model. The natural frequency, pile deflections and moment distribution along the pile are compared and analyzed in this section.

5.7.1 Natural Frequency and Foundation Stability

By replacing the soil springs derived from Plaxis 3D with its equivalent in API method, deviation in natural frequency can be examined. Table 5.10 shows that for all water depths, the natural frequency increases by about 0.01 Hz which is equivalent to around 0.15 seconds decrease in the natural period. This implies that the API method predicts higher soil stiffness, although the effect in the natural frequency is not significant.

Table 5.10 Comparison of natural frequency between FE method and API method

Water Depth [m]	Plaxis 3D	API	Deviation [%]
20	0.251	0.262	4.5
30	0.251	0.261	4.1
40	0.249	0.260	4.3
50	0.251	0.261	4.0

The criteria set for foundation stability were also compared for both methods as shown in Table 5.11. In general, API method predicts lower deformations. Considering lateral deflections and rotation at seabed, the average deviations between the calculated values are about 30% and 19%, respectively. For lateral deflection at pile toe, a higher deviation can be observed for monopiles designed for water depths 30 m and 50 m. Note that preliminary monopile designs for water depths 30 m and 50 m have embedment depths of 45 m, which is 10 m higher than that of water depths 20 m and 40 m. This high deviation at higher penetration depth shows that the API overestimates the soil stiffness with depth.

Table 5.11 Comparison of stability check results between FE method and API method

Water Depth [m]	Lateral deflection at seabed [mm]			Lateral deflection at pile toe [mm]			Rotation at seabed [deg]		
	Plaxis 3D	API	Deviation [%]	Plaxis 3D	API	Deviation [%]	Plaxis 3D	API	Deviation [%]
20	33.3	20.7	37.7	-4.9	-4.1	16.9	0.0020	0.0016	20.3
30	52.5	38.3	27.0	-2.7	-1.0	63.3	0.0020	0.0017	16.6
40	87.2	61.5	29.4	-6.4	-6.7	4.5	0.0022	0.0018	21.0
50	101.9	77.5	23.9	-4.0	-2.3	44.1	0.0022	0.0018	17.3

5.7.2 Pile Deflection and Moment Distribution

The calculated pile deflections and moment distribution for each preliminary monopile design are illustrated in Figure 5.8, Figure 5.9, Figure 5.10 and Figure 5.11. Considering lateral deflections, the monopiles modeled with soil springs derived from Plaxis 3D have a relatively rigid behaviour. This is generally associated with higher lateral deflections at both seabed and pile toe, and the occurrence of "toe kick" at the pile end. This implies that the API method, by overestimating soil stiffness, generally underestimates lateral deflection at both seabed and pile toe. A similar study conducted by Lesny and Wiemann [38] also concludes that for large diameter monopiles, the API method overestimates soil stiffness at greater soil depths.

For the bending moment along the monopile, similar behaviors are observed for both methods with a slight deviation in magnitude occurring starting at 15 m depth. The maximum bending moment along the pile is approximately the same for both Plaxis 3D and API method, which is similar to the results obtained by Augustesen, Brødbæk [13] in their study on numerical modeling of large-diameter steel piles at Horns Rev.

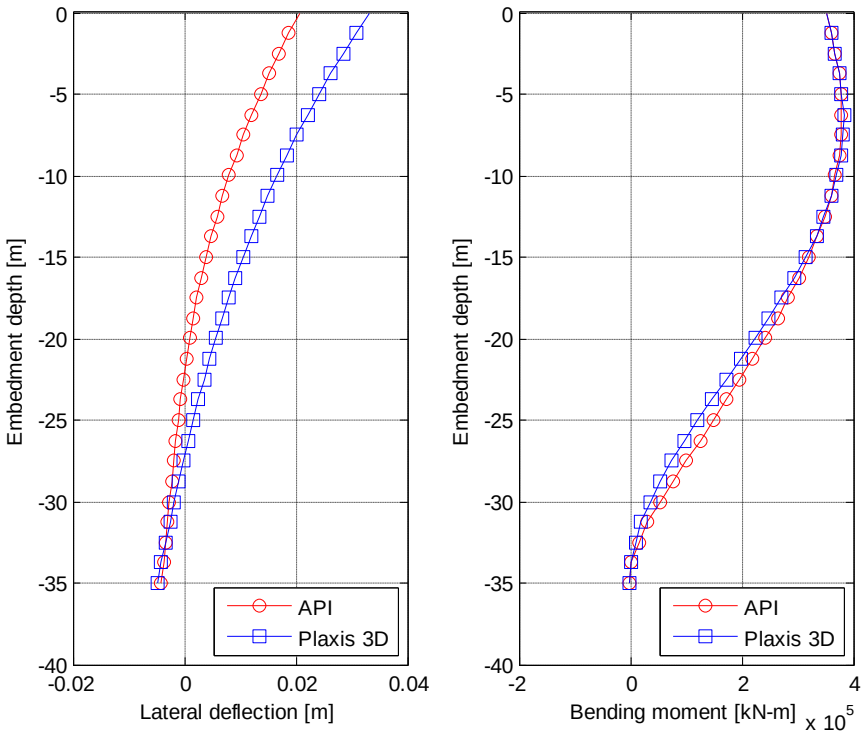

Figure 5.8 Lateral deflections and moment distribution for the 20 m water depth pile

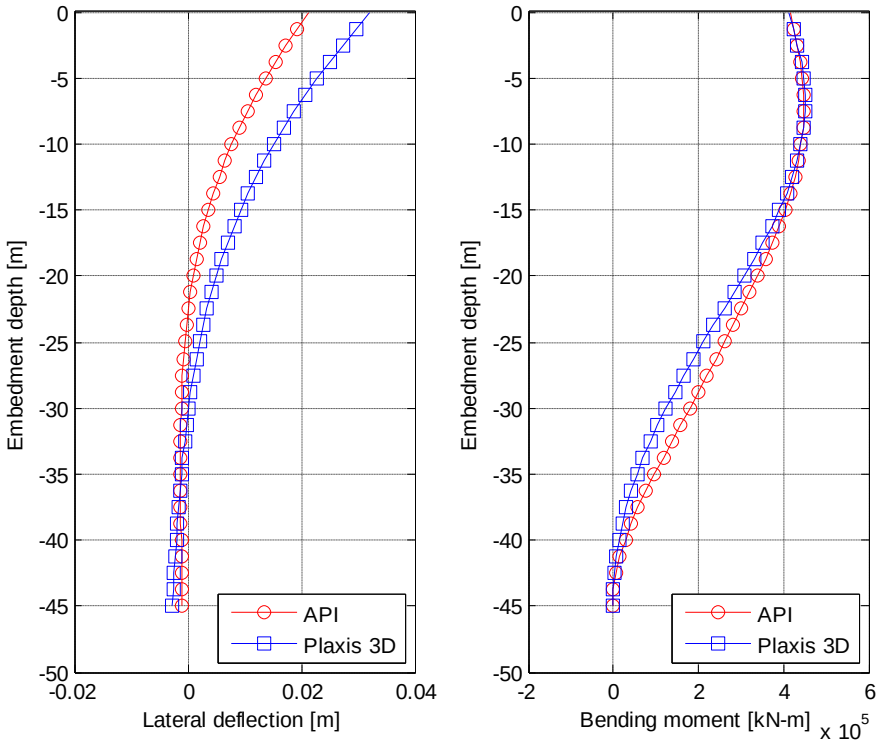

Figure 5.9 Lateral deflections and moment distribution for the 30 m water depth pile

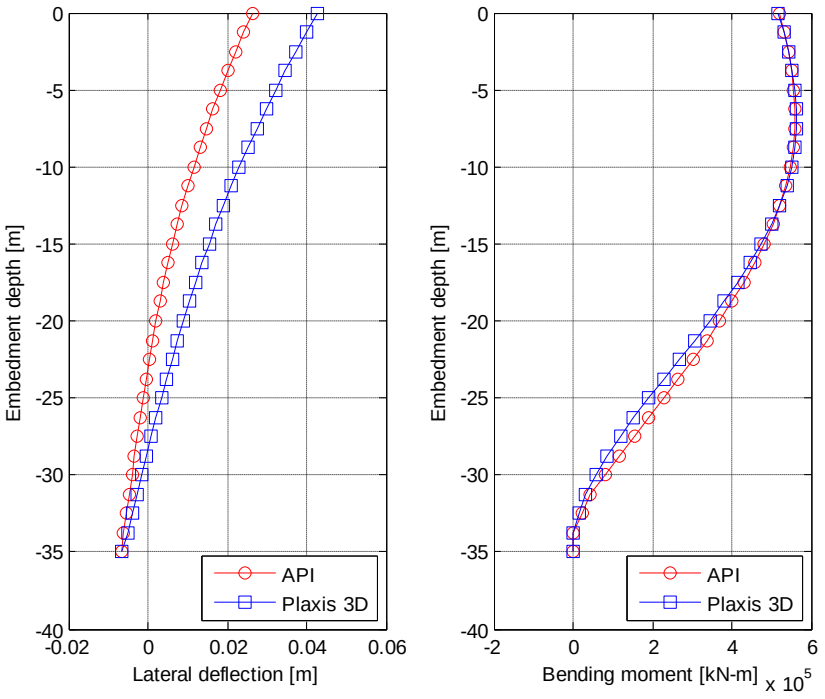

Figure 5.10 Lateral deflections and moment distribution for the 40 m water depth pile

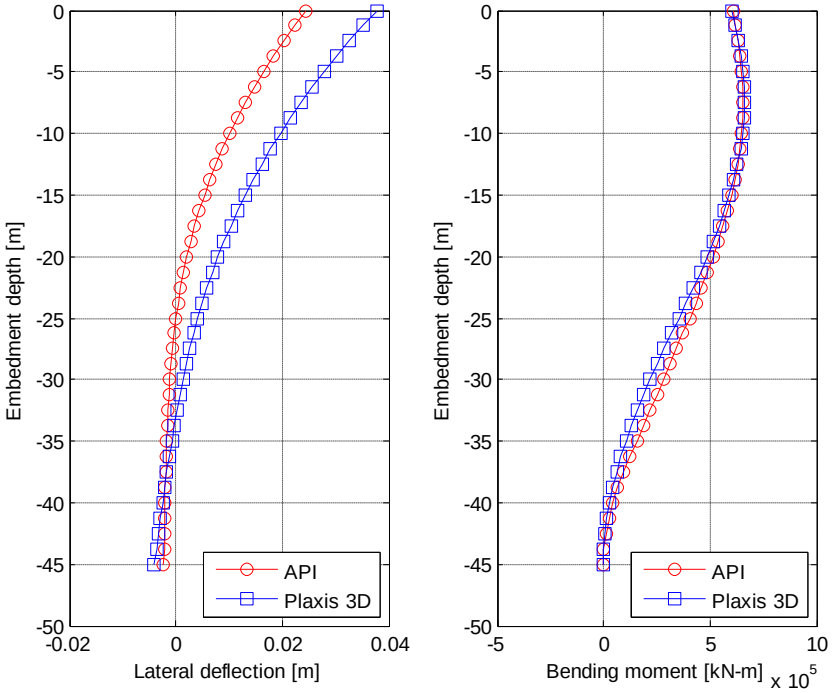

Figure 5.11 Lateral deflections and moment distribution for the 50 m water depth pile

Chapter 6.
Ultimate Limit State Analysis

To investigate the structural integrity of the monopile designs with respect to ultimate limit state, representative design load cases were selected. This chapter presents the selected representative wind and wave conditions, the effect of marine growth on structural response, and the resulting wind turbine response at different water depths. Emphasis is given on how different hydrodynamic models affect ULS analysis.

6.1 Design Load Cases

The IEC [7] defines necessary design load cases (DLC) for different design situations, covering power production, emergency shutdown, parked and fault conditions, up to transport, assembly and maintenance. For this study, the aim is to verify the design's structural responses and load effects during operation at extreme weather conditions. Reasonable load cases are those related to power production, particularly DLC 1.3 and 1.6a. DLC 1.3 couples extreme turbulence with normal sea state, while DLC 1.6a couples normal turbulence with severe sea state. Table 6.1 defines the selected DLCs for ULS analysis.

Table 6.1 Selected design load cases for ULS

DLC	Wind condition	Waves	Wind and wave directionality	Sea currents	Water level	Partial safety factor
1.3	Extreme Turbulence Model (ETM)	Normal Sea State (NSS)	Codirectional, Unidirectional	Normal Current Model (NCM)	MSL	Normal (N)
1.6	Normal Turbulence Model (NTM)	Severe Sea State (SSS)	Codirectional, Unidirectional	Normal Current Model (NCM)	MSL	Normal (N)

6.1.1 Most Probable Wind and Wave Conditions

Before any simulations can be made, the turbulence models and sea states have to be defined in terms of wind speed at hub height (U_{hub}), significant wave height (H_s) and peak spectral period (T_p). For DLC 1.3, two cases are defined by setting U_{hub} to be equal to the rated and cut-out wind speeds which potentially results in more severe aerodynamic loading on the wind turbine. The corresponding sea states (H_s, T_p) are calculated based on the long-term wind and wave distribution discussed in section 3.3.2. Given a wind speed at 10 m above MSL, the most probable values of sea states (Hs, Tp) are found using the joint probability density function (PDF). Figure 6.1 shows PDF of H_s conditional to U_w and PDF of T_p conditional to H_s for both rated and cutout wind speeds. Note that the most probable value corresponds to the peak value of PDF.

For DLC 1.6a, severe sea states are selected based on the 50-year environmental contour surface presented in section 3.3.3. The severe sea states and associated wind speeds are selected based on the maximum H_s and maximum U_w.

In total, there are four DLCs to be considered which comes from two standard DLCs having two sets of representative wind and wave conditions as shown in Table 6.2. A wind speed power profile is assumed in translating wind speeds between hub height and reference height of 10 m above MSL. In addition to wind and wave loading, design current velocity is accounted for ULS simulation. Figure 6.2 illustrates the logarithmic current profile assumed for all design load cases and water depths.

Table 6.2 Representative wind and wave conditions for ULS analysis

ULS	Design Load Case	U_w [m/s]		H_s [m]	T_p [s]
		at 10 m above MSL	at hub height		
1	1.3	8.9	11.4	1.9	6.5
2	1.3	21.2	27.1	6.2	10.3
3	1.6a	27.1	34.7	8.6	12.7
4	1.6a	25.3	32.5	9.9	14

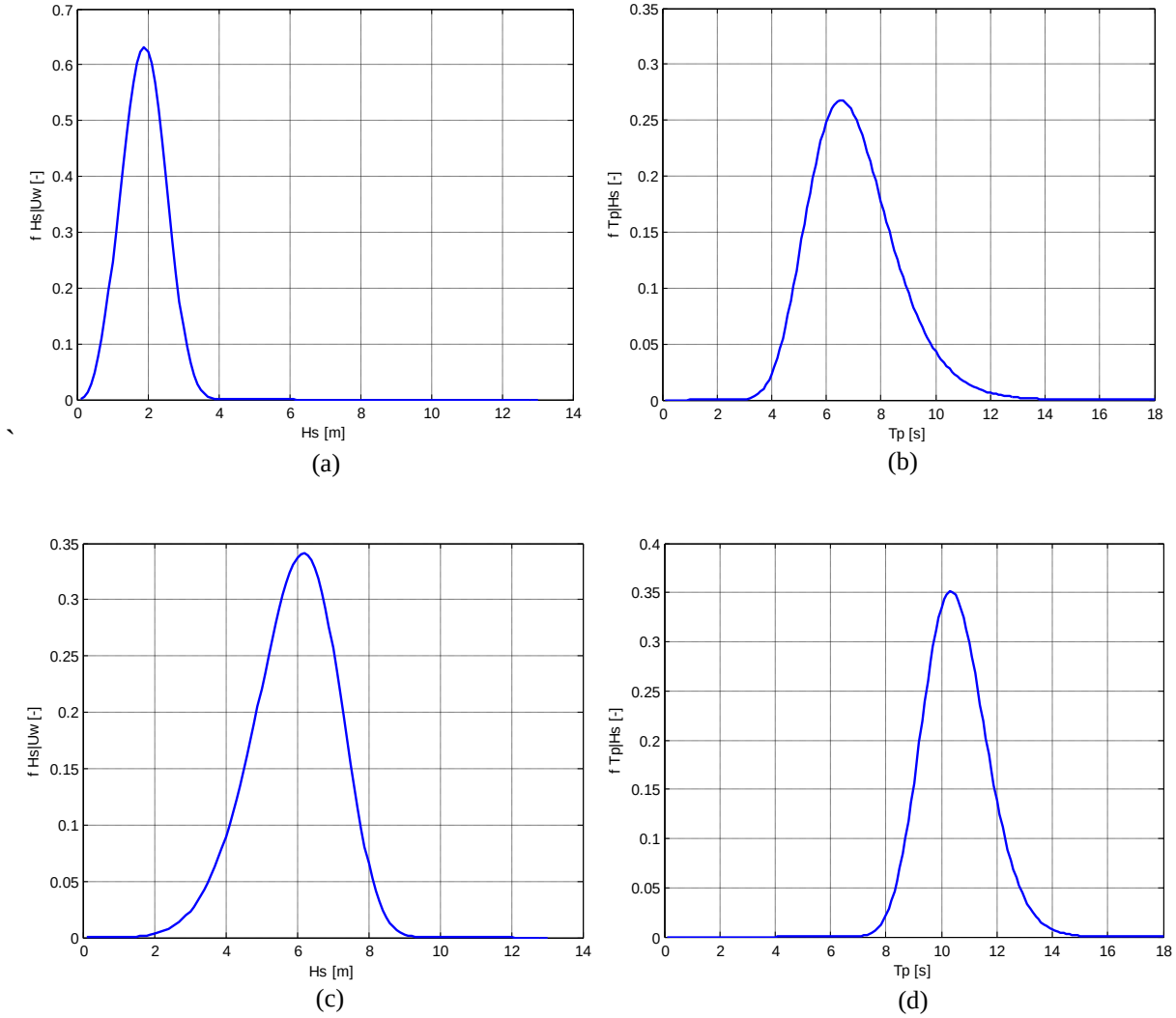

Figure 6.1 Probability density function for H_s and T_p
(a) H_s at rated U_w (b) T_p at rated U_w (c) H_s at cutout U_w (d) Tp at cutout U_w

6.1.2 Wind Field Generation

The wind field is generated using TurbSim with the necessary parameters summarized in Table 6.3. For the 10-minute simulation, a 1000 second analysis time is used to account for wind turbine start-up and transient responses. The extreme turbulence model (ETM) and normal turbulence model (NTM) are both used for DLC 1.3 and 1.6a, respectively. A Kaimal wind spectrum is adapted for ULS analysis.

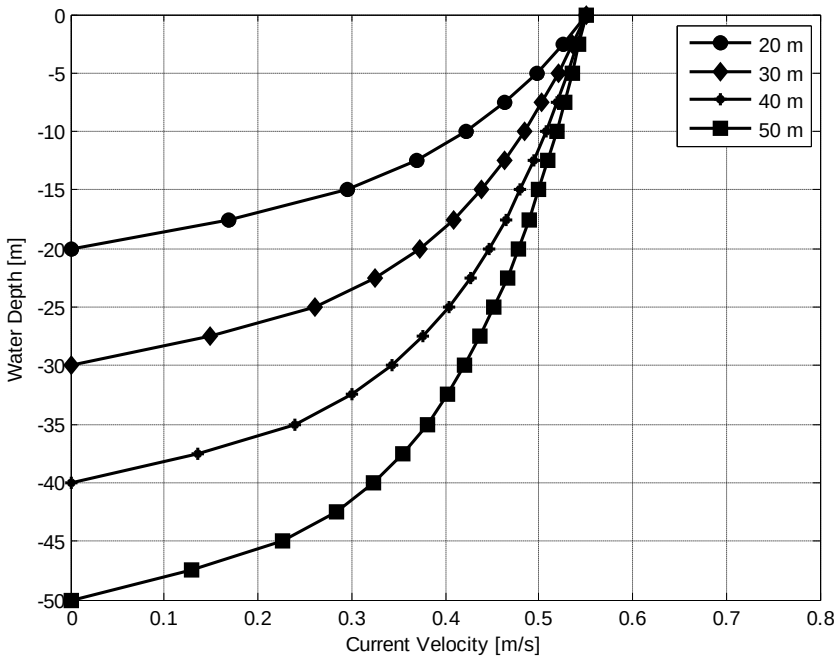

Figure 6.2 Current velocity profiles for different water depths

Table 6.3 TurbSim parameters for wind field generation - ULS

TurbSim Parameter	Value
Analysis Time [s]	1000
Time Step [s]	0.05
Grid Height [m]	180
Grid Width [m]	180
Grid point dimension [-]	32 x 32
Turbulence Model	Kaimal Wind Spectrum
IEC Turbulence Characteristic	A
IEC Turbulence Type	ETM/NTM
Wind Profile	Power Law
Power Law exponent	0.1
Surface Roughness Length [m]	0.03

6.2 Sensitivity to Marine Growth

The sensitivity of the wind turbine load and load effects to the presence of marine growth is investigated for the monopile design at the 20 m water depth. For simplicity, a 130 mm marine growth thickness is assumed from mean sea water level up to seabed. Applying DLC 1.3 (U_w = 11.4 m/s, H_s = 1.9 m, T_p = 6.5 m), the 10-minute monopile axial force and bending moment at seabed are shown in Figure 6.3 and Figure 6.4, respectively. For the results in be more comparable, the same wind field and wave generation seed numbers are used for both models.

The corresponding thrust, whose variation is also reflected by the bending moment time series, is also shown in Figure 6.5. Note that the initial transient responses for these results are not shown and no stretching of wave kinematics is done in the simulation.

Accounting for marine growth generally increases the axial force due to the additional weight on the structure. These results in similar trend in axial force time series, where the model that accounts for marine growth has values shifted higher than the model without marine growth. The bending moment time series, on the other hand, is not significantly affected by including marine growth in the model. This is explained by to the fact that the marine growth thickness is very small relative to the large monopile dimensions, such that the increase in hydrodynamic load and change in dynamic property of the monopile causes a relatively small difference in bending moment. Lastly, the bending moment time series follows the variation the thrust time series, indicating that the thrust force dominates wind turbine response. Such can be explained by the fact that this particular design load case has a wind speed that causes the maximum thrust.

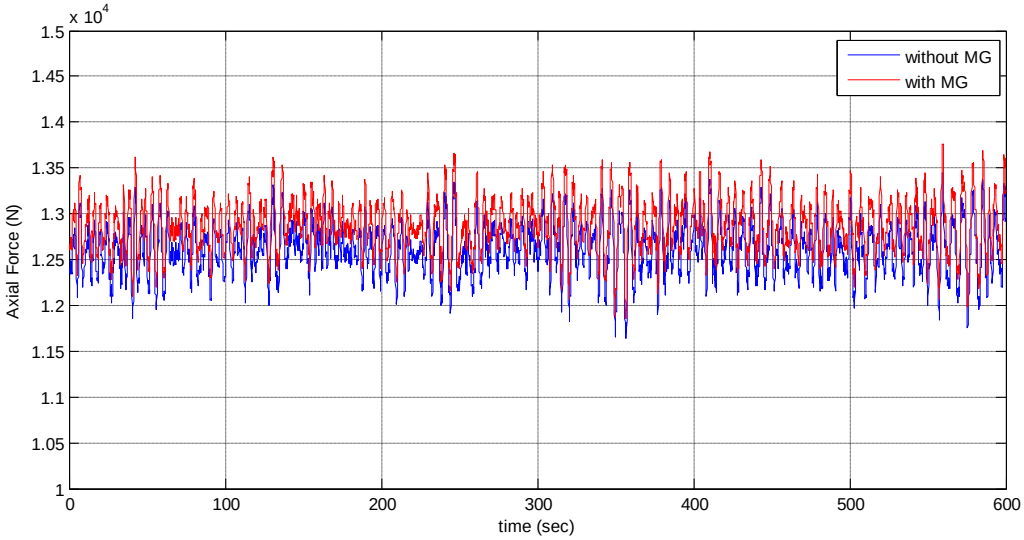

Figure 6.3 Monopile axial force at seabed

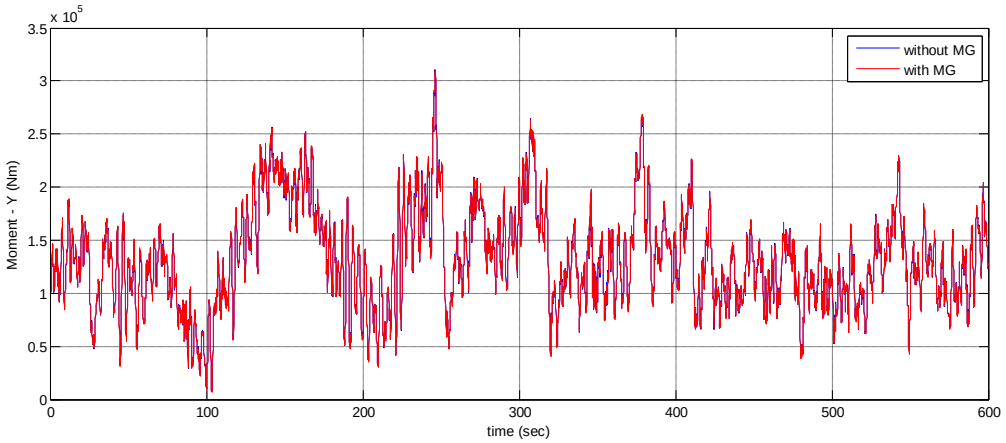

Figure 6.4 Monopile bending moment along load direction at seabed

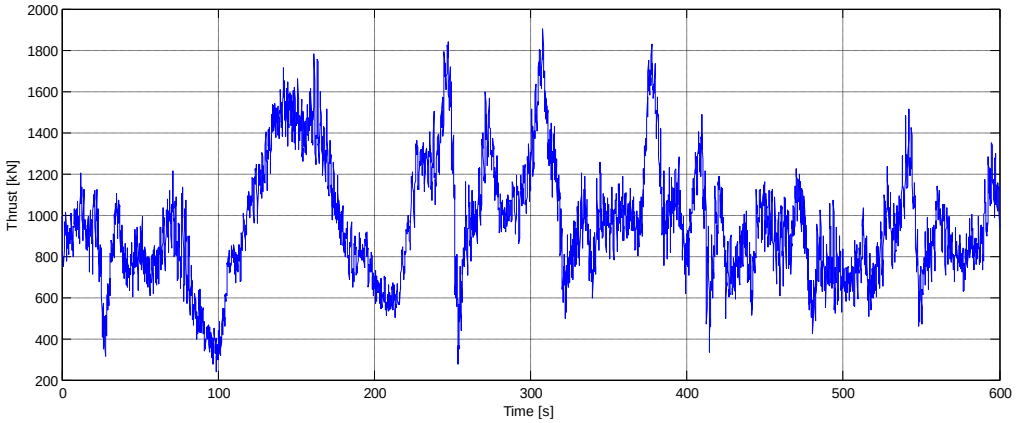

Figure 6.5 Generated thrust for DLC 1.3_11.4m/s

Using the time series of axial force and bending moment about axes parallel and perpendicular to the load direction, the combined axial and bending stresses can be calculated. Four points along the monopile outer diameter are defined for this calculation as illustrated in Figure 6.6. The total stresses at these specified points are calculated for the cross section at mean sea level and at seabed as shown in Figure 6.7 and Figure 6.8, respectively. It is assumed that compressive stress is positive.

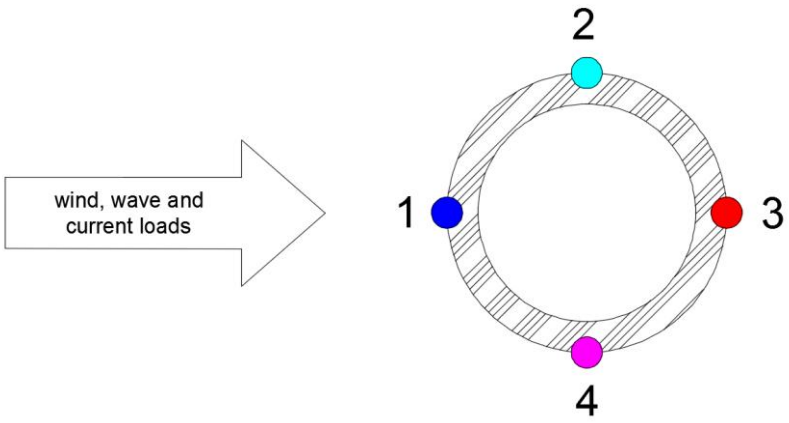

Figure 6.6 Selected points at monopile cross-section for total stress calculation

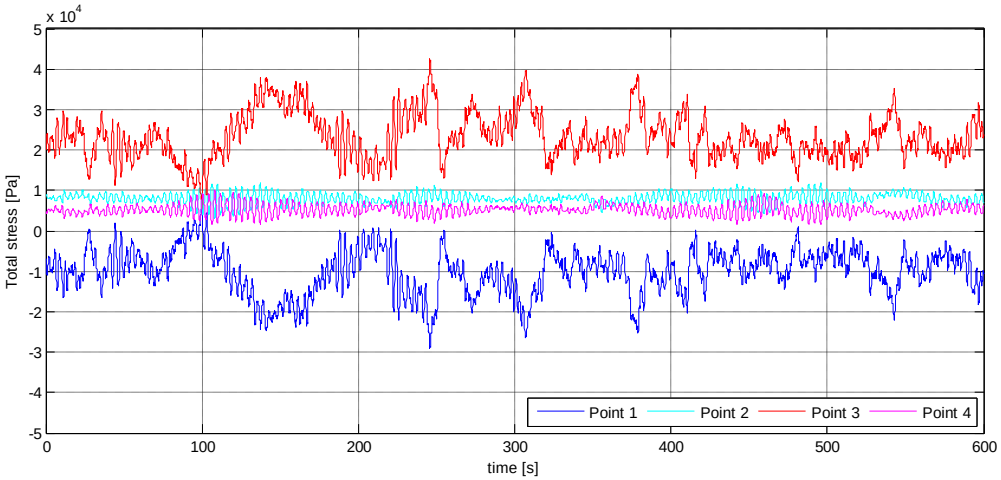

Figure 6.7 Combined axial and bending stresses for four selected points at mean sea level

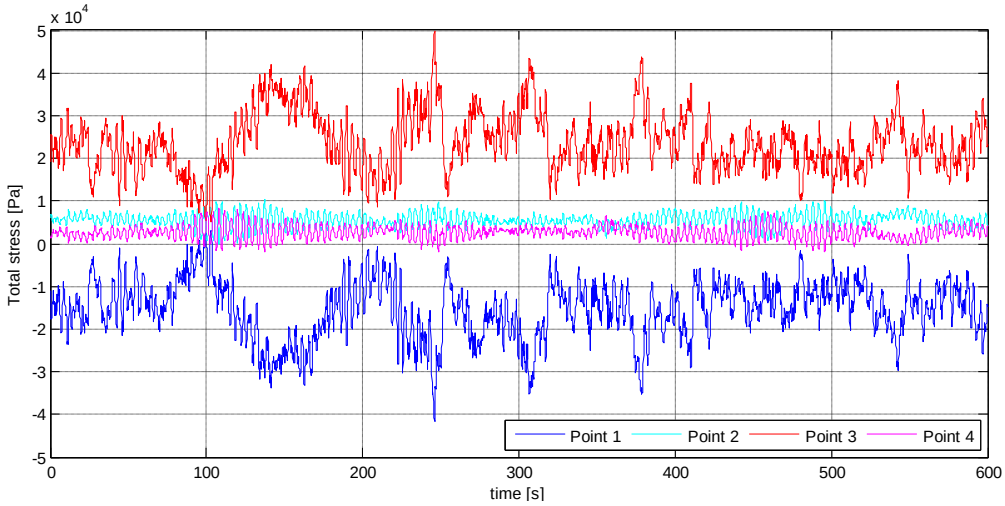

Figure 6.8 Combined axial and bending stresses for four selected points at seabed

For both cross sections and defined load direction, points 1 and 3 give the maximum tensile and compressive stresses, respectively. Points 2 and 4, on the other hand, have smaller magnitudes that oscillate about the mean axial force since the direction of the load is less likely to generate high bending moments at these points. Comparing stresses at two different cross sections, the peak stresses at points 1 and 3 at seabed cross section are higher than that of the mean sea level due to the increasing internal bending moment with depth. Lastly, the absolute maximum combined stress is more likely to be found at point 3 where the bending moment produces a compressive stress with the axial force. For this reason, the combined stresses at point 3 are expected to give the absolute maximum stress in all cross sections of the monopile.

Finally, the maximum stresses along the monopile are calculated using 10-minute simulations for both monopile designs with and without marine growth. The results for four identified points are summarized in Figure 6.9. As implied by the time series of axial force and bending moment presented above, the difference in magnitude when accounting for marine growth is relatively small for large monopile structures. An average difference of 0.6% is calculated for points 1 and 3, while and average difference of 4.0% is found for points 2 and 4 when accounting for marine growth. The lower percentage difference for points 1 and 3 is due to the

insignificant increase in stress due to the mass of marine growth relative to the bending stresses. Nevertheless, the rest of the ULS analysis is done accounting for marine growth.

It should be noted that the presence of marine growth could also change the surface roughness of the structure, which has a direct influence on the drag coefficient used in calculation of hydrodynamic loads. This effect is not considered in this study.

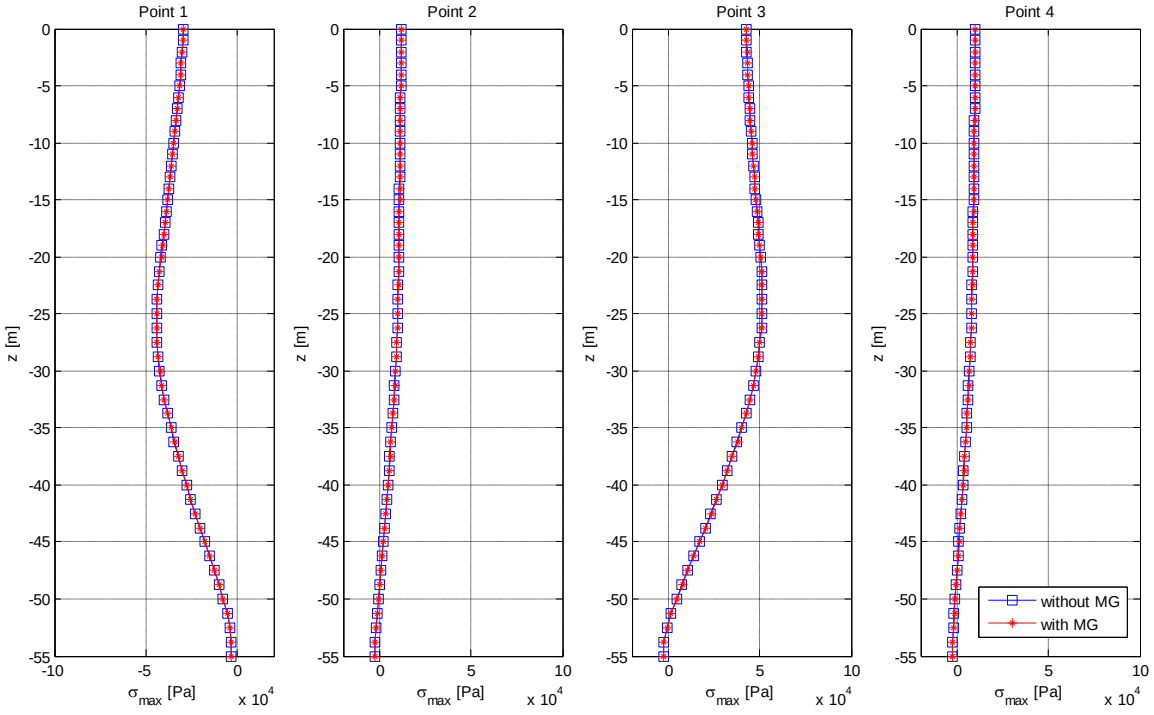

Figure 6.9 Maximum stress along the monopile
Monopile has a 35 m penetration depth at 20 m water depth

6.3 Sensitivity to Hydrodynamic Model

Following the sensitivity analysis of monopile loads to the presence of marine growth, a number of simulations are done in accordance with established design load cases. The variable simulation parameters include the four water depths being investigated, the three hydrodynamic load models being compared and the four selected load cases. Applying six seed numbers for each case results in a total of 288 10-minute simulations. A comparison of wave kinematics for different water depths and hydrodynamic models is first presented, followed by the simulation results presented per water depth.

Two of the three hydrodynamic models are 1st order wave models. One of which has the hydrodynamic force integrated to mean water level (1st order - MWL) and shall be referred to as ”M1” (Model 1). The other has the hydrodynamic force integrated to water surface assuming constant potential (1st order – constant ϕ) and shall be referred to as ”M2”. The third hydrodynamic model is a 2nd order model integrated to instantaneous water level (2nd order – IWL) and shall be referred to as ”M3” throughout the study.

6.3.1 Wave kinematics variation with water depth

The variation of wave kinematics with water depth is investigated by applying ULS 4, which represents the design load case with the 50-year maximum wave height. Using six different seeds, the mean variance of wave particle acceleration is calculated for four water depths as shown in Figure 6.10.

Both M1 and M2 exhibit identical acceleration variance, except that M1 is only integrated to mean water level. M3 shows a relatively higher acceleration variance at shallow water depth. Results show that as the water depth increases, acceleration variance of 1st order wave models approaches that of the 2nd order wave model such that the values are almost identical at 50 m water depth. This is observed for both shallow and deep water with the same H_s. This implies that 2nd order wave loads can have a more significant effect for shallow water depths as compared to deeper water.

The mean maximum wave particle acceleration is also calculated as shown in Figure 6.11. The variation of the mean maximum acceleration with both water depth and hydrodynamic model shows agreement with the calculated mean variance of acceleration. For the given sea state and for a shallow water depth of 20 m, the predicted mean maximum acceleration by the 2nd order wave model (7 m/s^2) is about 75% higher than the 1st order wave model (4 m/s^2) prediction.

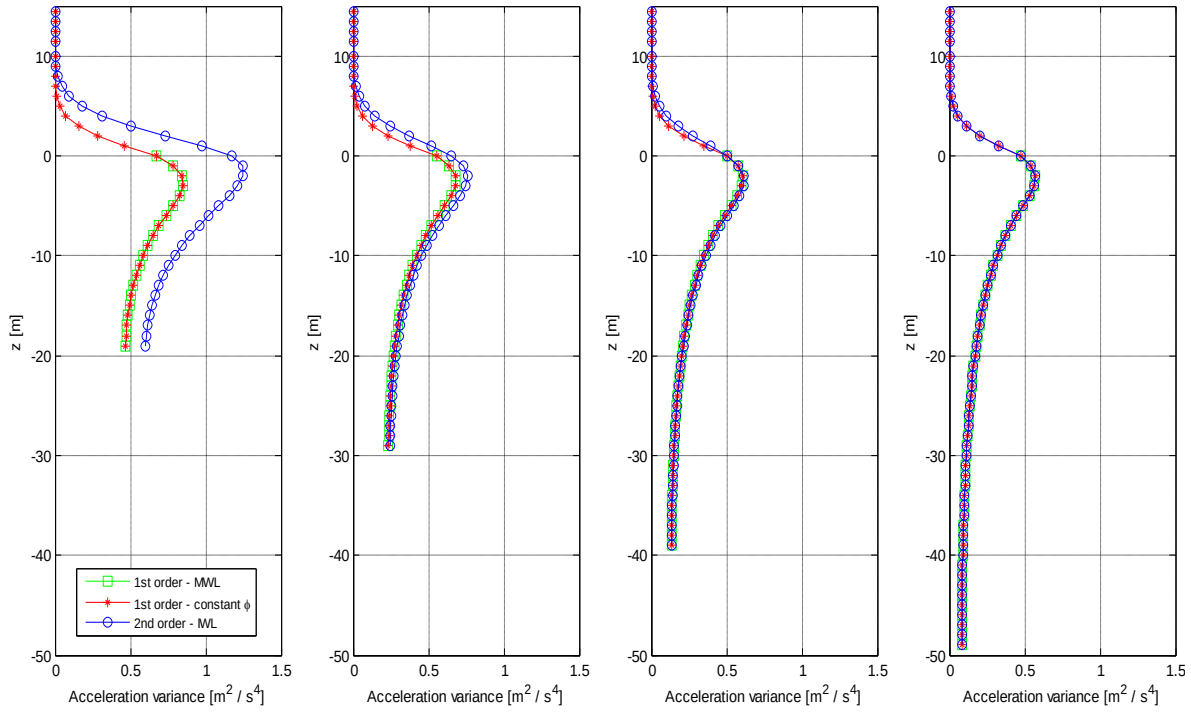

Figure 6.10 Mean variance of acceleration at different water depths

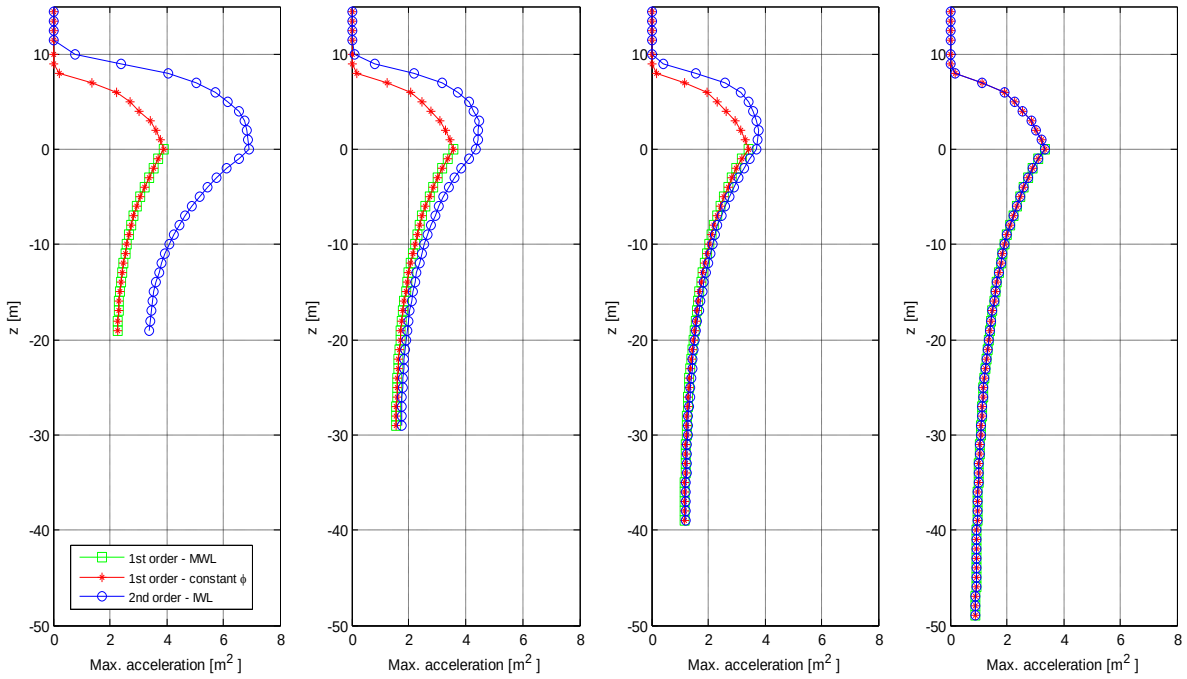

Figure 6.11 Mean maximum acceleration at different water depths

6.3.2 Governing hydrodynamic model

For each design load case and hydrodynamic model, the mean maximum bending moment about the global y-axis is calculated from simulations using six random seed numbers. The results are plotted against the monopile length for water depths 20 m, 30 m 40 m and 50 m as shown in Figure 6.12, Figure 6.13, Figure 6.14 and Figure 6.15, respectively.

For all water depths and design load cases, the maximum bending moment in the pile generally occurs between 5 to 10 meters below the seabed surface. This generally determines the critical section not only for ultimate limit state analysis, but also for fatigue limit state analysis. Such result is logically sound, since the monopile only starts to have lateral support at the seabed surface.

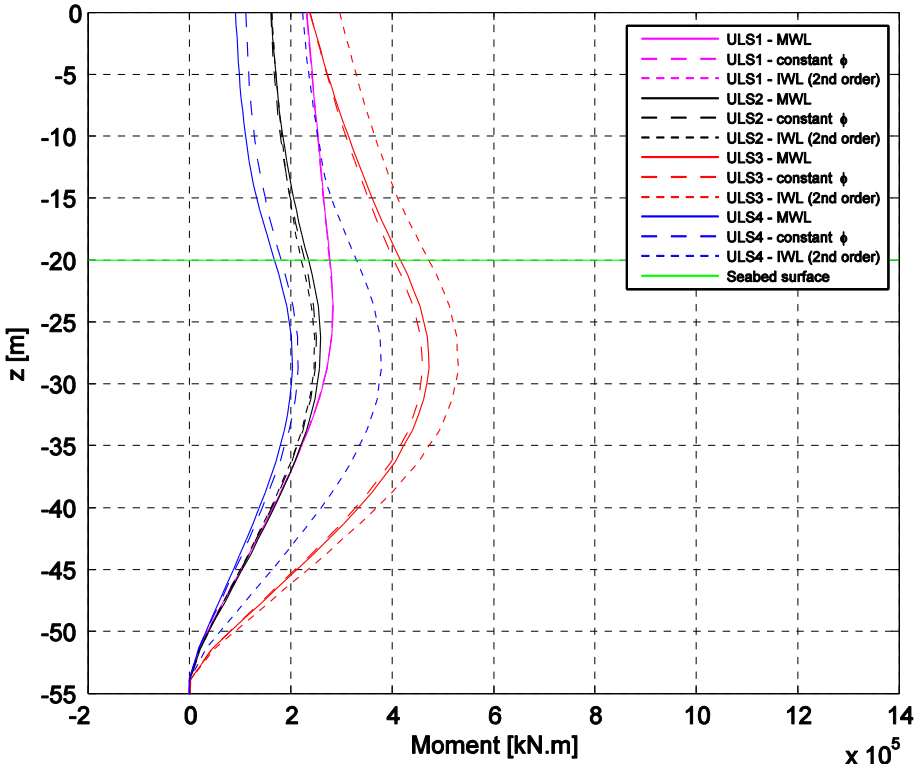

Figure 6.12 Mean maximum moment about y-axis – 20m water depth pile design

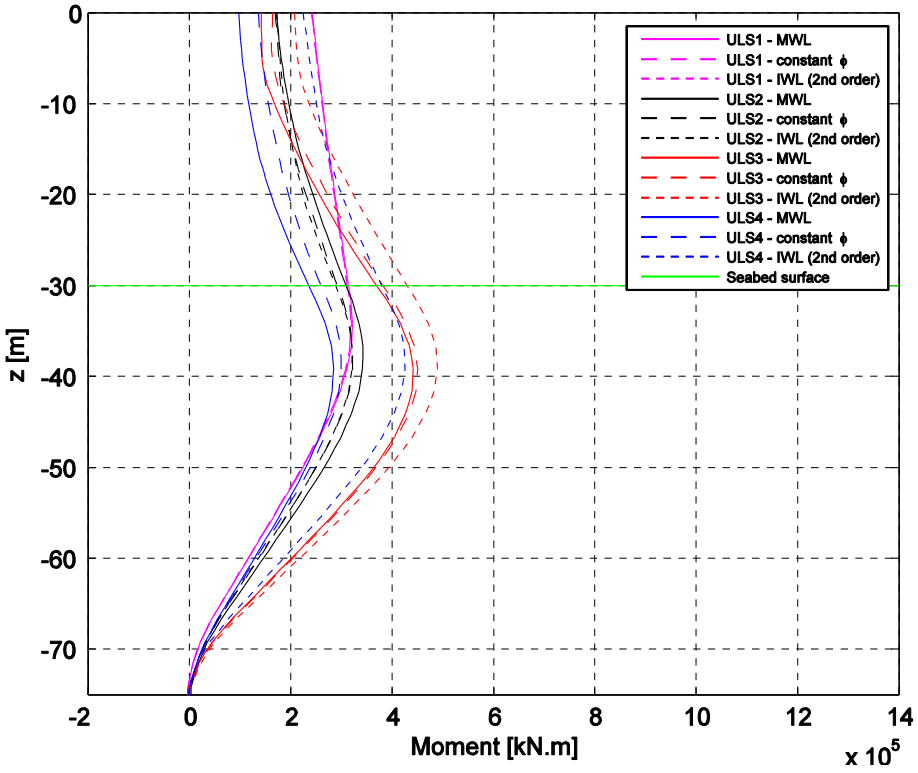

Figure 6.13 Mean maximum moment about y-axis – 30m water depth pile design

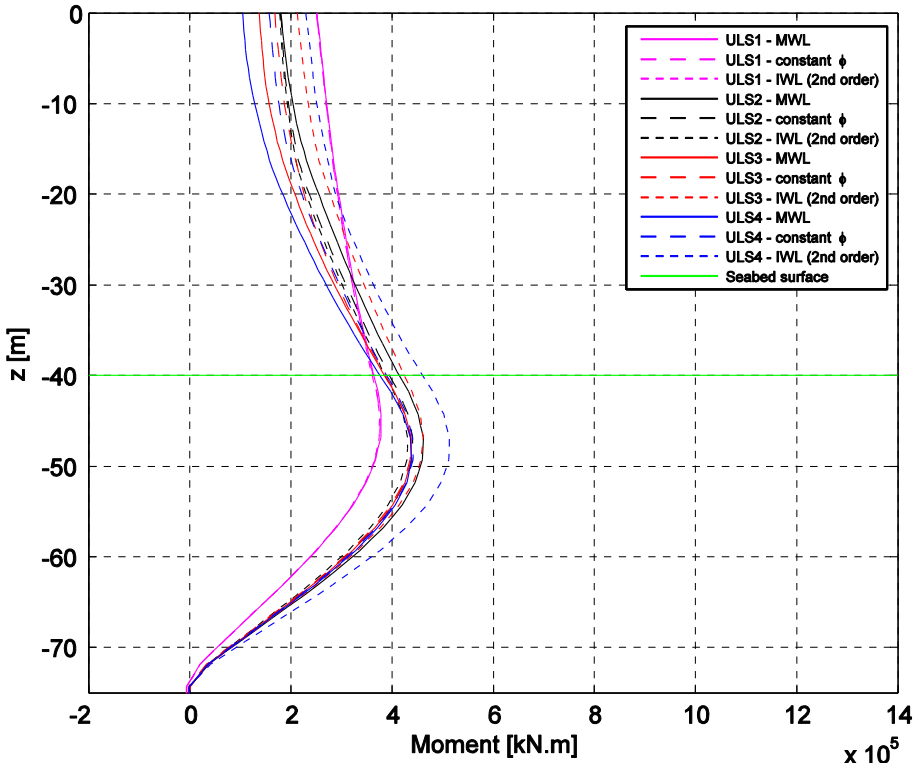

Figure 6.14 Mean maximum moment about y-axis – 40m water depth pile design

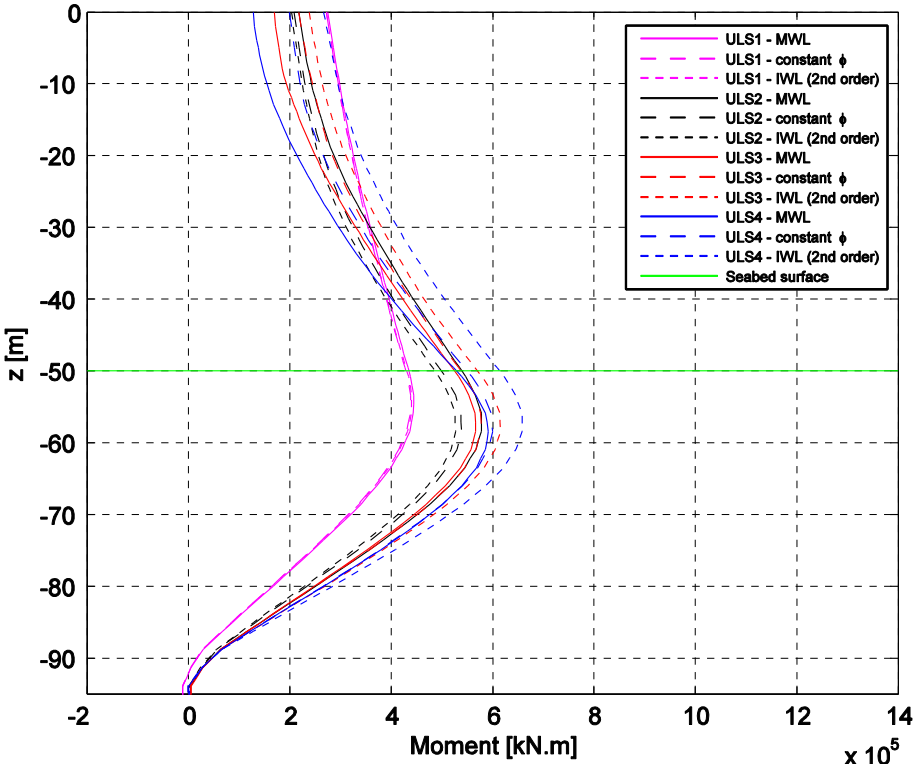

Figure 6.15 Mean maximum moment about y-axis – 50m water depth pile design

Governing design load case and hydrodynamic model

For water depths 20 m and 30 m, the governing design load case is ULS 3 which corresponds to the sea state with maximum wind speed at hub height. But for higher water depths 40 m and 50 m, the governing design load case is ULS 4, which corresponds to the sea state with maximum significant wave height. Such shift in governing design load case with increasing water depth is reasonable, considering that ULS 4 tends to generate relatively higher loads with higher water depth.

For all water depths, the 2nd order wave model generally gives higher loads compared to 1st order models. This is highly influenced by the design load case, in particular whether aerodynamic or hydrodynamic loads dominate loading conditions. For ULS 1 and 2, the extreme turbulence model is adapted and the wind turbine is not parked. It is then expected that aerodynamic loads dominate overall structural response, which also means that differences between hydrodynamic models are less pronounced as illustrated by ULS 1 results for all water depths. Although the wind turbine is not parked for ULS 2, the variation of mean maximum moment between hydrodynamic models becomes more pronounced relative to ULS1 due to the cutout wind speed adapted for this case. The generated stochastic wind field oscillates around cutout wind speed and periodically exceeds it, resulting to a lower thrust and a higher hydrodynamic load contribution. Since the governing hydrodynamic model for ULS 2 changes for each water depth, there is no conclusion that can be made on which hydrodynamic model is governing.

For ULS 3 and 4, severe wind and wave conditions are adapted for the parked wind turbine. Since the thrust is relatively low for parked wind turbines, hydrodynamic loads have relatively high contributions. Results show that the sensitivity of mean maximum moment with hydrodynamic model is more pronounced for both ULS 3 and 4 for all water depths. For these conditions, it can be concluded that M3 gives the highest response, followed by the M2 and M1, respectively. M3 as a governing model can be explained by the sum frequency effect associated with 2^{nd} order waves, which generates excitation frequencies close to the natural frequency of the structure for high sea states. Another reason is the wave kinematics investigated in the previous section, particularly by the wave particle acceleration where the

calculated mean variance and mean maximum value is highest for the second order wave model.

In addition, the variation of wave particle acceleration with water depth is also reflected by the results. Since both 1st order and 2nd order wave models predict more comparable wave particle acceleration with increasing water depth, the difference between calculated maximum bending moments also decreases with increasing water depth. Results show that load predictions are closer at higher water depths 40 m and 50 m, as compared to water depths 20 m and 30 m. Considering ULS 4, the ratio of predicted ultimate load using a 2nd order wave model to that of the 1st order model for water depths 20 m, 30 m, 40 m and 50 m are 1.9, 1.5, 1.2 and 1.1, respectively.

Monopile combined stresses

The resulting maximum combined axial and bending moment stresses along the monopiles are shown in Figure 6.16. The load distribution generally follows the bending moment distribution since the axial load due to the weight of the wind turbine and tower are relatively smaller compared to wind and wave-induced loads.

The calculated maximum stresses with no safety factor applied for water depths 20 m, 30 m, 40 m and 50 m are 82 Mpa, 75 Mpa, 55 Mpa and 70 Mpa, respectively. Note that monopile designs (diameter, thickness and penetration depth) also vary with water depth, which makes load comparison with respect to water depth variation more complex. Nonetheless, large diameter monopiles with relatively higher structural section modulus are less likely to fail for ULS.

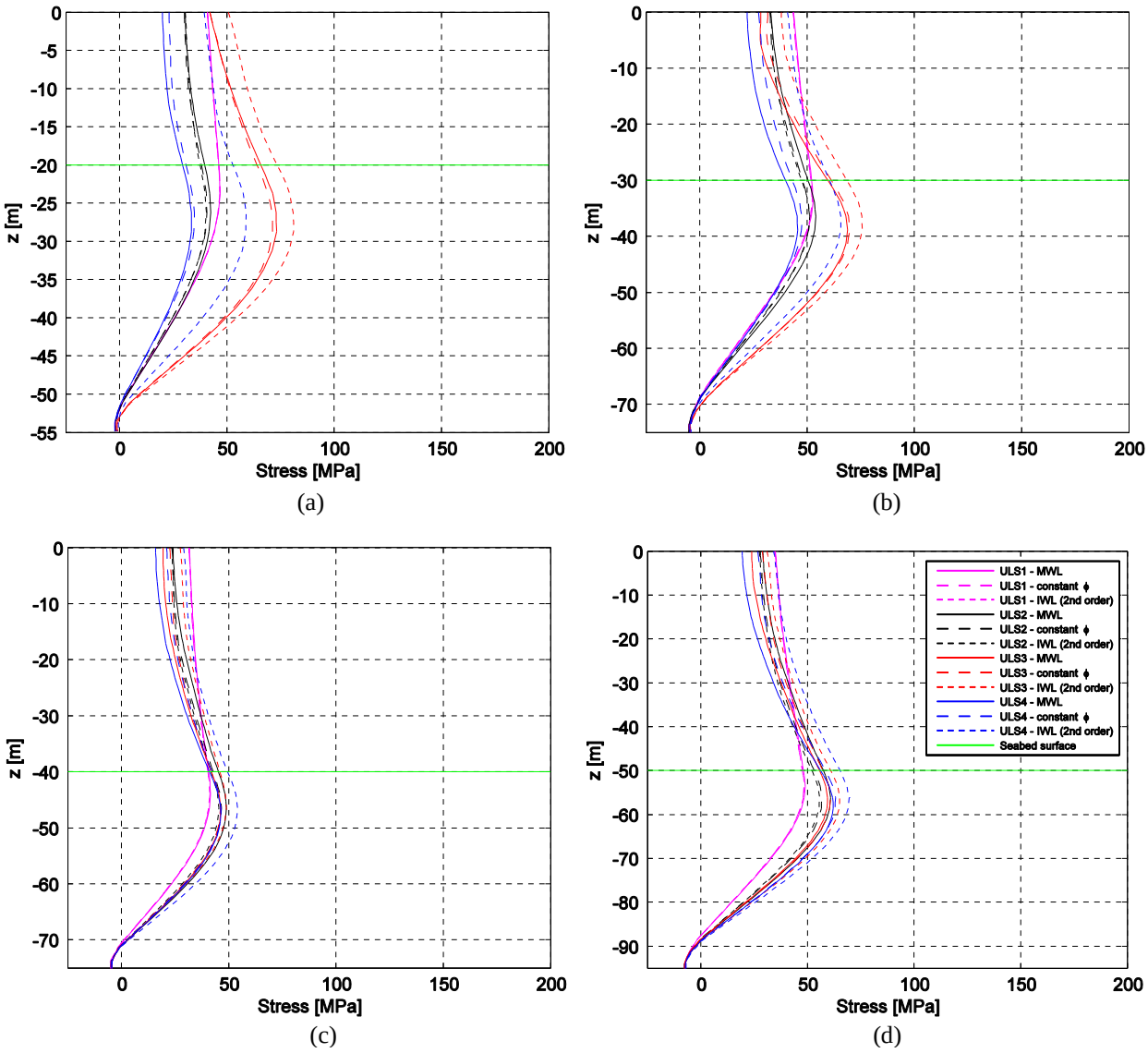

Figure 6.16 Mean maximum stresses for all water depths
(a) h = 20 m (b) h = 30 m (c) h = 40 m and (d) h = 50m

Chapter 7.
Fatigue Limit State Analysis

This chapter mainly investigates the fatigue life of the established preliminary design and the sensitivity of fatigue damage calculation with different hydrodynamic models. For this purpose, a design load case specific to normal power production is chosen.

A detailed description of the derivation of representative environmental conditions is first presented. Since both drag and inertia coefficients varies with Reynolds number, Keulegan-Carpenter number and relative roughness, the validity and uncertainties of assumed hydrodynamic coefficients is discussed. The total fatigue damage and relative contribution of each environmental condition to fatigue damage is then investigated, followed by a simple frequency-domain fatigue damage estimate to verify the time-domain results. Lastly, an investigation of how MacCamy-Fuchs theory modifies the hydrodynamic loads is presented.

7.1 Design Load Case and S-N Curve

In the design of offshore wind turbines, fatigue damage assessment is normally done by running several design load cases. In this study, fatigue damage is calculated only during operational conditions to underline the differences in damage prediction of different hydrodynamic models. Table 7.1 shows the modified DLC 1.2, where wind and waves are assumed to be unidirectional and fatigue contributions from wind speeds below cut-in are accounted for.

A representative S-N curve applicable for structures in seawater with cathodic protection is selected from DNV [29]. S-N curves calculated for tubular sections having 110 mm and 125 mm are shown in Figure 7.1. For simplicity, a stress concentration factor of 1.0 is used in fatigue damage calculation.

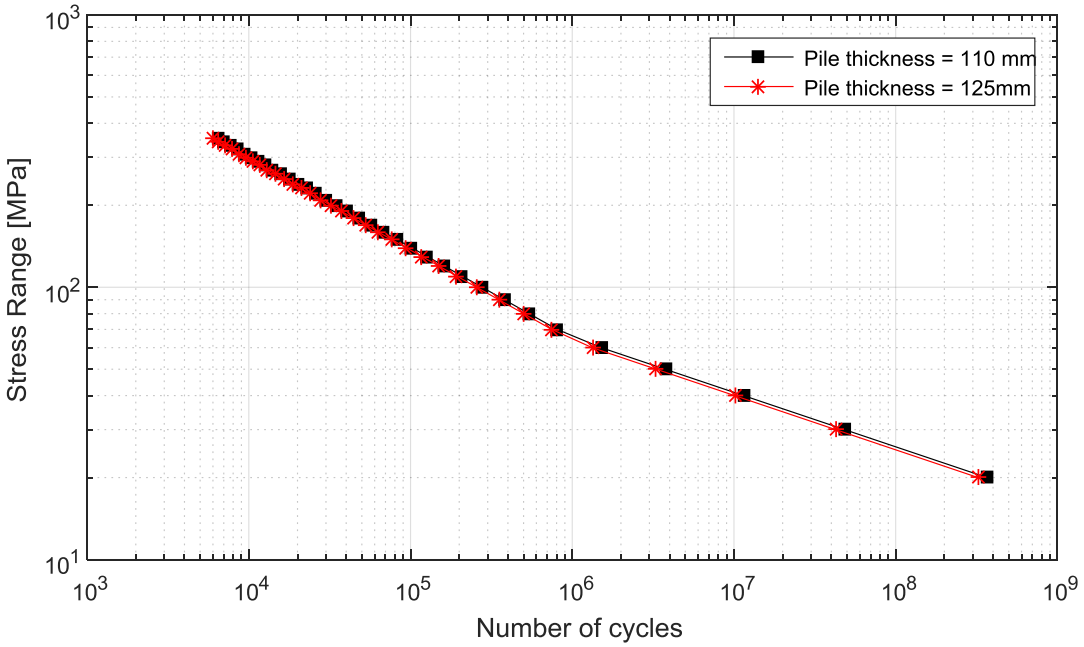

Figure 7.1 S-N curves in seawater with cathodic protection

Table 7.1 Selected design load case for FLS analysis

DLC	Wind condition	Waves	Wind and wave directionality	Sea currents	Water level
1.2	Normal Turbulence Model (NTM) [$0 < V_{hub} < V_{out}$]	Normal Sea State (NSS)	Codirectional, Unidirectional	No currents	MSL

7.2 Representative Sea States

For fatigue damage calculation, a number of representative sea states based on long term distributions shall be selected. Similar to the approach done in ULS analysis, the sea state (H_s, T_p) corresponding to a given wind speed is calculated based on the long-term wind and wave distribution discussed in section 3.3.2. The derived scatter diagram and representative sea states are presented in this section, followed by the analysis of hydrodynamic force coefficients applicable for each environmental condition.

7.2.1 Scatter diagram

The number of environmental conditions in a scatter diagram depends on the selected bin sizes. According to Tempel [6], typical bin size for H_s and T_p are 0.50 m and 2.0s, respectively. To avoid losing information on the long-term distribution, a smaller bin size is adapted for both H_s and T_p. The derived significant wave height (H_s), peak period (T_p) and probability of occurrence specific to the given location are summarized in Table 7.2, Table 7.3 and Table 7.4, respectively.

Table 7.2 Derived H_s as a function of windspeed

	U_w [m/s]	1	2	3	4	5	6	7	8	9	10	11	12
		H_s [m]											
1	**2.2**	0.49	1.15	2.08	3.05	4.04	5.03	6.03	7.02	8.02	9.02	10.02	11.01
2	**5.0**	0.64	1.26	2.12	3.07	4.05	5.03	6.03	7.02	8.02	9.01	10.01	11.01
3	**8.0**	0.73	1.43	2.22	3.11	4.07	5.04	6.03	7.02	8.02	9.01	10.01	11.01
4	**11.1**	0.77	1.56	2.37	3.21	4.11	5.07	6.05	7.03	8.02	9.02	10.01	11.01
5	**14.3**	0.80	1.63	2.51	3.35	4.21	5.12	6.07	7.05	8.03	9.02	10.02	11.01
6	**17.4**	0.81	1.66	2.58	3.48	4.35	5.22	6.13	7.08	8.05	9.04	10.03	11.02
7	**20.5**	0.83	1.69	2.61	3.55	4.47	5.36	6.23	7.14	8.09	9.06	10.04	11.03
8	**23.6**	0.84	1.71	2.63	3.59	4.54	5.47	6.37	7.25	8.16	9.10	10.06	11.04
9	**26.8**	0.85	1.72	2.65	3.61	4.57	5.53	6.47	7.38	8.27	9.18	10.11	11.07
10	**29.9**	0.86	1.74	2.66	3.62	4.59	5.56	6.53	7.48	8.40	9.30	10.20	11.13

Table 7.3 Derived T_p as a function of windspeed

	U_w [m/s]	1	2	3	4	5	6	7	8	9	10	11	12
		T_p [m]											
1	**2.2**	5.93	6.47	7.18	7.93	8.71	9.53	10.37	11.25	12.17	13.12	14.11	15.14
2	**5.0**	6.06	6.55	7.20	7.94	8.71	9.53	10.37	11.25	12.16	13.11	14.10	15.13
3	**8.0**	6.13	6.68	7.28	7.97	8.73	9.54	10.38	11.25	12.17	13.12	14.10	15.13
4	**11.1**	6.17	6.78	7.40	8.05	8.77	9.56	10.39	11.26	12.17	13.12	14.11	15.13
5	**14.3**	6.19	6.83	7.50	8.16	8.85	9.60	10.41	11.27	12.18	13.12	14.11	15.14
6	**17.4**	6.20	6.86	7.56	8.26	8.96	9.68	10.46	11.30	12.20	13.14	14.12	15.14
7	**20.5**	6.22	6.88	7.58	8.32	9.06	9.80	10.55	11.36	12.23	13.16	14.13	15.15
8	**23.6**	6.23	6.89	7.60	8.35	9.11	9.89	10.67	11.46	12.29	13.20	14.16	15.17
9	**26.8**	6.24	6.90	7.61	8.36	9.14	9.95	10.76	11.58	12.41	13.27	14.21	15.20
10	**29.9**	6.24	6.92	7.62	8.37	9.16	9.97	10.81	11.66	12.52	13.39	14.30	15.26

Table 7.4 Derived sea state probability as a function of windspeed

	U_w [m/s]	1	2	3	4	5	6	7	8	9	10	11	12
		Probability [-]											
1	**2.2**	0.048	0.003	0.000	0.000	0.000	0.000	0.000	0.000	0.000	0.000	0.000	0.000
2	**5.0**	0.123	0.055	0.000	0.000	0.000	0.000	0.000	0.000	0.000	0.000	0.000	0.000
3	**8.0**	0.075	0.163	0.018	0.000	0.000	0.000	0.000	0.000	0.000	0.000	0.000	0.000
4	**11.1**	0.020	0.124	0.089	0.006	0.000	0.000	0.000	0.000	0.000	0.000	0.000	0.000
5	**14.3**	0.003	0.037	0.080	0.037	0.002	0.000	0.000	0.000	0.000	0.000	0.000	0.000
6	**17.4**	0.000	0.006	0.024	0.033	0.013	0.001	0.000	0.000	0.000	0.000	0.000	0.000
7	**20.5**	0.000	0.001	0.003	0.009	0.010	0.004	0.000	0.000	0.000	0.000	0.000	0.000
8	**23.6**	0.000	0.000	0.000	0.001	0.002	0.002	0.000	0.000	0.000	0.000	0.000	0.000
9	**26.8**	0.000	0.000	0.000	0.000	0.000	0.000	0.000	0.000	0.000	0.000	0.000	0.000
10	**29.9**	0.000	0.000	0.000	0.000	0.000	0.000	0.000	0.000	0.000	0.000	0.000	0.000

Table 7.4 shows 120 environmental conditions, from which a number of conditions have a very low probability of occurrences. Conditions having probabilities less than 0.001 are assumed to have insignificant contribution to fatigue damage. This leads to a reduced number of 29 representative conditions. The numbering of representative conditions according to increasing H_s is shown in Table 7.5, while the list of representative conditions together with their probabilities is summarized in Table 7.6. Reducing the number of sea states to 29 gives a total probability of 99.4%, which can be assumed accurate representation of all conditions.

Table 7.5 Numbering of representative sea states

	Uw [m/s]	1	2	3	4	5	6
		Sea state					
1	**2.2**	1	6				
2	**5.0**	2	7				
3	**8.0**	3	8	13			
4	**11.1**	4	9	14	18		
5	**14.3**	5	10	15	19	23	
6	**17.4**		11	16	20	24	27
7	**20.5**		12	17	21	25	28
8	**23.6**				22	26	29

Waves are generated based on JONSWAP spectrum with default peak enhancement factor (γ) of 3.3 and time step (Δt) of 0.10 seconds. To make fatigue damage prediction comparable for different models and to avoid unphysical high frequency components, a cut-off frequency $\left(\omega = \sqrt{2g/H_s}\right)$ is applied to the 1st order wave spectrum [27].

The wind field is generated using TurbSim with the necessary parameters summarized in Table 7.7. A Kaimal wind spectrum is used with a time step (Δt) of 0.05 seconds. For the 10-minute simulation, a 1000 second analysis time is used to account for wind turbine start-up and transient responses.

Table 7.6 Summary of representative sea states from scatter diagram

Sea state	Uw [m/s]	Hs [m]	Tp [s]	Probability [%]	Occ./year [hrs]
1	2.2	0.49	5.93	4.8	424.7
2	5.0	0.64	6.06	12.3	1081.4
3	8.0	0.73	6.13	7.5	658.2
4	11.1	0.77	6.17	2.0	175.9
5	14.3	0.80	6.19	0.3	27.5
6	2.2	1.15	6.47	0.3	26.6
7	5.0	1.26	6.55	5.5	483.2
8	8.0	1.43	6.68	16.3	1427.8
9	11.1	1.56	6.78	12.4	1088.0
10	14.3	1.63	6.83	3.7	324.8
11	17.4	1.66	6.86	0.6	52.0
12	20.5	1.69	6.88	0.1	5.2
13	8.0	2.22	7.28	1.8	161.2
14	11.1	2.37	7.40	8.9	777.8
15	14.3	2.51	7.50	8.0	696.9
16	17.4	2.58	7.56	2.4	208.0
17	20.5	2.61	7.58	0.3	30.4
18	11.1	3.21	8.05	0.6	53.5
19	14.3	3.35	8.16	3.7	322.2
20	17.4	3.48	8.26	3.3	291.4
21	20.5	3.55	8.32	0.9	78.6
22	23.6	3.59	8.35	0.1	9.7
23	14.3	4.21	8.85	0.2	19.2
24	17.4	4.35	8.96	1.3	113.1
25	20.5	4.47	9.06	1.0	89.9
26	23.6	4.54	9.11	0.2	20.1
27	17.4	5.22	9.68	0.1	7.1
28	20.5	5.36	9.80	0.4	33.7
29	23.6	5.47	9.89	0.2	21.1
				99.4	**8709.1**

Table 7.7 TurbSim parameters for wind field generation - FLS

TurbSim Parameter	Value
Analysis Time [s]	1000
Time Step [s]	0.05
Grid Height [m]	180
Grid Width [m]	180
Grid point dimension [-]	32 x 32
Turbulence Model	Kaimal Wind Spectrum
IEC Turbulence Characteristic	A
IEC Turbulence Type	NTM
Wind Profile	Power Law
Power Law exponent	0.1
Surface Roughness Length [m]	0.03

7.2.2 Hydrodynamic coefficients

For all 29 environmental conditions, the assumed drag and inertia coefficients are **0.9** and **2.0**, respectively. These hydrodynamic coefficients vary as functions of Keulegan-Carpenter number (K_C), Reynolds number (R_e) and relative roughness (k/D). To investigate the validity of the assumption made, R_e and K_C for all conditions and four water depths are calculated as shown in Figure 7.2 and Figure 7.3, respectively. Maximum particle velocity assuming regular waves at mean water level (z = 0) are used for the calculations. Large diameter pile designs generally result in very high R_e and low values of K_C.

The experimental study by Sarpkaya [22] presented in the literature review, verifies dependence of hydrodynamic coefficients to R_e, K_C and k/D. The study, though, does not cover the range of low K_C numbers. Environmental conditions with high R_e and low values of K_C fall outside the range of results of the study.

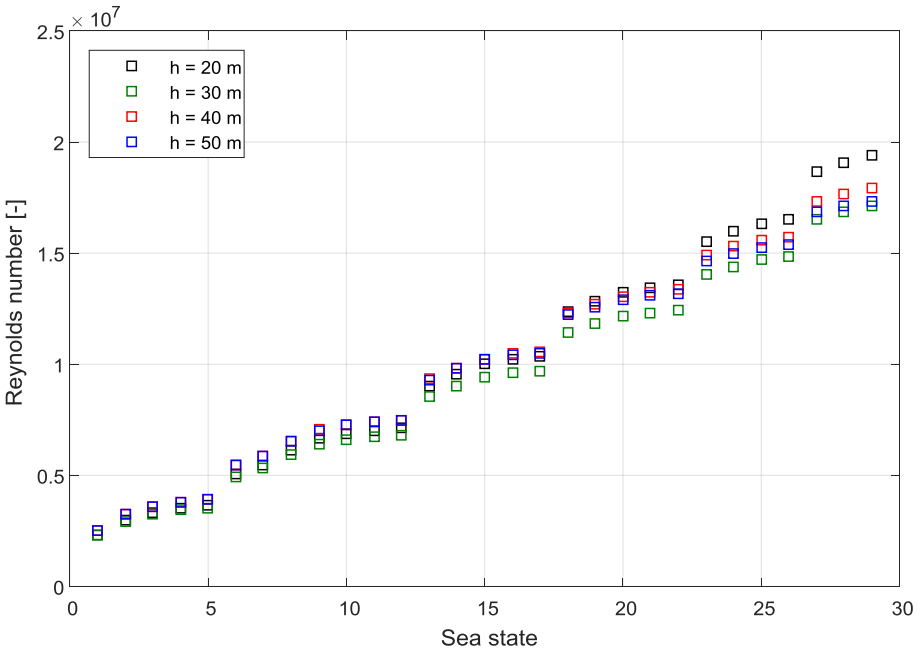

Figure 7.2 Reynolds number for all representative sea states

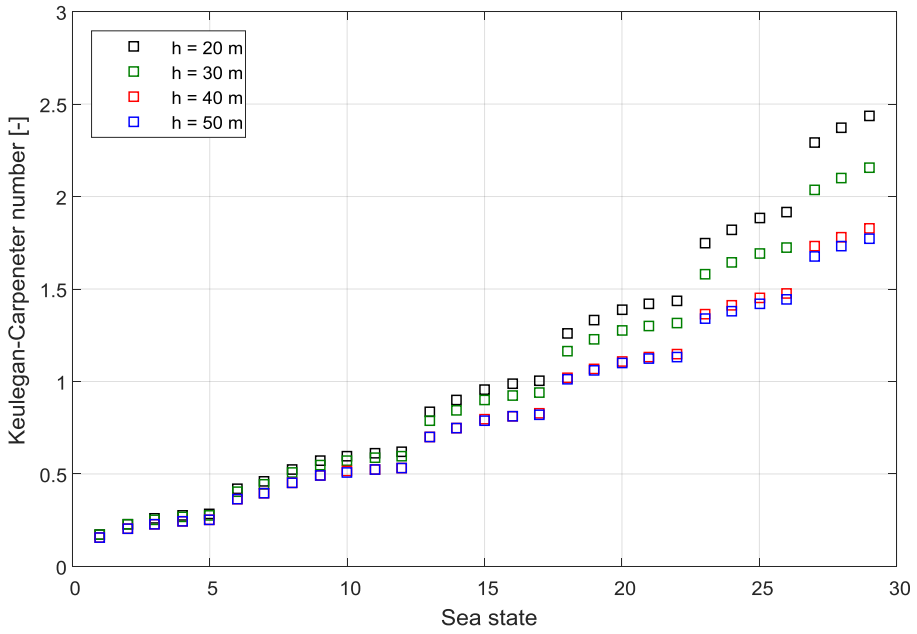

Figure 7.3 Keulegan-Carpenter number for all representative sea states

DNV [5] recommends both drag and inertia coefficients for oscillatory flows for both smooth and rough surfaces, where the calculation is based on drag coefficients for steady-state flow conditions. These coefficients are calculated based on the provisions as a function of K_C and

are shown in Figure 7.4. For K_C values less than 3.0 where most environmental conditions lie, added mass coefficients can be assumed independent of K_C number. Thus, the inertia coefficient (C_M) can be assumed equal to **2.0**. The drag coefficients, on the other hand, are more sensitive to variation in small K_C values and also differ between smooth and rough surfaces. An intermediate value of **0.9**, which lies in the middle of the range of possible values, is a reasonable assumption in this case. DNV [5] also recommends a roughness value of 0.005 m to 0.05 m for marine growth. This results in a relative roughness of 1/2000 to 1/200 for the 10 m diameter pile, which based on DNV, lies closer to the smooth surface's hydrodynamic coefficients.

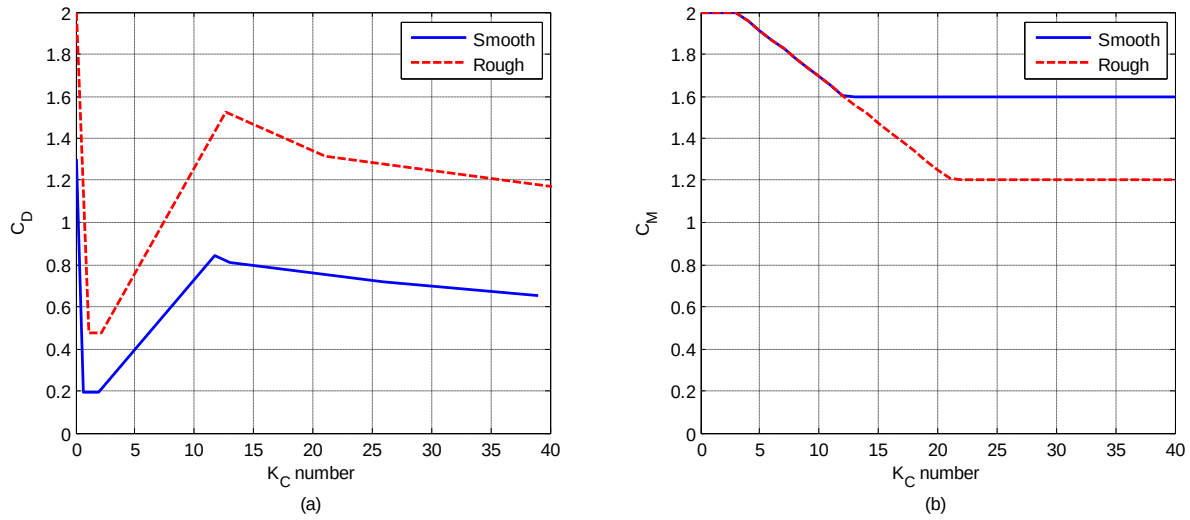

Figure 7.4 (a) C_D and (b) C_M versus K_C based on DNV recommendation

Although there is less certainty in the assumed drag coefficient, the associated error is also minimal due to the hydrodynamic forces being inertia-dominated as reflected by low K_C values. Recommendations by DNV [5], though, does not incorporate the effect of Reynolds number to the hydrodynamic coefficients. Since no information is available, this adds uncertainty to the assumed hydrodynamic coefficients. In addition, there is uncertainty in the effect of relative roughness since marine growth develops throughout the life cycle of the structure.

7.3 Sensitivity to Hydrodynamic Model

Similar to the ULS analysis, a number of simulations are done in FLS analysis to investigate how the choice of hydrodynamic model affects fatigue damage prediction. The three hydrodynamic models being compared include M1 (1st order - MWL), M2 (1st order – constant ϕ) and M3 (2nd order – IWL). Using the established design load case, simulations are done for four water depths, three hydrodynamic models and 29 representative environmental conditions. Applying six seeds for each case results in a total of 2,088 10-minute simulations.

For each selected cross sections along the monopile, a 10-minute stress time series is calculated from 10-minute time series of axial force and bending moment. The stress calculation considers the point on the upwind direction of the cross section defined as point 3 in Figure 6.6. For each stress time series, stress cycle amplitudes are calculated using rainflow count method. Fatigue damage is then calculated based on Palmgren-Miner summation and the established S-N curve, which gives the allowed number of cycles to failure.

Fatigue damage predictions from different hydrodynamic models are presented, followed by a simple frequency domain estimate. The contribution to fatigue damage of each environmental condition is also investigated.

7.3.1 Governing hydrodynamic model

The calculated fatigue damage from hydrodynamic models M1, M2 and M3 is shown in Figure 7.5. Among the four monopile designs for each water depth, only the design for the 20 m water depth is satisfactory considering fatigue limit state. Higher fatigue damage for higher water depths are reasonable results, due to increased moment arm and higher wave loads. Thus, design iterations for water depths 30 m, 40 m and 50 m are recommended by increasing the pile diameter and/or pile thickness.

With regards to the different wave models, fatigue limit state analysis is generally less sensitive to wave models as compared to ultimate limit state analysis. M1, M2 and M3 predict similar fatigue damage for the 20 m water depth, but the predictions slightly diverge as water depth increases. In addition, M1 (1st order - MSL) predicts a higher fatigue damage compared to M2 and M3 whose forces are integrated up until the instantaneous water line. Such result is unexpected, but could be due to increased hydrodynamic damping associated with integrating the force up until the instantaneous water line.

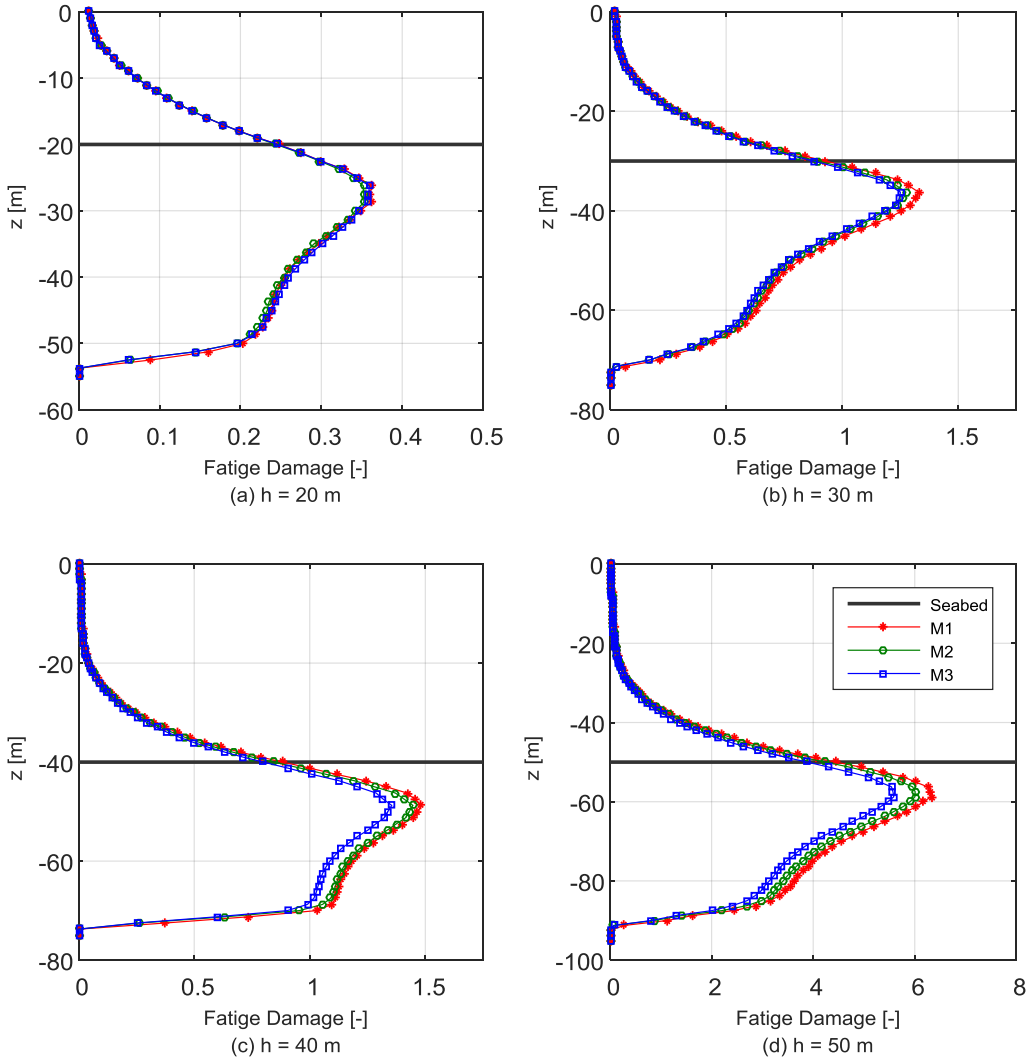

Figure 7.5 Fatigue damage prediction of M1, M2 and M3

To further investigate why M1 predicts higher fatigue damage than M2 and M3, simulations were done when the on wind turbine is parked. This situation aims to demonstrate how the presence of an operating wind turbine affects fatigue damage predictions. Conditions 9 (U_w = 11.1 m/s) and 29 (U_w = 23.6 m/s), associated with high and low thrust, were chosen and the results are shown in Figure 7.6 and Figure 7.7, respectively. For both conditions, having the wind turbine parked results in larger differences in damage predictions between the models. Larger fatigue damage can also be observed when the wind turbine is parked due to reduced aerodynamic damping, particularly for water depths 30 m, 40 m and 50 m. The governing wave model, though, is different for both conditions where M2 and M3 giving higher fatigue damage for higher sea states. It is then hypothesized that wave models whose forces are integrated up to instantaneous water line (M2, M3) give higher fatigue damage at higher sea states. The hypothesis is consistent with ULS analysis results, where M3 gives the highest damage for the load cases associated with the 50-year environmental conditions.

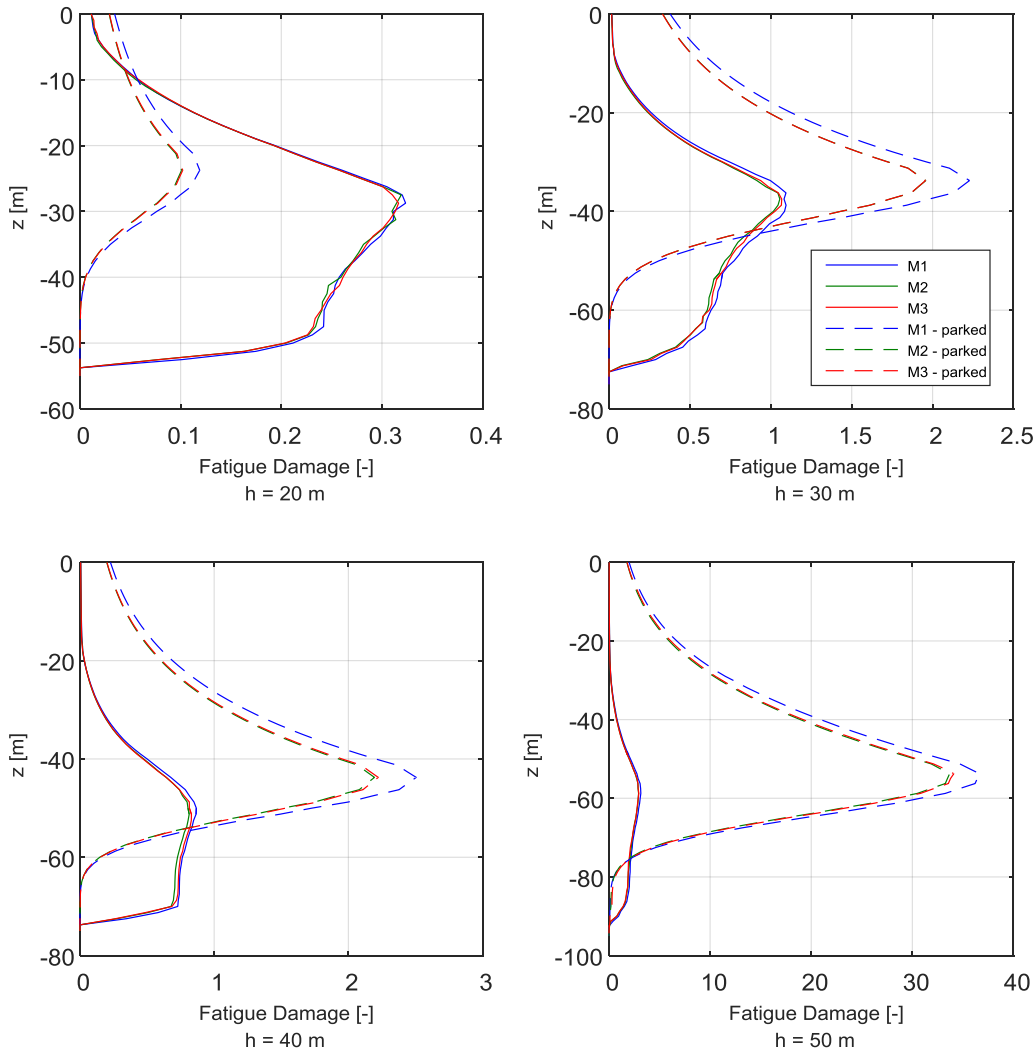

Figure 7.6 Fatigue damage prediction of M1, M2 and M3 (H_s = 1.56 m , T_p = 6.78)

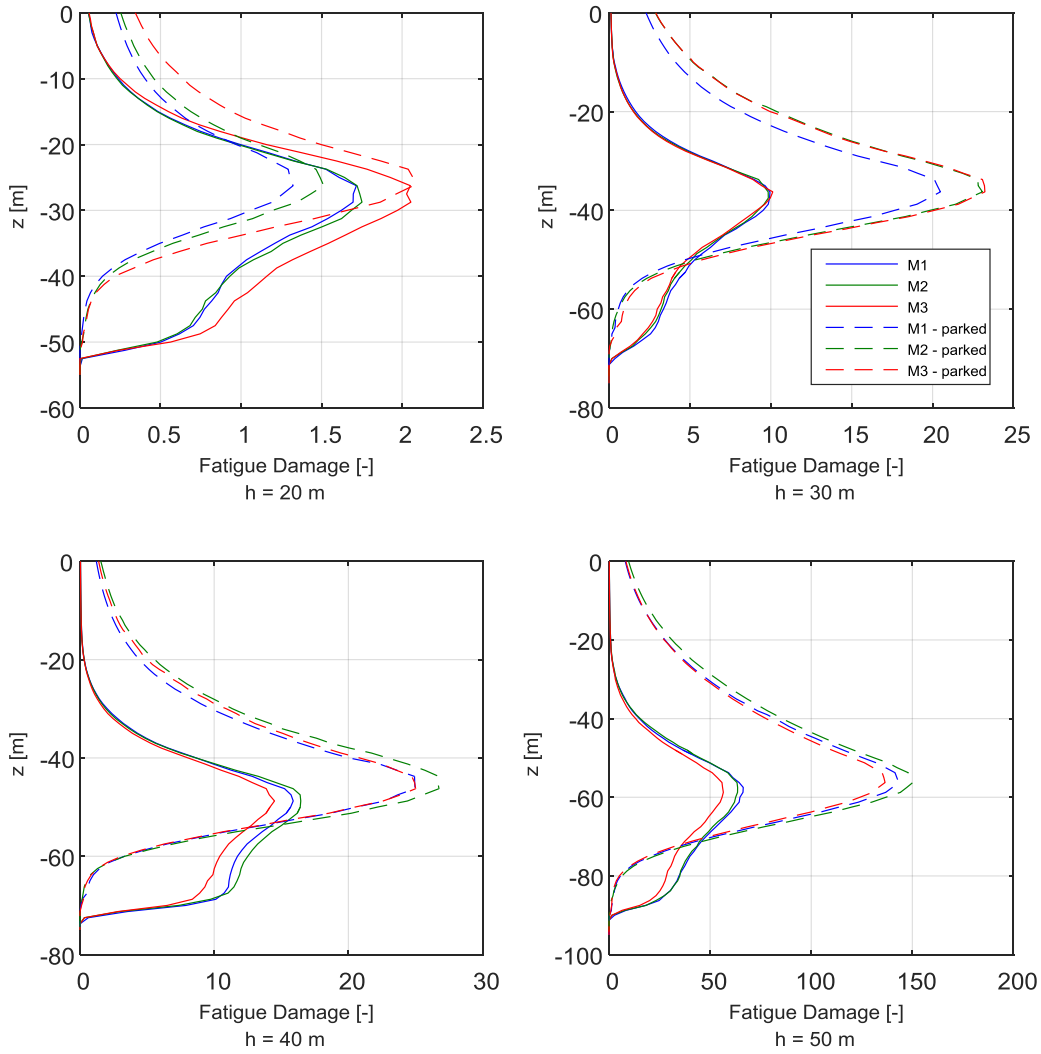

Figure 7.7 Fatigue damage prediction of M1, M2 and M3 (H_s = 5.47 m , T_p = 9.89)

Lastly, the stress spectra of M1, M2 and M3 are compared for low, intermediate and high sea states as shown in Figure 7.8. For low sea states (a, b), the stress spectra of all models are comparable. For intermediate sea states (c, d), M1 generates higher power spectra, particularly at frequencies close to the natural frequency. This explains the higher differences in fatigue prediction with increasing water depth, since the influence of hydrodynamic loads increases with depth as to be discussed in the succeeding sections. And for higher sea states represented by the 50-year conditions (e, f), M3 has a significantly higher power spectrum close to the natural frequency. Note that the wind turbine is parked when for the 50-year conditions.

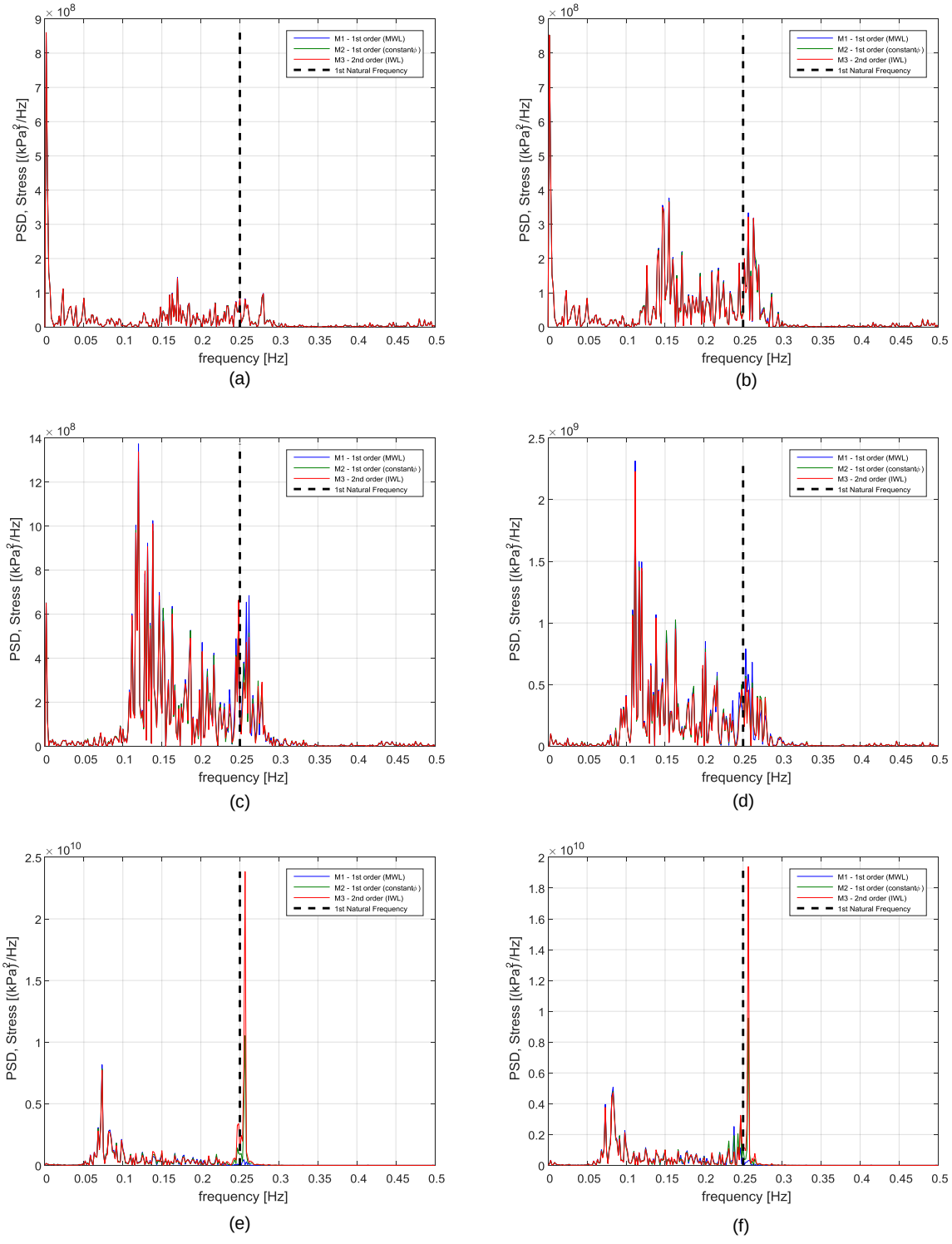

Figure 7.8 Investigation of spectra of M1, M2 and M3

(a) Condition 5 (H_s = 0.80 m, T_p = 6.19 s), (b) Condition 10 (H_s = 1,63 m, T_p = 6.83 s), (c) Condition 20 (H_s = 3.48 m, T_p = 8.26s), (d) Condition 25 (H_s = 4.47 m, T_p = 9.06 s), (e) ULS 3 (H_s = 8.6 m, T_p = 12.7 s), (f) ULS 4 (H_s = 9.9 m, T_p = 14.0 s)

A further investigation is recommended to explain how M1 governs in intermediate sea states, particularly the possibility of having increased hydrodynamic damping when forces are integrated up to instantaneous water line. The effect of the operating or non-operating wind turbine can also be studied.

Fatigue damage for different water depths

The fatigue damage distribution for different water depths can be investigated by plotting fatigue damage at a common seabed reference line. Using results from M2, the damage distribution along the length of the pile can be illustrated as shown in Figure 7.9. For all water depths, fatigue damage increases until it reaches a maximum value a few meters below the seabed, and then gradually reduces to zero at the end of the pile.

The maximum fatigue damage for different water depths and its location are summarized in Table 7.8. Note that monopile designs for 20 m and 30 m water depths have 9.0 m diameter, while designs for 40 m and 50 m water depths have 10.0 m diameter. Regardless of pile design, the location of maximum fatigue damage falls between 7.0 m and 9.0 m below the seabed.

Table 7.8 Location of maximum fatigue damage

Water Depth	Maximum fatigue damage	Node	Elevation from mudline [m]
20	0.35	28	-8.75
30	1.27	36	-6.25
40	1.45	48	-8.75
50	6.00	57	-7.5

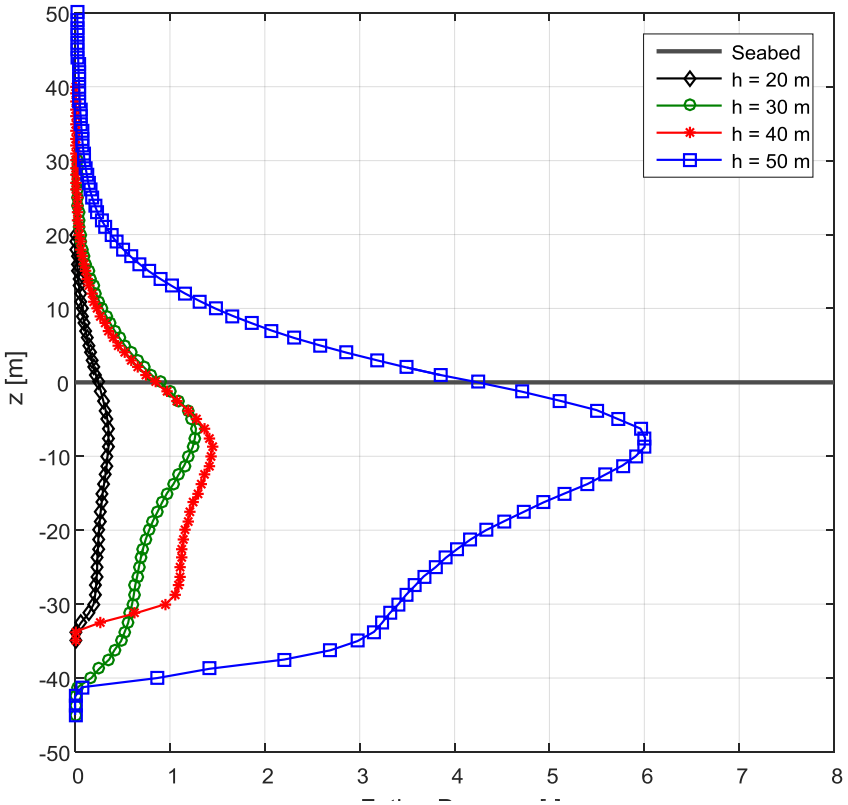

Figure 7.9 Total fatigue damage for all water depths from M2 (1st order – constant ϕ)

7.3.2 Relative contribution of sea states

The relative contribution to fatigue damage of each environmental condition is investigated by looking at fatigue damage prediction of M2. Figure 7.10 shows how much each condition contributes to the total fatigue damage at different section of the pile designs. Considering results for the 20 m water depth, a larger part of the fatigue damage is given by lower sea states. As water depth increases, contribution from higher sea states becomes larger. This implies that hydrodynamic loads become more significant with higher depths.

Both environmental condition (U_w, H_s and T_p) and its probability of occurrence affects the relative damage contribution. Thus, the 20-year fatigue damage (for h = 20 m) and probability for each condition are shown in Figure 7.11. Since the sea states are arranged in increasing H_s, it shows that fatigue damage generally increases with H_s. The probability of occurrence, on the other hand, generally follows the probability distribution over wind speed.

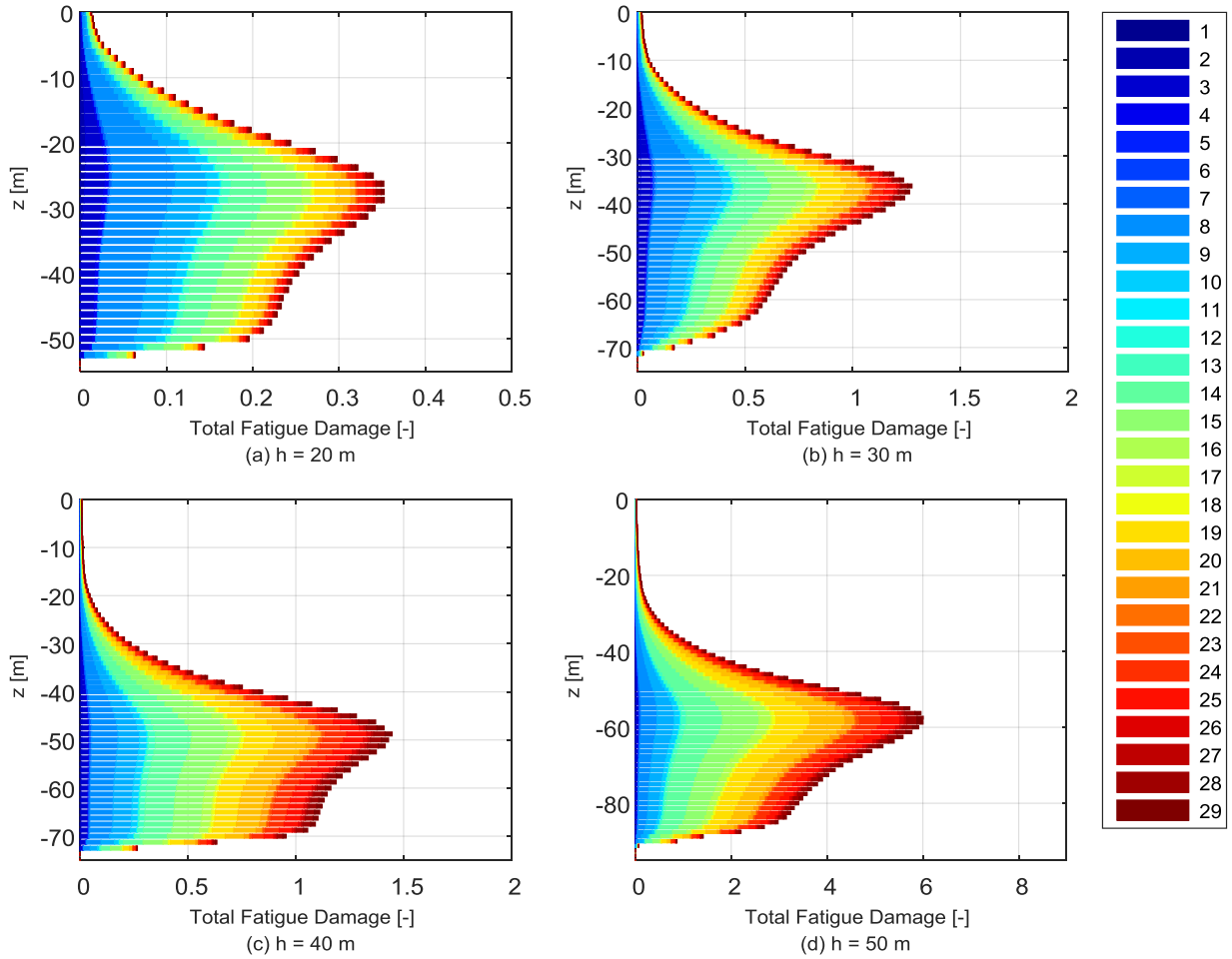

Figure 7.10: Total fatigue damage using 1st order – constant ϕ model (a) h = 20 m, (b) h = 30 m, (c) h = 40 m and (d) h = 50 m

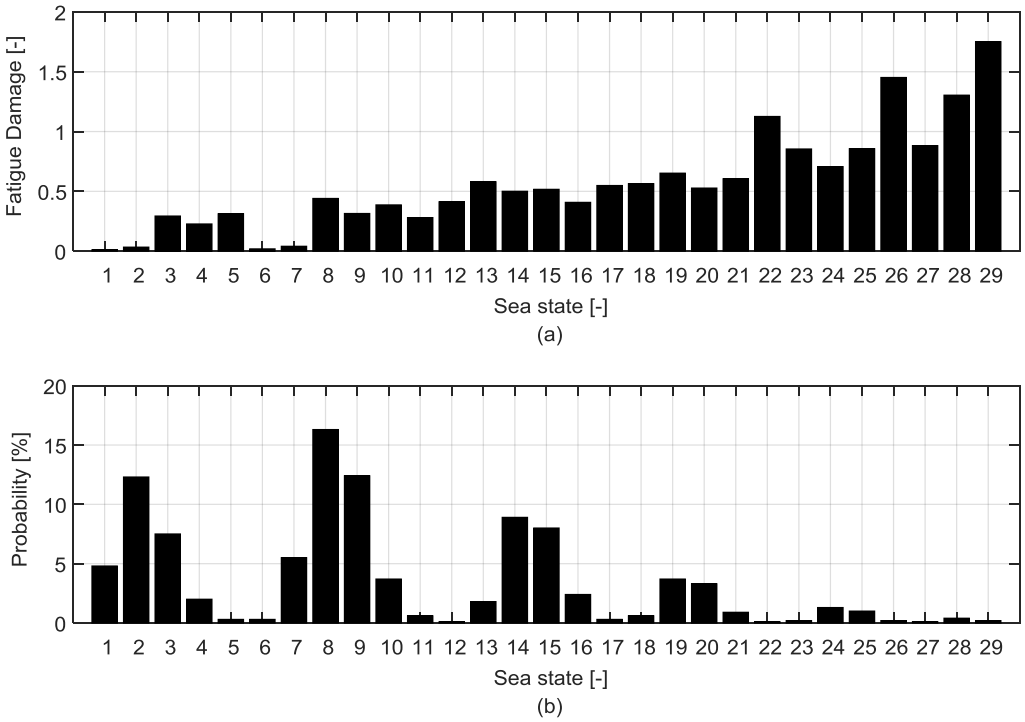

Figure 7.11 fatigue damage (20 years) for h = 20 m and probability for each condition

For each water depth, the relative damage contributions of each sea state for the point with maximum damage are illustrated in Figure 7.12. The combined effect of 20-year fatigue damage and probability is apparent, particularly the peaks associated with probability distribution over wind speed. Lower sea states, despite having high probability of occurrence, exhibit low contribution due to relatively low 20-year fatigue damage. Higher sea states, despite having high fatigue damage, also exhibit low contribution due to low probability of occurrence.

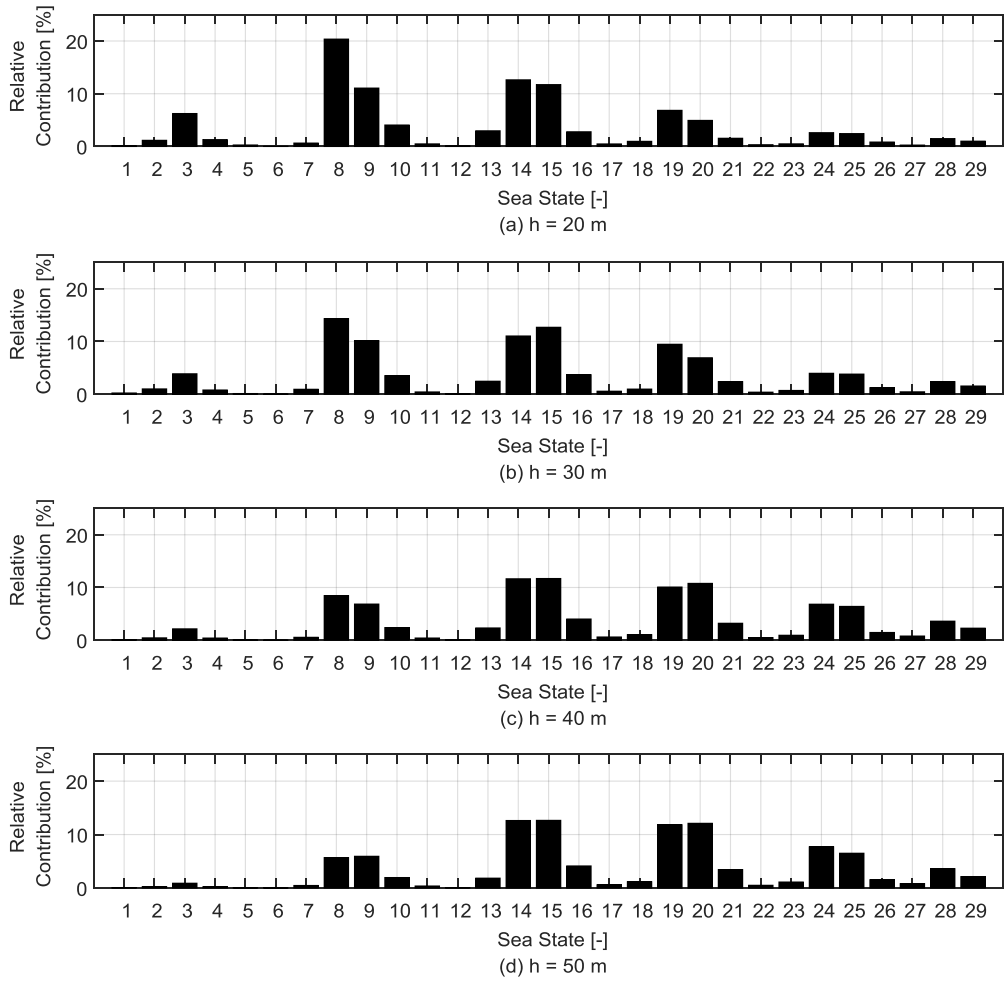

Figure 7.12 Relative contribution of each sea state to total fatigue damage

Lastly, fatigue contributions are further lumped according to wind speed as shown in Figure 7.13. The distribution generally resembles either the thrust curve or the long term probability distribution over wind speed. In either case, it implies higher influence of wind speed to fatigue damage relative to significant wave height. Furthermore, fatigue damage contribution spans more to higher wind speeds as water depth increases. Since wind speed is correlated with significant wave height, this reflects higher relative contribution from hydrodynamic loads as water depth increases.

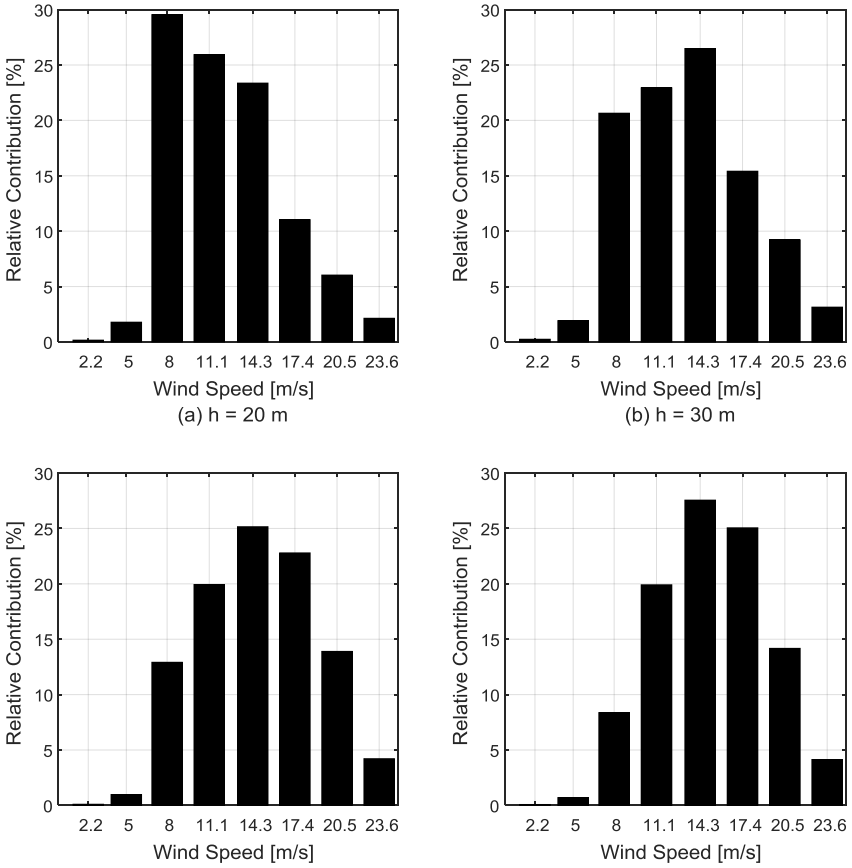

Figure 7.13 Relative contribution of each wind speed to total fatigue damage

7.3.3 Frequency domain estimate

To check that the results of time domain fatigue calculations are reasonable, an estimate of the fatigue damage is calculated from the frequency domain results. A narrow-banded assumption is made to simplify the calculation. For this purpose, results from the 20 m water depth and wave model M2 are used.

The time domain results of wave elevation (η), thrust and stress are presented together with their corresponding power spectral density (PSD) for two representative environmental conditions. Figure 7.14 shows the plot for condition 8, which has the highest probability of occurrence, and Figure 7.15 shows the plot for condition 9, which has the second highest probability of occurrence and a wind speed closest to the rated wind speed. Time domain results do not include transient region and a red line on the PSD marks the natural frequency of the structure. For both sea states, the PSD implies that stresses are more influenced by thrust force compared to hydrodynamic force. Minimal stress response can be observed around the natural frequency.

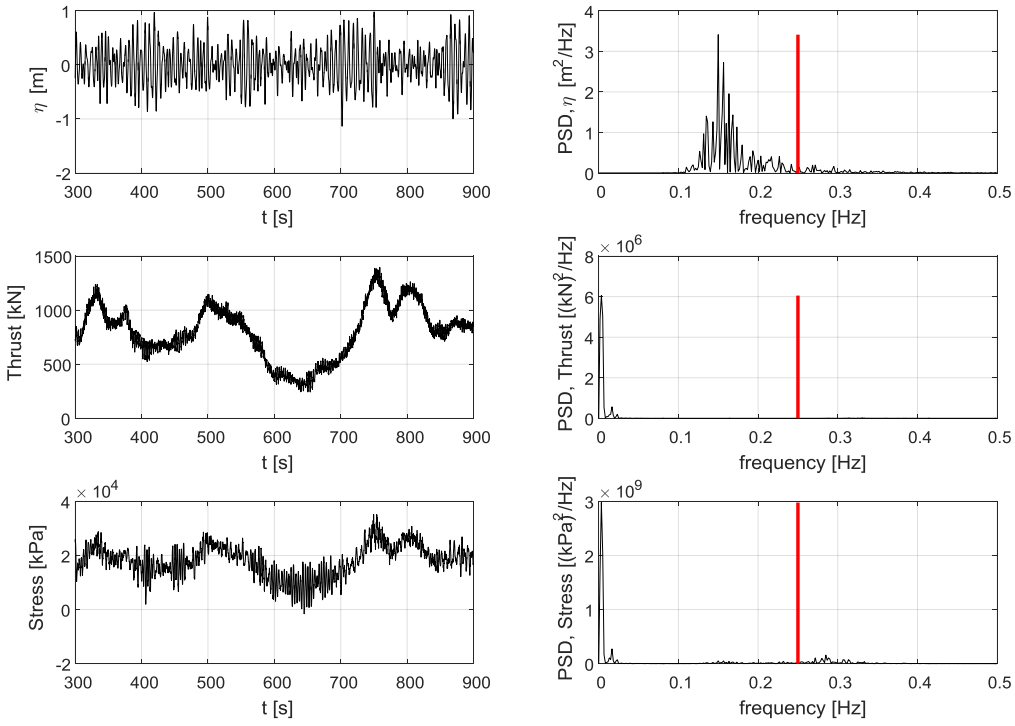

Figure 7.14 PSD of wave elevation, thrust and stress (h = 20 m, condition 8)

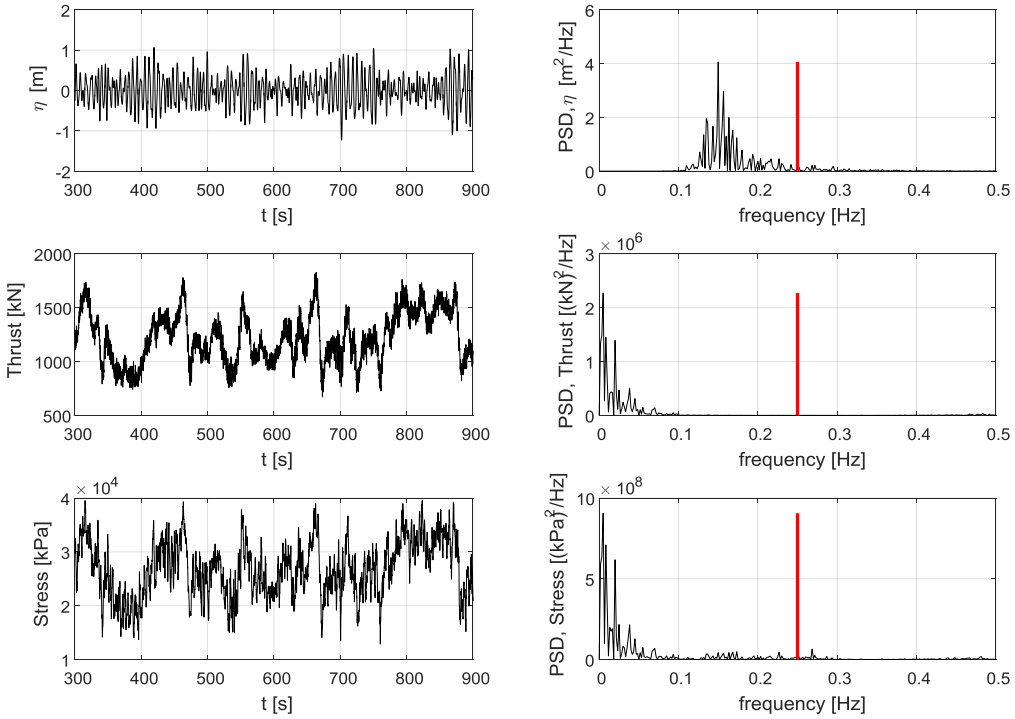

Figure 7.15 PSD of wave elevation, thrust and stress (h = 20 m, condition 9)

The standard deviation or amplitude of stress is calculated from the area under stress spectrum, while the number of cycles is calculated from the representative frequency of the spectrum. Based on the stress amplitude, a maximum number of cycles is calculated based on the defined S-N curve. For the 29 environmental conditions, fatigue damage is calculated based on Palmgren-Miner summation and scaled for 20 years.

The time domain and frequency domain fatigue damage estimate for the 20 m water depth is shown in Figure 7.16. The frequency domain calculation generally overestimates fatigue damage above mudline and underestimates fatigue damage below the point where maximum damage occurs. Nevertheless, the magnitude of predicted damage well matches that of the time domain prediction and thus verifies the time domain calculation.

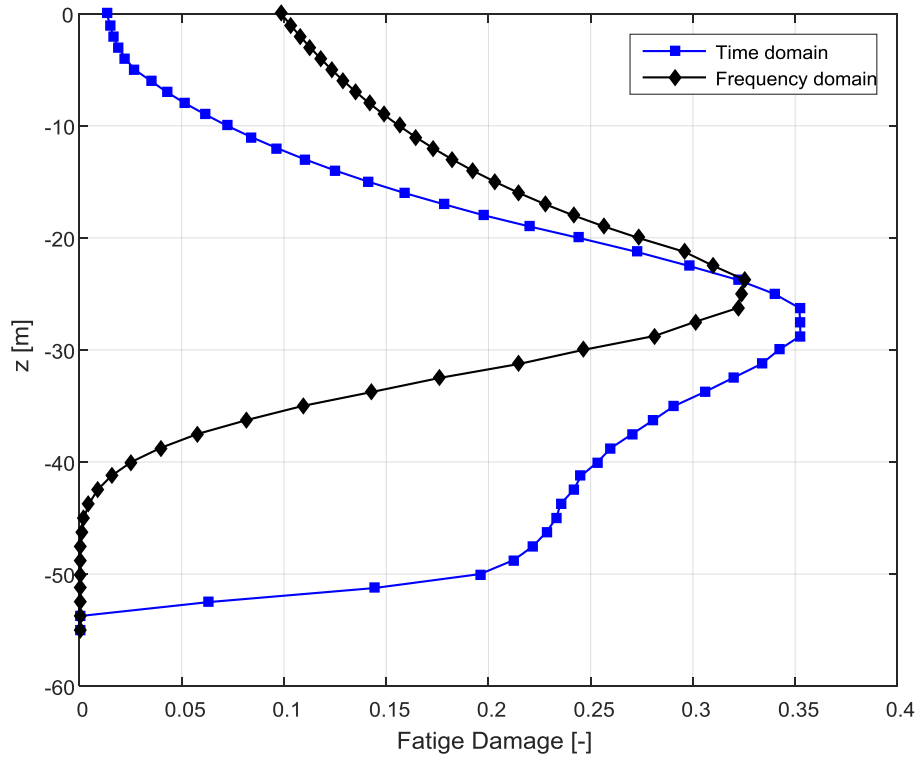

Figure 7.16 Fatigue damage check from frequency domain calculation

7.3.4 Effect of diffraction in hydrodynamic load

Considering the large monopile dimensions, a major uncertainty in the calculated fatigue damage is the effect of diffraction. The effect of free surface diffraction on hydrodynamic loads is investigated using MacCamy-Fuchs equation and irregular linear wave inputs. The inertia force is modified following the MacCamy-Fuchs formulation presented in Chapter 2. MacCamy-Fuchs equation is only valid up to the mean water line and the calculation of wave force does not consider the motion of the structure. Considering the relative motion of the monopile, though, would have a little effect on the calculated loads due to the structure's small deformations.

The calculated C_M and phase angle applicable to four preliminary designs are presented in Figure 7.17. It shows that C_M generally decreases with increasing wave frequency, with a slightly lower value for the larger diameter pile at higher frequencies.

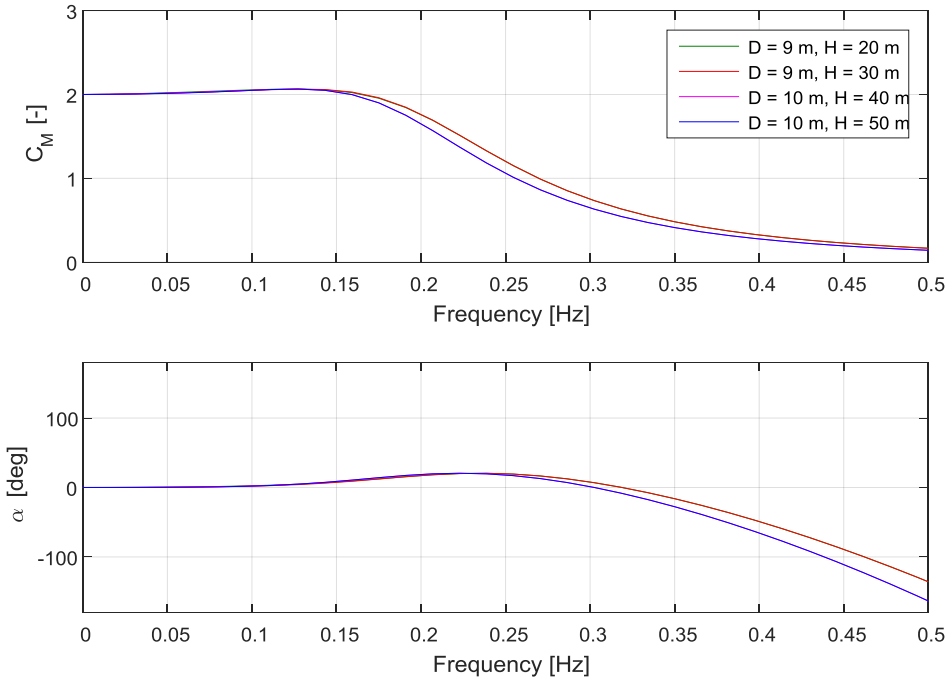

Figure 7.17 Added mass (C_M) and phase angle (α) based on MacCamy-Fuchs equation

Irregular first order wave elevations of representative environmental conditions generated from RIFLEX (same as model M1) are used to calculate equivalent nodal forces in Matlab. Nodal forces are calculated for every 1.0 meter section for all water depths. Modifications on the inertia force are applied for each wave components, which are derived from the irregular time history by FFT. The drag force contribution to nodal force is also calculated based on linear wave theory using a $C_D = 0.9$.

A representative wave elevation input and the corresponding hydrodynamic force with and without modification for C_M are shown in Figure 7.18 for a water depth of 20 m. For a low sea state with a peak period of 6.13 seconds ($\omega = 1.02$ rad/s), the deviation from mean of the total force are generally reduced. Due to the decay of acceleration from still water level to the seabed, most of the reduction in inertia force occurs at nodes close to the mean water line as implied by Figure 7.18 (c) and Figure 7.18 (d).

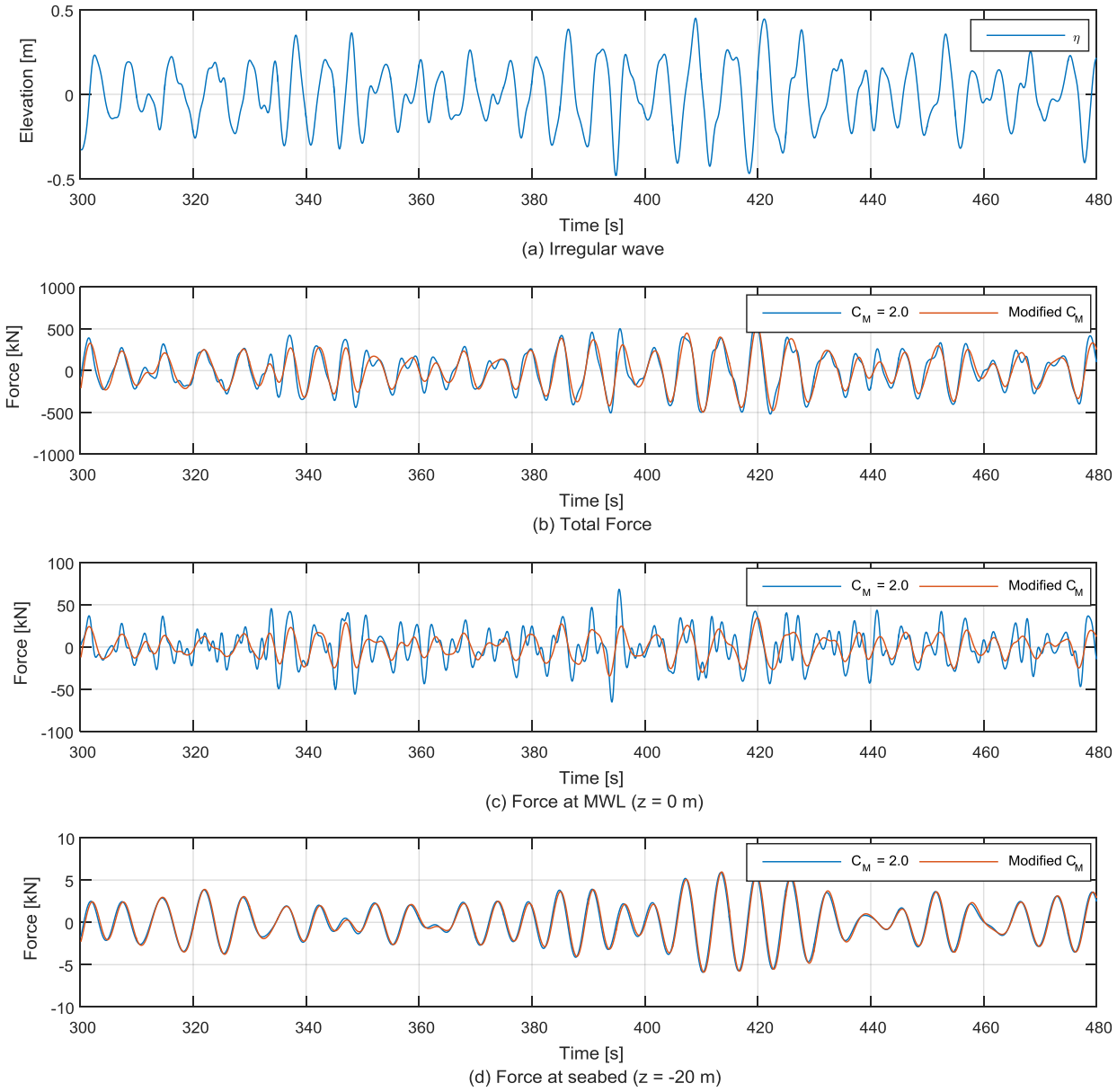

Figure 7.18 Effect of modified C_M on hydrodynamic loads (H_s = 0.73 m, T_p = 6.13 s)

The discussion of the validity of assumed hydrodynamic coefficients on section 7.2.2 showed that all representative sea states for FLS are inertia-dominated with KC values less than 2.5. A comparison of the inertia force (modified) and drag force magnitudes for both low and high sea states is shown in Figure 7.19. Considering a 10-minute time series, the maximum inertia force for low and high sea states are about 145 and 13 times higher, respectively, than the

maximum drag force. Since inertia force dominates drag force contribution, modification of the inertia force significantly affects the total hydrodynamic force.

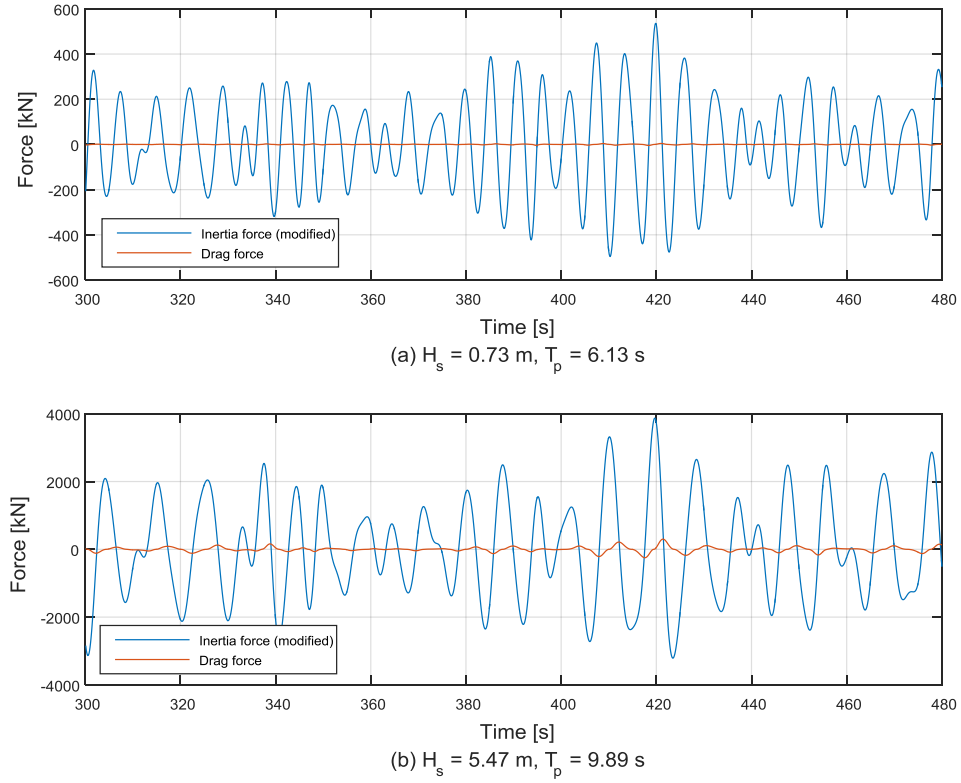

Figure 7.19 Comparison of inertia and drag force magnitudes

Lastly, the effect of MacCamy-Fuchs theory on the wave force spectra is investigated for selected low and high sea states as shown in Figure 7.20. The three-minute time histories of nodal forces indicate that modification of forces is more significant for lower sea states. The force spectra based on a 10-minute time history also shows that there is more modifications for lower sea states, which is due to higher wave frequencies where higher reduction of C_M is applied (see Figure 7.17). For all water depths, it was found that considering diffraction could reduce the standard deviation of the total hydrodynamic force by 10% to 14%, particularly for lower sea states with $T_p < 6.2$ seconds ($f < 0.16$ Hz).

The modification of inertia force minimizes wave loads occurring at higher frequencies, which includes blade passing frequencies (3P region) at 0.30 Hz to 0.48 Hz. At this point, though, it is difficult to predict how much the fatigue damage will be reduced by applying

MacCamy-Fuchs theory without the resulting structural response. For an operating wind turbine, it was found that wind loads have generally higher contribution to fatigue damage. Thus, a time-domain simulation accounting for both wind and wave loads is further recommended.

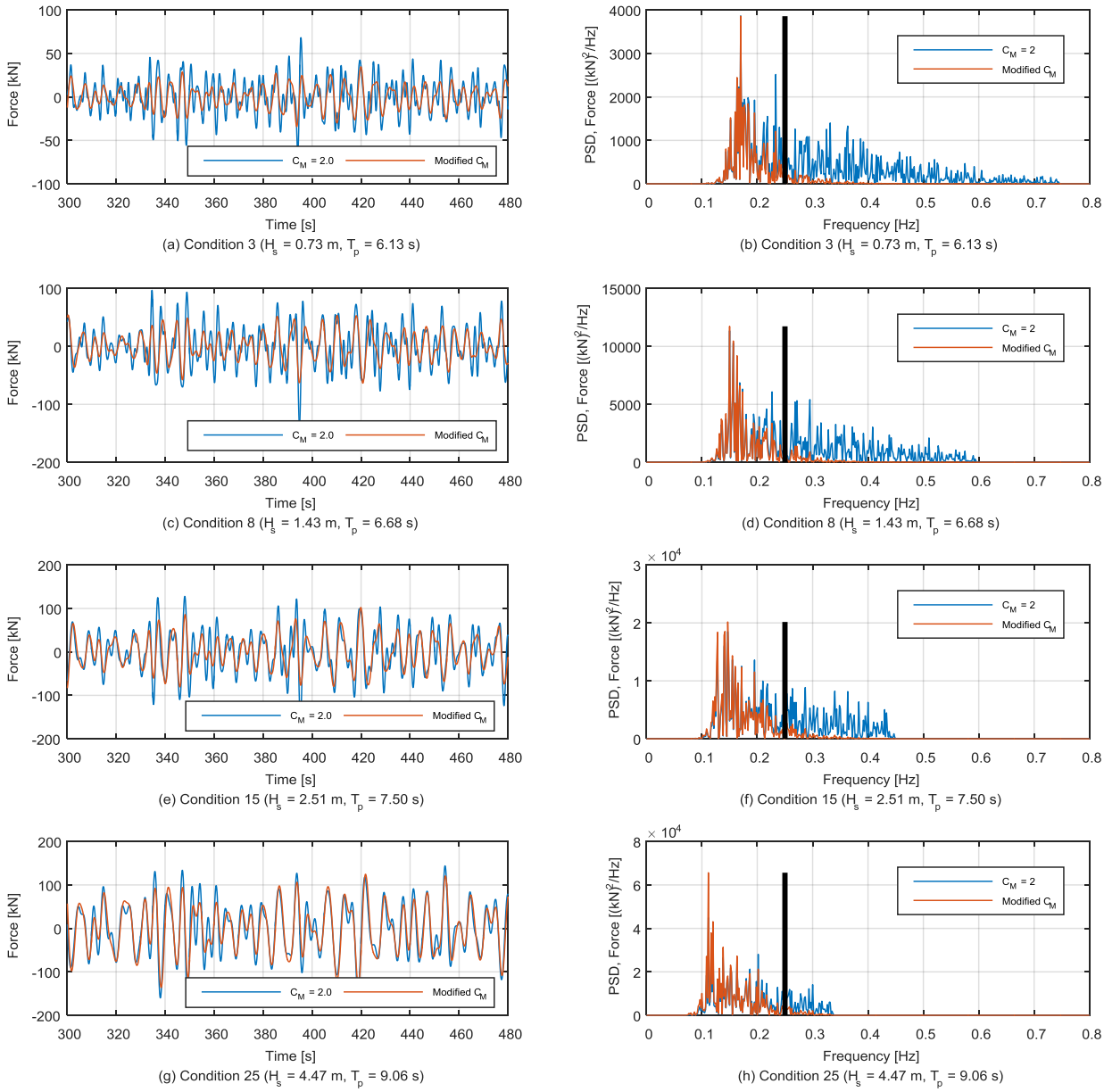

Figure 7.20 Comparison of nodal force (at z = 0 m) spectra for selected sea states (h = 20 m)

Chapter 8.

Fatigue Damage Parameter

In this chapter, a Fatigue Damage Parameter (FDP) is established to correlate fatigue damage of an environmental condition with parameters thrust, H_s and T_p. The main motivation for establishing an FDP is to quantify how much each environmental condition contributes to fatigue damage and select a number of representative conditions to predict fatigue damage. The proposed approach eliminates the need for running all conditions, thus significantly reducing computation time for FLS.

Specific objectives of this study include (1) deriving the relationship between fatigue damage and parameters thrust, H_s and T_p, (2) defining a general approach for fatigue damage prediction using fewer number of representative conditions, (3) evaluating the accuracy of this approach at varying water depths and pile designs, and (4) identifying uncertainties in the proposed methodology.

In this section, fatigue damage prediction from hydrodynamic model M2 (1^{st} order – constant ϕ) are used as reference fatigue damage for all water depths.

8.1 Theoretical value of constants

This section derives the relationship between fatigue damage and environmental parameters U_w, H_s and T_p. The derived relationship is then evaluated by running fatigue analysis considering wind and wave load effects separately. A power curve is fitted in evaluating the strength of correlation.

8.1.1 Derivation

Using Morison's equation, the hydrodynamic force can be written as the sum of the drag and inertia force. For inertia-dominated regimes, the drag force contribution can be assumed insignificant and force can be simplified as follows:

$$F = F_{Drag} + F_{Inertia} \tag{8.1}$$

$$F \approx F_{Inertia} \tag{8.2}$$

$$F = \rho\, C_M\, A\, \dot{u} \tag{8.3}$$

For finite water depths, the acceleration $(\dot{u}_x)$ of the fluid particle in the direction of wave propagation is given by [23]:

$$\dot{u}_x = \omega^2 \zeta_a \frac{\cosh k(z+h)}{\sinh kh} \cos(\mathrm{wt} - \mathrm{kx}) \tag{8.4}$$

The circular frequency(ω) and wave amplitude (ζ_a) can be expressed in terms of wave period (T) and wave height(H), respectively as follows:

$$\dot{u}_x = \left(\frac{2\pi}{T}\right)^2 \frac{H}{2} \frac{\cosh k(z+h)}{\sinh kh} \cos(\mathrm{wt} - \mathrm{kx}) \tag{8.5}$$

The hydrodynamic force can now be expressed in terms of wave height and wave period. Similarly, the corresponding bending moment can be calculated for every section knowing the moment arm(d):

$$F = \frac{H}{T^2}\left[\rho\, C_M\, A \frac{(2\pi)^2}{2} \frac{\cosh k(z+h)}{\sinh kh} \cos(\mathrm{wt} - \mathrm{kx})\right] \tag{8.6}$$

$$M = \frac{H}{T^2}\left[\rho\, C_M\, A \frac{(2\pi)^2}{2} \frac{\cosh k(z+h)}{\sinh kh} \cos(\mathrm{wt} - \mathrm{kx}) \cdot \mathrm{d}\right] \tag{8.7}$$

For monopile foundations supporting a wind turbine, the axial stress is relatively small compared to bending stress. Neglecting the axial force contribution, the sectional stresses can be expressed in terms of bending stress knowing the moment of inertia (I) and distance from the centroidal axis (y):

$$\sigma = \frac{M \cdot y}{I} \tag{8.8}$$

$$\sigma = \frac{H}{T^2} C_1 \tag{8.9}$$

where

$$C_1 = \left[\rho\, C_M\, A \frac{(2\pi)^2}{2} \frac{\cosh k(z+h)}{\sinh kh} \cos(\mathrm{wt} - \mathrm{kx}) \cdot \mathrm{d} \frac{\mathrm{y}}{\mathrm{I}}\right] \tag{8.10}$$

Assuming that damage accumulates linearly with the number of stress cycles, the Wöhler's equation relates cycles of constant stress range ($\Delta\sigma$) with number of cycles to failure (N_f) as follows [28]:

$$N_f \cdot (\Delta\sigma)^m = \bar{a} \tag{8.11}$$

$$\log(N_f) = \log(\bar{a}) - m\log(\Delta\sigma) \tag{8.12}$$

The material parameter m refers to the negative inverse slope of the S-N curve while the parameter $\log(\bar{a})$ refers to the intercept of log (N) axis. The representative S-N curve shown in Figure 7.1 has two slopes defined by m = 3 and m = 5. For fatigue limit state analysis, most stress cycles amplitudes lie on the lower region of the S-N curve defined by m = 5. Thus, N_f can be expressed as follows:

$$N_f = \bar{a} \cdot (\Delta\sigma)^{-5} \tag{8.13}$$

The fatigue damage (D) is predicted using the Palmgren-Miner summation:

$$D = \sum_{i=1}^{I} \frac{n_i(\Delta\sigma_i)}{N_{f,i}(\Delta\sigma_i)} \tag{8.14}$$

Assuming a narrow-banded wave frequency spectrum, the actual number of stress cycles (n_i) can be expressed as a function of wave period. Using the relations derived for N_f and σ, the fatigue damage can now be expressed as follows:

$$D \approx \frac{\left(\frac{1}{T}\right)}{\bar{a} \cdot (\Delta\sigma)^{-5}} \tag{8.15}$$

$$D \approx \frac{\left(\frac{1}{T}\right)}{\bar{a} \cdot \left(\frac{H}{T^2} C_1\right)^{-5}} \tag{8.16}$$

$$D \approx \frac{H^5 \, T^{-11}}{\bar{a} \cdot {C_1}^{-5}} \tag{8.17}$$

Note that the derived relation does not include influence of thrust due to wind, whose validity is evaluated in the next section.

8.1.2 FDP Formulation

In addition to U_w, H_s and T_p, the probability of occurrence (P) of each condition is accounted in FDP to improve selection of representative sea states. The FDP is defined as:

$$FDP = [T(U_w)]^{\alpha} \, {H_s}^{\beta} \, {T_p}^{\gamma} P \tag{8.18}$$

In the equation, $T(U_w)$ refers to the normalized thrust as a function of wind speed at hub height as summarized in Table 8.1, while the constants (α, β, γ) are arbitrary constants. The physical reasoning behind the equation is the fact that fatigue damage increases as the standard deviation or amplitude of stress cycles increases. As thrust and H_s increase, it is hypothesized that amplitude of stress cycles also increase. On the other hand, it is anticipated that T_p is inversely proportional to fatigue damage since higher T_p leads to a lower frequency of stress cycles. This implies that it is expected for α and β to have positive values, while γ is expected to have a negative value.

Table 8.1 Normalized thrust input

Wind speed [m/s]	U (Thrust - Norm) [-]
0	1
4	1
5	1.56
6	2.20
7	2.85
8	3.53
9	4.47
10	5.51
11	6.67
12	5.63
13	4.79
14	4.28
15	3.94
16	3.65
17	3.43
18	3.24
19	3.09
20	2.96
21	2.84
22	2.74
23	2.66
24	2.58
25	2.51

8.1.3 Behaviour of FDP according to constants

To investigate how each constant influences FDP, sets of constants defined by $\alpha = [0, 1, 3, 5]$, $\beta = [0, 1, 3, 5]$ and $\gamma = [0, -5, -10, -15]$ are assumed. This results in 64 sets of constants that uniquely define FDP values for all 29 conditions. The influence of including the probability in FDP formulation generally favors selection of sea states with higher probabilities. This avoids over-prediction, which could occur when scaling up selections of higher sea states with high damage but low probabilities.

The calculated normalized FDPs, grouped according to α, are shown in Figure 8.1. Using a higher α increases the contribution of wind speed in terms of normalized thrust, as exhibited by conditions 4, 9, 14 and 18 with wind speeds equal to 11.1 m/s (close to rated wind speed of 11.4 m/s). Conditions with wind speeds higher than the rated wind speed do not achieve higher FDP with increasing α, since the thrust curve increases up to rated wind speed and decreases thereafter.

To investigate the influence of β on normalized FDP, different values of β (with α = 0) are shown in Figure 8.2. Having the sea states arranged in increasing H_s, the plot implies that higher values of β increases contribution of H_s to FDP and selection of representative sea states shifts towards higher sea states. Similarly, the influence of γ on normalized FDP is investigated (with α = 0 and β = 5) as shown in Figure 8.3. Due to the inverse relation, higher absolute values of γ (more negative) shifts selection of representative sea states to lower sea states which are associated with lower T_p.

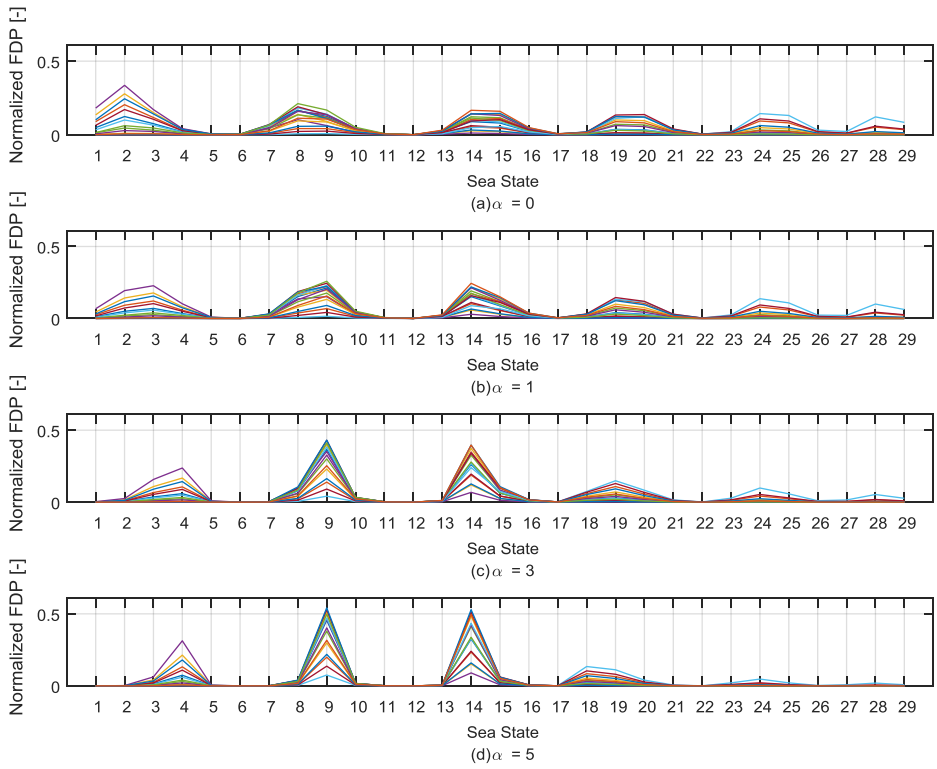

Figure 8.1 Normalized FDP of 29 conditions according to alpha

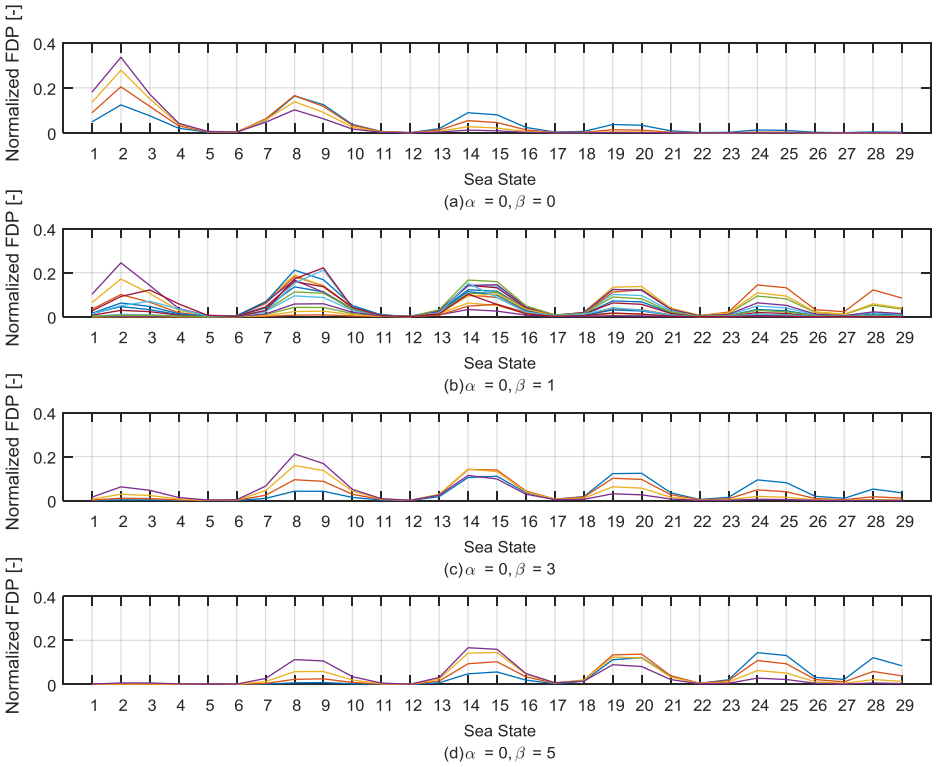

Figure 8.2 Normalized FDP of 29 conditions according to beta

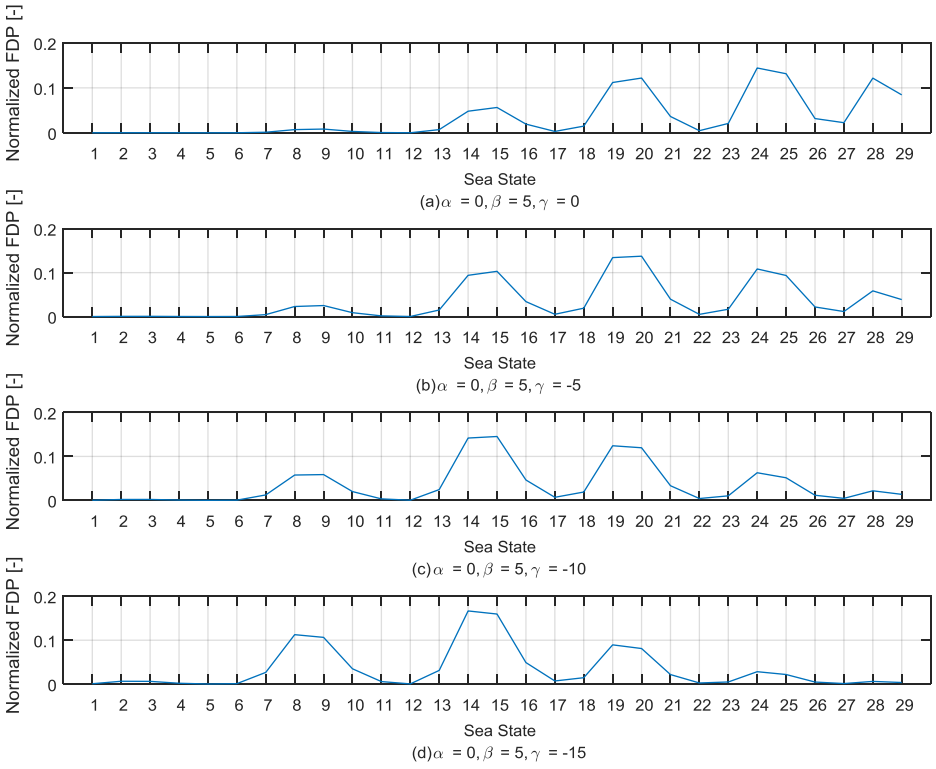

Figure 8.3 Normalized FDP of 29 conditions according to gamma

8.1.4 Regression analysis

To investigate how much wind and wave contribute to fatigue damage and how fatigue damage is correlated with U_w, H_s and T_p, three additional fatigue analysis were performed. One of which only considers wind loads (no wave, with hydrodynamic damping), the second only considers wave loads (no wind), and the third considers wave loading with constant mean wind speed. The presence of constant mean wind speed on the latter provides aerodynamic damping without significantly contributing to fatigue. These simulations directly provide relationship between sea states and the fatigue damage, but do not consider interaction between wind and wave loading.

The simulation is done for the 20 m water depth and 29 environmental conditions. In addition to the predictions from three additional simulations, the calculated fatigue damage from combined wind and wave loading is also added as shown in Figure 8.4. Results show that considering the effect of aerodynamic damping significantly reduces fatigue damage due to waves. Considering fatigue damage from waves with aerodynamic damping accounted, fatigue damage from wind is about 30 times higher than that of the wave at the point of maximum fatigue damage (z = -28.75 m). Another difference between separate wind and wave simulations is the fatigue damage distribution along the pile. Since thrust acts at a higher elevation compared to hydrodynamic loads, it results in a more sustained effect along the depth of the pile.

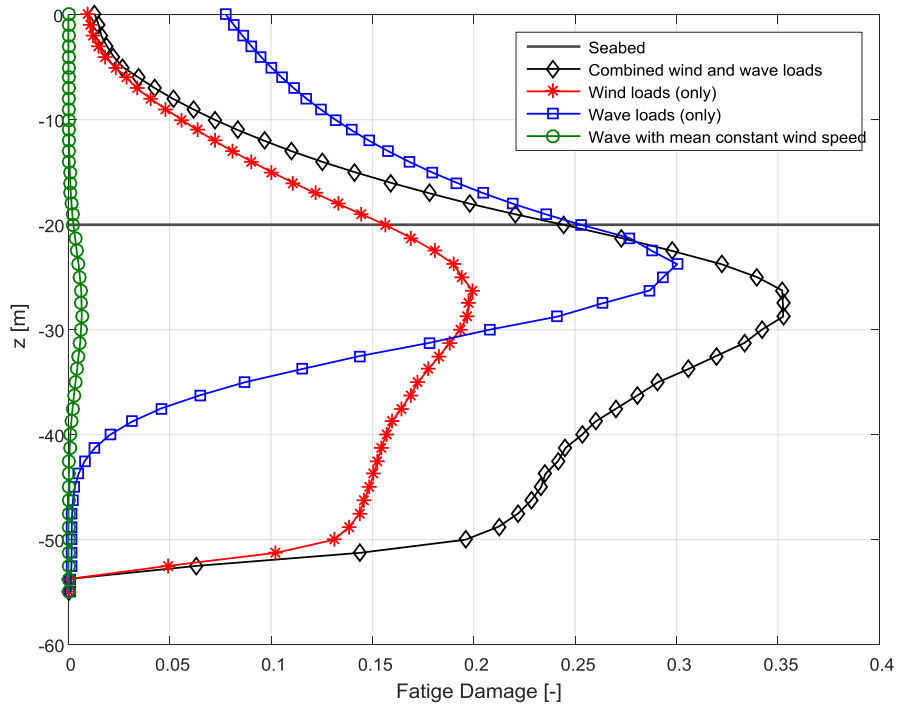

Figure 8.4 Fatigue damage prediction for different design situation (h = 20m)

The fatigue damage distribution for 29 representative sea states is investigated considering the location of maximum fatigue damage (z = -28.75 m) as shown in Figure 8.5. It implies that fatigue damage due to wind is generally higher than wave particularly for lower sea states. The distribution of fatigue damage due to wave implies a power law relation, while correlation with wind speed is more difficult to observe since the sea states are arranged in increasing H_s.

To verify theoretically derived constants, a power curve is fitted between fatigue damage due to wind loads and normalized mean thrust for different sea states. Similarly, a power curve is fitted between fatigue damage and wave parameters H_s and T_p using simulation results that accounts for aerodynamic damping. The curves that best fits the data are shown in Figure 8.6, while Table 8.2 summarizes derived and calculated constants and corresponding coefficient of determination (R^2).

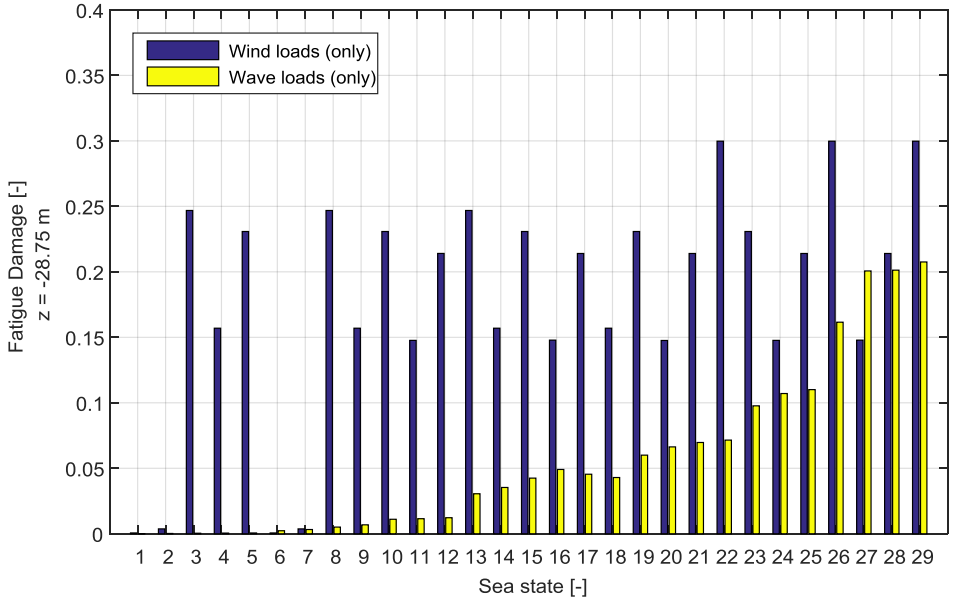

Figure 8.5 Wind and wave fatigue damage distribution for different sea states

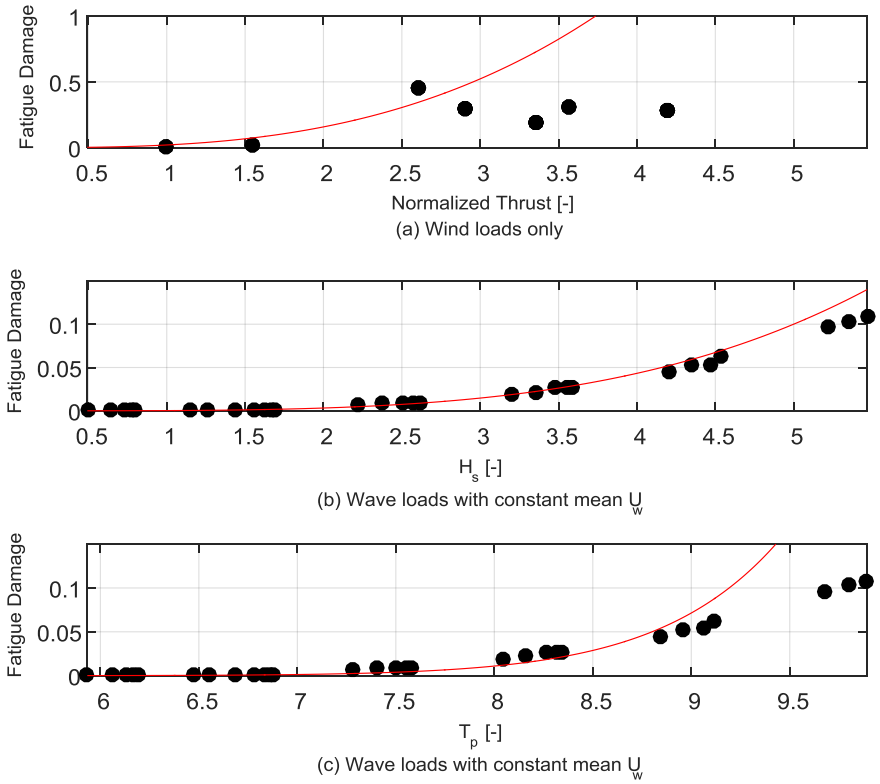

Figure 8.6 Polynomial regression for FDP using damage at z = -28.75

Table 8.2 Comparison between derived and calculated constants

FDP Constant	Derived Value	Calculated	
		Value	Coefficient of determination (R^2)
alpha	0*	1.48	0.48
beta	5.0	3.8	0.99
gamma	-11.0	15.9	0.90

*assumed

Figure 8.6 (a) with R^2 = 0.48 indicates that there is no good correlation between fatigue damage and normalized mean thrust, from which an α value of zero can be assumed. Having **$\alpha = 0$** in FDP removes direct dependence of the parameter to thrust or wind speed.

On the other hand, Figure 8.6 (b) and Figure 8.6 (c) show good correlation with a calculated β = 3.8 and γ = 15.9, but the calculated γ is far from the derived value. Hypothetically, it is expected that higher wave periods cause lower fatigue damage due to associated lower wave frequency. The positive value calculated for γ can be explained by H_s being correlated with T_p, and that fatigue damage increases with H_s more significantly than it decreases with T_p. Thus, there is no direct way of deriving the relationship between fatigue damage and T_p given a set of environmental conditions. A better representation of how T_p affects fatigue damage can be investigated by assuming a single H_s and varying T_p values.

The difference in derived (β = 5) and calculated value (β = 3.8) for parameter β can be attributed to neglecting the wind and wave interaction, and by the derivation assumption that all stress cycles fall at the lower amplitude range defined by the parameter m = -5. The study proceeds with the assumption that fatigue damage is not correlated with wind speed (α = 0) and with the derived relation for H_s and T_p (β = 5, γ = -11). FDP is now defined as:

$$FDP = {H_s}^5 {T_p}^{-11} P \tag{8.19}$$

8.2 Fatigue Damage Prediction

The proposed procedure for calculating fatigue damage and its accuracy are discussed in this section. The influence of including the probability in FDP and the sensitivity of the method for varying number of representative conditions are also discussed.

8.2.1 FDP Procedure

The procedure for calculating the total fatigue damage is illustrated in a flowchart shown in Figure 8.7. A number of representative environmental conditions (N), out of the total number of conditions in the scatter diagram, shall be selected based on the calculated FDP. The accuracy of the proposed method for different number of conditions (N) is investigated in the succeeding sections.

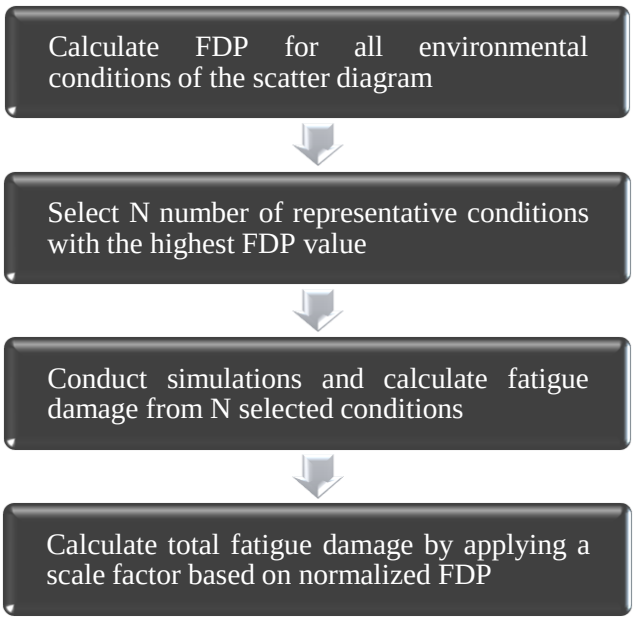

Figure 8.7 FDP procedure for calculating fatigue damage

Initially, the scale factor is calculated only from the probabilities such that the sum of the probabilities of the selected conditions is equal to 1.0. It is found that scaling up the damage

based on normalized FDP, which includes probability of occurrence, gives a better prediction than depending solely on probability. Given the total number of conditions (M) in the scatter diagram and the number of representative conditions (N), the normalized FDP for each condition (i) and the scale factor (SF) can be calculated as follows:

$$(\mathrm{FDP}_{\mathrm{normalized}})_{\mathrm{i}} = \frac{FDP_i}{\sum_{i=1}^{M}(FDP_i)} \tag{8.20}$$

$$\mathrm{SF} = \frac{\sum_{i=1}^{M}(\mathrm{FDP}_{\mathrm{normalized}})_i}{\sum_{i=1}^{N}(\mathrm{FDP}_{\mathrm{normalized}})_i} = \frac{1}{\sum_{i=1}^{N}(\mathrm{FDP}_{\mathrm{normalized}})_i} \tag{8.21}$$

8.2.2 Selection of sea states

Following the FDP approach presented in the preceding section, the representative sea states are selected based on normalized FDP which includes the probability of each sea state. A comparison of normalized FDP calculated with and without including the probability is shown in Figure 8.8. Without including the probability, the normalized FDP tends to be larger at higher sea states due to T_p raised to a power of -11. The selection of higher sea states leads to overestimation of fatigue damage due to a higher base damage and a higher scale factor. On the other hand, including the probability removes this bias and is found to give amore accurate fatigue damage estimate.

The selection of conditions for varying number of representative conditions is illustrated in Figure 8.9. Since FDP only depends on the environmental condition, the selection of sea states is independent of both water depth and structural design.

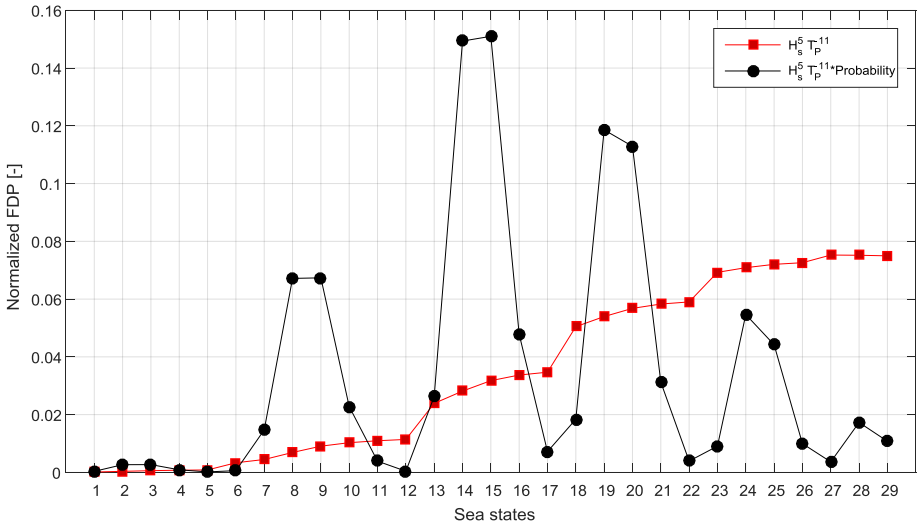

Figure 8.8 Effect of including probability on selection of sea states

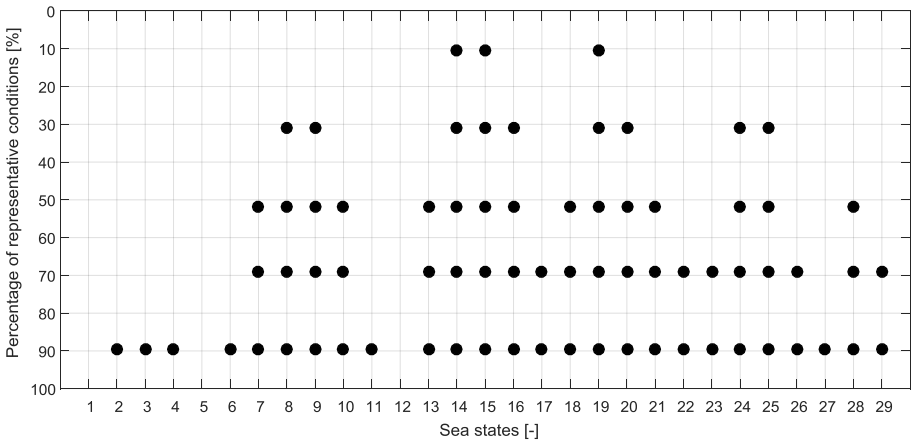

Figure 8.9 Selection of representative sea states according to number of conditions

8.2.3 Results

The FDP approach is used to predict fatigue damage for different number of representative conditions (N = 3, 9, 15, 20, 26) out of 29 sea states. The results are shown in Figure 8.10 with the black line indicating prediction using the complete number of sea states. The fatigue predictions from FDP approach are generally underestimated, but demonstrates good prediction if the number of conditions used are at least 30% of the total number of conditions.

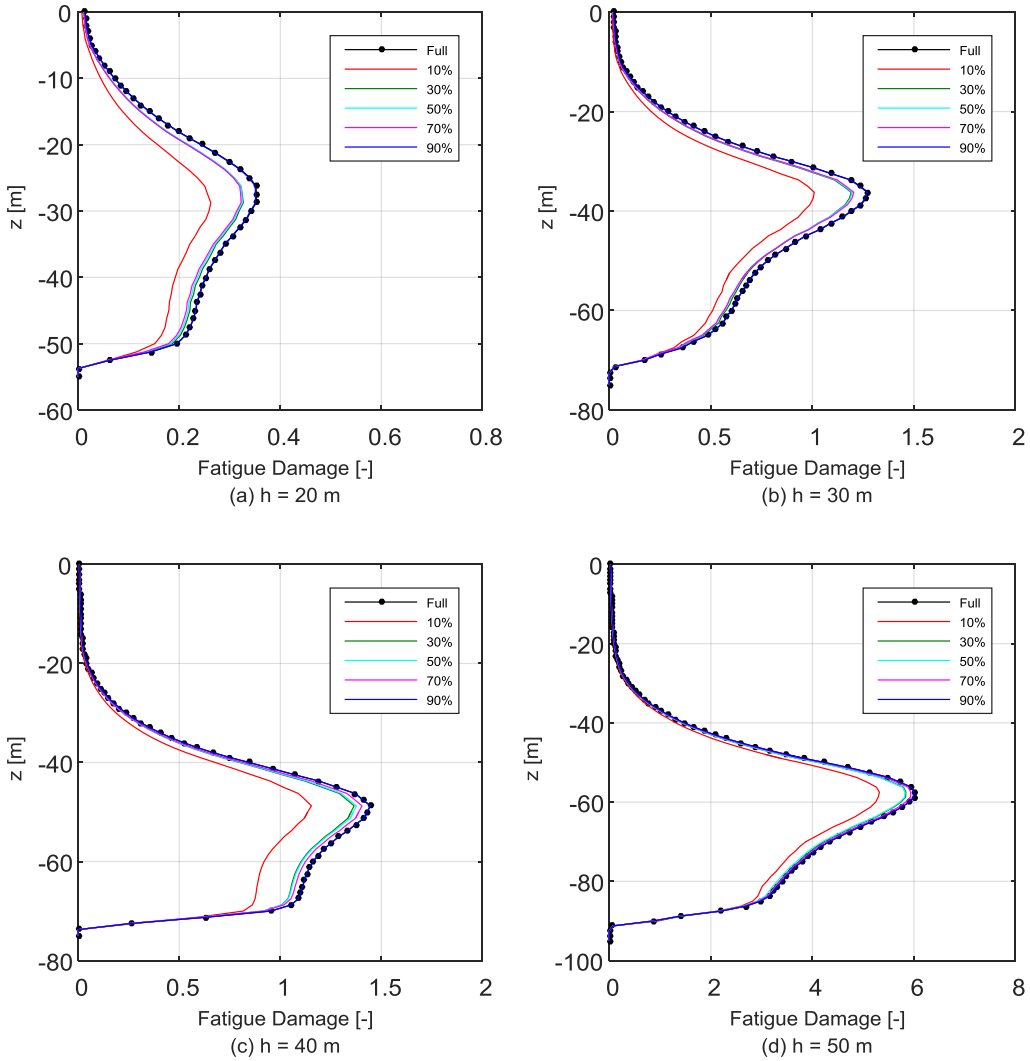

Figure 8.10 Fatigue damage prediction for various N representative conditions

The accuracy of damage prediction at the section where maximum fatigue damage occurs (refer to Table 7.8) is calculated for varying number of representative conditions. The results shown in Figure 8.11 indicate that using more representative conditions generally increases the accuracy of prediction, and that the method is more accurate for higher water depths. Using at least 30% of the total number of conditions results in at least 90% accuracy, but increasing the number of representative conditions from 30% to 70% does not result in a significant increase in accuracy, particularly for water depths 20 m and 30 m.

The corresponding scale factors calculated for varying N are also shown in Figure 8.12. Using at least 50% of the total number of conditions results in a very small scale factor. This indicates that the method of selection is effective in capturing majority of the damage contributions. The scale factor for 50% of the sea states is 1.06, which implies that the selected half of the total number of sea states gives 94% of total damage. Note that the scaling method, being calculated from the selected conditions, results in scale factors that are also independent of both water depth and structural design.

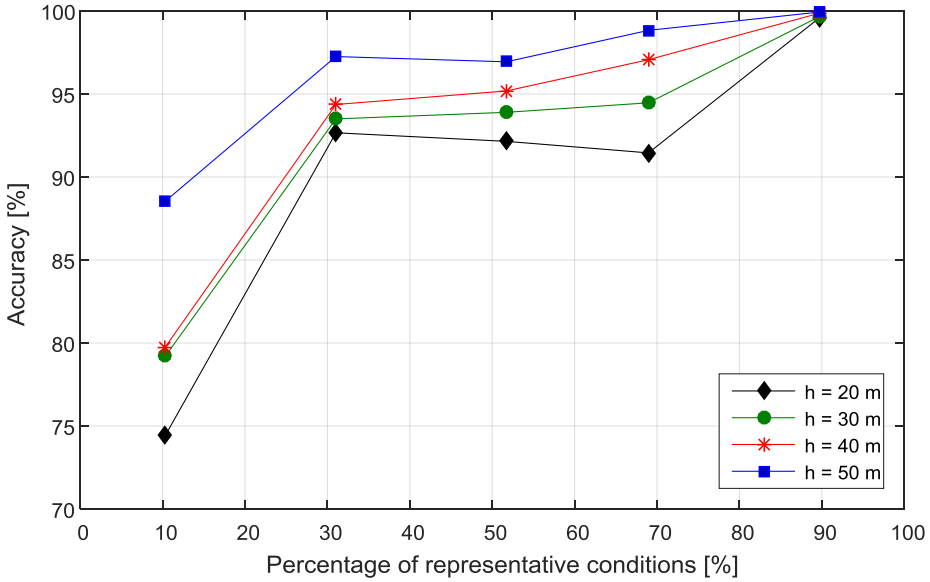

Figure 8.11 Accuracy of prediction at location of maximum damage

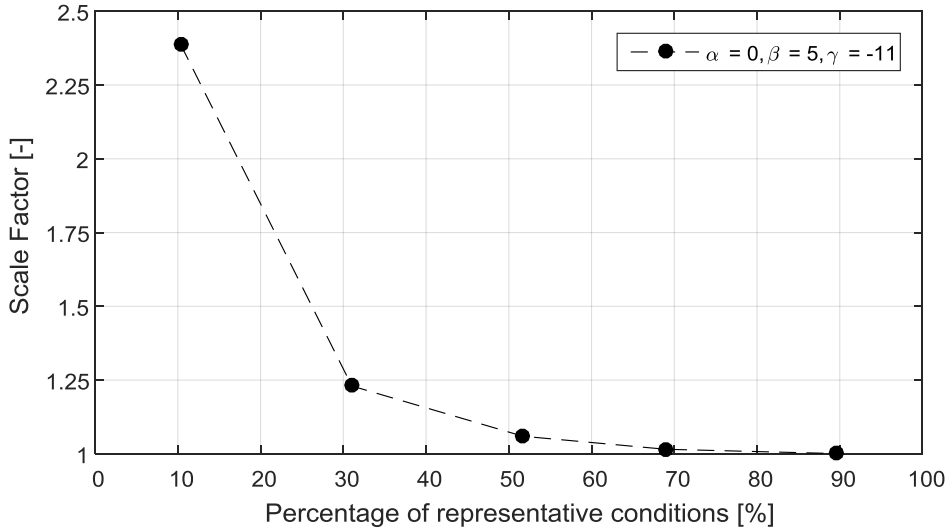

Figure 8.12 Scale factors for different number of representative conditions

8.3 Uncertainties

The proposed FDP approach is a simple method for predicting fatigue damage using less number of conditions from the scatter diagram. The evaluation of the method is based on preliminary designs for four different water depths and environmental conditions specific for the site location. Results show that the method is applicable for varying water depths and different pile diameters. Nonetheless, several uncertainties are identified which are related to variation of the following:

Structural design

Water depths 20 m and 30 m have a pile diameter of 9.0 m, while water depths 40 m and 50 m have a pile diameter of 10.0 m. Although the fatigue estimate given by FDP approach does not seem to be sensitive to the monopile design, a more detailed investigation is necessary. Applicability to other types of support structures, whether floating or bottom-fixed, can also be investigated.

Environmental Conditions

The derived values of constants ($\alpha = 0$, $\beta = 5$, $\gamma = -11$) shall be investigated if also applies to different environments. The variation in scale factors, which mainly depends on probability of occurrences, is also of interest.

Lumping of sea states

The lumping of sea states, particularly the spacing of U_w, H_s and T_p bins, can also affect the results.

Hydrodynamic wave model

The applicability of the procedure with the hydrodynamic wave model can also be investigated, particularly when accounting for diffraction or when using a more sophisticated load model.

Chapter 9.
Conclusion and Further Work

9.1 Conclusion

In this study, a preliminary monopile design was established for water depths 20 m, 30 m, 40 m and 50 m. The design procedure applied includes determining the design elevations, defining the target natural frequency based on DTU 10 MW RWT characteristics, determining the pile embedment depth according to the target natural frequency, optimization of monopile dimensions (D, L) and analysis of the design with respect to foundation strength and stability requirements. Soil-structure interaction was accounted by deriving lateral soil stiffness from Plaxis 3D, while the design loads used in foundation strength and stability analysis were derived from the established design basis specific to the project location. The effect of using soil springs derived from API method was also investigated.

The API method is empirically derived from piles with diameters of approximately 2 meters or less, which implies a flexible pile behaviour. Large-diameter monopiles, on the other hand, are expected to have a rigid behaviour which makes the stiffness values predicted using API method incorrect. The preliminary monopile designs were then based on soil stiffness derived from Plaxis 3D using the Hardening Soil (HS) Model. To reach the target natural frequency, a minimum monopile diameter of 9.0 m is necessary for water depths 20 m and 30 m, while a 10.0 m monopile diameter is necessary for water depths 40 m and 50 m. The required pile embedment depths for water depths 20 m, 30 m, 40 m and 50 m are 35 m, 45 m, 35 m and 45 m, respectively.

The resulting pile deflection verifies a relatively rigid behaviour compared to the API method. Satisfying the vertical tangent or ”zero-toe-kick” criterion, as proposed by GL [8], results in overly conservative pile embedment depth. For large diameter monopiles, pile embedment length can be reduced such that the pile has a rigid behaviour, and still satisfy both natural

frequency and lateral stability requirements. Employing such design approach leads to a more cost-effective design for large diameter piles.

Using lateral soil stiffness derived from API method in the established preliminary design changes the natural frequency from 0.25 Hz to 0.26 Hz, which can be considered as an insignificant effect. This is a result of the natural frequency being highly dependent on the soil stiffness at the shallow depths, where close agreement between API method and FE method can still be observed. Similarly, the magnitude of the maximum bending moment is found to be approximately the same for both FE method and API method. The API method, on the other hand, predicts lower lateral deflections and rotation at seabed by an average of 30% and 19%, respectively. For lateral deflections at the pile toe, higher deviation at greater embedment depths was calculated. It implies that the API overestimates the soil stiffness with depth. The same conclusion was made by Lesny and Wiemann [38] in a similar study of modeling large diameter monopiles using finite element method. Overestimation of soil stiffness leads to underestimation of predicted lateral deflections under design loads, which are necessary criteria in the design process.

With the preliminary design established, ULS analysis was conducted using four defined design load cases and three different wave models. It was found that for large diameter piles, accounting for marine growth does not results in significant increase in combined axial and bending stresses. This is explained by the marine growth thickness being relatively small compared to large monopile dimensions. An average difference in total stress of 0.6% is calculated at the critical point 3 at the seabed cross section.

The comparison of wave kinematics of wave models M1, M2 and M3 show that as water depth increases, both the wave particle acceleration variance and maximum acceleration of 1st order wave models approach that of the 2nd order wave model such that the values are almost identical at 50 m water depth. Considering the design load case with the 50-year maximum wave height (Hs = 9.9 m, Tp = 14 s) and a water depth of 20 m, the predicted mean maximum acceleration by the 2nd order wave model (7 m/s^2) is about 75% higher than the 1st order wave model (4 m/s^2) prediction.

For water depths 20 m and 30 m, the governing design load case is ULS 3 which corresponds to the 50-year design condition with maximum wind speed. But for higher water depths 40 m and 50 m, the governing design load case is ULS 4, which corresponds to the 50-year design condition with maximum H_s. Such shift in governing design load case with increasing water depth is reasonable, considering that ULS 4 tends to generate relatively higher loads with higher water depth. It can be concluded that M3 generally gives the highest ULS load, followed by the M2 and M1, respectively. M3 as a governing model can be explained by the sum frequency effect associated with 2^{nd} order waves and by the wave kinematics, particularly the wave particle acceleration where M3 has the highest maximum value.

The investigation of wave kinematics also shows that 1st order and 2nd order wave models predict more comparable wave particle acceleration with increasing water depth. This explains results of 1^{st} order and 2^{nd} order models giving closer predictions of maximum bending moments as water depth increases. Considering ULS 4, the ratio of predicted ultimate load using a 2nd order wave model to that of the 1st order model for water depths 20 m, 30 m, 40 m and 50 m are 1.9, 1.5, 1.2 and 1.1, respectively.

After the ULS analysis, the design evaluation proceeded with the FLS analysis. The validity of the assumed drag and inertia coefficients were investigated. Large diameter pile designs generally result in very high R_e and low values of K_C. For K_C values less than 3.0 where most environmental conditions lie, added mass coefficients can be assumed independent of K_C number. Thus, the inertia coefficient (C_M) can be assumed equal to **2.0**. The drag coefficients, on the other hand, are more sensitive to variation in small K_C values and also differ between smooth and rough surfaces. An intermediate value of **0.9**, which lies in the middle of the range of possible values, is a reasonable assumption in this case.

Among the four monopile designs for each water depth, only the design for the 20 m water depth is satisfactory considering FLS. A frequency-domain estimate assuming narrow-banded spectra verifies the time-domain calculation. The FLS analysis is generally less sensitive to wave models as compared to ULS analysis. As water depth increases, contribution from higher sea states becomes larger, implying that hydrodynamic loads become more significant.

Lastly, a Fatigue Damage Parameter (FDP) is established to correlate fatigue damage of an environmental condition with parameters Thrust, H_s and T_p. The derived theoretical value of the constants **α**, **β** and **γ** are **0**, **-5** and **-11** respectively. The fatigue predictions from FDP procedure generally demonstrates good prediction if the number of conditions used are at least 30% of the total number of conditions. Using at least 30% of the total number of conditions results in at least 90% accuracy, but increasing the number of representative conditions from 30% to 70% does not result in a significant increase in accuracy. In applying the FDP approach, it is recommended to use at least 50% of the total number of conditions as it results in a very small scale factor, indicating that the method of selection is effective in capturing majority of the damage contributions.

9.2 Further Work

Several improvements can be done to reduce uncertainties in the results and to improve the study. With regards to soil modeling, the use of other soil models, such as the Linear Elastic (LE) and Mohr-Coulomb (MC) model, can be investigated and compared the currently used Hardening Soil (HS) model. In addition to the lateral soil stiffness, rotational stiffness can also be derived in Plaxis 3D. The rotational stiffness can also be implemented in Riflex to have a more accurate model. The preliminary design of the monopile is done assuming a uniform sand layer. The effect of other soil types or combinations of different soil types on the monopile design can also be investigated. The effect of scour protection in soil stiffness is also neglected in the study. It is expected that the presence of scour protection could increase the stiffness in shallow depths of the soil.

With regards to the optimization procedure, the monopile design is optimized based on a constant pile diameter-thickness ratio of 80. The optimization of the pile thickness can also be done. Changing the monopile thickness, though, changes the pile lateral deflection behaviour, which means that soil P-Y curves need to be updated. In addition, the transition piece is accounted as a point mass in the Riflex model. The detailed design of the transition piece, including the grout connection, would lead to a more accurate overall natural frequency and structural response.

For ULS analysis, higher order wave models, such as the second order FNV-method, can be implemented to verify magnitude of predicted ultimate loads and stresses.

For FLS analysis, further investigation is recommended to explain how M1 governs FLS in intermediate sea states, particularly the possibility of having increased hydrodynamic damping when forces are integrated up to instantaneous water line. The effect of the operating or non-operating wind turbine can also be studied. With regards to the effect of diffraction on fatigue life, there is no conclusion can be made from the calculated total force with MacCamy-Fuchs modification of inertia force. Time domain simulations are necessary to verify how much fatigue damage could be reduced. Other factors, such as the wind-wave misalignment, can also be investigated. It is expected that a higher damage would occur due to the loss of aerodynamic damping, particularly in the perpendicular direction

Lastly, the accuracy and applicability of the FDP approach with other types of support structures, floating or bottom-fixed, can also be investigated. Its applicability to other site-specific environmental conditions and sensitivity to lumping of sea states are also of interest.

References

1. EWEA, *The European offshore wind industry - key trends and statistics 2014*. 2015.

2. EWEA, *Wind energy scenarios for 2030*. 2015.

3. Bhattacharya, S., *Challenges in Design of Foundations for Offshore Wind Turbines.* Engineering and Technology Reference, 2014.

4. de Vries, W., *Final Report WP4.2: Support Structure Concepts for Deep Water*, in *WP4: Offshore Foundations and Support Structures*. 2011, Delft University of Technology: Delft, The Netherlands.

5. DNV, *OFFSHORE STANDARD DNV-OS-J101 - Design of Offshore Wind Turbine Structures*. 2014, DET NORSKE VERITAS.

6. Tempel, J.v.d., *Design of Support Structures for Offshore Wind Turbines*, in *Offshore Engineering*. 2006, Technische Universiteit Delft.

7. IEC, I.E.C., *IEC 61400-3, Wind turbines – part 3: Design requirements for offshore wind turbines*2009: Geneva, Switzerland.

8. GL, *Guideline for the Certification of Offshore Wind Turbines*. 2012, GL Renewables Certification, Hamburg.

9. Krolis, V.D., G.L. van der Zwaag, and W. de Vries, *Determining the Embedded Pile Length for Large-Diameter Monopiles*, in *Marine Technology Society Journal, Mar. Technol. Soc. J, Mar Tech Sj, Mar Technol Soc J*. 2010, MARINE TECHNOLOGY SOC INC. p. 24-31.

10. Arshad, M. and B.C. O'Kelly, *Analysis and Design of Monopile Foundations for Offshore Wind-Turbine Structures.* Marine Georesources & Geotechnology, 2015.

11. API, *Recommended Practice for Planning, Designing and Constructing Fixed Offshore Platforms—Working Stress Design*. 2003, API Publishing Services: Washington, D.C.

12. S. P. H. Sørensen , K.T.B., M. Møller, *Evaluation of Load-Displacement Relationships for Large-Diameter Piles*, in *Faculties of Engineering, Science and Medicine*. 2009, Aalborg University.

13. Augustesen, A.H., et al., *Numerical modelling of large-diameter steel piles at Horns Rev.* Proceedings of the 12th International Conference on Civil, Structural and Environmental Engineering Computing, 2009.

14. Versteijlen, W.G.v.D., K. N.; Metrikine, A. V.; Hamre, L., *Assessing the small-strain soil stiffness for offshore wind turbines based on in situ seismic measurements.* Journal of Physics. Conference Series, J Phys Conf, J Phys Conf Ser, J. Phys. Conf. Ser, J Phys, Journal of Physics, 2014. 524(1).

15. PLAXIS, *PLAXIS 2015*. 2015: The Netherlands.

16. PLAXIS, *Material Models Manual*. 2015.

17. Hanssen, S.B., *On the determination of spring stiffness for laterally loaded piles*, in *unpublished manuscript*, N.U.o.S.a. Technology, Editor. 2016: Trondheim, Norway.

18. Gerolymos, N. and G. Gazetas, *Winkler model for lateral response of rigid caisson foundations in linear soil.* Soil Dynamics and Earthquake Engineering, Soil Dyn. Earthq. Eng, Soil Dyn Ea, Soil Dyn Earthq Eng, Soil Dynam Earthquake Eng, Soil Dyn Earthquake Eng, Soil Dynamics and Earthquake Engineering, 2006. 26(5): p. 347-361.

19. PLAXIS, *Scientific Manual*. 2015.

20. Sumer, B.M. and J. Fredsøe, *Hydrodynamics around cylindrical structures*. 1997: World scientific.

21. DNV, *RECOMMENDED PRACTICE DNV-RP-C205 - ENVIRONMENTAL CONDITIONS AND ENVIRONMENTAL LOADS* 2007.

22. Sarpkaya, T., *IN-LINE AND TRANSVERSE FORCES ON CYLINDERS IN OSCILLATORY FLOW AT HIGH REYNOLDS-NUMBERS.* Journal of Ship Research, J. Ship Res, J Ship Res, 1977. 21(4): p. 200-216.

23. Faltinsen, O.M., *Sea loads on ships and offshore structures*. 1998: Cambridge University Press.

24. Veldkamp, H.K. and J. van der Tempel, *Influence of wave modelling on the prediction of fatigue for offshore wind turbines.* Wind Energy, Wind Energy, Wind Energy, 2005. 8(1): p. 49-65.

25. Haver, S.K., C.T. Stansberg, and O.T. Gudmestad, *Kinematics under extreme waves.* Journal of Offshore Mechanics and Arctic Engineering, 2008. 130(2).

26. Greco, M., *TMR 4215: Sea Loads*. 2012, Department of Marine Hydrodynamics, NTNU.

27. Bachynski, E. and O. Harald, *HYDRODYNAMIC MODELING OF LARGE-DIAMETER BOTTOM-FIXED OFFSHORE WIND TURBINES.* Ocean, Offshore and Arctic Engineering OMAE2015, 2015.

28. Yeter, B., Y. Garbatov, and C. Guedes Soares, *Fatigue damage assessment of fixed offshore wind turbine tripod support structures.* Engineering Structures, Eng. Struct, Eng Struct, Engineering Structures the Journal of Earthquake Wind and Ocean Engineering, 2015. 101: p. 518-528.

29. DNV, *Fatigue Design of Offshore Steel Structure*. 2010, DET NORSKE VERITAS.

30. Trumars, J.M.V., N.J. Tarp-johansen, and T. Krogh, *"Copenhagen Offshore Wind 2005" The Effect of Wave Modelling on Offshore Wind Turbine Fatigue Loads.* 2014.

31. C. Bak, F.Z., R. Bitsche, T. Kim, A. Yde, L.C. Henriksen, P.B. Andersen, A. Natarajan, M.H. Hansen, *Design and performance of a 10 MW wind turbine.* DTU Wind Energy Report, 2013(I-0092).

32. Lin Li, Z.G., Torgeir Moan, *Environmental Data at Five Selected Sites for Concept Comparison*, in *Marine Renewable Integrated Application Platform*. 2012, Centre for Ships and Ocean Structures, Norwegian University of Science and Technology: Norway.

33. Li, L., Z. Gao, and T. Moan, *Joint environmental data at five European offshore sites for design of combined wind and wave energy devices.* Proceedings of the International Conference on Offshore Mechanics and Arctic Engineering - Omae, Proc Int Conf Offshore Mech Arct Eng - Omae, 2013. 8.

34. DNV, *OFFSHORE STANDARD DNV-OS-E301 - Position Mooring*, D.N. VERITAS, Editor. 2010.

35. Kelley, N.D.J., B.J. , *Overview of the TurbSim Stochastic Inflow Turbulence Simulator*. 2007, National Renewable Energy Laboratory.

36. Kelley, N.D.J., B.J. ; Scott, G.N. ; Bialasiewicz,J.T. ; Redmond,L.S., *The Impact of Coherent Turbulence on Wind Turbine Aeroelastic Response and Its Simulation*, in *WindPower 2005*. 2005, NREL: Denver, Colorado.

37. Section, O.E., *Monopile Design - Part I*, in *Lecture Notes on Offshore Wind Support Structures (OE5665)*. 2015, Delft University of Technology.

38. Lesny, K. and J. Wiemann, *Finite-Element-Modelling of Large Diameter Monopiles for Offshore Wind Energy Converters*, in *GeoCongress 2006*. 2006. p. 1-6.

Appendix A. Extraction of Soil Springs

This section presents the shape functions and integration points employed in extraction of the non-linear soil PY curves.

Table A.1 summarizes the weighting factors and defines the position of the integration points in terms of the local coordinates ($\boldsymbol{\xi}, \boldsymbol{\eta}$), while Figure A.1 shows the local numbering and the position of nodes and integration points. The auxiliary coordinates (ζ), shape functions (N_j), stresses for each Gaussian integration point ($\sigma_{x,i}$) and representative stress in each element in x-direction (σ_x) defined by the following expressions:

$$\zeta = 1 - \xi - \eta \tag{A.1}$$

$$\begin{aligned} N_1 &= \zeta(2\zeta - 1) \\ N_2 &= \xi(2\xi - 1) \\ N_3 &= \eta(2\eta - 1) \\ N_4 &= 4\zeta\,\xi \\ N_5 &= 4\,\xi\eta \\ N_6 &= 4\eta\zeta \end{aligned} \tag{A.2}$$

$$\sigma_{x,i} = \sum_{j=1}^{6} N_j \sigma_{x,j} \tag{A.3}$$

$$\sigma_x = \sum_{i=1}^{3} \sigma_{x,i} w_i \tag{A.4}$$

Table A.1 Position and weight factors of integration points
Applied in a 3-point Gaussian integration for 6-node triangular elements [19]

Point	ξ_i	η_i	w_i
1	1/6	2/3	1/3
2	1/6	1/6	1/3
3	2/3	1/6	1/3

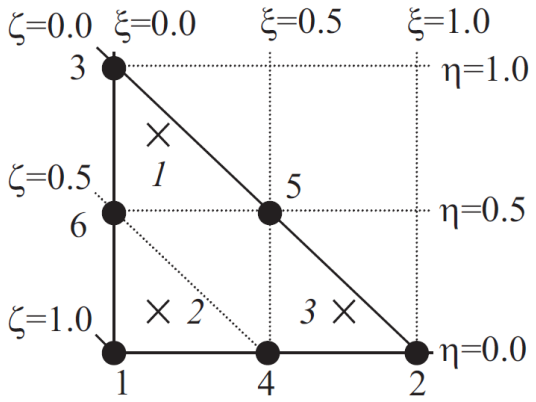

Figure A.1 6-noded triangular element
Local numbering and positioning of nodes (•) and integration points (x) of the element [19]

The force contribution from each element in the x-direction is calculated by multiplying the representative stress by the element area, which is defined in terms of the three corner nodes of the element as:

$$A = \frac{1}{2}\sqrt{\begin{vmatrix} x_1 & x_2 & x_3 \\ y_1 & y_2 & y_3 \\ 1 & 1 & 1 \end{vmatrix}^2 + \begin{vmatrix} y_1 & y_2 & y_3 \\ z_1 & z & z_3 \\ 1 & 1 & 1 \end{vmatrix}^2 + \begin{vmatrix} z_1 & z_2 & z_3 \\ x_1 & x_2 & x_3 \\ 1 & 1 & 1 \end{vmatrix}^2} \tag{A.5}$$

Appendix B. Non-linear PY curves

This section presents all the nonlinear PY curves calculated and post-processed from Plaxis 3D. These PY curves are used as main inputs for the monopile models implemented in SIMA Riflex.

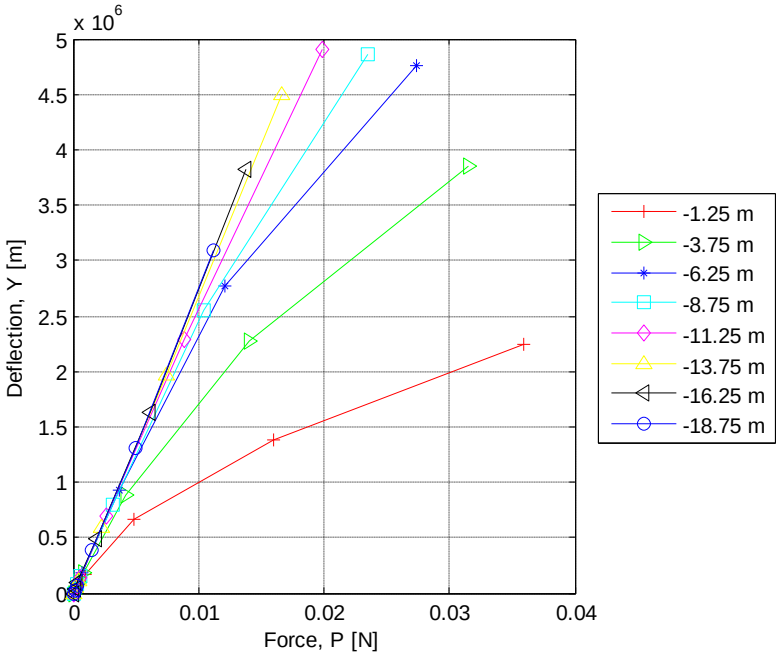

Figure B.1 Nonlinear PY curves set 1 (Pile diameter = 9.0 m, Length = 9D)

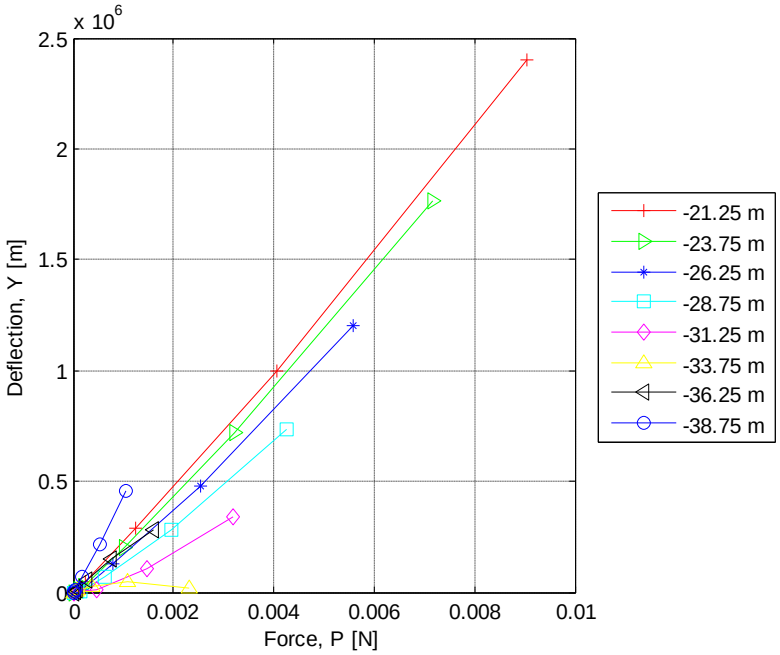

Figure B.2 Nonlinear PY curves set 2 (Pile diameter = 9.0 m, Length = 9D)

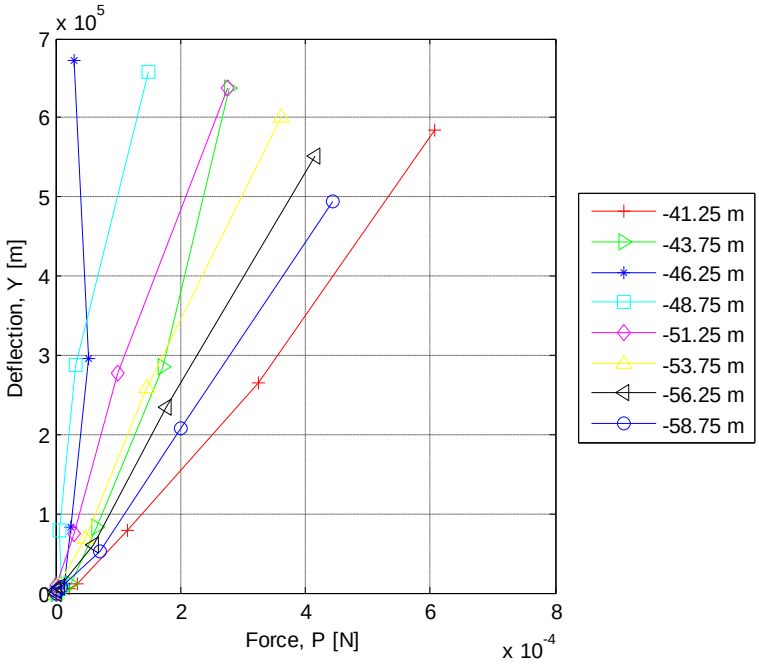

Figure B.3 Nonlinear PY curves set 3 (Pile diameter = 9.0 m, Length = 9D)

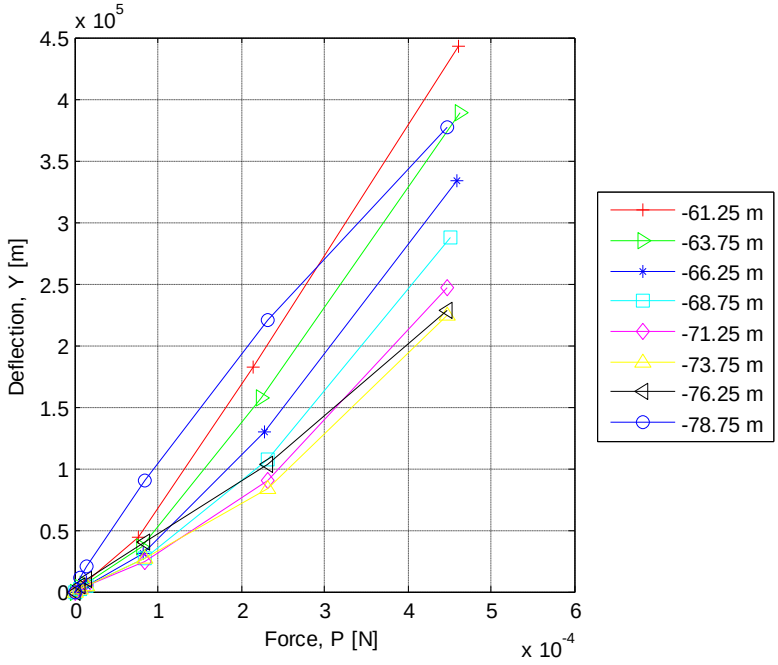

Figure B.4 Nonlinear PY curves set 4 (Pile diameter = 9.0 m, Length = 9D)

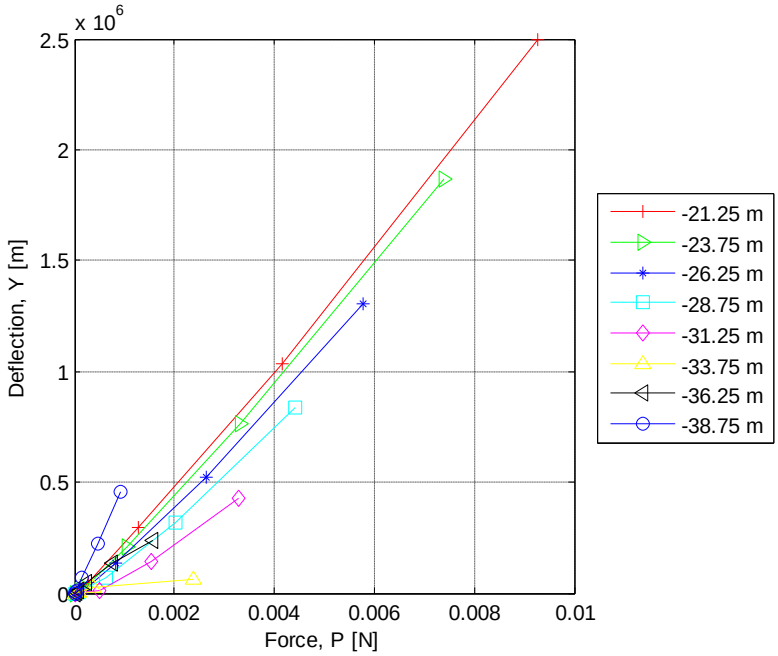

Figure B.5 Nonlinear PY curves set 1 (Pile diameter = 9.0 m, Length = 6D)

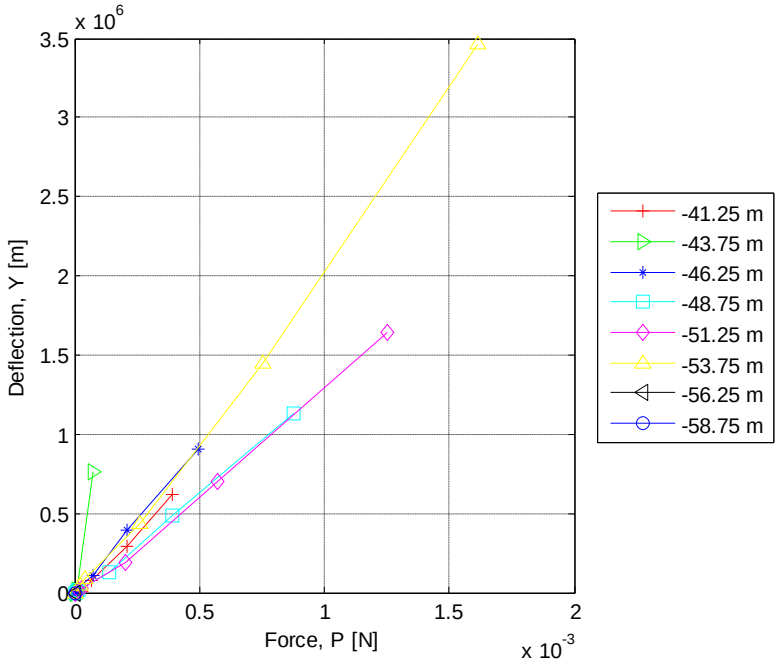

Figure B.6 Nonlinear PY curves set 2 (Pile diameter = 9.0 m, Length = 6D)

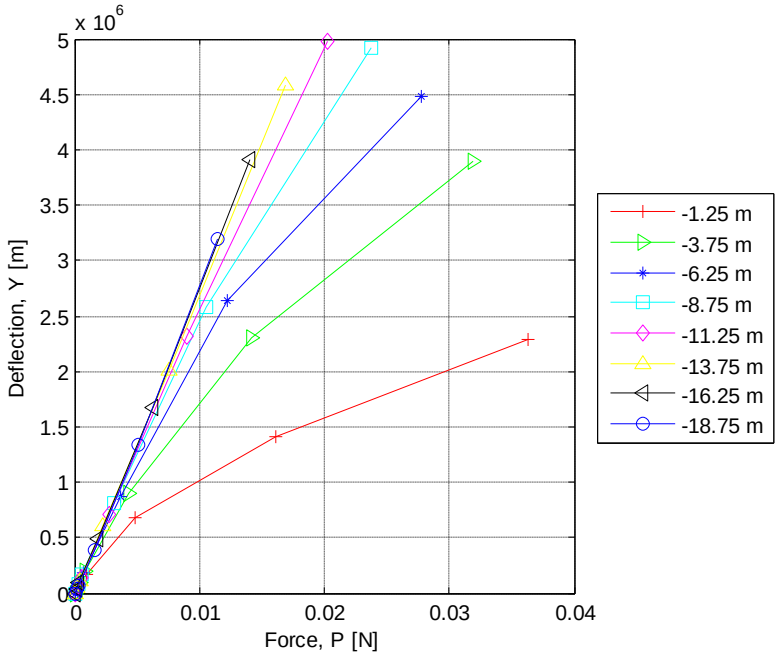

Figure B.7 Nonlinear PY curves set 3 (Pile diameter = 9.0 m, Length = 6D)

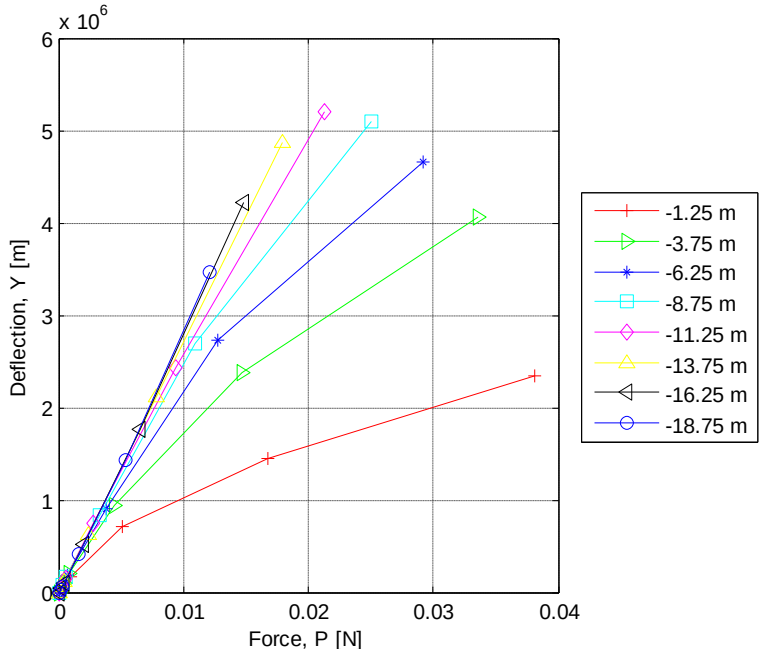

Figure B.8 Nonlinear PY curves set 1 (Pile diameter = 9.0 m, Length = 5D)

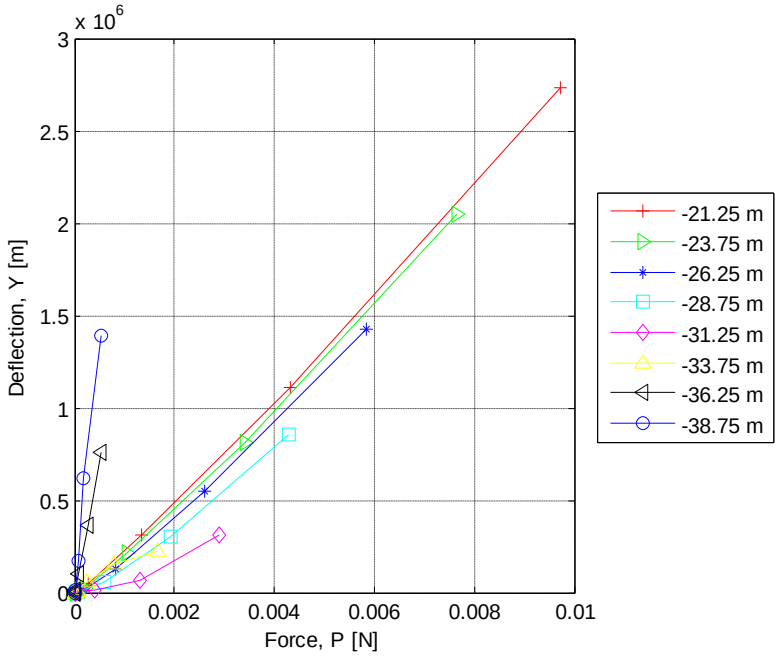

Figure B.9 Nonlinear PY curves set 2 (Pile diameter = 9.0 m, Length = 5D)

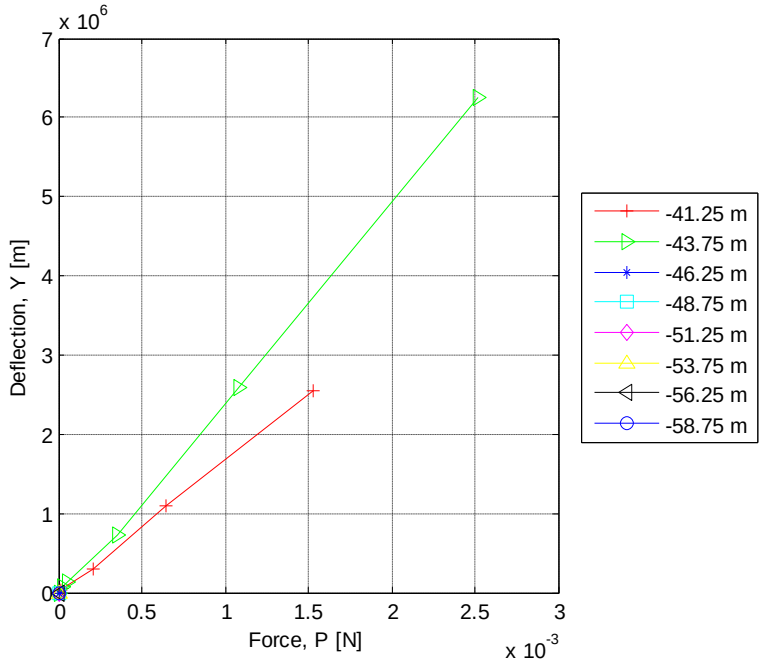

Figure B.10 Nonlinear PY curves set 3 (Pile diameter = 9.0 m, Length = 5D)

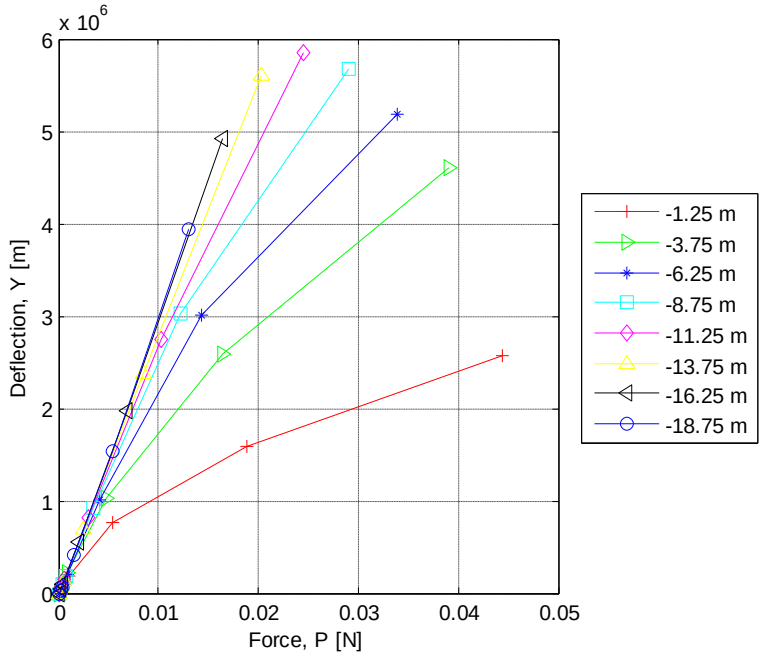

Figure B.11 Nonlinear PY curves set 1 (Pile diameter = 9.0 m, Length = 4D)

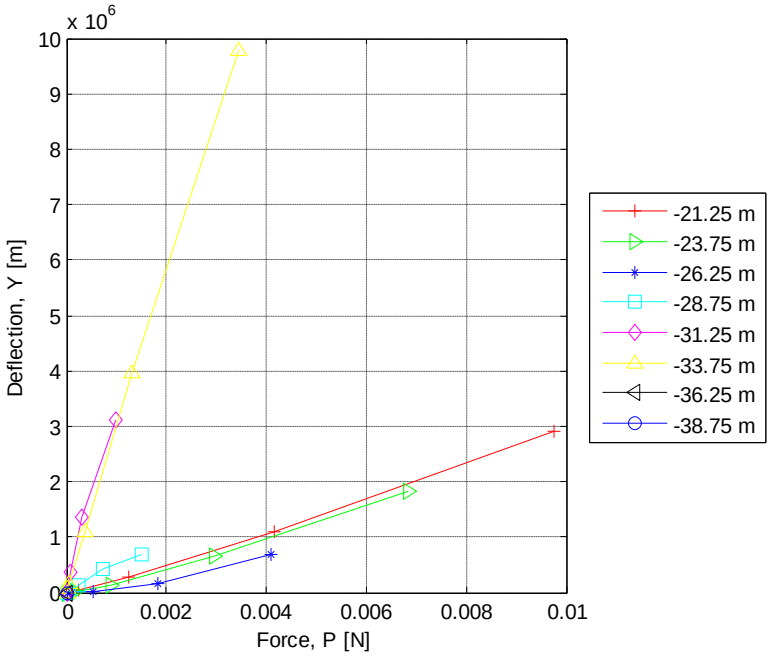

Figure B.12 Nonlinear PY curves set 2 (Pile diameter = 9.0 m, Length = 4D)

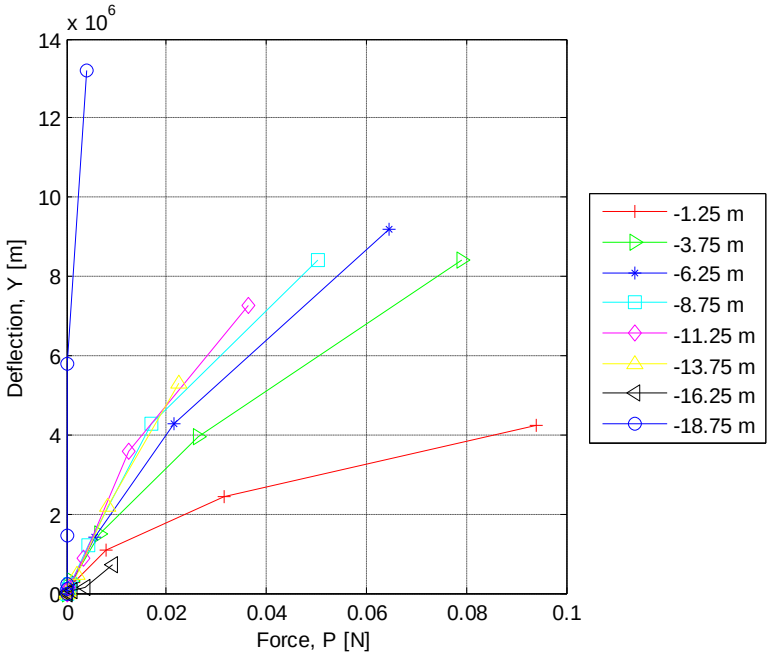

Figure B.13 Nonlinear PY curves set 1 (Pile diameter = 9.0 m, Length = 2D)

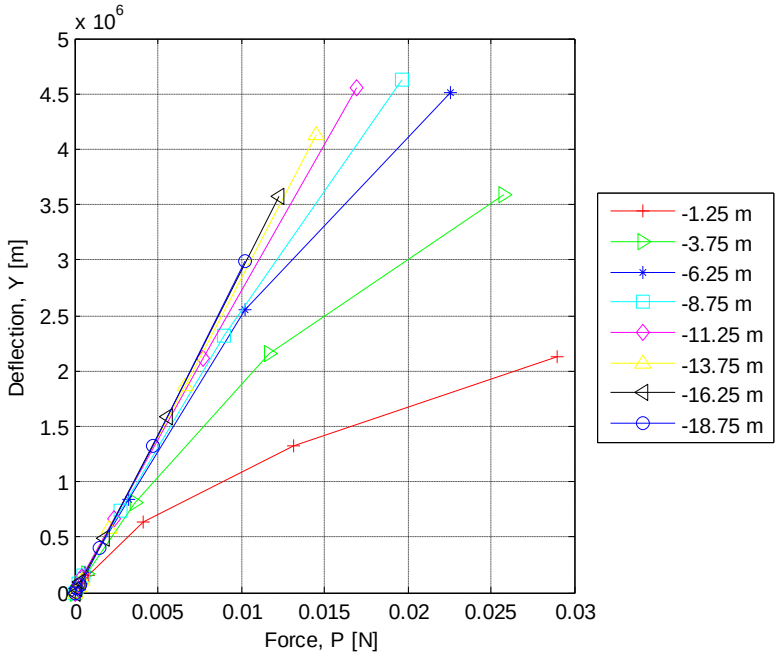

Figure B.14 Nonlinear PY curves set 1 (Pile diameter = 10.0 m, Length = 8D)

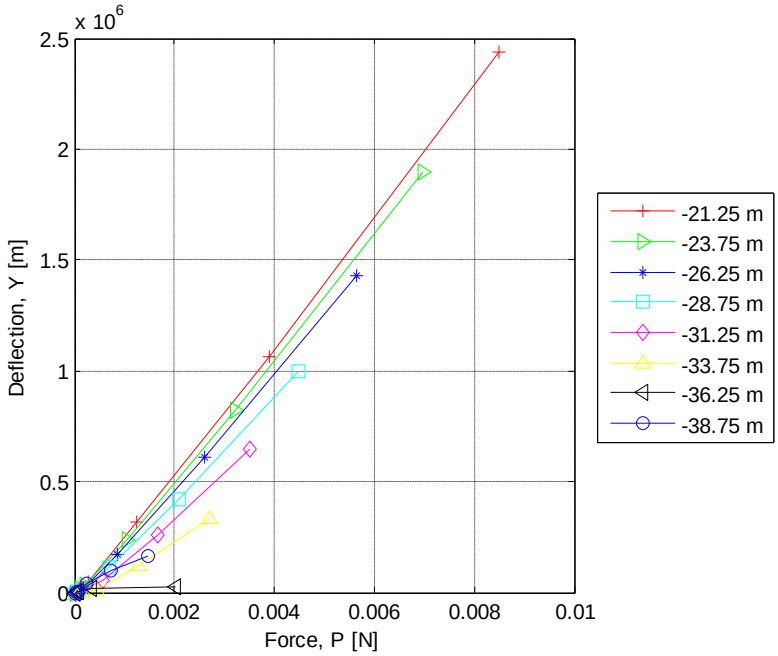

Figure B.15 Nonlinear PY curves set 2 (Pile diameter = 10.0 m, Length = 8D

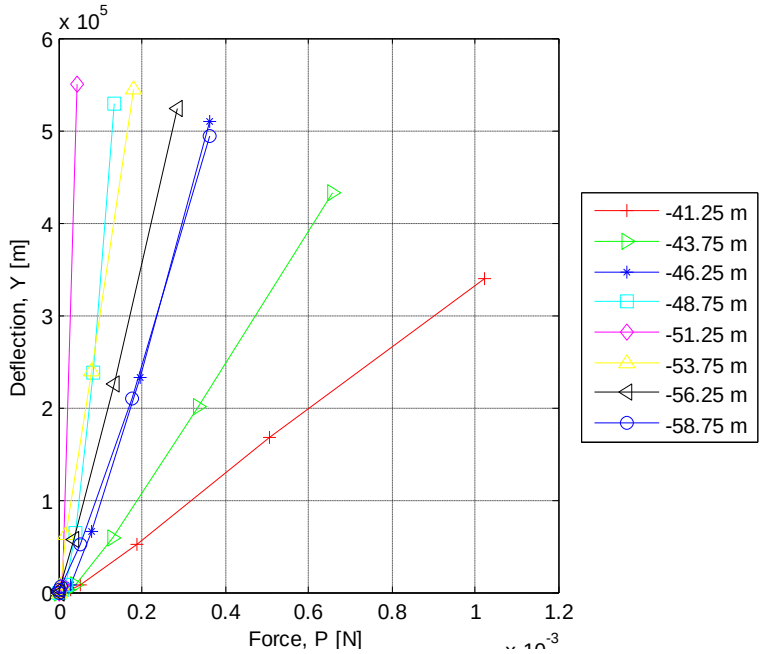

Figure B.16 Nonlinear PY curves set 3 (Pile diameter = 10.0 m, Length = 8D)

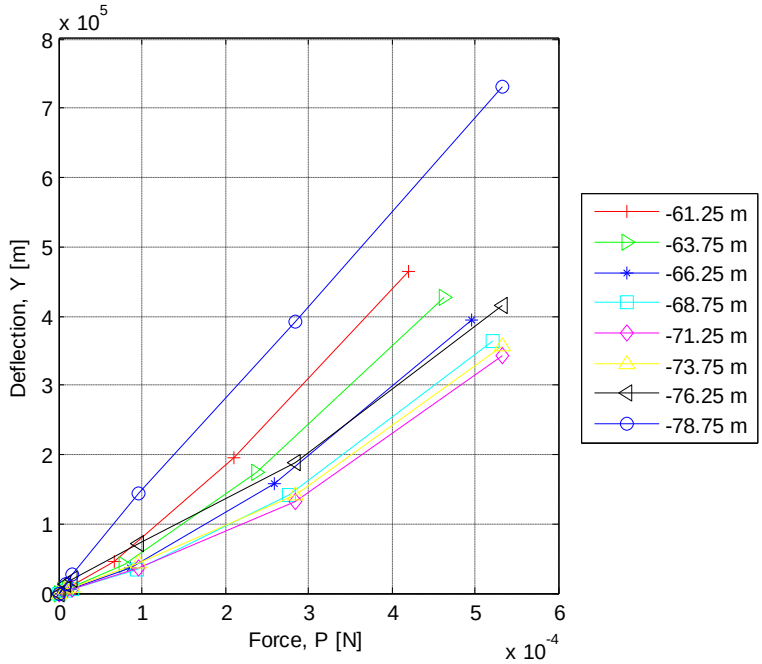

Figure B.17 Nonlinear PY curves set 4 (Pile diameter = 10.0 m, Length = 8D)

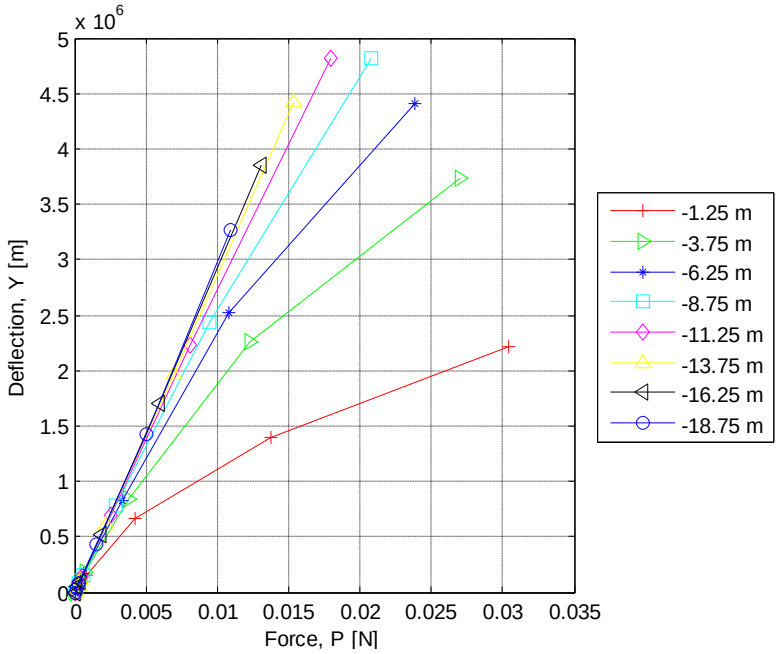

Figure B.18 Nonlinear PY curves set 1 (Pile diameter = 10.0 m, Length = 5D)

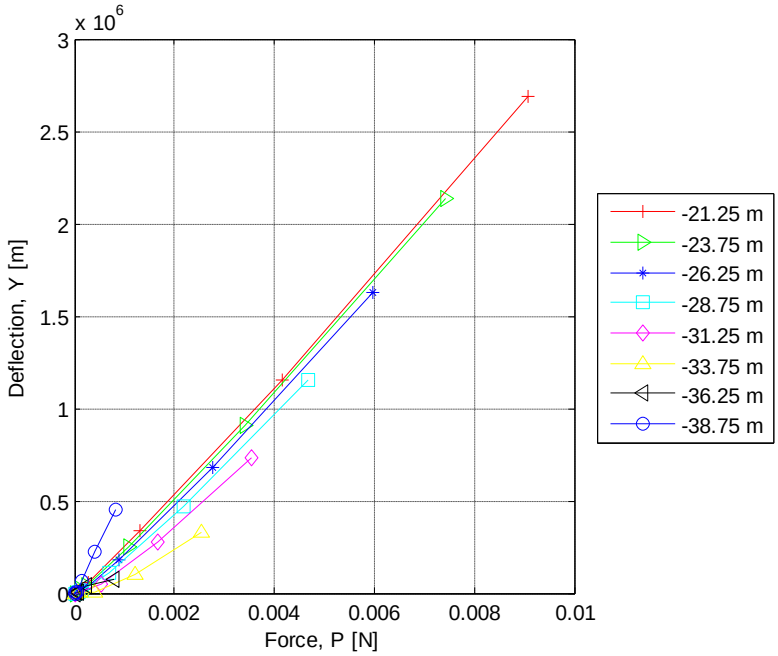

Figure B.19 Nonlinear PY curves set 2 (Pile diameter = 10.0 m, Length = 5D)

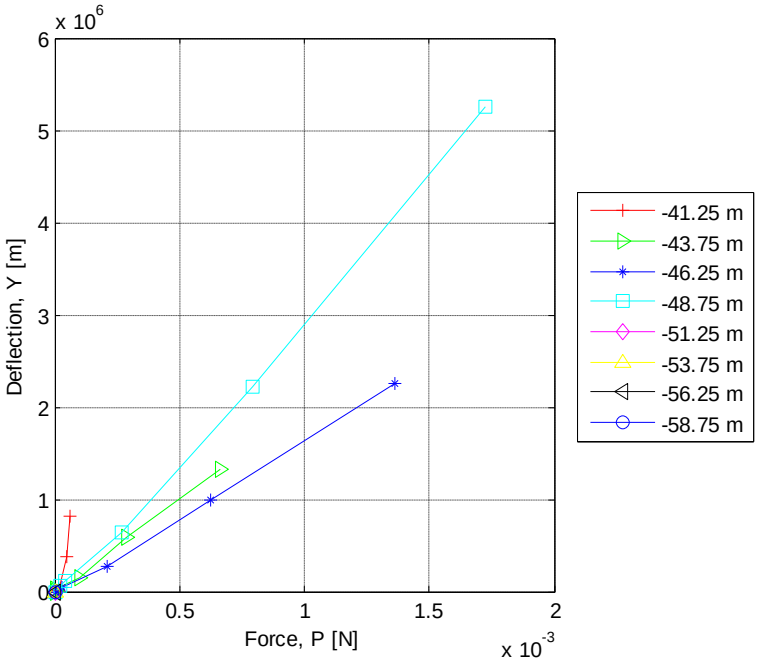

Figure B.20 Nonlinear PY curves set 3 (Pile diameter = 10.0 m, Length = 5D)

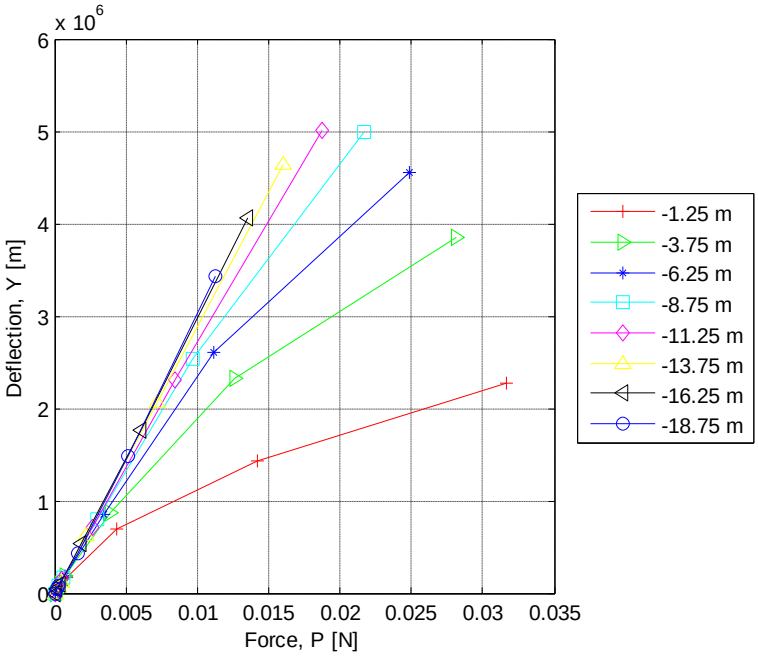

Figure B.21 Nonlinear PY curves set 1 (Pile diameter = 10.0 m, Length = 4.5D)

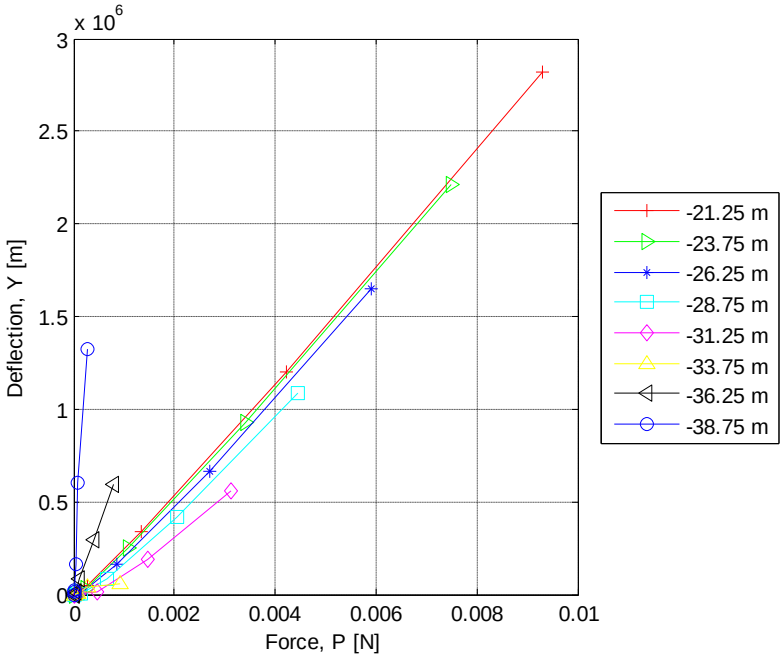

Figure B.22 Nonlinear PY curves set 2 (Pile diameter = 10.0 m, Length = 4.5D)

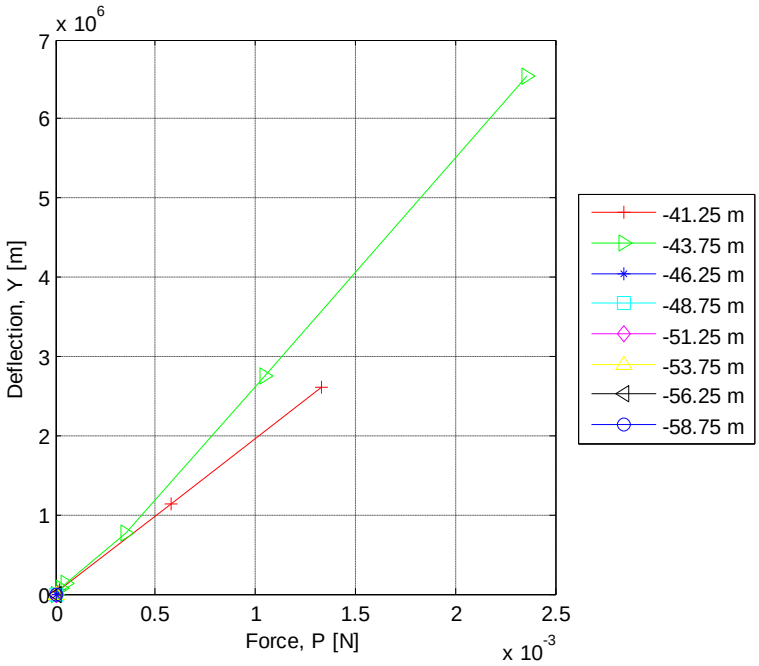

Figure B.23 Nonlinear PY curves set 3 (Pile diameter = 10.0 m, Length = 4.5D)

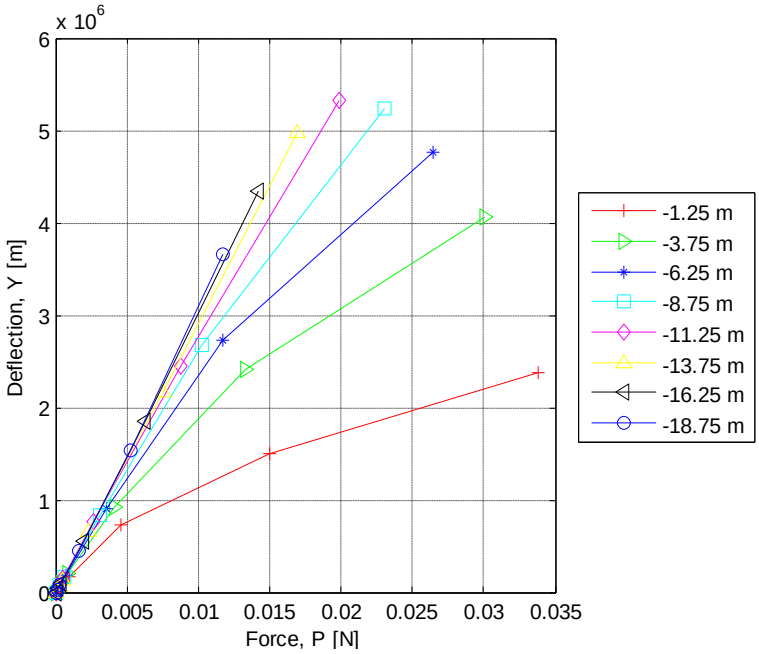

Figure B.24 Nonlinear PY curves set 1 (Pile diameter = 10.0 m, Length = 4D)

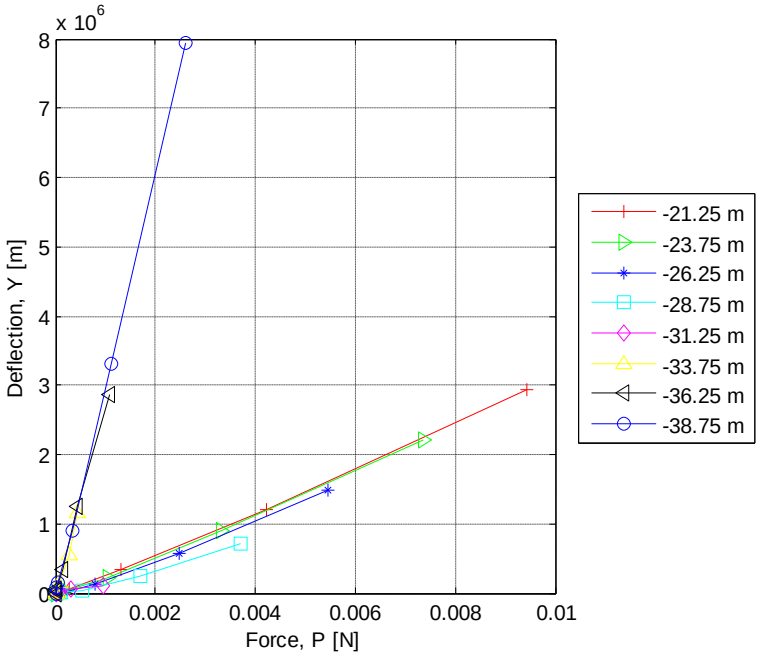

Figure B.25 Nonlinear PY curves set 2 (Pile diameter = 10.0 m, Length = 4D)

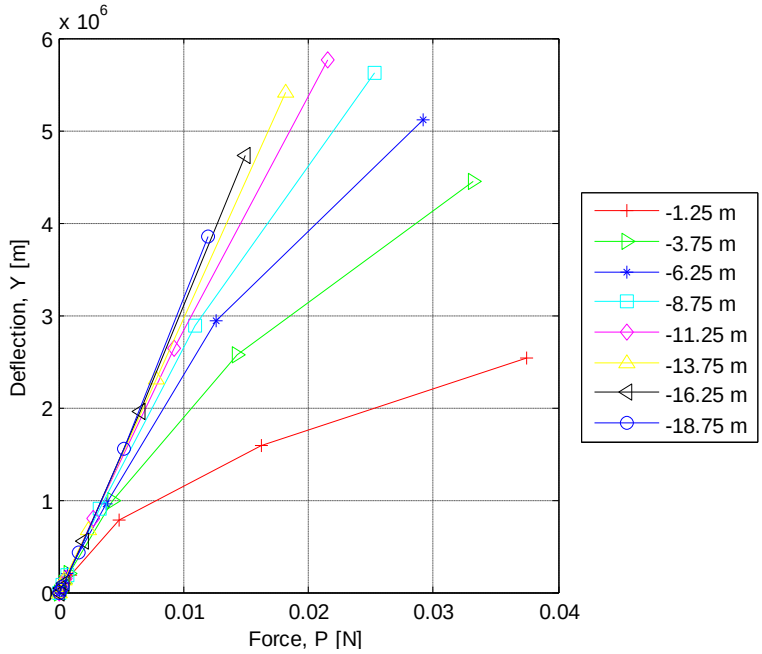

Figure B.26 Nonlinear PY curves set 1 (Pile diameter = 10.0 m, Length = 3.5D)

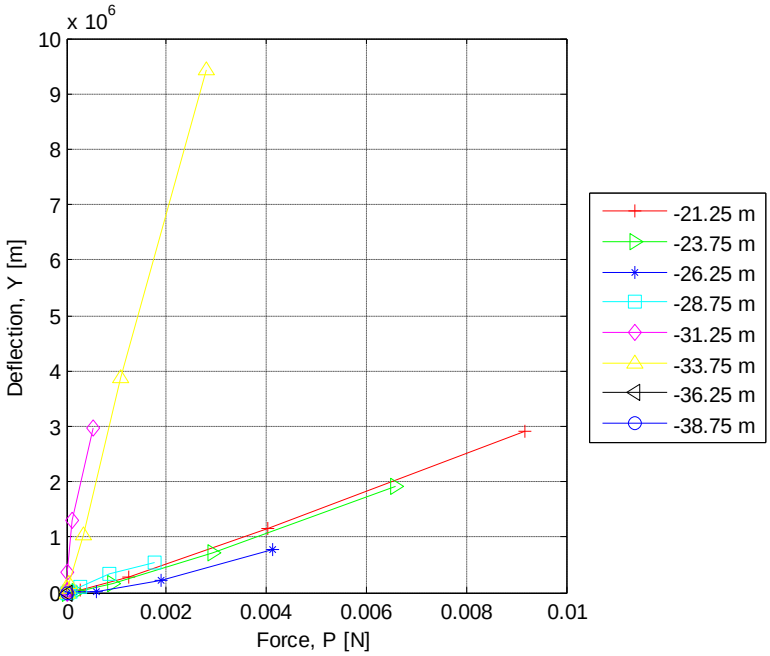

Figure B.27 Nonlinear PY curves set 2 (Pile diameter = 10.0 m, Length = 3.5D)

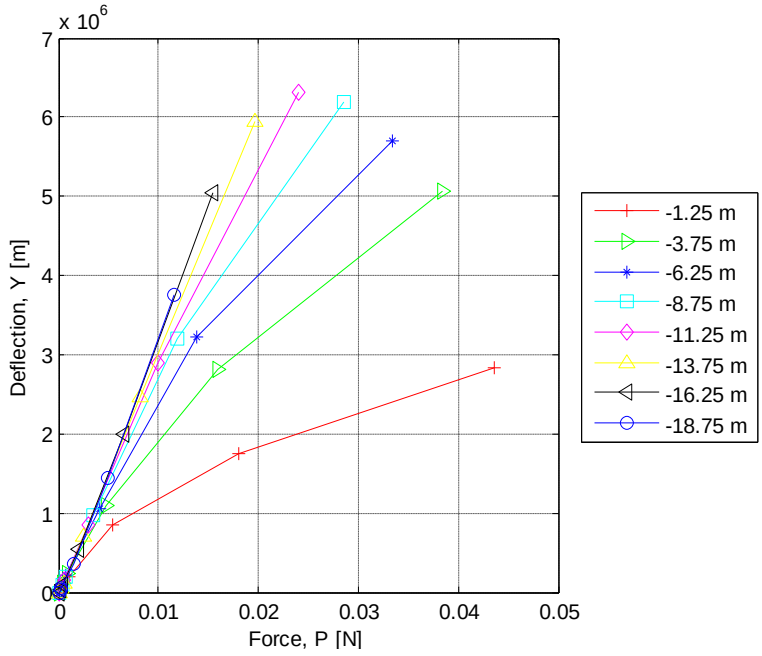

Figure B.28 Nonlinear PY curves set 1 (Pile diameter = 10.0 m, Length = 3D)

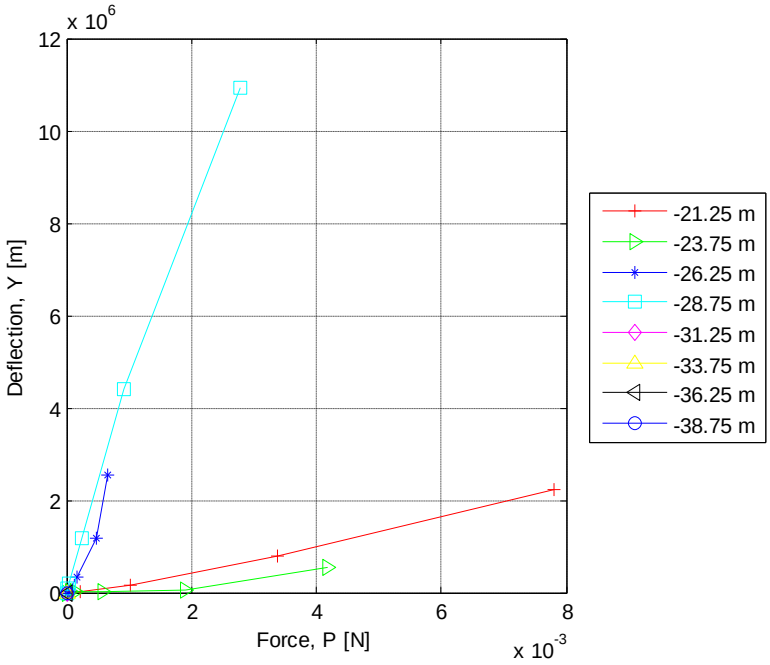

Figure B.29 Nonlinear PY curves set 2 (Pile diameter = 10.0 m, Length = 3D)

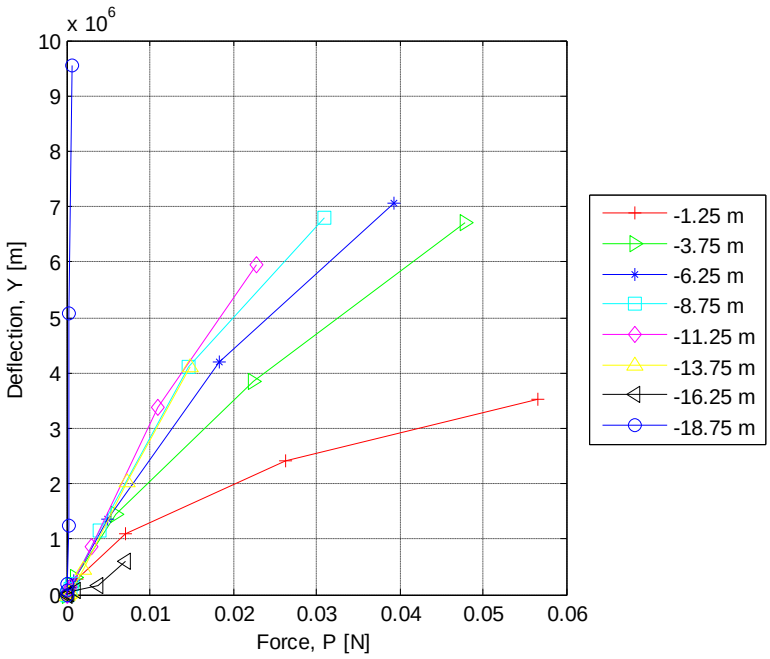

Figure B.30 Nonlinear PY curves set 1 (Pile diameter = 10.0 m, Length = 2D)